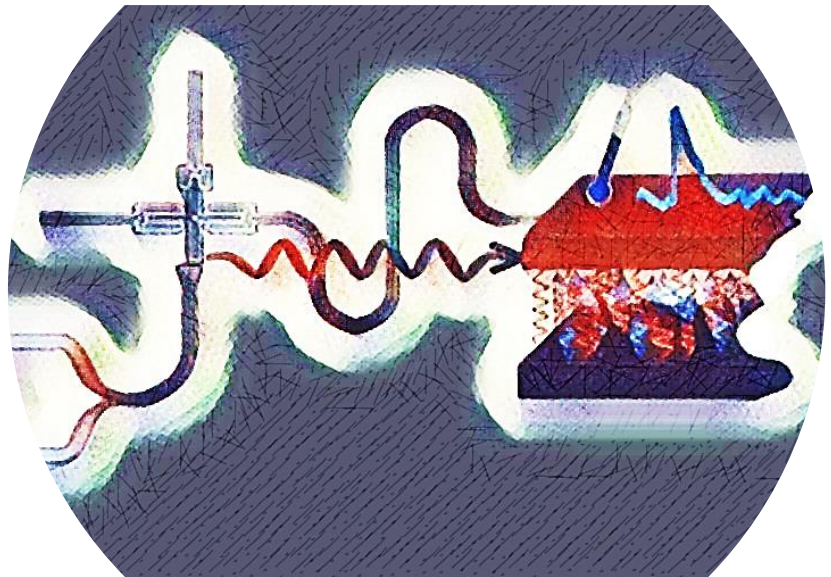


# Circuit Quantum Thermodynamics - from photonic heat transport to ultra-sensitive nanocalorimetry

---

Bayan Karimi



# Circuit Quantum Thermodynamics - from photonic heat transport to ultra- sensitive nanocalorimetry

**Bayan Karimi**

A doctoral thesis completed for the degree of Doctor of Science (Technology) to be defended, with the permission of the Aalto University School of Science, at a public examination in a hybrid mode, held at the lecture hall AS2 of the school (Maarintie 8, Espoo) and via remote connection at <https://aalto.zoom.us/j/69640778733> on the 5th of April, 2022 at 16:00.

**Aalto University  
School of Science  
Department of Applied Physics  
Pico group**

**Supervising professor**

Prof. Jukka P. Pekola, Aalto University, Finland

**Preliminary examiners**

Prof. Elisabetta Paladino, Universita' di Catania, Italy

Prof. Björn Sothmann, Universität Duisburg-Essen, Germany

**Opponents**

Prof. Michael L. Roukes, California Institute of Technology, United States of America

Dr. Rafael Sánchez , Universidad Autónoma de Madrid, Spain

Aalto University publication series

**DOCTORAL THESES 41/2022**

© 2022 Bayan Karimi

ISBN 978-952-64-0737-1 (printed)

ISBN 978-952-64-0738-8 (pdf)

ISSN 1799-4934 (printed)

ISSN 1799-4942 (pdf)

<http://urn.fi/URN:ISBN:978-952-64-0738-8>

Unigrafia Oy

Helsinki 2022

Finland



Printed matter  
4041-0619

**Author**

Bayan Karimi

**Name of the doctoral thesis**

Circuit Quantum Thermodynamics - from photonic heat transport to ultra-sensitive nanocalorimetry

**Publisher** School of Science**Unit** Department of Applied Physics**Series** Aalto University publication series DOCTORAL THESES 41/2022**Field of research** Engineering Physics**Manuscript submitted** 8 March 2022**Date of the defence** 5 April 2022**Permission for public defence granted (date)** 20 December 2021**Language** English **Monograph** **Article thesis** **Essay thesis****Abstract**

Quantum thermodynamics deals with open quantum systems. The word 'open' here means that the system is interacting with its environment, which in the thermodynamics context is a heat bath. Presently a lot of activity is devoted to questions in heat transport, heat engines, refrigerators and ultra-sensitive detectors facilitated by quantum systems as working medium. In this thesis, we investigate both experimentally and theoretically phenomena and devices in quantum thermodynamics realized by superconducting and metal circuits on a chip at low millikelvin temperatures. This is a novel area of research coined circuit quantum thermodynamics, cQTD. The building blocks in the experiments are formed of harmonic oscillators (superconducting cavities), non-linear oscillators (Josephson junctions), and heat baths formed of resistors and phonons on the chip substrate. These systems form well-characterized elements that can be described theoretically, quantitatively accurately, by means of theoretical tools applied earlier to structures in mesoscopic physics. What is new here is the full thermal description of these systems, including various thermal transport mechanisms, like radiative heat by thermal microwave photons, electronic heat transport in metals, superconductors and tunnel contacts, and electron-phonon heat transport.

There are two central topics on which we present new results in the thesis. The first one is the utilization of photonic heat transport on a chip. We develop a theoretical model for a quantum Otto refrigerator, where a superconducting qubit is coupled alternately to two different heat baths, and by the cyclic variation of the qubit energy by external field one can pump heat from the cold bath to the hot one. We demonstrate explicitly the quantum contribution in this heat arising from coherences built into the qubit. We then propose ideas and develop theoretical models to describe superconducting transmon qubit-based quantum heat valves and rectifiers that were realized experimentally in our laboratory during the course of this thesis.

The experimental achievement of the thesis is the demonstration of an ultra-sensitive thermal detector reaching the ultimate noise level dictated by the fundamental thermal fluctuations. This allows us to consider the scheme of detecting single microwave photons in a continuous manner, calorimetrically. The key ingredients of the calorimeter are an ultrasensitive proximity supercurrent thermometer (ZBA thermometer) and a tiny proximitized normal metal absorber. A scheme of coupling a superconducting qubit to this calorimeter is presented and we conclude positively about the possibility of having sufficient signal-to-noise ratio (SNR) in detecting a photon emitted by it. As a final boost to enhance the SNR, we propose splitting of the photon to two uncorrelated baths and performing a cross-correlation measurement of their temperatures.

**Keywords** Quantum thermodynamics, thermometry, nanocalorimetry, quantum heat transport, superconducting circuits, mesoscopic devices

**ISBN (printed)** 978-952-64-0737-1**ISBN (pdf)** 978-952-64-0738-8**ISSN (printed)** 1799-4934**ISSN (pdf)** 1799-4942**Location of publisher** Helsinki**Location of printing** Helsinki**Year** 2022**Pages** 329**urn** <http://urn.fi/URN:ISBN:978-952-64-0738-8>



*To my parents*



# Preface

The work summarized in this thesis was carried out in the Pico group led by Prof. Jukka Pekola at the Department of Applied Physics, Aalto University. Whilst my name is alone on the front cover of this thesis, I am by no means its sole contributor: there are many people behind this work who surely deserve to be acknowledged. Therefore, do not stop here:)

With no doubt, my deepest and utmost gratitude goes to my supervisor, Prof. Jukka Pekola for his endless support and guidance. His infinite enthusiasm, motivation, and immense knowledge of physics both in theory and experiment, make him a source of inspiration and at the same time a wonderful teacher, especially when with his remarkable talent he explains complicated things in a simple and enlightening way. Simply, he enjoys physics and always is ready for discussions and give accurate advice with a perfect blend of insight and humor. His brilliant and skillful supervision enriched this study much higher than my expectation. Thank you Jukka!

I acknowledge my two pre-examiners, Prof. Elisabetta Paladino and Prof. Björn Sothmann for their generous time allocated reading this thesis and for their positive reports! I appreciate Prof. Michael L. Roukes and Dr. Rafael Sanchez for accepting to be opponents and devoting their time and expertise to read and examine this thesis.

One of the valuable and enjoyable things in science is collaboration. I was lucky that I had opportunities to meet and exchange ideas with several brilliant colleagues and friends, and importantly to learn a lot from them, including the ones below, who contributed to the papers which this thesis is based upon. Locally, I would like to express my gratitude to Dr. Joonas Peltonen and Dr. Yu-Cheng (Randy) Chang for teaching me practical skills and advanced techniques in the lab and cleanroom, and for the lively and useful discussions on science and beyond. I would like to thank Dr. Alberto Ronzani, Dr. Jorden Senior, Dr. Azat Gubaydullin, Dr. George Thomas, Dr. Libin Wang, Dr. Dmitry (Dima) Golubev, and Tuomas Tuukkanen. I am very grateful to all of you for the fruitful and educating discussions. My sincere thanks also go to the international collaborators: Dr. Michele Campisi of CNR Pisa, Prof. Rosario Fazio of ICTP Trieste, Prof. ChiiDong

Chen of National Taiwan University-Republic of China, Prof. Joachim Ankerhold of University of Ulm, Dr. Ken Funo from RIKEN, Prof. Dmitri Averin of Stony Brook University, Dr. Fredrik Brange and Prof. Peter Samuelsson of Lund University, Dr. Hans He, M.Sc. Naveen Shetty, Prof. Samuel Lara-Avila and Prof. Sergey Kubatkin of Chalmers University of Technology (thank you also for hosting me during my stay at Chalmers), and Dr. Danilo Nikolic and Prof. Wolfgang Belzig of University of Konstanz (thank you for the numerous and still on-going on-line meetings).

Pico is a unique group with smart and talented people from different cultures and backgrounds. The special and amazing thing about Pico is that it creates bonds between the group members to keep it as a unit. Lively discussions about science or almost everything else either in our offices, in the labs or during lunch times make Pico a pleasant and addictive group to work in. I wish to extend my special thanks to the former and present Picos: Dr. Anna Feshchenko, Prof. Ville Maisi, Dr. Olli-Pentti Saira, Dr. Jonne Koski, Dr. Olivier Maillet, Dr. Leila Najafi, Prof. Matthias Gramich, M.Sc. Jesse Muhojoki, Dr. Shilpi Singh, Dr. Brecht Donvil, Dr. Florian Blanchet, Dr. Klaara Viisanen, Dr. Elsa Mannila, Dr. Andrew Guthrie, Dr. Sergei Lemziakov, Dr. Walter Talarico, Dr. Matteo Rossi, Dr. Caterina Foti, M.Sc. Rishabh Upadhyay, M.Sc. Diego Subero Rengel, M.Sc. Marco Marin Suarez, M.Sc. Dmitrii Lvov, M.Sc. Christoforus Dimas Satrya, M.Sc. Kuan-Hsun Chiang, Eemil Praks, Elias Ankerhold, Ilari Mäkinen, and Minh Pham Nguyen. Thank you all for creating such a wonderful environment in the group. Special thanks go to Dr. Minna Günes, our senior academic coordinator for her endless support and kindness. You are awesome Minna!

Before Corona (BC), Pico has hosted several visitors with whom I had a pleasure to meet and discuss. I would like to thank all of them, especially Prof. Alexander Melnikov, Dr. Ivan Khaymovich, Prof. Andrew Cleland, Prof. Erik Aurell, Prof. Christian Enss, Prof. Klaus Mølmer, Prof. Yuri Galperin, Prof. Haitao Quan, Dr. Francesco Giazotto, Prof. Yuri Pashkin, Prof. Yasuhiro Utsumi, Prof. Keiji Saito, Dr. Paolo Erdman, Dr. Bivas Dutta, Dr. Danial Majidi, Dr. Jonathan Wise, M.Sc. Willy Lim, M.Sc. Ananthu Surendran, M. Sc. Laura Sobral Rey and recently Dr. Kazuyuki Kuroyama. I also thank Dr. Paolo Muratore-Ginanneschi and Brecht for the inspiring discussions that we had.

I wish to extend my special thanks to the groups in the QTF Centre of Excellence, especially to QCD led by Prof. Mikko Möttönen, KVANTTI led by Dr. Sorin Paraoanu (also thank you for being the reviewer of my mid-term), TQT in Turku and presently HelTeC at the University of Helsinki led by Prof. Sabrina Maniscalco. Moreover, I would like to thank colleagues from School of Electrical Engineering on the fourth floor in Micronova.

I am grateful to QuESTech Innovative Training Network (Marie Skłodowska-Curie actions) not only for providing the funding for this thesis but for

introducing me to many brilliant and talented people in this European network. I thank all my friends and colleagues from QuESTech for a great time that we spent together. I wish to show my appreciation to Prof. Hervé Courtois for his unflagging support and to Prof. Clemens Winkelmann especially during the time that I spent in CNRS, and to Mrs. Hendrika (Erika) Borsje Hekking for all her patience and understanding. I would also like to thank Dr. Guido Piaszenski and Dr. Axel Rudzinski for hosting me during my stay at Raith. I acknowledge the facilities and technical support of Otaniemi Research Infrastructure for Micro and Nanotechnologies (OtaNano), OtaNano - Low Temperature Laboratory and OtaNano - Micronova Nanofabrication Centre infrastructures at Aalto University.

It is important to strike a balance with life outside work. I would like to thank all my friends inside and outside Finland who have supported me over the last few years. I want to express the deepest appreciation to my best friend here, Leila who always supported me by her unlimited kindness. You are amazing Leila, I am truly thankful for all those things that you did for me. I want to extend my special thanks to another close friend Dr. Negin Karimi for inspiring and supporting me all the time. Many thanks to all other friends including Dr. Yalda Shoja, M. Sc. Fahimeh Emadi, and especially to the wonderful beach volleyball team! (Although I broke my bone:)).

I am forever indebted to my beloved parents, Habib and Farideh, for their tremendous support, love, and encouragement throughout my life. I am so sad that I could not show this book to you, Father. Deepest thanks to my siblings: Adib, Ahdieh, Forough, and Nadia, thank you for always supporting my adventures, and for your love and belief in me and being joyful and full of life and encouraging me all the time. Special thanks go to my uncle and role model in the childhood, Dr. Ali A. Karimi (Dashi) for continuous support and encouragement in pursuing the scientific path. At the end, Big thanks to my Big family.

Room 4110, Finland, March 8, 2022,

Bayan Karimi



# Contents

<b>Preface</b>	<b>iii</b>
<b>Contents</b>	<b>vii</b>
<b>List of Publications</b>	<b>xi</b>
<b>Author's Contribution</b>	<b>xiii</b>
<b>List of Figures</b>	<b>xix</b>
<b>List of Tables</b>	<b>xxi</b>
<b>Abbreviations</b>	<b>xxiii</b>
<b>1. Introduction</b>	<b>1</b>
<b>I Open quantum systems - concepts and basic methods</b>	<b>9</b>
<b>2. Concepts</b>	<b>11</b>
2.1 Open quantum systems . . . . .	11
2.2 Density matrix of a two-level system . . . . .	12
2.3 Driven two-level system . . . . .	13
2.3.1 Heat current . . . . .	14
2.3.2 Fluctuations of heat current . . . . .	15
2.4 Two-level system between two baths . . . . .	16
<b>3. Systems - realizations in condensed matter</b>	<b>17</b>
3.1 Electrons in a conductor as an open system . . . . .	17
3.1.1 Tunneling . . . . .	17
3.2 Electron-phonon system . . . . .	21
3.3 Quantum heat transport by photons . . . . .	24
3.4 Thermal detector . . . . .	28
3.4.1 Temperature fluctuations . . . . .	29

3.5 Heat capacity . . . . .	30
3.5.1 Comparison of signal-to-noise ratio of different types of calorimeters . . . . .	31
<b>II Quantum thermodynamics in circuits</b>	<b>33</b>
<b>4. Tunneling thermometry</b>	<b>35</b>
4.1 Thermometry by a hybrid junction . . . . .	35
4.1.1 Thermometry based on quasiparticle tunneling .	36
4.1.2 Heat transport in a tunnel junction . . . . .	40
4.1.3 Thermometry based on supercurrent - "ZBA thermometer" . . . . .	42
4.2 RF thermometry . . . . .	46
4.3 Self-heating of the local thermometer . . . . .	51
4.4 Sample fabrication . . . . .	51
4.5 Experimental considerations . . . . .	53
<b>5. Control of photonic heat in cQED structures</b>	<b>55</b>
5.1 Quality factor . . . . .	55
5.2 Analysis of the photonic heat valve in the weak coupling regime . . . . .	58
5.2.1 Local regime . . . . .	59
5.2.2 Global regime . . . . .	62
5.3 Qubit-cavity-bath — cross-over from global to local regime	66
5.4 Thermal rectifier . . . . .	71
5.4.1 Rectification in a two-level system . . . . .	71
5.4.2 Experiment on heat rectification using a resonator-qubit-resonator assembly . . . . .	72
<b>6. Dynamic properties of two-bath systems</b>	<b>75</b>
6.1 Quantum Otto refrigerator . . . . .	75
6.1.1 Basic description . . . . .	75
6.1.2 Different operation regimes . . . . .	80
6.1.3 Supremacy of incoherent cycles . . . . .	80
6.2 Multi-qubit Otto refrigerators . . . . .	82
6.2.1 Correlated versus uncorrelated baths . . . . .	86
<b>7. Calorimetric quantum detector – ultimate resolution</b>	<b>91</b>
7.1 Temperature response of a calorimeter . . . . .	91
7.1.1 Ideal calorimeter . . . . .	92
7.1.2 Influence of non-zero response time of a thermometer . . . . .	93
7.1.3 SNR ratio of a calorimeter in response to absorption of quanta . . . . .	94

7.2	Experimental assessment of a calorimetric quantum detector . . . . .	96
7.2.1	Principles in the experiment . . . . .	96
7.2.2	Results on equilibrium fluctuations . . . . .	99
7.2.3	Discussion . . . . .	101
7.2.4	Results on nonequilibrium fluctuations . . . . .	103
7.3	Proposal of microwave photon detection . . . . .	105
<b>8.</b>	<b>Summary and outlook</b>	<b>111</b>
<b>References</b>		<b>115</b>
<b>Publications</b>		<b>129</b>



# List of Publications

This thesis consists of an overview and of the following publications which are referred to in the text by their Roman numerals.

**I** B. Karimi and J. P. Pekola. Otto refrigerator based on a superconducting qubit: Classical and quantum performance. *Phys. Rev. B*, **94**, 184503, November 2016.

**II** B. Karimi, J. P. Pekola, M. Campisi and R. Fazio. Coupled qubits as a quantum heat switch. *Quantum Sci. Technol.*, **2**, 044007, August 2017.

**III** Bayan Karimi and Jukka P. Pekola. Correlated versus uncorrelated noise acting on a quantum refrigerator. *Phys. Rev. B*, **96**, 115408, September 2017.

**IV** Jukka P. Pekola and Bayan Karimi. Quantum noise of electron–phonon heat current. *J. Low Temp. Phys.*, **191**, 373, January 2018.

**V** Alberto Ronzani, Bayan Karimi, Jorden Senior, Yu-Cheng Chang, Joonas T. Peltonen, ChiiDong Chen, and Jukka P. Pekola. Tunable photonic heat transport in a quantum heat valve. *Nat. Phys.*, **14**, 991, July 2018.

**VI** Bayan Karimi and Jukka P. Pekola. Noninvasive thermometer based on the zero-bias anomaly of a superconducting junction for ultrasensitive calorimetry. *Phys. Rev. Appl.*, **10**, 054048, November 2018.

**VII** Yu-Cheng Chang, Bayan Karimi, Jorden Senior, Alberto Ronzani, Joonas T. Peltonen, Hsi-Sheng Goan, Chii-Dong Chen, and Jukka P. Pekola. Utilization of the superconducting transition for characterizing low-quality-factor superconducting resonators. *Appl. Phys. Lett.*, **115**, 022601, July 2019.

**VIII** Jukka P. Pekola, Bayan Karimi, George Thomas, and Dmitri V. Averin. Supremacy of incoherent sudden cycles. *Phys. Rev. B*, **100**, 085405, August 2019.

**IX** Bayan Karimi, Fredrik Brange, Peter Samuelsson, and Jukka P. Pekola. Reaching the ultimate energy resolution of a quantum detector. *Nat. Commun.*, **11**, 367, January 2020.

**X** Jorden Senior, Azat Gubaydullin, Bayan Karimi, Joonas T. Peltonen, Joachim Ankerhold, and Jukka P. Pekola. Heat rectification via a superconducting artificial atom. *Commun. Phys.*, **3**, 40, February 2020.

**XI** Bayan Karimi and Jukka P. Pekola. Quantum trajectory analysis of single microwave photon detection by nanocalorimetry. *Phys. Rev. Lett.*, **124**, 170601, April 2020.

**XII** Bayan Karimi, Danilo Nikolić, Tuomas Tuukkanen, Joonas T. Peltonen, Wolfgang Belzig, and Jukka P. Pekola. Optimized proximity thermometer for ultrasensitive detection. *Phys. Rev. Appl.*, **13**, 054001, May 2020.

**XIII** Bayan Karimi, Hans He, Yu-Cheng Chang, Libin Wang, Jukka P. Pekola, Rositsa Yakimova, Naveen Shetty, Joonas T. Peltonen, Samuel Lara-Avila, and Sergey Kubatkin. Electron-phonon coupling of epigraphene at millikelvin temperatures measured by quantum transport thermometry. *Appl. Phys. Lett.*, **118**, 103102, March 2021.

**XIV** Jukka P. Pekola and Bayan Karimi. Colloquium: Quantum heat transport in condensed matter systems. *Rev. Mod. Phys.*, **93**, 041001, October 2021.

**XV** Jukka P. Pekola and Bayan Karimi. Ultrasensitive calorimetric detection of single photons from qubit decay. *Phys. Rev. X*, **12**, 011026, February 2022.

**XVI** Bayan Karimi and Jukka P. Pekola. Down-conversion of quantum fluctuations of photonic heat current in a circuit. *Phys. Rev. B*, **104**, 165418, October 2021.

# Author's Contribution

## **Publication I: “Otto refrigerator based on a superconducting qubit: Classical and quantum performance”**

J. P. P. conceived the model and proposed the problems to be addressed. **B. K.** and J. P. P. contributed equally to the analysis of the system and writing the paper.

## **Publication II: “Coupled qubits as a quantum heat switch”**

**B. K.** and J. P. P. conceived the model. **B. K.** performed most of the calculations. **B. K.** and J. P. P. wrote the paper. M. C. and R. F. guided the work on entanglement.

## **Publication III: “Correlated versus uncorrelated noise acting on a quantum refrigerator”**

Both authors contributed equally to all aspects of the work and publication.

## **Publication IV: “Quantum noise of electron–phonon heat current”**

J. P. P. proposed the problem and presented initial results on it. **B. K.** performed the calculations of the paper. **B. K.** wrote the paper with contributions from J. P. P.

**Publication V: “Tunable photonic heat transport in a quantum heat valve”**

**B. K.** and J. P. P. conceived the theory model of the experiment and performed the calculations. The other authors were responsible for the experimental realization. A. R. performed the experiment. A. R., J. S. and Y.-C. C. designed and fabricated the samples. Data analysis was performed by A. R. Y.-C. C. performed the spectroscopy measurements. J. T. P. provided technical support in fabrication, low-temperature set-ups and measurements. All authors have been involved in the discussion of scientific results and implications of this work. The manuscript was written by A. R. with contributions from J. P. P., **B. K.** and J.S. **B. K.** wrote the supplementary material.

**Publication VI: “Noninvasive thermometer based on the zero-bias anomaly of a superconducting junction for ultrasensitive calorimetry”**

**B. K.** fabricated the sample and took the main responsibility of performing the experiment. The analysis of the data was done by **B. K.** with contributions from J. P. P. **B. K.** and J. P. P. wrote the paper.

**Publication VII: “Utilization of the superconducting transition for characterizing low-quality-factor superconducting resonators”**

Y-C. C. designed and fabricated the samples and performed the measurements with the help of J. S. and J. T. P. All authors have been involved in the discussion of scientific results and implications of this work. **B. K.** and J. P. P. calculated properties of the resonator terminated by a SNS junction. **B. K.** wrote parts of the manuscript.

**Publication VIII: “Supremacy of incoherent sudden cycles”**

J. P. P. conceived the model. **B. K.** and J. P. P. analyzed the sudden cycle together with contributions from G. T. and D. A. All the authors contributed equally to the writing of the manuscript.

**Publication IX: “Reaching the ultimate energy resolution of a quantum detector”**

**B. K.** designed and fabricated the sample and was responsible for carrying out the experiments. Data analysis and modeling were done by **B. K.** and J. P. P. with contributions from F. B. and P. S. The manuscript was written by **B. K.** with contributions from J. P. P.

**Publication X: “Heat rectification via a superconducting artificial atom”**

J. S. and A. G. designed, fabricated, and measured the samples. Modelling of the work, which is detailed in the Supplementary Information, was done by **B. K.** and J. P. P. with a contribution from J. A. Support in fabrication, low-temperature set-ups, and measurements was provided by J. T. P. All authors have been involved in the analysis and discussion of scientific results and implications of this work. The manuscript was written by J. S., **B. K.**, J. A., and J. P. P.

**Publication XI: “Quantum trajectory analysis of single microwave photon detection by nanocalorimetry”**

Both authors contributed equally to all aspects of the work and publication.

**Publication XII: “Optimized proximity thermometer for ultrasensitive detection”**

**B. K.** designed and fabricated the sample and performed the experiments with the help from T. T. **B. K.** analyzed the experimental data. The theory model for the experiment and the numerical calculations presented in the figures were done by D. N. and W. B. Support in fabrication, low-temperature set-ups, and measurements was provided by J. T. P. All authors have been involved in the analysis and discussion of scientific results and implications of this work. **B. K.** wrote the experimental part of the manuscript with contributions from J. P. P. The theoretical part was written by D. N. and W. B.

**Publication XIII: “Electron-phonon coupling of epigraphene at millikelvin temperatures measured by quantum transport thermometry”**

H. H. and **B. K.** fabricated the sample. The measurements and data analysis at 2 K were done at Chalmers by H. H. with the help of N. S. and supervision of S. K. and S. L.-A. Measurements at sub-kelvin temperatures were done by **B. K.** with the help of Y.-C. C. and L. W. with support from J. T. P. Data analysis was done by **B. K.** with the contributions from J. P. P. All authors have been involved in the discussion of scientific results and implications of this work. The paper was written by **B. K.**, J. P. P. and H. H.

**Publication XIV: “Colloquium: Quantum heat transport in condensed matter systems”**

Both authors contributed equally to all aspects of the publication, including derivation of previously unpublished results on heat noise.

**Publication XV: “Ultrasensitive calorimetric detection of single photons from qubit decay”**

J. P. P. conceived the model and proposed the problems to be addressed. **B. K.** performed most of the calculations of the paper. **B. K.** and J. P. P. contributed equally to the writing of the paper.

**Publication XVI: “Down-conversion of quantum fluctuations of photonic heat current in a circuit”**

Both authors contributed equally to all aspects of the work and publication.

## List of other publications

The author has also contributed to the following related publications and manuscripts, which are not included in this thesis.

**XVII** F. Brange, P. Samuelsson, B. Karimi, and J. P. Pekola. Nanoscale quantum calorimetry with electronic temperature fluctuations. *Phys. Rev. B*, **98**, 205414, November 2018.

**XVIII** Ken Funo, Neill Lambert, Bayan Karimi, Jukka P. Pekola, Yuta Masuyama, and Franco Nori. Speeding up a quantum refrigerator via counterdiabatic driving. *Phys. Rev. B*, **100**, 035407, July 2019.

**XIX** E. S. Tikhonov, A. O. Denisov, S. U. Piatrusha, I. N. Khrapach, J. P. Pekola, B. Karimi, R. N. Jabdaraghi, and V. S. Khrapai. Spatial and energy resolution of electronic states by shot noise. *Phys. Rev. B*, **102**, 085417, August 2020.

**XX** Florian Blanchet, Yu-Cheng Chang, Bayan Karimi, Joonas T. Peltonen, and Jukka P. Pekola. Radio frequency Coulomb blockade thermometry. *Phys. Rev. Applied*, **17**, L011003, January 2022.



# List of Figures

1.1	Electronics versus heattronics . . . . .	1
1.2	Thermal model of photonic heat transport . . . . .	5
2.1	Open quantum system . . . . .	11
2.2	Two key configurations in quantum thermodynamic experiments . . . . .	15
3.1	Thermal model for e-ph coupling . . . . .	22
3.2	Photonic heat transport in the Johnson-Nyquist setup of two resistors . . . . .	26
3.3	Two types of thermal detectors . . . . .	29
4.1	A typical SINIS structure . . . . .	37
4.2	The role of leakage parameter $\gamma$ in calibration of the thermometer . . . . .	39
4.3	Heat transport properties of a NIS tunnel junction . . . . .	41
4.4	Principle and basic characteristics of the S $\bar{N}$ IS proximity thermometer . . . . .	44
4.5	Main characteristics of the optimized S $\bar{N}$ IS proximity thermometer . . . . .	45
4.6	Basics of the RF transmission measurement . . . . .	47
4.7	Radio-frequency measurement of a hybrid junction . . . . .	48
5.1	Quality factor of a resonator terminated by a dissipative element . . . . .	57
5.2	Quantum heat valve and rectifier in the weak coupling regime and in local picture . . . . .	60
5.3	Local regime in quantum heat valve . . . . .	61
5.4	Global regime in quantum heat valve . . . . .	63
5.5	Relaxation of the qubit to heat bath in different operation regimes . . . . .	66
5.6	The principle of a thermal rectifier . . . . .	70

5.7	Thermal rectifier; principle, sample and result. . . . .	73
6.1	Schematic illustration of quantum refrigerators . . . . .	76
6.2	Thermodynamic cycle of the Otto refrigerator based on the superconducting qubit . . . . .	77
6.3	Cooling power of a quantum Otto refrigerator and the three operation regimes . . . . .	79
6.4	Scheme of quantum heat switch . . . . .	83
6.5	Performance of a heat switch with coupled qubits . . . . .	84
6.6	Comparing the impact of correlated, uncorrelated, and anticorrelated noise sources on a quantum device . . . . .	88
7.1	The calorimeter . . . . .	94
7.2	Temperature response of a calorimeter . . . . .	95
7.3	Measurements of the background noise . . . . .	98
7.4	Equilibrium fluctuations . . . . .	100
7.5	Nonequilibrium temperature fluctuations . . . . .	103
7.6	Two-level system (qubit) coupled to an absorber . . . . .	105
7.7	Splitting the qubit-emitted energy $\hbar\omega_Q$ into two heat baths	106
7.8	Predicted results of a cross-correlation measurement . . .	107

# List of Tables

- |     |   |    |
|-----|---|----|
| 4.1 | Comparison of different thermometry techniques employed<br>in this work from the point of view of self-heating. . . . . | 50 |
|-----|---|----|



# Abbreviations

**cQTD** circuit quantum thermodynamics

**cQED** circuit quantum electrodynamics

**TLS** two-level system

**FDT** fluctuation-dissipation theorem

**DOS** density of states

**SNR** signal-to-noise ratio

**NET** noise-equivalent temperature

**ZBA** zero-bias anomaly



# 1. Introduction

Quantum mechanics is by now a century-old theory which describes and accounts for the physical properties of nature on the atomic and subatomic scales. When a quantum-mechanical system is coupled to an environment, it is called an open quantum system. In reality, all quantum systems must be considered as open quantum systems, since interaction of these systems with their environments is inevitable [1]. Although quantum theory was limited only to atomary physics, in the early twentieth century, and later to materials physics, towards the end of the millennium, other fields like quantum thermodynamics emerged [2, 3]. Essentially, quantum thermodynamics which is a combination of two physical theories, quantum mechanics and thermodynamics, is an exciting and rapidly developing research field and it can be described as "thermodynamics of quantum systems and processes" [4, 5]. One of the most important domains of quantum thermodynamics is in mesoscopic systems, in the low temperature or specifically sub-kelvin temperature range, which is within the scope of our interest here and also reviewed in Publication XIV. Thanks to the advances in not only cryogenics but micro- and nano-fabrication techniques, quantum thermodynamics has grabbed a lot of attention in a unique platform for emergent quantum technologies, the circuit quantum electrodynamics (cQED), now coined as circuit quantum thermodynamics (cQTD).

In order to clarify the connection between cQED and cQTD, we compare the two basic setups as shown in the left side of Fig. 1.1. In the known  $RC$  setup ( $G \equiv R^{-1}$  here), one writes the electrical current through the

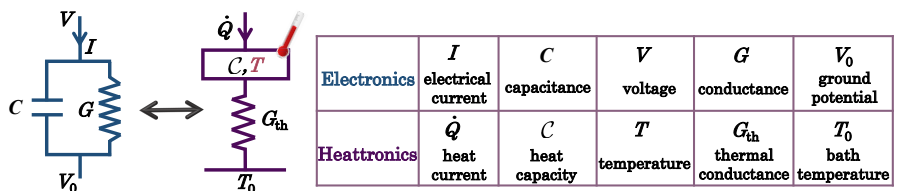


**Figure 1.1.** Electronics versus heattronics. Simple realization in cQED and cQTD basic setups is shown by the circuits on the left. The correspondence of the relevant quantities governing the properties in each case is tabulated on the right.

circuit as  $I = C\dot{V} + G(V - V_0)$ . As to the thermal circuit on the right, an absorber with heat capacity  $\mathcal{C}$  at temperature  $T$  is coupled to a heat bath at temperature  $T_0$  with thermal conductance  $G_{\text{th}}$ . This is one of the central setups in cQTD. The heat current  $\dot{Q}$  which can be a continuous flux or in form of a pulse, through the absorber is then given by  $\dot{Q} = \mathcal{C}\dot{T} + G_{\text{th}}(T - T_0)$ . For a linearized system, the table shown in the right side of Fig. 1.1 presents the correspondence in the parameters of the two setups. A key element here is the temperature of the absorber that can be monitored by proper local thermometers. One can easily see that under steady state conditions, measuring heat current with thermometers for linear system is like Ohm's law, i.e.  $I = G(V - V_0)$  in electronics versus  $\dot{Q} = G_{\text{th}}(T - T_0)$  in heattronics. Often for steady state conditions, the heat current is given by  $\dot{Q} = \mathcal{K}(T^n - T_0^n)$ , where  $\mathcal{K}$  and  $n$  are constants characteristic to the absorber and the process of thermalization. For instance for coupling of metal electrons in an absorber to the phonon bath, the standard expression for the heat current is given by  $\dot{Q} = \Sigma\mathcal{V}(T^5 - T_0^5)$  [6, 7, 8, 9, 10], where  $\Sigma$  is a material specific parameter and  $\mathcal{V}$  the volume of the absorber. For small temperature difference, the thermal conductance reads  $G_{\text{th}} = 5\Sigma\mathcal{V}T_0^4$ . In Section 3.2, we will come back to this with details. Another option in this work is heat carried by microwave photons where  $n = 2$ , and it will be discussed in Section 3.3.

In this thesis, we investigate open quantum systems and quantum thermodynamics in circuits. More specifically, this thesis dwells on an up to now pristine research field of quantum thermodynamics on a chip. Most of the time, the goal is to monitor and control the physical properties of such circuits, which are composed of either one or a few subsystems and their surroundings. Among these subsystems we have resistors, inductors, capacitors and physical substrates forming thermal baths, cavities, and qubits. They host elementary excitations of electrons, photons, and phonons. In what follows we briefly comment on each of these elements in our quantum circuits. Resistor, which is made of normal metal and it has a finite volume  $\mathcal{V}$ , here typically  $\mathcal{V} \sim 10^{-21} \text{ m}^3$ , is a fermionic system (consists of about  $10^8$  electrons). Due to the fast electron-electron relaxation time and weak electron-phonon coupling, normal metal introduces a separation of time scales and as a result it becomes a natural choice to be used either as a thermal bath or an absorber in cQTD experiments, depending on the focus of the problem in quantum heat transport devices or nanocalorimetry, respectively. Microscopically, a resistor can be modeled as a collection of bosonic oscillators, as will be discussed in details in Section 3.3. Importantly, a resistor with temperature  $T$  can serve as a thermal photon source [11, 12, 13, 14]. Next element is a  $LC$  resonator, which can be characterized either by its inductance  $L$  and capacitance  $C$  or, equivalently, by its angular frequency  $\omega_0 = 1/\sqrt{LC}$  and characteristic impedance  $Z_0 = \sqrt{L/C}$ . The Hamiltonian of such a  $LC$  resonator is com-

posed of two terms  $q^2/(2C) + \Phi^2/(2L)$ , where the first term refers to the kinetic energy with  $q$  the charge on the capacitor and the second one is the potential energy with  $\Phi$  the flux threading the inductor. Since charge is the conjugate momentum to flux as  $q = C\dot{\Phi}$ , the Hamiltonian can be written in the same way as before but this time with the charge and flux operator that satisfy  $[\hat{\Phi}, \hat{q}] = i\hbar$ , in analogy to position and momentum in mechanical systems. By introducing the annihilation  $\hat{c}$  and creation  $\hat{c}^\dagger$  operators such that  $[\hat{c}, \hat{c}^\dagger] = 1$ , the flux and charge operators can be written as  $\hat{\Phi} = \sqrt{\hbar Z_0/2}(\hat{c} + \hat{c}^\dagger)$  and  $\hat{q} = -i\sqrt{\hbar/(2Z_0)}(\hat{c} - \hat{c}^\dagger)$ , respectively. This leads to another equivalent expression for the Hamiltonian of a *LC* resonator  $\hat{H} = \hbar\omega_0(\hat{c}^\dagger\hat{c} + 1/2)$  the standard harmonic oscillator Hamiltonian. In this thesis we use two types of *LC* oscillators: planar-spiral and coplanar waveguide resonators, whose resonance frequencies are in the range of  $0.1 - 10$  GHz, respectively. The coplanar waveguide resonator acts as a transmission line and it is used to convey microwave-frequency signals. The characteristic impedance  $Z_0 = \sqrt{\ell_0/c_0} \sim 50\Omega$  and the speed of light in the waveguide  $v_0 = 1/\sqrt{\ell_0 c_0}$  with  $\ell_0$  and  $c_0$  as inductance per unit length and capacitance to ground, respectively, are the two parameters describing the electromagnetic properties of a coplanar waveguide resonator [15, 16]. Based on imposing different boundary conditions to a coplanar waveguide at its two end points which are separated by a distance  $d$ , one forms typically  $\lambda/2$ - and  $\lambda/4$ -resonators. The two boundary conditions are either zero voltage (shorted boundary) or zero current (open boundary).  $\lambda/2$ -resonator is a type of coplanar waveguide which has open boundary conditions at both ends. The fundamental frequency of  $\lambda/2$ -resonator is  $f_0 = v_0/2d$  with harmonics at  $f_m = (m + 1)f_0$ . Differently,  $\lambda/4$ -resonator is obtained with one open end and one grounded end with fundamental frequency  $f_0 = v_0/4d$  [15, 17]. To avoid dissipation, coplanar waveguide resonators usually are made of superconductors such as aluminum or niobium on sapphire or high-resistivity silicon substrates [18, 19]. In order to estimate the value of  $v_0$ , one can use another equivalent expression for speed of light on a substrate which is given by  $v_0 = 1/\sqrt{\epsilon\mu}$ . Since on the mentioned substrates  $\mu \approx \mu_0$  (vacuum permeability) and taking into account that half of the space is vacuum, we have  $v_0 \sim 1 \times 10^8$  m/s for silicon and sapphire substrates, respectively. Up to now we discussed a linear element i.e. a harmonic oscillator. To exploit genuine quantum properties, one needs a non-linear element in a circuit. The Josephson tunnel junction serves this purpose. It is typically made of a thin insulating barrier interrupting a superconducting wire and it admits tunneling effects between the two electrodes [20]. The insulating barrier causes a phase difference  $\phi$  across the junction which is related to flux by  $\phi = (2e/\hbar)\Phi$ . Current  $I$  and voltage  $V$  at the junction which are given by the AC- and DC-Josephson relations [20, 21], as

$$\hbar\dot{\phi} = 2eV, \quad I = I_c \sin \phi, \quad (1.1)$$

where  $I_c = \pi\Delta/(2eR_n)$  is the critical current of the junction. Here,  $\Delta$  and  $R_n$  are the superconducting gap and normal state resistance of the junction, respectively. Note that, for different types of weak links, sinusoidal dependence does not necessarily hold [22]. In order to calculate the energy stored in the junction, one integrates the work done on this nonlinear inductor. We then have

$$E = \int^{\Phi} I d\Phi = -E_J \cos \phi, \quad (1.2)$$

where  $E_J = \hbar I_c/(2e)$  is the Josephson energy. Importantly,  $E_J$  along with charging energy  $E_C = e^2/2C_J$  with  $C_J$  the capacitance of the junction, are the two energies that characterize a Josephson junction. The Hamiltonian of this element then reads  $\hat{H} = \hat{q}^2/2C - E_J \cos \hat{\phi}$ . In this case unlike for the linear inductor with the parabolic potential, the energy levels are not equidistant. For small values of  $\phi$ , the potential energy of the junction can be written as  $E \simeq \frac{\Phi^2}{2L_J}$ , where  $L_J = \hbar/(2eI_c)$  is the Josephson inductance. In this “linear regime” a Josephson junction can also be considered as a harmonic oscillator and what is written earlier for a harmonic oscillator can be rewritten by replacing  $L$  with  $L_J$ . Yet the actual non-linearity of a Josephson junction makes it an invaluable component in quantum information processing and in quantum thermodynamics. A practically useful tool in a quantum circuit is DC superconducting quantum interference device (DC-SQUID) which is a superconducting loop containing two Josephson junctions [22, 23]. By applying magnetic flux  $\Phi$  to the SQUID loop, the inductance is periodic in magnetic flux (period  $\Phi_0 = h/2e$ , the flux quantum), i.e.  $L_J(\Phi) = \Phi_0/(2\pi I_c |\cos(\pi\Phi/\Phi_0)|)$ . In this thesis, we use a transmon-type qubit [24] which is practically a DC-SQUID capacitively coupled to a coplanar waveguide resonator and is excited with microwaves, i.e. the SQUID is used as a central element in the qubit.

Having introduced the various elements as circuit components, we combine these building blocks to form open quantum systems with well-defined properties. One can then utilize them in fundamental quantum thermodynamics experiments with tailored properties, or one can build useful devices out of them as will be described further in this thesis. The beauty indeed lies in that superconducting cavities, Josephson junctions and engineered heat baths in form of resistors can be modeled very accurately; thus, they provide a solid basis for the experiments to be described in this thesis. Furthermore, the low temperatures allow one to measure the tiny amounts of heat in quantum thermodynamic experiments directly as local temperature changes by using sensitive thermometers employed and developed further in this thesis.

The systems under study in this thesis can be presented by two schemes, shown schematically in Figs. 1.1 and 1.2. The simple scheme is shown in Fig. 1.1 displaying one of the basic setups in cQTD, a thermal detector realizing bolometry and calorimetry with ultrasensitive thermometry.

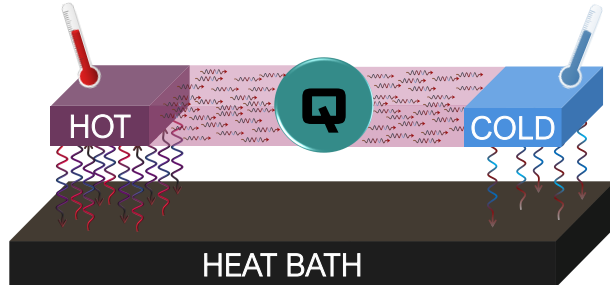


**Figure 1.2.** Thermal model of photonic heat transport. Two finite-sized absorbers each coupled to the heat bath and to each other via a quantum system.

Bolometry refers to detection of steady-state heat currents, whose sources can be injection of hot carriers, Joule dissipation, or coupling to photonic or phononic degrees of freedom in the circuit. On the other hand, calorimetry means thermal detection of single events, e.g., emission or absorption of a photon from a superconducting qubit. In both these tasks, one needs a thermometer with proper figures of merit. The principle of such thermal detectors will be discussed later in Section 3.4. The other scheme, shown in Fig. 1.2, presents a differential two-absorber setup. It allows for measurements of the temperatures of the two absorbers,  $T_1$  and  $T_2$ , separately, and to determine the heat flux between the two, without extra physical connections across the object of interest. In this case one can replace  $T, T_0$  by  $T_1, T_2$ , respectively, as compared to the previous setup in Fig. 1.1. By inserting a tunable quantum system between the two absorbers, heat transport is controlled by either magnetic or electric field to achieve useful functional operation. These devices include e.g., heat valves, heat interferometers, thermal rectifiers and quantum engines and refrigerators.

This thesis includes both experimental and theoretical results. After the present introductory chapter, we divide it into two parts. In Part I, the concepts and basic methods in open quantum systems are presented in two chapters (2 and 3). Both of these chapters give a brief theoretical background of the basic principles employed in Part II. In chapter 2, we start by clarifying the concept of an open quantum system in this thesis. The main focus is on a two-level system (TLS) coupled to an environment (thermal bath) in different configurations, which includes finding the density matrix of TLS in both non-driven and driven cases, while the TLS is placed between two baths. In some of the configurations the magnitude of heat current and its fluctuations are presented. Physical realizations of open quantum systems in the weak coupling regime that were discussed in chapter 2 are introduced in chapter 3. These examples are tunnel junctions, electron-phonon, and photonic coupling including some detailed theoretical calculations about heat current and its fluctuations in such systems. Some of these results are presented in Publication IV. In what follows in

this chapter, we first discuss quantum heat transport by photons, which covers the results in Publication XVI and second, thermal detectors. The operation principles of such thermal sensors along with the theoretical expectations of the fluctuations of their effective temperature are presented. At the end of the chapter, the influence of some parameters on the energy resolution of thermal detectors, one of the central quantity in these devices, is presented.

In Part II, we present quantum thermodynamics in circuits and summarize the publications listed at the beginning of the thesis in four chapters. A central task in performing an experiment in cQTD devices is local probing to determine the temperature of the electronic system. In chapter 4, two types of hybrid junctions that are working based on the quasiparticle tunneling and supercurrent, are explained. These local sensors are essential tools in performing experiments in all our setups. This chapter covers the research outcomes performed in Publication VI and Publication XII. This chapter also gives a brief summary of the relevant fabrication methods and experimental setups. After combining all the building blocks introduced above and different kinds of thermometers presented in chapter 4, one can construct various cQTD configurations like heat valves, thermal diodes (rectifiers), heat engines and refrigerators. Chapter 5 is devoted to such devices where a superconducting qubit or some other quantum element as a tunable component is placed between two thermal baths via coplanar waveguide resonators. Publication V, Publication VII, Publication X, and Publication XV are summarized in this chapter. The dynamical properties of open quantum systems for cQTD devices which are introduced in the previous chapters, are discussed in chapter 6. Here, we analyze the cyclic refrigerator in particular in form of an Otto cycle. We start with realistic description of two types of physical systems and analyze their performance in the quasistatic regime. Thereafter, we introduce the relevant master equation which allows us to look at finite frequency properties. We pay special attention to the influence of coherence on the performance of the Otto refrigerator; likewise, we study how the degree of correlation in heat baths affects its properties. We summarize Publication I, Publication II, Publication III, and Publication VIII in this chapter.

The last but not least topic of the thesis is discussed in chapter 7, where we present an ultra-sensitive thermal detector reaching the ultimate noise level dictated by the fundamental thermal fluctuations. This allows us to consider the scheme of detecting single microwave photons in a continuous manner, calorimetrically. A scheme of coupling a superconducting qubit to this calorimeter is presented and we conclude positively about the possibility of having sufficient signal-to-noise ratio ( $\text{SNR}$ ) in detecting them. As a final boost to enhance this  $\text{SNR}$ , we propose “splitting of the photon” to two uncorrelated baths and performing a cross-correlation measurement of their temperatures. This chapter covers the research outcomes

in Publication IX, Publication XI, Publication XIII, and Publication XV.



## **Part I**

### **Open quantum systems - concepts and basic methods**



## 2. Concepts

### 2.1 Open quantum systems

In this thesis, we discuss artificial quantum systems that are interacting with their environment. The basic approach to treat such open quantum systems [1] is to write the Hamiltonian of the whole "universe" such that the separate parts of it, the quantum system of interest and the environment are coupled weakly to each other. Then the properties of the system itself can be found out by taking the trace over the degrees of freedom of the environment. This scenario is schematically represented in the left side of Fig. 2.1, where the quantum system with Hamiltonian  $\hat{\mathcal{H}}_S$  is weakly coupled with interaction energy  $\hat{V}$  to the heat bath with Hamiltonian  $\hat{\mathcal{H}}_B$ . The total Hamiltonian is then given by

$$\hat{\mathcal{H}} = \hat{\mathcal{H}}_S + \hat{V} + \hat{\mathcal{H}}_B. \quad (2.1)$$

We aim to write the master equation for the reduced density matrix of an open quantum system. In the weak coupling regime, the total density matrix can be written as a product  $\rho_{\text{tot}} = \rho \otimes \rho_B$ , where  $\rho$  and  $\rho_B$  are

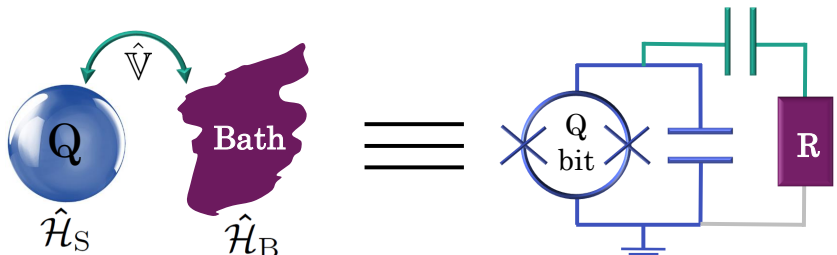


**Figure 2.1.** Open quantum system. (left) The quantum system is weakly coupled to a heat bath.  $\hat{\mathcal{H}}_S$  and  $\hat{\mathcal{H}}_B$  denote the Hamiltonian of the system and heat bath, respectively, and  $\hat{V}$  stands for interaction energy between them. (right) A representative circuit diagram of the system shown on the left. The qubit is shown in blue, capacitively coupled to a resistive element  $R$  in purple.

the density matrix of the system and environment, respectively. The Liouville–von Neumann equation in the interaction picture then reads

$$\dot{\rho}_{\text{tot}}(t) = \frac{i}{\hbar}[\rho_{\text{tot}}(t), \hat{V}_I(t)]. \quad (2.2)$$

At time  $t$  the total density matrix is  $\rho_{\text{tot}}(t) = \rho_{\text{tot}}(-\infty) + \int_{-\infty}^t dt' \dot{\rho}_{\text{tot}}(t')$ , then Eq. (2.2) yields

$$\dot{\rho}_{\text{tot}}(t) = \frac{i}{\hbar}[\rho_{\text{tot}}(-\infty), \hat{V}_I(t)] - \frac{1}{\hbar^2} \int_{-\infty}^t dt' [[\rho_{\text{tot}}(t'), \hat{V}_I(t')], \hat{V}_I(t)]. \quad (2.3)$$

The density matrix of an infinite heat bath does not change with time,  $\dot{\rho}_B = 0$ , and we are interested in the density matrix of the system only. Then we can trace over the bath,  $\text{Tr}_B$ , and obtain

$$\dot{\rho}(t) = \text{Tr}_B \left\{ \frac{i}{\hbar} [\rho(-\infty) \rho_B, \hat{V}_I(t)] \right\} - \frac{1}{\hbar^2} \text{Tr}_B \left\{ \int_{-\infty}^t dt' [[\rho(t') \rho_B, \hat{V}_I(t')], \hat{V}_I(t)] \right\}, \quad (2.4)$$

where the first term vanishes for noise. Equation (2.4) is a second-order master equation. We consider a real setup shown in the right side of Fig. 2.1, a representative circuit diagram of the system shown in the left, where the quantum bit (qubit) is weakly coupled to the environment. Next, we apply Eq. (2.4) to this setup.

## 2.2 Density matrix of a two-level system

In this section, we write the density matrix of a qubit, simply known as a quantum two-level system (TLS), coupled to a heat bath (environment) for the non-driven and driven case. The Hamiltonian of the system (qubit here) is  $\hat{H}_S = \hbar \omega_Q \hat{a}^\dagger \hat{a}$  where  $\hat{a} = |g\rangle\langle e|$  ( $\hat{a}^\dagger = |e\rangle\langle g|$ ) is the annihilation (creation) operator for the qubit with eigenstates  $|g\rangle$  and  $|e\rangle$  for the ground and excited state, respectively. Due to the weak coupling, the energy between the qubit (TLS) and the resistor (heat bath) works as a perturbation. Generally, in the linear coupling regime, the perturbation can be written as  $\hat{V} = \hat{A} \hat{X}_n(t)$ , where  $\hat{A}$  is the operator of the system and  $\hat{X}_n(t)$  is the noise operator of the environment. Depending the configuration of the setup, meaning voltage or current biasing, the coupling term is either  $\hat{V} = \hat{q} v_n(t)$  or  $\hat{V} = \hat{\Phi} i_n(t)$ . Here  $\hat{q} = -i\sqrt{\hbar/(2Z_Q)}(\hat{a} - \hat{a}^\dagger)$  and  $\hat{\Phi} = \sqrt{\hbar Z_Q/2}(\hat{a} + \hat{a}^\dagger)$  are the charge and phase operators of the system, respectively, where  $Z_Q = \sqrt{L_Q/C_Q}$  with the Josephson inductance and capacitance of the qubit, and  $v_n(t)$  ( $i_n(t)$ ) denotes the voltage (current) noise of the resistor. We take the first option. Then the coupling Hamiltonian in the interaction picture is given by

$$\hat{V}_I(t) = \gamma e^{i\mathcal{H}_{\text{st}} t/\hbar} (\hat{a}^\dagger - \hat{a}) e^{-i\mathcal{H}_{\text{st}} t/\hbar} \delta v(t), \quad (2.5)$$

where  $\gamma$  includes all the prefactors from the charge operator of the qubit and voltage noise of the resistor  $\delta v(t) = \zeta v_n(t)$  and can be obtained based

on the physical circuit parameters. Here  $\zeta$  depends on the equivalent circuit of the real setup. As an example, for the setup shown in the right side of Fig. 2.1, we have  $\zeta = C_g/(C_g + C_Q)$ , where  $C_g$  and  $C_Q$  are the capacitances shown in green and blue, respectively. For different couplings like inductive coupling and different setups,  $\zeta$  will change accordingly. Taking into account that, the average of the random noise is zero,  $\text{Tr}_B(\rho_B \delta v(t)) \equiv \langle \delta v(t) \rangle = 0$ , the first term in Eq. (2.4) vanishes. The nested commutator in (2.4) has four terms  $[[\rho(t')\rho_B, \hat{V}_I(t')], \hat{V}_I(t)] = \rho(t')\rho_B \hat{V}_I(t')\hat{V}_I(t) - \hat{V}_I(t')\rho(t')\rho_B \hat{V}_I(t) - \hat{V}_I(t)\rho(t')\rho_B \hat{V}_I(t') + \hat{V}_I(t)\hat{V}_I(t')\rho(t')\rho_B$ , and we can apply trace on them; the first term as an example reads

$$\text{Tr}_B(1) = -\gamma^2 \rho(t') e^{i\mathcal{H}t'/\hbar} (\hat{a}^\dagger - \hat{a}) e^{-i\mathcal{H}(t'-t)/\hbar} (\hat{a}^\dagger - \hat{a}) e^{-i\mathcal{H}t/\hbar} \langle \delta v(t') \delta v(t) \rangle, \quad (2.6)$$

where  $\text{Tr}_B\{\rho_B \delta v(t') \delta v(t)\} \equiv \langle \delta v(t') \delta v(t) \rangle$ . In order to obtain the time derivative of the population of the ground state  $\dot{\rho}_{gg}(t) \equiv \langle g | \dot{\rho}(t) | g \rangle$ , one needs to evaluate all the mentioned four terms in Eq. (2.4) yielding

$$\dot{\rho}_{gg}(t) = -\Gamma_\uparrow \rho_{gg}(t) + \Gamma_\downarrow \rho_{ee}(t), \quad (2.7)$$

where the excitation and relaxation rates are  $\Gamma_\uparrow = \frac{\gamma^2}{\hbar^2} S_v(-\omega_Q)$  and  $\Gamma_\downarrow = \frac{\gamma^2}{\hbar^2} S_v(\omega_Q)$ , respectively. Here  $S_v(\omega) = \int_{-\infty}^{\infty} du e^{i\omega u} \langle \delta v(u) \delta v(0) \rangle$  is the spectral density of voltage noise at frequency  $\omega/2\pi$  and  $\rho_{ee}(t) = 1 - \rho_{gg}(t)$  as the population of the excited state. With the same procedure the off-diagonal part of the master equation is given by

$$\dot{\rho}_{ge}(t) = -\frac{1}{2} \Gamma_\Sigma \rho_{ge}, \quad (2.8)$$

where  $\Gamma_\Sigma = \Gamma_\downarrow + \Gamma_\uparrow$ . In this analysis we have ignored the influence of low frequency noise on decoherence [25].

### 2.3 Driven two-level system

In this section we obtain the master equation of a weakly driven TLS coupled to the environment as shown in Fig. 2.2(a). The discussion about solving the master equation of this setup is pretty much similar to the previous section. As shown in the figure, the perturbative term is now composed of two parts; one comes from the environment, like a heat bath, which was discussed above and the other one from the drive  $V_d$ . In this case, the Liouville–von Neumann equation in the interaction picture (Eq. (2.2)) reads  $\dot{\rho}_{\text{tot}}(t) = \frac{i}{\hbar} [\rho_{\text{tot}}(t), \hat{V}_I(t) + \hat{V}_{d,I}(t)]$ . The first part represents again coupling of TLS to the heat bath. For the drive term we have  $\dot{\rho}_{\text{tot}}(t) = \frac{i}{\hbar} [\rho_{\text{tot}}(t), \hat{V}_{d,I}(t)]$ . The coupling energy of the drive reads  $\hat{V}_d = \lambda(t)(\hat{a} + \hat{a}^\dagger)$ , for instance, for a superconducting quantum interference device (SQUID)

driven by a flux perturbation as shown in the figure. The drive term in the interaction picture can then be written as

$$\hat{V}_{d,I} = \lambda(t) e^{i\hat{\mathcal{H}}_0 t/\hbar} (\hat{a} + \hat{a}^\dagger) e^{-i\hat{\mathcal{H}}_0 t/\hbar}, \quad (2.9)$$

where  $\hat{\mathcal{H}}_0 = \hat{\mathcal{H}}_S + \hat{\mathcal{H}}_B$  is the Hamiltonian of the unperturbed part. Following the procedure presented in Section 2.2, the diagonal term of the master equation  $\dot{\rho}_{gg}(t) \equiv \langle g | \frac{i}{\hbar} [\rho(t), \hat{V}_{d,I}(t)] | g \rangle$  is then given by

$$\begin{aligned} \dot{\rho}_{gg}(t) &= \frac{i\lambda(t)}{\hbar} \left\{ \langle g | \rho e^{i\hat{\mathcal{H}}_0 t/\hbar} \sum_{i=g,e} |i\rangle \langle i| (\hat{a} + \hat{a}^\dagger) e^{-i\hat{\mathcal{H}}_0 t/\hbar} |g\rangle \right. \\ &\quad \left. - \langle g | e^{i\hat{\mathcal{H}}_0 t/\hbar} (\hat{a} + \hat{a}^\dagger) \sum_{i=g,e} |i\rangle \langle i| e^{-i\hat{\mathcal{H}}_0 t/\hbar} \rho |g\rangle \right\} \\ &= -\frac{2\lambda(t)}{\hbar} \Im(\rho_{ge}(t) e^{i\omega_Q t}), \end{aligned} \quad (2.10)$$

where  $\hbar\omega_Q = E_e - E_g$  is the qubit's energy-level separation. Similarly the off-diagonal term reads

$$\dot{\rho}_{ge}(t) = \frac{i\lambda(t)}{\hbar} e^{-i\omega_Q t} (\rho_{gg} - \rho_{ee}). \quad (2.11)$$

Adding the noise from the heat bath and applying  $\rho_{ee} = 1 - \rho_{gg}$ , and additionally using the set of Eqs. (2.10), (2.11), (2.7), and (2.8), the master equation for the setup presented in Fig. 2.2(b) is given by

$$\begin{aligned} \dot{\rho}_{gg}(t) &= -(\Gamma_\uparrow + \Gamma_\downarrow)\rho_{gg}(t) + \Gamma_\downarrow - \frac{2\lambda(t)}{\hbar} \Im(\rho_{ge}(t) e^{i\omega_Q t}) \\ \dot{\rho}_{ge}(t) &= -\frac{1}{2}(\Gamma_\uparrow + \Gamma_\downarrow)\rho_{ge}(t) + \frac{i\lambda(t)}{\hbar} e^{-i\omega_Q t} (2\rho_{gg} - 1). \end{aligned} \quad (2.12)$$

### 2.3.1 Heat current

After obtaining the density matrix of the TLS for non-driven case, we now evaluate the heat current from the resistor to the qubit in the same setup. We start

$$\begin{aligned} d\hat{\mathcal{H}}_S/dt &= \frac{i}{\hbar} [\hat{V}(t), \hat{\mathcal{H}}_S] \\ &= \gamma\omega_Q (\hat{a}^\dagger + \hat{a}) \delta v(t). \end{aligned} \quad (2.13)$$

The expectation value of heat current into the qubit  $\dot{Q} \equiv \langle d\hat{\mathcal{H}}_S/dt \rangle$  is obtained by applying the Kubo formula [26] (linear response) in the interaction picture for both heat current and voltage noise operators,  $\hat{O}_I(t) = e^{i\hat{\mathcal{H}}_S t/\hbar} \hat{O} e^{-i\hat{\mathcal{H}}_S t/\hbar}$ . Applied to Eq. (2.13) we have

$$\dot{Q} = -\frac{i}{\hbar} \int_{-\infty}^0 dt' \langle [d\hat{\mathcal{H}}_{S,I}(0)/dt, \hat{V}_I(t)] \rangle, \quad (2.14)$$

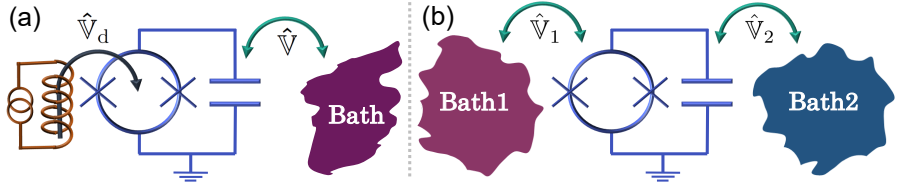


**Figure 2.2.** Two key configurations in quantum thermodynamic experiments. (a) A qubit coupled to one heat bath and to a driving circuit. We envision here coupling the drive via the flux through a SQUID loop in the qubit. (b) Two heat baths connected to each other via a qubit. In the modelling we assume that these two baths act as uncorrelated noise sources influencing the transition rates of the qubit. All couplings in this analysis are assumed to be weak to allow us to use the standard perturbation theory.

where the average is equivalent to applying trace to the system and bath meaning  $\langle \cdot \rangle \equiv \text{Tr}_S \text{Tr}_B(\cdot)$ . With the same procedure as mentioned for evaluating the density matrix, the heat current is obtained as

$$\dot{Q} = \hbar\omega_Q (\rho_{gg}\Gamma_\uparrow - \rho_{ee}\Gamma_\downarrow). \quad (2.15)$$

### 2.3.2 Fluctuations of heat current

In order to calculate heat current fluctuations  $S_{\dot{Q}}(\omega)$ , one needs to evaluate

$$S_{\dot{Q}}(\omega) = \int_{-\infty}^{\infty} dt e^{i\omega t} \langle \frac{d\hat{H}_S(t)}{dt} \frac{d\hat{H}_S(0)}{dt} \rangle. \quad (2.16)$$

Inserting the operator of heat current Eq. (2.13) into Eq. (2.16), and with the same procedure as in calculating the averaged heat current, the spectral density of heat current yields

$$S_{\dot{Q}}(\omega) = \gamma^2 \omega_Q^2 \left\{ \rho_{gg} \int_{-\infty}^{\infty} dt e^{i(\omega - \omega_Q)t} \langle \delta v(t) \delta v(0) \rangle + \rho_{ee} \int_{-\infty}^{\infty} dt e^{i(\omega + \omega_Q)t} \langle \delta v(t) \delta v(0) \rangle \right\}. \quad (2.17)$$

In the classical limit,  $\omega = 0$ , Eq. (2.17) leads to a known result

$$S_{\dot{Q}}(0) = \gamma^2 \omega_Q^2 \{ \rho_{gg}\Gamma_\uparrow + \rho_{ee}\Gamma_\downarrow \}. \quad (2.18)$$

On the other hand, at non-vanishing frequencies, Eq. (2.17) reads

$$S_{\dot{Q}}(\omega) = 2\gamma^2 \omega_Q^2 R \hbar \left\{ \rho_{gg} \frac{\omega - \omega_Q}{e^{\beta \hbar(\omega - \omega_Q)} - 1} + \rho_{ee} \frac{\omega + \omega_Q}{e^{\beta \hbar(\omega + \omega_Q)} - 1} \right\}, \quad (2.19)$$

where we used  $\int_{-\infty}^{\infty} dt e^{i(\omega \pm \omega_Q)t} \langle \delta v(t) \delta v(0) \rangle = S_v(\omega \pm \omega_Q)$  with  $S_v(\Omega) = 2R\hbar\Omega/(1 - e^{-\beta\hbar\Omega})$  as the spectral density of the voltage noise of a bare resistor  $R$  at angular frequency  $\Omega$ .

## 2.4 Two-level system between two baths

After describing the TLS coupled to a heat bath, now we step further and describe a configuration where the TLS is coupled to two heat baths as shown in Fig. 2.2(a). One of the interesting aspects of such setups is heat transport from one bath to the other via the TLS. The total Hamiltonian of this setup is similar to the one given in Eq. (2.1) with the difference that coupling energy  $\hat{V}$  and Hamiltonian of the bath  $\hat{\mathcal{H}}_B$  now are given by

$$\hat{V} = \hat{V}_1 + \hat{V}_2, \text{ and } \hat{\mathcal{H}}_B = \hat{\mathcal{H}}_{B1} + \hat{\mathcal{H}}_{B2}, \quad (2.20)$$

where  $\hat{V}_i$  and  $\hat{\mathcal{H}}_{Bi}$  are the coupling energy between TLS and bath  $i$  and with Hamiltonian  $\hat{\mathcal{H}}_{Bi}$  for  $i = 1, 2$ . The procedure of calculating the density matrix, heat current and its noise is as for TLS coupled to one bath. Like Eq. (2.5), the coupling Hamiltonian between the TLS and each reservoir reads  $\hat{V}_i = i\gamma_i(\hat{a}^\dagger - \hat{a})\delta v_i(t)$  for  $i = 1, 2$ . We start by writing the master equation given in Eq. (2.3). Since the average of random noise vanishes  $\langle \delta v_i \rangle = 0$ , the first term of Eq. (2.3) for this setup will be zero. The nested commutator  $[[\rho(t')\rho_B, \hat{V}_{1,I}(t') + \hat{V}_{2,I}(t')], \hat{V}_{1,I}(t) + \hat{V}_{2,I}(t)]$  in this case is composed of sixteen terms instead of four, but since we assume our two heat baths are independent with uncorrelated noise sources then the cross terms vanish, i.e.  $\langle \hat{V}_{i,I}\hat{V}_{j,I} \rangle = 0$  when  $i \neq j$ , and only the terms  $\langle \hat{V}_{i,I}\hat{V}_{i,I} \rangle$  survive. In this case only eight terms will survive. It turns out that the diagonal and off-diagonal components of the master equation have the same expression as in Eqs. (2.7) and (2.8), i.e.

$$\dot{\rho}_{gg}(t) = -\Gamma_\uparrow^{(t)}\rho_{gg}(t) + \Gamma_\downarrow^{(t)}\rho_{ee}(t), \text{ and } \dot{\rho}_{ge}(t) = -\frac{1}{2}\Gamma_\Sigma^{(t)}\rho_{ge}, \quad (2.21)$$

where now the total rates are sums of the corresponding ones from the two baths, meaning  $\Gamma_\uparrow^{(t)} = \sum_{i=1,2} \Gamma_{\uparrow,i}$ ,  $\Gamma_\downarrow^{(t)} = \sum_{i=1,2} \Gamma_{\downarrow,i}$ , and  $\Gamma_\Sigma^{(t)} = \sum_{i=1,2} \Gamma_{\Sigma,i}$ .

### 3. Systems - realizations in condensed matter

#### 3.1 Electrons in a conductor as an open system

In this section, we discuss two other examples that can be treated by the weak coupling open quantum system techniques: tunnel junctions and electron-phonon coupling. In both cases, the electronic system is coupled to another system composed of either electrons or phonons.

##### 3.1.1 Tunneling

A tunnel junction is a structure where two conducting electrodes are separated for instance by a thin insulating layer, working as a barrier. Although classically electrons (or quasiparticles) can not pass through this barrier, quantum mechanically transport occurs through a thin layer only, since the tunneling probability decays exponentially with respect to the distance between the electrodes. Here we derive the charge current, its noise, heat current and its noise for tunneling in such junctions.

###### *Tunneling charge current and its noise*

The total Hamiltonian of two electrodes with an insulator layer in between is formally similar to the one that we wrote in Eq. (2.1). In the subscripts we now use left and right (L and R) instead of system and bath (S and B), meaning  $\hat{\mathcal{H}} = \hat{\mathcal{H}}_L + \hat{V} + \hat{\mathcal{H}}_R$  with  $\hat{\mathcal{H}}_L(\hat{\mathcal{H}}_R)$  as the unperturbed Hamiltonian for the left (right) electrode. They read

$$\hat{\mathcal{H}}_{L(R)} = \sum_{l(r)} \epsilon_{l(r)} \hat{a}_{l(r)}^\dagger \hat{a}_{l(r)}. \quad (3.1)$$

Here  $\epsilon_{l(r)}$  is the energy of electron state in each electrode and  $\hat{a}_{l(r)}^\dagger$  and  $\hat{a}_{l(r)}$  are the creation and annihilation operators. In the tunneling event, the perturbation  $\hat{V}$  is given by

$$\hat{V} = \sum_{l,r} t_{lr} \hat{a}_l^\dagger \hat{a}_r + \text{h.c.}, \quad (3.2)$$

where h.c. stands for hermitian conjugate and  $t_{lr}$  is the tunneling amplitude from left to right. In order to calculate the tunneling charge current  $I = \langle \hat{I} \rangle$ , the straightforward way is to start with the electron number operator in the left electrode  $\hat{N}_L = \sum_l \hat{a}_l^\dagger \hat{a}_l$ , since the current operator is given by  $\hat{I} = -e d\hat{N}_L/dt$ , with  $e$  the elementary charge. The operator of the tunneling charge current is then given by

$$\hat{I} = -e \frac{\imath}{\hbar} [\hat{\mathcal{H}}, \hat{N}_L] = -e \frac{\imath}{\hbar} \sum_{l,r} (t_{rl} \hat{a}_r^\dagger \hat{a}_l - t_{rl}^* \hat{a}_l^\dagger \hat{a}_r). \quad (3.3)$$

The expectation value of the charge operator reads then according to Kubo formula

$$\langle \hat{I} \rangle = -\frac{\imath}{\hbar} \int_{-\infty}^0 dt' \langle [\hat{I}(0), \hat{V}_I(t')] \rangle_0. \quad (3.4)$$

The expectation value of the current operator in the unperturbed state vanishes because of no tunneling:  $\langle \hat{I} \rangle_0 = \langle \psi_I(0) | \hat{I} | \psi_I(0) \rangle = 0$ . In the process of calculating Eq. (3.4), we face the independent averages for fermionic operators in the L and R electrodes:  $\langle \hat{a}_r^\dagger \hat{a}_l \hat{a}_l^\dagger \hat{a}_r \rangle_0 = \langle \hat{a}_r^\dagger \hat{a}_r \rangle_0 \langle \hat{a}_l \hat{a}_l^\dagger \rangle_0 \equiv f_R(\epsilon_r)[1 - f_L(\epsilon_l)]$  and  $\langle \hat{a}_l^\dagger \hat{a}_r \hat{a}_r^\dagger \hat{a}_l \rangle_0 = \langle \hat{a}_l^\dagger \hat{a}_l \rangle_0 \langle \hat{a}_r \hat{a}_r^\dagger \rangle_0 \equiv f_L(\epsilon_l)[1 - f_R(\epsilon_r)]$ . Here  $f_i(\epsilon) = 1/(1 + e^{\beta_i \epsilon})$  is the Fermi distribution function for lead  $i=L,R$  with inverse temperature  $\beta_i = (k_B T_i)^{-1}$ . Taking these points into account, performing the integral and applying bias voltage  $V$  to the left electrode, we have

$$I \equiv \langle \hat{I} \rangle = -e \frac{2\pi}{\hbar} \sum_{l,r} |t_{rl}|^2 \{ (f_R(\epsilon_r)[1 - f_L(\epsilon_l - eV)] - f_L(\epsilon_l - eV)[1 - f_R(\epsilon_r)]) \delta(\epsilon_l - \epsilon_r) \}. \quad (3.5)$$

In the limit of low temperature and low voltage bias,  $k_B T, eV \ll E_F$ , with  $E_F$  the energy of the Fermi level,  $|t_{rl}|^2 \equiv |t|^2$  can be taken constant. Next, by replacing sum on all possible states by integral,  $\sum_i \rightarrow \int d\epsilon v(\epsilon) \equiv \int d\epsilon N_i(E_F) v_i(\epsilon)$ , where  $N_i(E_F)$  denotes the density of states (DOS) at Fermi energy in the  $i=L,R$  (left or right) electrode, and  $v_i(\epsilon)$  is the normalized by  $N_i(E_F)$  energy dependent DOS, the tunneling charge current is given by

$$I = \frac{1}{eR_T} \int d\epsilon v_L(\epsilon - eV) v_R(\epsilon) \{ f_L(\epsilon - eV) - f_R(\epsilon) \}, \quad (3.6)$$

where  $\frac{1}{R_T} = \frac{2\pi|t|^2 N_L(E_F) N_R(E_F) e^2}{\hbar}$  is the inverse resistance of the tunnel barrier and it determines the ohmic behaviour of the tunnel junction at high bias voltage. The tunneling charge current can also be written as  $I = e(\Gamma_{L \rightarrow R} - \Gamma_{R \rightarrow L})$ , where  $\Gamma_{L(R) \rightarrow R(L)}$  is the tunneling rate from left (right) to right (left) electrode, and is given by

$$\Gamma_{L \rightarrow R} = \frac{1}{e^2 R_T} \int d\epsilon v_L(\epsilon - eV) v_R(\epsilon) f_L(\epsilon - eV)[1 - f_R(\epsilon)], \quad (3.7)$$

and similarly for  $\Gamma_{R \rightarrow L}$ . In order to obtain the noise of the tunneling charge current first one calculates the two-time correlator for the quantity under

study, here the charge current. This correlator, based on Eq. (3.3), is given by

$$\begin{aligned} \langle \hat{I}(t)\hat{I}(0) \rangle &= \frac{e^2|t|^2}{\hbar^2} \sum_{l,r} \{ f_R(\epsilon_r)[1 - f_L(\epsilon_l)]e^{i(\epsilon_r - \epsilon_l)t/\hbar} \\ &\quad + f_L(\epsilon_l)[1 - f_R(\epsilon_r)]e^{i(\epsilon_l - \epsilon_r)t/\hbar} \}, \end{aligned} \quad (3.8)$$

where we used the time dependence of the creation and annihilation operators  $\hat{a}_i(t) = \hat{a}_i e^{-i\epsilon_i t/\hbar}$  and  $\hat{a}_i^\dagger(t) = \hat{a}_i^\dagger e^{i\epsilon_i t/\hbar}$  for  $i = l, r$ . The noise of tunneling charge current,  $S_I(\omega) = \int_{-\infty}^{\infty} d\omega e^{i\omega t} \langle \hat{I}(t)\hat{I}(0) \rangle$ , then reads

$$\begin{aligned} S_I(\omega) &= \frac{e^2|t|^2}{\hbar^2} \int_{-\infty}^{\infty} \sum_{l,r} \{ f_R(\epsilon_r)[1 - f_L(\epsilon_l)]e^{i(\hbar\omega + \epsilon_r - \epsilon_l)t/\hbar} \\ &\quad + f_L(\epsilon_l)[1 - f_R(\epsilon_r)]e^{i(\hbar\omega - \epsilon_r + \epsilon_l)t/\hbar} \}. \end{aligned} \quad (3.9)$$

Next, we again integrate over all possible states by replacing sum by integral. Moreover, we apply voltage bias to the left side, leading to

$$\begin{aligned} S_I(\omega) &= \frac{1}{R_T} \int_{-\infty}^{\infty} d\epsilon v_R(\epsilon) \{ v_L(\epsilon + \hbar\omega + eV)f_R(\epsilon)[1 - f_L(\epsilon + \hbar\omega + eV)] \\ &\quad + v_L(\epsilon - \hbar\omega + eV)f_L(\epsilon - \hbar\omega + eV)[1 - f_R(\epsilon)] \}. \end{aligned} \quad (3.10)$$

Later, we will specify the type of the left and right leads to be either normal metal (N) or superconductor (S). Here for a special case in the classical limit  $\omega = 0$ , we consider that two leads have the same temperature  $T_L = T_R = T$  and they are normal metals ( $v_L(\epsilon) = v_R(\epsilon) = 1$ ), the noise spectrum for the tunneling charge current will be

$$S_I(\omega) = 2k_B T / R_T, \quad (3.11)$$

which is the fluctuation-dissipation theorem (FDT) [27]. In this case, the tunneling charge current (Eq. (3.6)) is ohmic,  $I = V/R_T$ .

### *Tunneling heat current and its noise*

With the help of Eqs. (3.1) and (3.2), the operator of tunneling heat current to the left lead  $d\hat{\mathcal{H}}_L/dt = \frac{i}{\hbar}[\hat{\mathbb{V}}, \hat{\mathcal{H}}_L]$  reads

$$d\hat{\mathcal{H}}_L/dt = \frac{i}{\hbar} \sum_{l,r} \epsilon_l (t_{rl}\hat{a}_r^\dagger\hat{a}_l - t_{lr}\hat{a}_l^\dagger\hat{a}_r). \quad (3.12)$$

The heat current from the left lead  $\dot{Q}_L \equiv -\langle d\hat{\mathcal{H}}_L/dt \rangle = \frac{i}{\hbar} \int_{-\infty}^0 dt' \langle [d\hat{\mathcal{H}}_L(0)/dt, \hat{\mathbb{V}}_I(t')] \rangle_0$  when applying the voltage bias to the junction is given by

$$\dot{Q}_L = \frac{1}{e^2 R_T} \int_{-\infty}^{\infty} d\epsilon (\epsilon - eV)v_L(\epsilon - eV)v_R(\epsilon) \{ f_L(\epsilon - eV) - f_R(\epsilon) \}. \quad (3.13)$$

In the case of a basic NIN junction, with both electrodes being normal metal, the heat current from the left lead reads  $\dot{Q}_L = -V^2/(2R_T)$ , meaning

that the Joule power  $P = IV$  is dissipated equally in both left and right electrodes.

One of the central concepts in this thesis is thermal conductance  $G_{\text{th}}$ . In this setup, in equilibrium,  $T_L = T_R = T$  and  $V = 0$ , it is defined as  $G_{\text{th}}^{(\text{t})}(T) = d\dot{Q}_L/dT_L|_T$ , where the superscript stands for tunneling. With the help of Eq. (3.13) for a NIN tunnel junction, thermal conductance is given by

$$G_{\text{th}}^{(\text{t})}(T) = -\frac{1}{k_B T^2} \frac{1}{e^2 R_T} \int_{-\infty}^{\infty} d\epsilon \epsilon \frac{df_L(\epsilon)}{d\beta} \equiv \mathcal{L}_0 T G_T, \quad (3.14)$$

which is the Wiedemann-Franz law [28]. Here  $\mathcal{L}_0 = \pi^2 k_B T^2 / (3e^2)$  is the Lorenz number and  $G_T = R_T^{-1}$  denotes the electrical conductance of the tunnel junction.

Besides the average heat current, the fluctuations of it, are an equally important concept in this thesis. We use the heat current operator from the left lead, Eq. (3.12), to find the two-time correlator of it  $\langle d\hat{\mathcal{H}}_L(t)/dt \, d\hat{\mathcal{H}}_L(0)/dt \rangle$ . Applying the Fourier-transform to evaluate the spectral density of noise of heat current  $S_{\dot{Q}_L}(\omega)$  at finite (angular) frequency  $\omega$ , and finite voltage bias, we have

$$\begin{aligned} S_{\dot{Q}_L}(\omega) &= \frac{1}{e^2 R_T} \int_{-\infty}^{\infty} d\epsilon v_R(\epsilon) \{ v_L(\tilde{\epsilon} + \hbar\omega) (\tilde{\epsilon} + \hbar\omega)^2 f_R(\epsilon) [1 - f_L(\tilde{\epsilon} + \hbar\omega)] \\ &\quad + v_L(\tilde{\epsilon} - \hbar\omega) (\tilde{\epsilon} - \hbar\omega)^2 f_L(\tilde{\epsilon} - \hbar\omega) [1 - f_R(\epsilon)] \}, \end{aligned} \quad (3.15)$$

where  $\tilde{\epsilon} = \epsilon - eV$ . With the help of Eq. (3.15), one obtains the fluctuation-dissipation theorem for heat in tunneling. As an example, we assume again the special case of a NIN junction with the two leads at equal temperature at  $eV = 0$ . In this case the heat current noise at finite  $\omega$  is given by

$$\begin{aligned} S_{\dot{Q}_L}(\omega) &= \frac{1}{e^2 R_T} \int_{-\infty}^{\infty} d\epsilon (2\epsilon^2 + 2\epsilon\hbar\omega + \hbar^2\omega^2) f(\epsilon) [1 - f(\epsilon + \hbar\omega)] \\ &= \frac{1}{6e^2 R_T} [(2\pi k_B T)^2 + (\hbar\omega)^2] \frac{\hbar\omega}{1 - e^{-\beta\hbar\omega}}. \end{aligned} \quad (3.16)$$

For the general case, considering both positive and negative frequencies, the symmetrized noise  $S_{\dot{Q}_L}^{\text{symm}}(\omega) = \frac{1}{2} \{ S_{\dot{Q}_L}(\omega) + S_{\dot{Q}_L}(-\omega) \}$  is given by [29, 30, 31]

$$S_{\dot{Q}_L}^{\text{symm}}(\omega) = \frac{1}{12e^2 R_T} [(2\pi k_B T)^2 + (\hbar\omega)^2] \hbar\omega \coth\left(\frac{\hbar\omega}{2k_B T}\right). \quad (3.17)$$

In the classical limit  $\omega = 0$ , Eq. (3.17) reads

$$\begin{aligned} S_{\dot{Q}_L}(\omega) &= 2 \frac{1}{e^2 R_T} \int_{-\infty}^{\infty} d\epsilon \epsilon^2 f(\epsilon) [1 - f(\epsilon)] \\ &= 2k_B T^2 \left( \frac{\pi^2 k_B^2}{3e^2} G_T \right) \equiv 2k_B T^2 G_{\text{th}}, \end{aligned} \quad (3.18)$$

which is the classical fluctuation-dissipation theorem (FDT) for heat current in tunneling. Here we used Eq. (3.14) and  $\int_{-\infty}^{\infty} dx x^2 f(x)[1 - f(x)] = \pi^2/3$ . One of the interesting features of Eq. (3.17) is that at  $T = 0$ ,

$$S_{\dot{Q}_L}^{\text{symm}}(\omega) = \frac{1}{12e^2 R_T} (\hbar\omega)^3. \quad (3.19)$$

This result indicates non-vanishing noise of heat current even at zero temperature.

### 3.2 Electron-phonon system

Phonons represent a quantized vibration of a crystal lattice at a specific (angular) frequency  $\omega_p$  with momentum  $\vec{k}$ . This determines a normal mode of vibration in classical mechanics. One of the important systems under study in this thesis is an absorber composed of electrons at temperature  $T_e$  and with heat capacity  $C$  and with Hamiltonian  $\hat{\mathcal{H}}_e = \sum_k \epsilon_k \hat{a}_k^\dagger \hat{a}_k$  (the same electronic system as introduced in Eq. (3.1)), in contact with a thermal bath of phonons often called environment at temperature  $T_p$  with Hamiltonian  $\hat{\mathcal{H}}_p = \sum_q \hbar\omega_p \hat{c}_q^\dagger \hat{c}_q$ . With analogous notation to the electrons, phonons have eigenenergies  $\hbar\omega_p$ , wavevector  $\vec{q}$ , and  $\hat{c}_q^\dagger$  and  $\hat{c}_q$  bosonic creation and annihilation operators, respectively. This basic structure is shown in Fig. 3.1(a). The thermal conductance between the electrons and the phonon bath is indicated by  $G_{\text{th}}$ , when both electrons and phonons are internally in thermal equilibrium.

In this section we present results on noise obtained in Publication IV. Before starting to analyze this system, we need to make some assumptions [7, 32]. Due to fast electron-electron relaxation, electrons typically obey Fermi-Dirac distribution even under nonequilibrium conditions between electrons and phonons with a well-defined and uniform temperature  $T_e \ll T_F$  where  $T_e/T_F \sim 10^{-6}$  with  $T_F$  the Fermi temperature. The temperature of the phonons  $T_p$  that can differ from  $T_e$ , is also well-defined and uniform  $T_p \ll T_D$ , with the Debye temperature  $T_D \sim 300$  K. This means that only acoustic phonons with  $\omega_p = \vec{c}_l \cdot \vec{q}$  exist with  $\vec{c}_l$  as the speed of sound. We assume spherical Fermi surface for electrons and 3D distribution for phonons which implies that the dimensions of the system are larger than the thermal wavelength. Moreover, we take coupling in metals to be represented by a scalar deformation potential [7, 32]. At low temperatures, phonons couple weakly to electrons, and the coupling energy between them can be written as

$$\hat{V}_{ep} = \gamma \sum_{k,q} \omega_p^{1/2} (\hat{a}_k^\dagger \hat{a}_{k-q} \hat{c}_q + \hat{a}_k^\dagger \hat{a}_{k+q} \hat{c}_q^\dagger), \quad (3.20)$$

where the magnitude of  $\gamma$  depends on the material properties of the system [33]. The procedure to study heat current in the electron-phonon

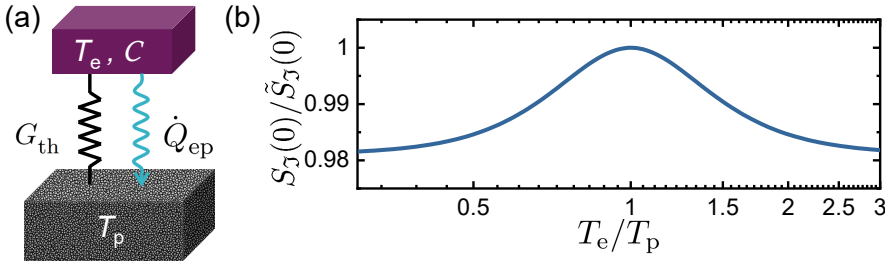


**Figure 3.1.** Thermal model for e-ph coupling. (a) A finite-sized reservoir with temperature  $T_e$  and heat capacity  $C$  coupled to a heat bath at fixed temperature  $T_p$  with thermal conductance  $G_{th}$ . The electron-phonon collisions lead to heat current indicated by  $\dot{Q}_{ep}$ . (b) Comparison of heat current noise for electron-phonon coupling system  $S_j(0)$  in the classical limit  $\omega = 0$ , between analytical and estimated solutions. These two results are: numerical solution of Eq. (3.28) for  $\omega = 0$  and the estimated solution  $\tilde{S}_j(0)$ , Eq. (3.30), that can be used for unequal temperatures. It is clear that even in a wide range, the ratio stays close to unity.

system is the same as in tunneling, but unlike in tunneling where the two subsystems were fermions (electrons), here one of them is fermion and the other one boson (phonon). The operator of heat current from the electron system to phonons,  $d\hat{\mathcal{H}}_p/dt = \frac{i}{\hbar}[\hat{V}_{ep}, \hat{\mathcal{H}}_p]$ , due to electron-phonon coupling is

$$d\hat{\mathcal{H}}_p/dt = i\gamma \sum_{k,q} \omega_p^{3/2} (\hat{a}_k^\dagger \hat{a}_{k-q} \hat{c}_q - \hat{a}_k^\dagger \hat{a}_{k+q} \hat{c}_q^\dagger). \quad (3.21)$$

In order to calculate the heat current in this system, few matters need to be considered. We assume that the electrons and phonons are independent from each other in the absence of weak coupling meaning that they can commute. We also neglect the double creation and double annihilation operators because they do not survive in the averaging. We discussed earlier the average of the product of the fermionic operators,  $\langle \hat{a}_k^\dagger \hat{a}_k \rangle = f(\epsilon_k)$ ; For bosons we have  $\langle \hat{c}_q^\dagger \hat{c}_q \rangle = n(\omega_p)$  and  $\langle \hat{c}_q \hat{c}_q^\dagger \rangle = 1 + n(\omega_p)$  where  $n(\omega_p) = (e^{\beta_p \hbar \omega_p} - 1)^{-1}$  is the Bose-Einstein distribution for phonon occupation, with  $\beta_p = (k_B T_p)^{-1}$  the inverse temperature of the phonons. Using the time dependence of the operators,  $\hat{a}_k = e^{-i\epsilon_k t/\hbar}$  and  $\hat{c}_q = e^{-i\omega_p t}$ , the electron-phonon heat current  $\dot{Q}_{ep} = \langle d\hat{\mathcal{H}}_p/dt \rangle$  reads

$$\begin{aligned} \dot{Q}_{ep} = 2\pi\gamma^2 \sum_{k,q} \omega_p^2 & \left\{ f(\epsilon_k)[1 - f(\epsilon_{k-q})][1 + n(\omega_q)]\delta(\epsilon_{k-q} - \epsilon_k + \hbar\omega_q) \right. \\ & \left. - f(\epsilon_k)[1 - f(\epsilon_{k+q})]n(\omega_q)\delta(\epsilon_{k+q} - \epsilon_k - \hbar\omega_q) \right\}. \end{aligned} \quad (3.22)$$

For electrons, integrating over all possible states, i.e. replacing sum by an integral was explained before,  $\sum_k \rightarrow \int d\epsilon v(E_F)$ . Since the absorber is normal metal,  $v(\epsilon) = 1$ . For 3D phonons in the spherical coordinates,

converting sum to integral is done as

$$\sum_k \rightarrow D(q) \int d^3q \equiv \frac{\mathcal{V}}{(2\pi)^2} \int_0^\infty q^2 dq \int_{-1}^{+1} d(\cos \theta), \quad (3.23)$$

where  $D(q) = \mathcal{V}/(2\pi)^3$  denotes the density of states of three-dimensional phonons with system volume  $\mathcal{V}$ , and  $\theta$  is the angle between  $\vec{k}$  and  $\vec{q}$ . The energy of the electron states is  $\epsilon_k = \frac{\hbar^2 k^2}{2m^*}$ . Moreover, we have  $\epsilon_{k\pm q} \simeq \epsilon_k \pm \frac{\hbar^2 k_F^2}{m^*} \cos \theta$ , where  $k_F$  and  $m^*$  are the Fermi wave vector of a spherical surface and effective mass of electron in the metal in question, respectively [28]. Here the last approximation was due to  $k \simeq k_F$  and  $q \ll k_F$ . Taking all these points into account, Eq. (3.22) reads

$$\begin{aligned} \dot{Q}_{\text{ep}} = & \frac{\gamma^2 c_l^2 N(\epsilon_F) \mathcal{V} m^*}{2\pi \hbar^2 k_F} \left\{ \int_{-\infty}^\infty d\epsilon_k \int_0^\infty dq q^3 f(\epsilon_k) [1 - f(\epsilon_k - \epsilon_q)] \right. \\ & \left. + \int_{-\infty}^\infty d\epsilon_k \int_0^\infty dq q^3 [f(\epsilon_k) - f(\epsilon_k - \epsilon_q)] n(\epsilon_q) \right\}. \end{aligned} \quad (3.24)$$

Calculating the integral over electron energies first, we have

$$\dot{Q}_{\text{ep}} = \frac{\gamma^2 c_l^3 N(\epsilon_F) \mathcal{V} m^*}{2\pi \hbar k_F} \int_0^\infty dq q^4 \left( \frac{1}{e^{\beta_e \hbar c_l q} - 1} - \frac{1}{e^{\beta_p \hbar c_l q} - 1} \right). \quad (3.25)$$

Since  $\int_0^\infty dx \frac{x^4}{e^{\beta x} - 1} = \frac{24\zeta(5)}{\beta^5}$ , where  $\zeta(z)$  denotes the Riemann zeta function, we have

$$\dot{Q}_{\text{ep}} = \Sigma \mathcal{V} (T_e^5 - T_p^5). \quad (3.26)$$

Here,  $\Sigma = \frac{12\gamma^2 N(\epsilon_F) m^* \zeta(5) k_B^5}{\pi k_F c_l^2 \hbar^6}$  is the electron-phonon coupling constant [7, 32]. With the help of Eq. (3.26), thermal conductance between electrons and phonons  $G_{\text{th}} = d\dot{Q}_{\text{ep}}/dT_e|_T$ , at  $T_e = T_p = T$  is given by  $G_{\text{th}} = 5\Sigma \mathcal{V} T^4$ . Equation (3.26) is specific for usual metals, whereas, e.g. in graphene we find in Publication XIII a different power law in temperatures.

After calculating the heat current in the electron-phonon system, computing its fluctuations will be straightforward. Essentially, we use the same assumptions and procedure as for the average heat current. For convenience, we start with obtaining the symmetric heat current operator  $\hat{\mathfrak{I}} = (d\hat{\mathcal{H}}_e/dt - d\hat{\mathcal{H}}_p/dt)/2$ , where  $d\hat{\mathcal{H}}_p/dt$  was introduced in Eq. (3.21) and  $d\hat{\mathcal{H}}_e/dt$  presents the operator for heat flux to the electron system it is given by

$$\hat{\mathfrak{I}} = -\frac{i\gamma}{2\hbar} \sum_{k,q} \sqrt{\omega_p} (\hbar\omega_p + \epsilon_k - \epsilon_{k-q}) (\hat{a}_k^\dagger \hat{a}_{k-q} \hat{c}_q - \hat{a}_{k-q}^\dagger \hat{a}_k \hat{c}_q^\dagger). \quad (3.27)$$

We note that for the average heat current  $\langle \hat{\mathfrak{I}} \rangle = \langle d\hat{\mathcal{H}}_e/dt \rangle = -\langle d\hat{\mathcal{H}}_p/dt \rangle$ . Then the spectral density of heat current fluctuations for electron-phonon

coupling system reads

$$S_J(\omega) = \frac{\Sigma\mathcal{V}}{96\zeta(5)k_B^5} \int_0^\infty d\epsilon \epsilon^2 \left[ (2\epsilon - \hbar\omega)^2 \frac{1}{1 - e^{-\beta_p\epsilon}} \frac{\epsilon - \hbar\omega}{e^{\beta_e(\epsilon - \hbar\omega)} - 1} \right. \\ \left. + (2\epsilon + \hbar\omega)^2 \frac{1}{e^{\beta_p\epsilon} - 1} \frac{\epsilon + \hbar\omega}{1 - e^{-\beta_e(\epsilon + \hbar\omega)}} \right]. \quad (3.28)$$

In the classical limit  $\omega = 0$  and at equal temperatures  $T_e = T_p = T$ , one can solve the above integral and we have

$$S_J(0) = 10\Sigma\mathcal{V}k_B T^6, \quad (3.29)$$

which is a well-known result [34], and it can be written as  $S_J(0) = 2k_B T^2 G_{\text{th}}$ , i.e. the fluctuation–dissipation theorem. In this classical limit, one can approximate the heat current noise by

$$\tilde{S}_J(0) = 5\Sigma\mathcal{V}k_B(T_e^6 + T_p^6). \quad (3.30)$$

Although this expression is not obtained directly from the integral of Eq. (3.28) at  $\omega = 0$ , numerical calculations shows that it is a good approximation. Figure 3.1(b) demonstrates that the ratio of  $S_J(0)/\tilde{S}_J(0)$  as a function of  $T_e/T_p$  stays close to unity. The important feature of Eq. (3.30), is that it can be used for unequal temperatures while the analytical result, Eq. (3.29), is obtained only for equal ones. Another important limit is at zero temperature when  $T_e, T_p \rightarrow 0$  in Eq. (3.28), where the heat current noise yields

$$S_J(0) = \frac{\Sigma\mathcal{V}}{96\zeta(5)k_B^5} \frac{(\hbar\omega)^6}{60}. \quad (3.31)$$

This non-vanishing heat current noise at zero temperature limit for electron-phonon coupling system is in analogy with the expressions of Eq. (3.19) for the same quantity in charge transport in a tunnel junction [29, 31, 30]. In the case of tunneling  $S_{Q_L}^{\text{symm}} \propto \omega^3$  with the thermal conductance  $G_{\text{th}}^{(t)} \propto T$  and here  $S_J \propto \omega^6$  with  $G_{\text{th}} \propto T^4$ . This leads us to conjecture that if  $G_{\text{th}} \propto T^k$ , the zero temperature noise scales as  $\propto \omega^{(k+2)}$ .

### 3.3 Quantum heat transport by photons

One of the central concepts in this thesis is “photonic heat transport” in a circuit. In order to illustrate it, we start with the archetypal Johnson-Nyquist [35, 36] setup consisting of two resistors  $R_1$  and  $R_2$  at inverse temperatures  $\beta_1 = (k_B T_1)^{-1}$  and  $\beta_2 = (k_B T_2)^{-1}$ , respectively, coupled directly to each other [37, 12, 13], as shown in Fig. 3.2. Here, we use two methods to calculate the heat transport from one resistor to another. The first model is the standard circuit theory and the second one is a

microscopic model where each resistor is formed of a collection of bosonic oscillators, as illustrated in Fig. 3.2(a). The results of this microscopic model are the main contents of Publication XVI. We start with the circuit theory [37]. Each resistor then produces thermal noise, e.g. voltage noise, with the spectrum  $S_{v_i}(\omega) = 2R_i\hbar\omega/(1 - e^{-\beta_i\hbar\omega})$  for  $i = 1, 2$ , i.e., they can be considered as photon sources as mentioned before, see Fig. 3.2(b). As a result,  $R_1$  generates noise current  $i_1$  on resistor  $R_2$  as  $i_1 = v_1/(R_1 + R_2)$ . Then the spectral density of current noise is  $S_{i_1}(\omega) = (R_1 + R_2)^{-2}S_{v_1}(\omega)$ . The power density produced by noise of  $R_1$  and dissipated in resistor  $R_2$  reads  $S_{P_2}(\omega) = \frac{R_2}{(R_1 + R_2)^2}S_{v_1}(\omega)$ . The corresponding total power dissipated in resistor  $R_2$  due to the noise of resistor  $R_1$  is

$$\begin{aligned} P_2 &= \int_{-\infty}^{\infty} \frac{d\omega}{2\pi} S_{P_2}(\omega) \\ &= \frac{4R_1R_2}{(R_1 + R_2)^2} \int_0^{\infty} \frac{d\omega}{2\pi} \hbar\omega [n_1(\omega) + \frac{1}{2}], \end{aligned} \quad (3.32)$$

where  $n_i(\omega) = (e^{\beta_i\hbar\omega} - 1)^{-1}$  is the Bose-Einstein distribution. The net heat flux from  $R_1$  to  $R_2$ ,  $P_{\text{net}}$ , is the difference between  $P_2$  and  $P_1$ , where  $P_1$  is the corresponding power produced by  $R_2$  on  $R_1$  by the uncorrelated voltage (current) noise described similarly. Thus

$$P_{\text{net}} = \frac{4R_1R_2}{(R_1 + R_2)^2} \frac{\pi k_B^2}{12\hbar} (T_1^2 - T_2^2). \quad (3.33)$$

Note that the integrals for  $P_1$  and  $P_2$  separately (see Eq. (3.32)) would diverge due to the zero point fluctuation term, but since these fluctuations cannot transport net power, this term cancels out in the physical quantity Eq. (3.33). We find that for a small temperature difference with  $T_1 = T_2 \equiv T$

$$G_\nu = \frac{dP_{\text{net}}}{dT_1}|_T = \frac{4R_1R_2}{(R_1 + R_2)^2} \frac{\pi k_B^2}{6\hbar} T, \quad (3.34)$$

which is equal to the quantum of heat conductance  $G_Q = G_Q = \pi k_B^2 T / (6\hbar)$  at temperature  $T$  [38] for  $R_1 = R_2$ . For a general combination of resistance values the factor

$$r = \frac{4R_1R_2}{(R_1 + R_2)^2} \quad (3.35)$$

represents a transmission coefficient. The circuit model for heat transport can be generalized to essentially any linear circuit composed of reactive elements and resistors as has been done, e.g., in [39, 40].

In the second approach to obtain this power, we consider that microscopically each resistor is formed of a collection of harmonic oscillators [41, 42] with bosonic ladder operators  $\hat{b}_j$  ( $\hat{b}_j^\dagger$ ) and  $\hat{c}_k$  ( $\hat{c}_k^\dagger$ ) for  $R_1$  and  $R_2$ , respectively, with subscripts  $j = 1 \dots N_1$  and  $k = 1 \dots N_2$ . Here  $N_1$  and  $N_2$  indicate the number of the harmonic oscillators in  $R_1$  and  $R_2$ , respectively. The charge

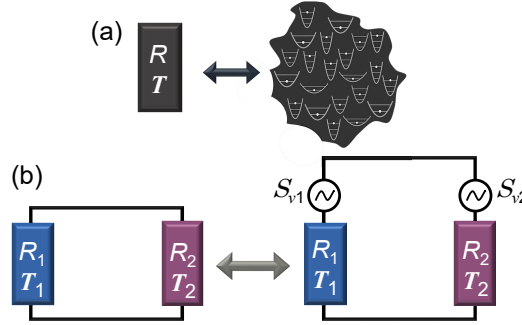


**Figure 3.2.** Photonic heat transport in the Johnson-Nyquist setup of two resistors. (a) Microscopically, a resistor is formed of a collection of bosonic oscillators. (b) The setup of two resistors  $R_1, R_2$  at temperatures  $T_1, T_2$ , respectively, are connected directly to each other and interacting via the respective thermal noises. In circuit theory each resistor is accompanied by a thermal voltage noise source and their noise sources are assumed to be uncorrelated.

operator of the oscillators forming resistor  $R_1$  and phase operator of the oscillators of  $R_2$  as linear combinations with coefficients  $\mu_j^{(1)}$  and  $\lambda_k^{(2)}$  in the interaction picture are given by

$$\hat{q}_1(t) = \sum_j i\mu_j^{(1)} (\hat{b}_j e^{-i\omega_j t} - \hat{b}_j^\dagger e^{i\omega_j t}) \quad (3.36)$$

$$\hat{\varphi}_2(t) = \sum_k \lambda_k^{(2)} (\hat{c}_k e^{-i\omega_k t} + \hat{c}_k^\dagger e^{i\omega_k t}). \quad (3.37)$$

The effective Hamiltonian, describing the system under study ( $R_2$ ) and its coupling to the bath  $R_1$  is then

$$\hat{\mathcal{H}} = \hat{\mathcal{H}}_2 - \hat{i}_2 \hat{\Phi}_2 \equiv \hat{\mathcal{H}}_2 + \hat{\mathbb{V}}, \quad (3.38)$$

where  $\hat{H}_2 = \sum_k \hbar\omega_k \hat{c}_k^\dagger \hat{c}_k$  is the Hamiltonian of the bare resistor  $R_2$  with oscillator energies  $\hbar\omega_k$ ,  $\hat{i}_2 = \frac{R_1}{R_1+R_2} d\hat{q}_1/dt$  (given based on the circuit analysis) denotes the current operator through  $R_2$ , and  $\hat{\Phi}_2 = \frac{\hbar}{e} \hat{\varphi}_2$ . With the help of Eq. (3.36), we then have

$$\hat{i}_2(t) = \frac{R_1}{R_1+R_2} \sum_j \mu_j^{(1)} \omega_j (\hat{b}_j^\dagger e^{i\omega_j t} + \hat{b}_j e^{-i\omega_j t}). \quad (3.39)$$

As a result, the coupling Hamiltonian  $\hat{\mathbb{V}}$  is given by

$$\hat{\mathbb{V}}(t) = -\frac{R_1}{R_1+R_2} \sum_{j,k} \lambda_k^{(2)} \mu_j^{(1)} \omega_j (\hat{b}_j^\dagger e^{i\omega_j t} + \hat{b}_j e^{-i\omega_j t})(\hat{c}_k^\dagger e^{i\omega_k t} + \hat{c}_k e^{-i\omega_k t}). \quad (3.40)$$

This is in the form what one obtains also by scattering theory imposing energy conservation [29, 43].

*Coefficients based on real circuit parameters*

Now a key question arises as how the coefficients  $\mu_j^{(1)}$  and  $\lambda_k^{(2)}$  correspond to the actual circuit parameters. This is one of the issues that is often overlooked in literature on open quantum systems. In order to establish consistency, we request the current  $\hat{i} = d\hat{q}_1/dt$  noise of resistor  $R_1$ ,  $S_i(\omega) = \int_{-\infty}^{\infty} dt e^{i\omega t} \langle \hat{i}(t)\hat{i}(0) \rangle$ , to be equal to the quantum current noise of that resistor, i.e.  $S_i(\omega) = \frac{2}{R_1} \frac{\hbar\omega}{1 - \exp(-\beta_1 \hbar\omega)}$ . Similarly we set the voltage  $\hat{v} = d\hat{V}_2/dt$  noise of resistor  $R_2$ ,  $S_v(\omega) = \int_{-\infty}^{\infty} dt e^{i\omega t} \langle \hat{v}(t)\hat{v}(0) \rangle$ , equal to  $S_v(\omega) = 2R_2 \frac{\hbar\omega}{1 - \exp(-\beta_2 \hbar\omega)}$  with similar notations. These conditions lead to the expressions

$$\mu_j^{(1)} = \left( \frac{\hbar}{\pi\nu_1(\omega_j)\omega_j R_1} \right)^{1/2}, \quad \lambda_k^{(2)} = \left( \frac{\hbar R_2}{\pi\nu_2(\omega_k)\omega_k} \right)^{1/2}, \quad (3.41)$$

where  $\nu_i(\omega)$  is the oscillator density of states in  $R_i$  with  $i = 1, 2$ .

The operator of heat current to  $R_2$ ,  $d\hat{\mathcal{H}}_2/dt = \frac{i}{\hbar} [\hat{\mathcal{H}}, \hat{\mathcal{H}}_2] = \frac{i}{\hbar} [\hat{V}, \hat{\mathcal{H}}_2]$  reads then

$$d\hat{\mathcal{H}}_2/dt = \frac{i\hbar\sqrt{r}}{2\pi} \sum_{j,k} \frac{\sqrt{\omega_j\omega_k}}{\sqrt{\nu_1(\omega_j)\nu_2(\omega_k)}} (\hat{b}_j^\dagger e^{i\omega_j t} + \hat{b}_j e^{-i\omega_j t})(\hat{c}_k^\dagger e^{i\omega_k t} - \hat{c}_k e^{-i\omega_k t}). \quad (3.42)$$

According to the Kubo formula, the expectation value of heat current (power)  $P_2 \equiv \langle d\hat{\mathcal{H}}_2/dt \rangle$  to  $R_2$  under stationary conditions is

$$P_2 = -\frac{i}{\hbar} \int_{-\infty}^0 dt' \langle [d\hat{\mathcal{H}}_2(0)/dt, \hat{V}(t')] \rangle_0, \quad (3.43)$$

where  $\langle \cdot \rangle_0$  denotes the expectation value of a quantity for the non-interacting resistor at a given temperature. Since  $\langle \hat{b}_j^\dagger \hat{b}_j \rangle_0 = n_1(\omega_j)$  with  $n_1(\omega) = 1/(e^{\beta_1 \hbar\omega} - 1)$  the Bose-Einstein distribution of resistor  $R_1$ , and similarly  $\langle \hat{c}_k^\dagger \hat{c}_k \rangle_0 = n_2(\omega_k)$  for resistor  $R_2$ , the heat current is given by

$$\dot{Q} = r \frac{\pi k_B^2}{12\hbar} (T_1^2 - T_2^2), \quad (3.44)$$

which is equal to the expression obtained by standard circuit theory in Eq. (3.33).

The advantage of the microscopic method is that it gives a direct access not only to the average of quantum heat current but also to the noise of it. In Publication XVI, we wrote down the two-time correlator with heat current operator of Eq. (3.42) and obtained the frequency dependent noise spectrum of it as a Fourier-transform of the correlator. The result is analogous to what has been obtained for other type of carriers [29, 30, 31], demonstrating explicitly heat current noise even at zero temperature at non-vanishing frequencies. Most interestingly we present a mixing method by which one can down-convert the quantum high-frequency heat current noise to zero frequency using a tunable reactive element, e.g., in form of a SQUID, between the two resistors.

### 3.4 Thermal detector

Thermal detectors [44, 45, 46] which convert energy or radiation into heat, to be detected by sensitive thermometers to be described in chapter 4, play an important role in exploration and utilization of radiation to the present date [47, 48, 49, 50, 51, 52, 53]. A thermal detector shown in Fig. 3.3 (a), composed of an absorber with electronic temperature  $T_e$  and heat capacity  $\mathcal{C}$  is exposed to the radiation and its temperature changes after the absorption of the radiation. The variation of its temperature is measured by a sensitive thermometer. Moreover, absorber is weakly coupled to the thermal bath at a fixed temperature  $T_p$  via thermal conductance  $G_{\text{th}}$ . Based on the incoming radiation which can be continuous or a single pulse, a thermal detector has two different operation modes. One interesting feature is to see how the thermal response of the absorber  $T(t)$  changes with time in these two modes. The net power absorbed  $\dot{Q}_{\text{net}}$  is simply the subtraction of input  $\dot{Q}_{\text{in}}$  and output power  $\dot{Q}_{\text{out}} = G_{\text{th}}(T_e - T_p)$ . The equation of motion for absorber temperature is given by

$$\mathcal{C}\dot{T} = \dot{Q}_{\text{in}} - G_{\text{th}}(T_e - T_p). \quad (3.45)$$

We start with continuous operation mode when constant incoming power, for instance in form of microwave photon radiation, has been switched on at  $t = 0$ , i.e.  $\dot{Q}_{\text{in}}(t) = 0$  for  $t < 0$  and  $\dot{Q}_{\text{in}}(t) = \dot{Q}_0$  at  $t > 0$ . For this power the thermal response of the absorber is

$$\Delta T(t) = \frac{\dot{Q}_0}{G_{\text{th}}}(1 - e^{-t/\tau})\theta(t), \quad (3.46)$$

where  $\Delta T(t) = T_e(t) - T_p$  and  $\tau = \mathcal{C}/G_{\text{th}}$  is the time constant. The plot in Fig. 3.3 (a) shows that the temperature increases exponentially with the time constant  $\tau$  towards the final value  $\dot{Q}_0/G_{\text{th}}$ . Such thermal detector operated in this regime for measuring the continuous radiation power is known as bolometer. Here, what we measure is temperature not with high time resolution but the steady state temperature of the absorber that is responding to the quasi-static radiation.

Another operation mode is when the absorber is exposed to radiation of a single pulse with energy  $E$  where the exposure time is much shorter than the thermal time constant. In this case the incoming power is  $\dot{Q}_{\text{in}}(t) = E\delta t$  at time  $t = 0$  and 0 elsewhere. The time evolution of temperature of the absorber is then

$$\Delta T(t) = \Delta T(0)e^{-t/\tau}, \quad (3.47)$$

where  $\Delta T(0) = \frac{E}{\mathcal{C}}$ , means that  $T$  responds to incoming energy quanta instantaneously and rises to the value  $T_p + E/\mathcal{C}$ , and then relaxes back to the bath temperature with the time constant  $\tau$ , as shown in Fig. 3.3 (b).

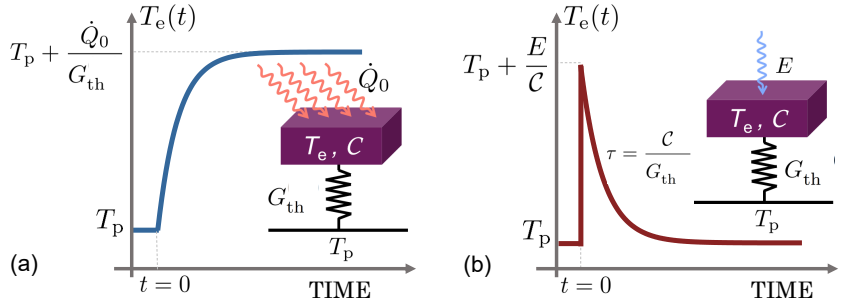


**Figure 3.3.** Two types of thermal detectors: bolometer in (a) and calorimeter in (b). The two thermal models shown in the insets are similar to the one presented in Fig. 3.1(a), with the difference in incoming power to the absorber, which is constant heating power  $\dot{Q}_0$  in the bolometric operation and a short pulse with energy  $E$  in the calorimetric operation. For both cases, the finite-size absorber at  $t < 0$ , is in thermal equilibrium with the phonon bath at fixed temperature  $T_p$ . (a) At  $t = 0$ , the absorber is exposed to continuous incoming power  $\dot{Q}_0$  and the electronic temperature of the absorber rises exponentially to the final value  $T_p + \dot{Q}_0/G_{\text{th}}$ . (b) After absorption of energy  $E$  at  $t = 0$ ,  $T_e$  jumps to the value  $T_p + E/C$ , and then drops back to equilibrium with time constant  $\tau = C/G_{\text{th}}$ .

### 3.4.1 Temperature fluctuations

Due to the noise of heat flow through the thermal conductance to the phonon bath, the effective temperature of the absorber fluctuates around its mean under steady-state conditions. The origin of heat current noise is randomness in time and energy. The first one is a standard randomness known for particle current noise and the latter one is caused by the random magnitude of excitations affecting heat current between the absorber and the bath. In order to obtain this noise in the classical regime, we start with the heat balance equation  $\dot{Q}(t) = \mathcal{C}\delta T(t) + G_{\text{th}}\delta T(t)$ . Here  $\delta T(t) = T_e(t) - T_p$  now including the fluctuations in  $T_e(t)$ . The two-time correlator of it is

$$\langle \dot{Q}(t)\dot{Q}(0) \rangle = \mathcal{C}^2 \langle \delta T(t)\delta T(0) \rangle + G_{\text{th}}^2 \langle \delta T(t)\delta T(0) \rangle, \quad (3.48)$$

since  $\langle \delta T(t)\delta T(0) \rangle = -\langle \delta T(t)\delta T(0) \rangle$ . Then the noise of heat current is  $S_{\dot{Q}}(\omega) = \int dt e^{i\omega t} \langle \dot{Q}(t)\dot{Q}(0) \rangle = \mathcal{C}^2 S_{\dot{T}}(\omega) + G_{\text{th}}^2 S_T(\omega)$ . Since  $S_{\dot{T}}(\omega) = \omega^2 S_T(\omega)$ , we have

$$S_{\dot{Q}}(\omega) = (\omega^2 \mathcal{C}^2 + G_{\text{th}}^2) S_T(\omega). \quad (3.49)$$

This equation lets us find the noise spectrum of temperature of the absorber  $S_T(\omega)$ . Let us now continue by making an estimation for the case of electron-phonon coupling. At low temperature, say  $T \simeq 100$  mK, the real Lorentzian cut-off (angular) frequency of the spectrum is  $\omega_0 = G_{\text{th}}/\mathcal{C} \sim 10^5$  (s) $^{-1}$  while the thermal (angular) frequency will be  $\omega_{\text{thermal}} = k_B T/\hbar \sim 10^{10}$  (s) $^{-1}$ . This means it is reasonable to consider that in this range  $S_{\dot{Q}}(\omega)$  is frequency independent and stays constant. Using FDT we then have

$S_{\dot{Q}}(\omega) \simeq S_{\dot{Q}}(0) = 2k_B T^2 G_{\text{th}}$  and  $S_T(\omega)$  reads

$$S_T(\omega) = \frac{2k_B T^2}{G_{\text{th}}} \frac{1}{1 + (\frac{\omega}{\omega_0})^2}. \quad (3.50)$$

This result at low frequencies yields  $S_T(0) = 2k_B T^2 / G_{\text{th}}$ . In the case of a system coupled to several equilibrium baths, if one takes  $G_{\text{th}}$  representing the sum of all the individual thermal conductances to these baths, all these results still hold.

The sensitivity of a thermal detector, as one of the central features in such sensors, can usually be expressed by its noise-equivalent temperature  $\text{NET} = \sqrt{S_T}$ , in K/ $\sqrt{\text{Hz}}$ . Based on the given equation above, at low frequency, the fundamental noise-equivalent temperature in equilibrium is given by  $\text{NET}_{\text{eq}} = \sqrt{2k_B T^2 / G_{\text{th}}}$ .

From the spectrum  $S_T(\omega)$  the root-mean-square (rms) fluctuations of temperature  $\langle \delta T^2 \rangle = \langle \delta T(0) \delta T(0) \rangle$  can be obtained

$$\begin{aligned} \langle \delta T^2 \rangle &= \int_{-\infty}^{\infty} \frac{d\omega}{2\pi} S_T(\omega) \\ &= \frac{k_B T^2}{C}, \end{aligned} \quad (3.51)$$

This is a result given in several textbooks, see [54].

### 3.5 Heat capacity

In this section, we explain the heat capacity of electron gas for a normal metal and superconductor, which is the central quantity determining the energy resolution of a thermal detector. We use the free electron model, which is known to work remarkably well in describing the properties of many metals. In this model, electrons in a metal behave like a gas of free particles and they move in a constant electrostatic potential. The internal energy of the electron gas at temperature  $T$  with respect to the  $T = 0$  energy is given by

$$\begin{aligned} U(T) - U(0) &= N(E_F) \mathcal{V} \left\{ \int_{-\infty}^{\infty} d\epsilon \epsilon v(\epsilon) f(\epsilon) - \int_{-\infty}^{\infty} d\epsilon \epsilon v(\epsilon) [1 - \theta(\epsilon)] \right\} \\ &= 2N(E_F) \mathcal{V} \int_0^{\infty} d\epsilon \epsilon v(\epsilon) f(\epsilon), \end{aligned} \quad (3.52)$$

where in the first line we use the fact that the Fermi distribution is a step function  $1 - \theta(\epsilon)$  at  $T = 0$ ,  $N(E_F)$  denotes again the DOS at Fermi level per unit volume. The factor 2 and the integration interval from 0 to  $\infty$  reflect electron-hole symmetry in equilibrium. Heat capacity, by definition, is given by  $C = dU(T)/dT$ , and thus for the electron gas we have

$$C = \frac{N(E_F) \mathcal{V}}{k_B T^2} \int_{-\infty}^{\infty} d\epsilon \epsilon^2 v(\epsilon) f(\epsilon) [1 - f(\epsilon)]. \quad (3.53)$$

This expression can now be applied to a normal metal and superconductor. Note that here for the final step we assume that Fermi distribution is the only temperature-dependent part which is fully correct for normal metal and for the superconductors at temperatures far below  $T_C$ . However, close to the critical temperature, the DOS of a superconductor is also temperature dependent, but we do not consider that regime here.

#### *Heat capacity of a normal metal*

In the normal state,  $v(\epsilon) = 1$ , the heat capacity reads

$$\mathcal{C} = \frac{\pi^2}{3} N(E_F) \mathcal{V} k_B^2 T \equiv \gamma \mathcal{V} T, \quad (3.54)$$

where  $\gamma$  refers to the Sommerfeld constant for electrons in the metal. In the free electron model, we have  $N(E_F) = m k_F / (\hbar \pi)^2$  with  $k_F$  as the Fermi wave vector. In this thesis, we use copper as an absorber, the numerical value for it is  $\gamma \simeq 70.7 \text{ JK}^{-2} \text{m}^{-3}$ .

#### *Heat capacity of a superconductor*

We consider a pure Bardeen–Cooper–Schrieffer (BCS) superconductor [55] with normalized density of states

$$v_S^{\text{BCS}}(\epsilon) = \frac{|\epsilon|}{\sqrt{\epsilon^2 - \Delta^2}} \theta(|\epsilon| - \Delta), \quad (3.55)$$

where  $\Delta$  is the gap of the superconductor. Using Eq. (3.53), we obtain the heat capacity of superconductor  $\mathcal{C}_S$

$$\mathcal{C}_S = \frac{2N(E_F)\mathcal{V}}{k_B T^2} \int_{\Delta}^{\infty} d\epsilon \epsilon^2 \frac{\epsilon}{\sqrt{\epsilon^2 - \Delta^2}} \frac{1}{1 + e^{\beta\epsilon}} \frac{1}{1 + e^{-\beta\epsilon}}. \quad (3.56)$$

In the low temperature regime,  $\beta\Delta \gg 1$ , and with standard approximations near the gap  $\epsilon^3/\sqrt{\epsilon^2 - \Delta^2} \simeq \Delta^3/\sqrt{2\Delta(\epsilon - \Delta)}$ , we have

$$\begin{aligned} \mathcal{C}_S &\simeq 2\sqrt{2} \frac{N(E_F)\mathcal{V}\Delta^3}{k_B T^2} e^{-\beta\Delta} \int_0^{\infty} dx e^{-\beta\Delta x^2} \\ &= \sqrt{2\pi} N(E_F) \mathcal{V} k_B \Delta \left( \frac{\Delta}{k_B T} \right)^{3/2} e^{-\Delta/k_B T}. \end{aligned} \quad (3.57)$$

The suppression factor of the heat capacity with respect to that in the normal state at the same temperature is

$$\mathcal{C}_S/\mathcal{C} = \frac{3\sqrt{2}}{\pi^{3/2}} \left( \frac{\Delta}{k_B T} \right)^{5/2} e^{-\Delta/k_B T}. \quad (3.58)$$

### 3.5.1 Comparison of signal-to-noise ratio of different types of calorimeters

Signal-to-noise ratio  $\text{SNR}$  denotes the ratio of the level of a desired signal to the background noise. For temperature fluctuation measurements,  $\text{SNR}$

reads  $\text{SNR} = \Delta T(0)/\sqrt{\langle \delta T^2 \rangle}$ . Since for the calorimeter we obtain that  $\Delta T(0) = E/\mathcal{C}$ , and for fundamental temperature fluctuations we have, Eq. (3.51),  $\text{SNR}$  in this case is given by

$$\text{SNR} = \frac{E}{\sqrt{k_B \mathcal{C} T}}. \quad (3.59)$$

Denominator is then the fundamental energy resolution of the calorimeter  $\delta\varepsilon = \sqrt{k_B \mathcal{C} T}$ . Energy resolution is an important feature of any detector. Based on the given expression, it is clear that  $\mathcal{C}$  plays an important role on the energy resolution of the calorimeter, and we win by having a small heat capacity which depends on the choice of material and its physical size. In this section we compare the normal metal and the superconductor cases. Based on the previous section and the equations therein, we can see that the improvement of  $\text{SNR}$  using a superconducting absorber with small gap compared to the aluminum gap  $\Delta_m \ll \Delta_{\text{Al}}$ , with respect to normal metal is

$$\begin{aligned} \frac{\text{SNR}_S}{\text{SNR}_N} &= \sqrt{\frac{\mathcal{C}}{\mathcal{C}_S}} \\ &= \frac{\pi^{3/4}}{\sqrt{3\sqrt{2}}} \left(\frac{k_B T}{\Delta_m}\right)^{5/4} e^{-\Delta_m/2k_B T}. \end{aligned} \quad (3.60)$$

Let us make a rough estimate, of how one can win by using a superconducting absorber. In order to absorb microwave photons with frequency  $f = 5 \text{ GHz}$ , the superconductor's gap has to be  $\Delta_m < hf$ , which is the condition for Cooper-pair breaking. Here  $h$  is the Planck constant. Since based on the BCS theory we have  $\Delta_m = 1.764 k_B T_{c,m}$ , the minimum critical temperature of the superconductor  $T_{c,m}$  for the given frequency is  $T_{c,m} \sim 130 \text{ mK}$ . Equation (3.60) is then given by

$$\frac{\text{SNR}_S}{\text{SNR}_N} = \frac{\pi^{3/4}}{\sqrt{3\sqrt{2}}} \left(\frac{T}{1.764 T_{c,m}}\right)^{5/4} e^{-0.882 T_{c,m}/T}. \quad (3.61)$$

As an example if we take  $T_{c,m} = 100 \text{ mK}$ , at  $T = 10 \text{ mK}$ , the improvement of  $\text{SNR}$  is 200-fold, while at  $T = 20 \text{ mK}$  this ratio is only 6.

## **Part II**

### **Quantum thermodynamics in circuits**



## 4. Tunneling thermometry

The low temperature domain provides a unique environment and setting for studying quantum thermodynamics. In this chapter we focus on one important element in thermal transport experiments, thermometry in the sub-kelvin temperature regime. Measuring temperature accurately in this regime is a key element for successful experiments, since it is more difficult and only slightly less important than reaching these temperatures. Conceivably, the most severe difficulty in thermometry in this temperature range is whether the thermometer is in equilibrium with the body whose temperature is to be measured. In principle every physical property which changes with temperature  $T$ , can be employed as a thermometric parameter [56]. Practically, the physical property should meet some stringent requirements: i) it must be easily, quickly, and accurately measurable, ii) its temperature dependence should be sufficiently simple or at least it can be modeled theoretically, iii) its sensitivity must be high, iv) its heat capacity low, and v) the thermometer should be non-invasive or at least should have low self-heating. The temperature sensors can be divided into two main categories: primary and secondary thermometers. Primary thermometers are well defined physical systems, and they provide the absolute temperature based on known temperature independent quantities and without calibration. Contrarily, secondary thermometers are based on the equations which must be calibrated at least at one known temperature that is usually provided by the primary thermometers. Secondary thermometers have desirable properties: besides easier operation, higher speed and precision, their sensitivity  $\Delta T/T$  is typically high. On the other hand, primary thermometers are rare and often difficult to operate, and they are not necessarily as sensitive as the secondary ones.

### 4.1 Thermometry by a hybrid junction

Temperature in mesoscopic structures at low temperatures can vary substantially even over micrometer distances. This happens because of the

thermal isolation, e.g., by superconductivity or by very weak electron-phonon coupling. This provides us on one hand an opportunity, but it also means that local probes of temperature are needed. In this section we will discuss two hybrid junctions that serve as local thermometers in our setups.

#### 4.1.1 Thermometry based on quasiparticle tunneling

A common local probe in this thesis is a hybrid tunnel junction between a normal conductor (N) and superconductor (S) separated by an insulating oxide barrier (I), i.e., a NIS junction. The scanning electron micrograph (SEM) image of such a junction is presented in Fig. 4.1(a), where we have two back-to-back NIS junctions connected in series. Superconducting gap yields temperature dependent tunneling. Tunneling at a fixed current yields a voltage that is monotonic, with simple dependence (linear in  $T$  over wide range) at temperatures deep below the transition temperature  $T_C$  of the superconductor. Its basic properties can be accounted for by the general tunneling formulae introduced earlier. Substituting subscripts N instead of L for the left electrode and S for the right one, we can obtain some of the important properties of such a hybrid junction, e.g., charge and heat current. But first we need some further prerequisites and have to describe the main properties of the normal metals and superconductors. Let us start with normal metals. We deal with a 3D electron gas, since the Fermi wavelength  $\lambda_F \ll d$ , where  $d$  is the smallest dimension of the sample we consider. Typically  $\lambda_F < 1 \text{ nm}$  for a metal and dimensions of structures to be presented are  $d \sim 100 \text{ nm}$  or larger. In this case the density of states (DOS) has the dependence  $v_N \propto \sqrt{\epsilon}$  for a normal metal. The Fermi temperature  $E_F/k_B \sim 10^5 \text{ K}$  for typical metals. This means that both the operating temperature of  $T \leq 1 \text{ K}$ , and similarly bias voltages  $V \lesssim 1 \text{ mV}$  with  $eV/k_B \simeq 10 \text{ K}$  are in the range of  $\ll E_F/k_B$ . Therefore we can safely approximate the DOS in the normal state as constant  $v(E_F)$  over these relevant energies around the Fermi level. For the superconductors, the DOS in a superconductor, based on BCS theory [55], is  $v_S^{\text{BCS}}(\epsilon) = |\Re e \frac{\epsilon}{\sqrt{\epsilon^2 - \Delta^2}}|$  (Eq. (3.55)), where  $\epsilon = (\epsilon - E_F)/\Delta$ . In general, the gap of the superconductor is a temperature dependent parameter. At zero temperature, it is given by  $\Delta \approx 1.76 k_B T_C$ , and at temperatures close to  $T_C$  it is decreasing as  $1.746\sqrt{1 - T/T_C}$ . Since in this thesis we do the experiments in the range of temperatures far below  $T_C$ , we assume  $\Delta$  to be constant. As an example, the gap of aluminum is about  $\Delta/k_B \sim 2 \text{ K}$ . Taking all these points into account, the charge current in tunneling process of Eq. (3.6) reads for a NIS junction  $I = \frac{1}{eR_T} \int d\epsilon v_S(\epsilon)[f_N(\epsilon - eV) - f_S(\epsilon)]$ . Due to electron-hole symmetry the  $I(V)$  is odd,  $I(-V) = -I(V)$ , and we obtain a symmetric

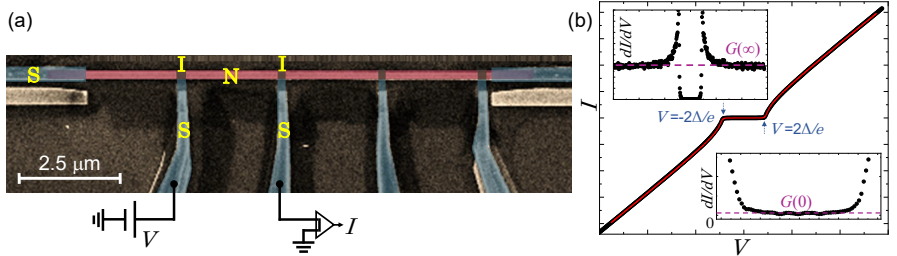


**Figure 4.1.** A typical SINIS structure (two NIS junctions in series). (a) The scanning-electron micrograph (SEM) of SINIS with a scheme of the experimental setup. Here Cu is used as a normal metal (N), Al as a superconductor (S) and  $\text{AlO}_x$  as an insulating barrier (I). By applying a voltage bias  $V$  to the junctions, the current  $I$  through them can be measured. (b) The  $I - V$  characteristic of the SINIS presented in (a) shown with black symbols measured at  $T = 50 \text{ mK}$ . The resistance of the two junctions in series  $R_T = 34 \text{ k}\Omega$  and superconducting gap  $\Delta/e = 230 \mu\text{V}$  can be extracted from the data, with the help of the theory fit from Eq. (4.1) indicated by the red line. (Insets) The conductance  $G = dI/dV$  demonstrating how to estimate the leakage parameter  $\gamma = G(0)/G(\infty)$  from the experimental data. For this sample we then obtain  $\gamma = 1.6 \times 10^{-3}$ .

form

$$I = \frac{1}{2eR_T} \int d\epsilon v_S(\epsilon) [f_N(\epsilon - eV) - f_N(\epsilon + eV)]. \quad (4.1)$$

This equation has an important message: the  $I - V$  curve depends on the distribution, i.e. temperature in N, but not at all on that in the superconductor as long as  $v_S(\epsilon)$  is temperature independent, i.e. for  $T_S \ll \Delta/\epsilon$ . The  $I - V$  characteristic of a SINIS structure is measured as presented in Fig. 4.1(b). At  $T_e = 0$ , the current reads  $I = \frac{1}{R_T} \sqrt{V^2 - (\Delta/e)^2}$ , which means that in the subgap regime,  $|eV| < \Delta$ , there is no charge current,  $I = 0$ , and far above the gap  $|eV| \gg \Delta$ , we have  $I = V/R_T$ . For  $\epsilon \gtrsim 1$ , using the approximation for BCS DOS,  $\epsilon/\sqrt{\epsilon^2 - 1} \simeq (\sqrt{2}\sqrt{\epsilon - 1})^{-1}$ , one can solve Eq. (4.1) analytically and we have

$$I \simeq I_0 e^{-(\Delta - eV)/k_B T_e}, \quad (4.2)$$

where  $I_0 = \sqrt{2\pi\Delta k_B T_e}/(2eR_T)$  [57, 58, 59]. Equation (4.2) demonstrates that such a temperature dependence is universal in view of the fact that  $d\ln(I/I_0)/dV = e/(k_B T_e)$ , [60] therefore making NIS a primary thermometer. Note that this is true only for an ideal junction, i.e. for BCS superconductor with DOS,  $v_S^{\text{BCS}}(\epsilon)$ . Experimentally, it is hard to have such an ideal junction. Due to subgap states, external radiation, and higher order tunneling etc., the DOS for the junction is effectively smeared beyond that of ideal BCS into

$$v_S(\epsilon) = |\Re e \frac{\epsilon + i\gamma}{\sqrt{(\epsilon + i\gamma)^2 - 1}}|, \quad (4.3)$$

where  $\gamma$  is known as the Dynes parameter and responsible for smearing, and the expression (4.3) as Dynes density of states [61, 62]. This new

expression modifies the  $I - V$  characteristic of the NIS junction. In the same range as before  $eV < \Delta$ , we can use the Taylor expansion in Eq. (4.3) for small  $\gamma$ , and we then have  $(\varepsilon + i\gamma)/\sqrt{(\varepsilon + i\gamma)^2 - 1} \simeq \varepsilon/\sqrt{\varepsilon^2 - 1} + i\gamma/(\varepsilon^2 - 1)^{3/2}$ . Substituting this expansion for DOS in Eq. (4.1), we have two terms: the first one which leads to the same result as for an ideal junction at low  $T$  given in Eq. (4.2) and the second term which is the low temperature leakage current of a NIS junction, we have  $I_{\text{leak}} = \frac{\Delta}{2eR_T} \int_{-eV/\Delta}^{eV/\Delta} d\varepsilon \frac{\gamma}{(1-\varepsilon^2)^{3/2}}$ . Here for the correction term we use  $f(\varepsilon) \simeq 1 - \theta(\varepsilon)$  with  $\theta(\varepsilon)$  the Heaviside step function. The tunneling charge current is then given by

$$I \simeq I_0 e^{-(\Delta - eV)/k_B T_e} + \frac{\gamma V}{R_T \sqrt{1 - (eV/\Delta)^2}}. \quad (4.4)$$

Although  $\gamma$  may originate from various sources, one can extract the value of it directly from the measurement. In this case,  $\gamma$  is the ratio of the zero-bias conductance of the junction  $G(0)$  to the conductance at voltages  $|eV| \gg \Delta$ , meaning  $\gamma = G(0)/G(\infty)$ . This principle is shown in the two insets of Fig. 4.1(b). The conductance of the junctions can be measured either directly from the  $I - V$  curve or using the derivative of it. In this figure we used the latter option. In general, one can extract three parameters for the SINIS structure (two NIS junctions in series) from the  $I - V$  characteristic presented in Fig. 4.1:  $\gamma$ ,  $\Delta/e$ , and  $R_T$ . For junctions that are influenced by weak superconducting proximity effect, one predicts that the Dynes parameter  $\gamma$  obeys the relation  $\gamma \sim R_K/(nR_T)$  where  $R_K = h/e^2 \simeq 25.8 \text{ k}\Omega$ , the von Klitzing constant, denotes the resistance quantum and  $n$  refers to the effective number of conduction channels in the junction  $n = A/A_{\text{ch}}$  [63, 64, 65, 66]. Here  $A_{\text{ch}}$  stands for the effective area of one conduction channel. According to previous experiments  $A_{\text{ch}} \sim 30 \text{ nm}^2$  [65, 67, 68], and the junction area  $A \sim 150 \times 150 \text{ nm}^2$  which is estimated roughly from the scanning electron micrograph. We have then  $\gamma \sim 1 \times 10^{-3}$  which is of the same order of magnitude as from our experimental estimate,  $\gamma = 1.6 \times 10^{-3}$ . In junctions not affected by Andreev effects, the microwave radiation yields the dominant contribution of  $\gamma$  [69]. Next, we use the parameters  $\gamma$ ,  $R_T$ , and  $\Delta/e$  and simulate the  $I - V$  curves at various temperatures based on Eq. (4.1) with the help of Eq. (4.3) for describing the DOS of the actual sample. This set of curves is presented in the left panel of Fig. 4.2. It is clear that by increasing temperature, the  $I - V$  curves become increasingly smeared. The inset of this panel shows the zoom of the  $I - V$ s in a narrow current range. Basic temperature measurement is done by applying a fixed current  $I_m$  to the SINIS (or NIS) structure. This way the voltage across the junction is changing as a function of temperature and thus this measurement works as a calibration for our system. The right panel of Fig. 4.2 displays such calibrations for different values of  $\gamma$ . The leakage  $\gamma$  plays an important role in determining the sensitivity of the thermometer. Based on this figure it is vivid that for

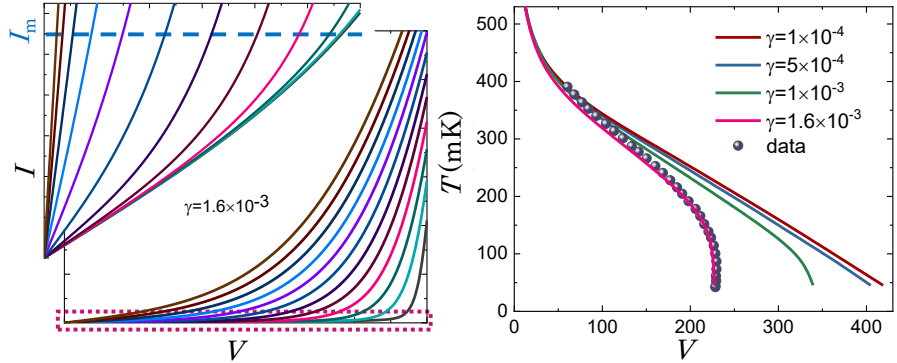


**Figure 4.2.** The role of leakage parameter  $\gamma$  in calibration of the thermometer. (left) Calculated  $I - V$  characteristics of the SINIS structure presented in Fig. 4.1(a) from Eq. (4.1) at different temperatures, with parameters  $R_T = 34 \text{ k}\Omega$  and  $\Delta/e = 230 \mu\text{V}$ . The zoom of the red rectangle is presented in the inset. The presence of the leakage,  $\gamma$ , induces a slope in the subgap region which leads to sensitivity loss at low temperatures. Applying a fixed current  $I_m$  (blue dashed line), one can extract voltages at different temperatures which gives a thermometer. Calibrations of such a thermometer for different values of  $\gamma$  are presented in the right panel with a few values of  $\gamma$ . By increasing  $\gamma$  the calibration saturates at low temperature. The experimental data shown with black symbols catches the curve presenting  $\gamma = 1.6 \times 10^{-3}$ , which was obtained as in Fig. 4.1.

small  $\gamma$ s the thermometer is sensitive down to low temperatures while by increasing it the curves saturate at low  $T$  at voltage  $V_0$  given by

$$V_0 = \frac{I_m R_T}{\sqrt{\gamma^2 + (\frac{e I_m R_T}{\Delta})^2}}. \quad (4.5)$$

This expression can be obtained from Eq. (4.4) by setting  $T_e = 0$  and  $I \equiv I_m$ . The experimental data is shown as symbols in the same panel and matches quantitatively with the predicted dependence using the independently determined parameters  $\gamma$ ,  $R_T$  and  $\Delta/e$  (no extra fit parameters). Responsivity  $\mathcal{R}$  is an important figure of merit of a sensor which is defined as the rate of change of the measured quantity (here voltage) with respect to temperature, meaning  $\mathcal{R} = dV/dT$ . In the next chapters, the expression for  $\mathcal{R}$  needs to be redefined for other quantities of interest. Using Eq. (4.4), one can compare the ratio of  $\mathcal{R}$  of the SINIS thermometer in the presence,  $\mathcal{R}(\gamma)$ , and absence,  $\mathcal{R}(\gamma = 0)$ , of the leakage as

$$\begin{aligned} \frac{\mathcal{R}(\gamma)}{\mathcal{R}(\gamma = 0)} &\equiv \frac{dV/dT}{(dV/dT)_{\text{ideal}}} \\ &= \left(1 + \gamma \frac{k_B T}{e R_T (I_m - \frac{\gamma V}{R_T})}\right)^{-1}. \end{aligned} \quad (4.6)$$

The above expression indicates that responsivity of the thermometer decreases with increasing leakage current, as one might expect.

### 4.1.2 Heat transport in a tunnel junction

The other important feature of the NIS junction lies in its thermal properties. In an analogous manner with charge current, heat current in NIS junction can be obtained. We have given the heat current in tunneling between two electrodes in Eq. (3.13); substituting  $L \rightarrow N$  and  $R \rightarrow S$ , and using the corresponding DOS for N and S, we have

$$\dot{Q}_N = \frac{1}{e^2 R_T} \int_{-\infty}^{\infty} d\epsilon (\epsilon - eV) v_S(\epsilon) [f_N(\epsilon - eV) - f_S(\epsilon)]. \quad (4.7)$$

With the same argument the heat from the superconductor reads

$$\dot{Q}_S = \frac{1}{e^2 R_T} \int_{-\infty}^{\infty} d\epsilon \epsilon v_S(\epsilon) [f_S(\epsilon) - f_N(\epsilon - eV)]. \quad (4.8)$$

Equations (4.7) and (4.8) leads to  $\dot{Q}_N + \dot{Q}_S = -IV$ , securing energy conservation, meaning that what goes out from the both electrodes equals to what goes out from the battery. In equilibrium,  $eV = 0$ , thermal conductance of the junction  $G_{th}^{(t)} = d\dot{Q}_N/dT$  is then given by

$$G_{th}^{(t)} = \frac{1}{e^2 R_T k_B T^2} \int_{-\infty}^{\infty} d\epsilon \epsilon^2 v_S(\epsilon) f_N(\epsilon) [1 - f_N(\epsilon)], \quad (4.9)$$

where  $f_N$  is now the common Fermi distribution of the two electrodes at the same temperature. The numerically calculated dimensionless cooling power  $\dot{Q}_N$  of normal-metal as a function of dimensionless voltage for a few values of temperature is plotted in Fig. 4.3(a). By applying voltage of about the superconducting gap,  $eV/\Delta \lesssim 1$ , heat is carried away from the N lead i.e., it acts as a refrigerator of N, but at the same time S is heated. For the voltages above the gap  $eV/\Delta \gg 1$  the junction heats up and presents usual Joule heating. This property allows one to use the NIS junction either as a heater or cooler of the absorber as shown in Fig. 4.1(a).

Next, we aim to obtain an analytical expression for the cooling power of a NIS junction of Eq. (4.7). First, we assume that  $k_B T \ll eV, \Delta$ , and that the superconductor is not overheated. As a result  $f_S(\epsilon) \sim 0$ , and one can expand the Fermi distribution of the normal metal for  $eV/\Delta < 1$  as  $(1 + e^{\tilde{\beta}(\varepsilon-v)})^{-1} = \sum_{n=1}^{\infty} (-1)^{n+1} e^{-n\tilde{\beta}(\varepsilon-v)}$ , which converges for  $\varepsilon \geq 1$ , i.e. in the integration interval. Here  $\tilde{\beta} = \Delta/k_B T$ ,  $\varepsilon = \epsilon/\Delta$ , and  $v = eV/\Delta$ . Substituting  $u = \sqrt{\varepsilon - 1}$  in the integral, we obtain

$$\dot{Q}_N \simeq \frac{\Delta^2}{e^2 R_T} \sum_{n=1}^{\infty} (-1)^{n+1} e^{-n\tilde{\beta}(1-v)} \int_0^{\infty} du (1 + u^2 - v) \frac{1 + u^2}{\sqrt{2 + u^2}} e^{-n\tilde{\beta}u^2}. \quad (4.10)$$

Using the Taylor expansion for the fraction in the integrand we have  $\frac{1+u^2}{\sqrt{2+u^2}} \simeq (\frac{1+u^2}{\sqrt{2}})(1 - u^2/4 + 3u^4/32)$ . Here for simplicity, we only solve the first order correction for  $\epsilon = \Delta$ , we then have

$$\dot{Q}_N \simeq \sqrt{\frac{\pi}{2\tilde{\beta}}} \frac{\Delta^2}{e^2 R_T} e^{-\tilde{\beta}(1-v)} [(1-v) + \frac{1}{2\tilde{\beta}}]. \quad (4.11)$$

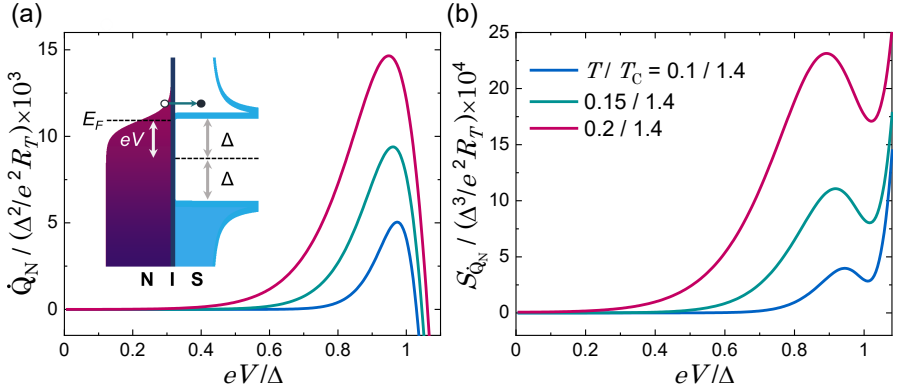


**Figure 4.3.** Heat transport properties of a NIS tunnel junction. (a) The cooling power of the N electrode as a function of bias voltage at three different temperatures demonstrating a maximum just below the gap voltage  $V = \Delta/e$ . The energy diagram illustrating the cooling effect is shown in the inset: hot electrons tunnel out from N to states just above the gap in the S electrode when biased near the optimum voltage. (b) The corresponding low frequency noise  $S_{\dot{Q}_N}$  under the same conditions as in (a). Here one observes both a maximum and minimum below the gap voltages as discussed in the text.

In this case the optimum cooling power reads

$$\dot{Q}_N^{\max} \simeq 0.76 (k_B T_e/\Delta)^{3/2} \Delta^2/(e^2 R_T),$$

at position  $V_{\text{opt}} = (\Delta - 0.5k_B T)/e$ . In order to obtain the voltage bias where the optimum cooling power occurs, we assume a simple representative toy model where the singularity of DOS can be approximated by a delta function at  $\epsilon = \Delta$ . In this case solving the integral of Eq. (4.7) is straightforward; in the same limit (low  $T$  and  $f_S(\epsilon) \rightarrow 0$ ), we have

$$\dot{Q}_N \sim \frac{1}{e^2 R_T} (\Delta - eV) f_N(\Delta - eV). \quad (4.12)$$

Assuming  $\Delta - eV \equiv \delta$ , cooling power is maximized when  $\mathcal{J}(\delta) \equiv \delta f_N(\delta)$  is maximum. For low  $T$ ,  $\mathcal{J}(\delta) \approx \delta e^{-\beta\delta}$  and  $\dot{\mathcal{J}}(\delta) \approx (1 - \beta\delta)e^{-\beta\delta}$ .  $\dot{\mathcal{J}}(\delta) = 0$  when  $\delta = \frac{1}{\beta}$ , then  $V_{\text{opt}} \sim (\Delta - k_B T_e)/e$ . With the more precise value for the optimum voltage bias  $V_{\text{opt}} \simeq (\Delta - 0.66k_B T_e)/e$ , [59] and considering the superconductor to be at temperature  $T_S$  [70, 59] we have

$$\dot{Q}_N^{\max} \simeq \frac{\Delta^2}{e^2 R_T} \left\{ 0.59 \left( \frac{k_B T_e}{\Delta} \right)^{\frac{3}{2}} - \sqrt{\frac{2\pi k_B T_S}{\Delta}} e^{-\frac{\Delta}{k_B T_S}} \right\}, \quad (4.13)$$

which is useful for quantitative performance estimates of realistic coolers.

Beyond the average heat current, its noise can be obtained in a straightforward manner as well. Noise of heat current is important for applications, e.g., in thermometry, where this noise leads to temporal fluctuations of effective temperature of the measured object. Noise is either thermal equilibrium noise or shot noise under non-equilibrium conditions. Both of these contributions are present in thermometry, where both non-zero

temperature and non-zero biasing (either dc or ac) are needed. Based on Eq. (3.15), heat current noise for a NIS junction at low frequency is then given by

$$S_{\dot{Q}_N}(0) = \frac{1}{e^2 R_T} \int_{-\infty}^{\infty} d\epsilon (\epsilon - eV)^2 v_S(\epsilon) \times \\ \{f_S(\epsilon)[1 - f_N(\epsilon - eV)] + f_N(\epsilon - eV)[1 - f_S(\epsilon)]\}. \quad (4.14)$$

Figure 4.3 (b) displays the numerically calculated dimensionless heat current noise against dimensionless voltage for few different values of  $T_e$ . The curves include a maximum and a minimum at subgap voltages, above which the noise increases monotonically. Based on the expansion model that we explained for heat current and with the same assumptions, the first approximate expression at  $n = 1$ , the heat current noise reads

$$S_{\dot{Q}_N}(0) \simeq \frac{\sqrt{2}\Delta^3}{e^2 R_T} e^{-\tilde{\beta}(1-v)} \left\{ \frac{(1-v)^2}{2} \sqrt{\frac{\pi}{\tilde{\beta}}} + (1-v) \frac{\sqrt{\pi}}{2\tilde{\beta}^{3/2}} + \frac{3\sqrt{\pi}}{8\tilde{\beta}^{5/2}} \right\}. \quad (4.15)$$

From this first-order approximation, the maximum of noise at position  $V_{\max} \sim (\Delta - k_B T_e)/e$  reads  $S_{\dot{Q}_N}^{(\max)} \sim 1.26(k_B T_e/\Delta)^{5/2}\Delta^3/(e^2 R_T)$ , on the other hand the minimum is  $S_{\dot{Q}_N}^{(\min)} \sim 0.94(k_B T_e/\Delta)^{5/2}\Delta^3/(e^2 R_T)$  happens at  $V_{\min} \sim \Delta/e$ . These extrema can also be obtained based on our toy model which we explained earlier average for heat current. One can say that  $S_{\dot{Q}_N}$  is maximized when  $\mathcal{J}(\delta) \equiv \delta^2 f_N(\delta)$  is maximum. For low  $T$ ,  $\mathcal{J}(\delta) \approx \delta^2 e^{-\beta\delta}$  and  $\dot{\mathcal{J}}(\delta) \approx (2 - \beta\delta)\delta e^{-\beta\delta}$ .  $\dot{\mathcal{J}}(\delta) = 0$  when  $\delta = \frac{2}{\beta}$ , then  $V_{\max} = \Delta - 2k_B T_e/e$ , while a more precise estimate yields  $V = (\Delta - 1.21 k_B T_e)/e$ . The root  $\delta = 0$  predicts a minimum exactly at gap voltage, also seen in Fig. 4.3 (b). These results demonstrate that the maximum of noise is twice further away from the gap voltage as compared to that of cooling power.

In summary of this section, the leakage current influences dramatically the sensitivity of the NIS thermometer at low temperatures (Fig. 4.2). Making a more ideal junction is one way to fight this issue: in many cases it is doable. Most of the time the source of leakage in our samples is not because of the quality of the junctions but due to the inevitable design of the samples. Based on Fig. 4.1 (a), the absorber (N electrode) is directly coupled to superconductors on both left and right sides by direct NS contacts. In the next subsection we will explain what the consequence of such a clean contact is, and how we can use it in favour of thermometry. This new generation of sensors can then be used directly at low temperatures and it has potential of detecting low-energy quanta, e.g., single microwave photons.

#### 4.1.3 Thermometry based on supercurrent - "ZBA thermometer"

In a clean NS contact, meaning a good electrical contact between the two, the normal metal can assume superconducting properties. In other words, a

Cooper pair can penetrate from the superconductor to the normal metal [71, 72, 22] by the process of Andreev reflection [73, 74]. The mechanism of a charge transfer through a NS interface is as follows: an incident electron with energy smaller than the superconductor gap from N side can produce a Cooper pair in S together with a retroreflective hole in N [73]. In the N side, the penetration depth of the proximity effect which is also called the thermal coherence length reads  $\xi_N = \sqrt{\hbar D/(2\pi k_B T)}$ , where  $D = v_F \ell_e / 3$  denotes the diffusion coefficient with  $v_F$  the Fermi velocity and  $\ell_e$  the elastic mean free path. Similarly, in the superconductor side, the superconducting coherence length is  $\xi_S = \sqrt{\hbar D/(2\Delta)}$ . In what follows we will discuss how this proximity effect can be used to improve thermometry at low temperatures.

We illustrate the principle of proximity thermometry in Fig. 4.4 together with central experimental observations. The upper panel of Fig. 4.4(a) displays schematically the NIS junction connected to another superconducting lead via direct metal-to-metal contact (NS). As explained above, this superconductor lead induces the proximity effect to the N lead and permits supercurrent via the tunnel junction; we called this structure S $\mathfrak{N}$ IS, where  $\mathfrak{N}$  stands for proximitized normal metal. Moreover, the  $\mathfrak{N}$ S contact which is directly grounded at the sample stage provides a fixed chemical potential for the absorber and acts as a heat mirror. The SEM image of one of the typical S $\mathfrak{N}$ IS thermometers in use is shown in the lower panel of Fig. 4.4(a), which has the same colour code as the upper one. The corresponding  $I - V$  characteristics of such samples in the range of  $\pm 50 \mu\text{V}$  are given in the inset of Fig. 4.4(b) which indicates the nonvanishing current in the small bias range. Intuitively the shorter the distance  $L$  between the clean contact and junction, the more proximity in the normal metal there is. Figure 4.4(b) illustrates this property where the measured peak-to-peak current  $I_{\max}$  for ten different samples is plotted against the distance  $L$ . The black dashed line shows a fit illustrating approximately decreasing  $I_{\max}$  as a function of  $L$ .

This rapid increase in the  $I_{\max}$  with decreasing distance of the clean contact from the junction suggests the potential of having higher responsivity for smaller values of  $L$ . Figure 4.4(c) is the proof of this statement where  $I_{\max}$  is plotted against temperature for two samples with  $L = 50 \text{ nm}$  and  $L = 100 \text{ nm}$ . Comparing the two curves with the one presented in the left panel of Fig. 4.2 for NIS junction indicates better performance of S $\mathfrak{N}$ IS proximity thermometer than NIS, especially at lower temperatures, in particular weaker saturation of the measured parameters at low  $T$ . Yet, one can see that the  $I_{\max}$  loses its temperature sensitivity below approximately 50 mK. The origin of saturation is obviously self-heating. The dissipation at the peak of the supercurrent is given by  $IV \sim 30 \text{ aW}$ , which may sound like a small power but as was demonstrated in Publication XII, it leads to significant over-heating of the electrode. Next, we suggest an even less

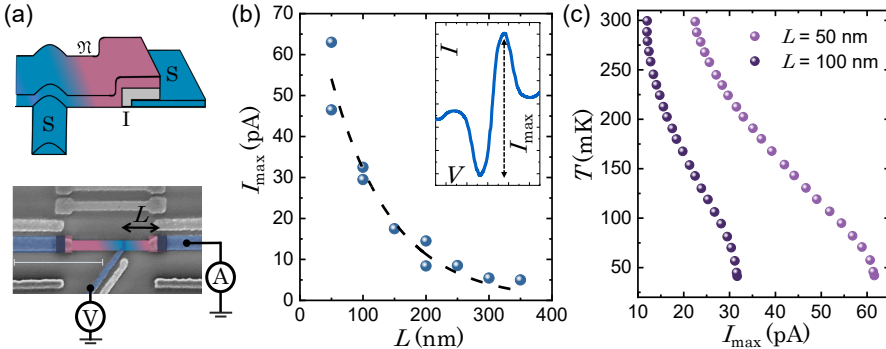


**Figure 4.4.** Principle and basic characteristics of the SMIIS proximity thermometer. (a) Schematic illustration of the tunnel junction for proximity thermometer (upper panel) together with the SEM image of one of the typical samples (lower panel) with the same colour code. The superconductor (S) in blue has a direct contact to the normal metal (N) in pink and induces proximity effect to it. The distance  $L$  between the clean contact and the junction is the key parameter here. The typical measured  $I - V$  for SMIIS proximity thermometer for  $L = 50$  nm at  $T = 50$  mK in the range of  $V = \pm 50$   $\mu$ V indicating non-vanishing supercurrent is shown in the inset. (b) Measured peak-to-peak current  $I_{\max}$  at base temperature as a function of  $L$ . Dashed line  $I_{\max}[\text{pA}] = 91.25 \exp(-L[\text{nm}]/95.66)$  is a fit through experimental data. (c) Temperature dependence of  $I_{\max}$  for SMIIS junctions for two samples with different  $L$ .

invasive measurement of temperature using the very same probe.

As shown in Fig. 4.4(b) it is possible to decrease the distance down to  $L \sim 50$  nm. Figure 4.5 demonstrates the main characteristics of the optimized SMIIS proximity thermometer for  $L \sim 50$  nm. Measuring  $I - V$  characteristics of the SMIIS junction has a better performance as compared to a NIS thermometer at low temperatures, but still it suffers from self-heating. An option is to measure the conductance of the junction in a quasi-DC measurement, meaning with low-frequency ( $\lesssim 100$  Hz) lock-in techniques applying typically an excitation voltage of approximately  $\sim 1 - 2$   $\mu$ V ac which is small enough not to average over the bias dependent features in conductance. Figure 4.5(a) represents the optimized SMIIS proximity thermometer with  $L \lesssim 100$  nm together with the simplified measurement setup. The measured charge current  $I$  and conductance  $G$  of the optimized SMIIS junction against applied voltage bias  $V$  in the ranges  $\pm 170$   $\mu$ V and  $\pm 0.7$  mV are shown in panels 4.5(b) and 4.5(c), respectively. The main feature in Fig. 4.5(c) is the zero-bias anomaly (ZBA) around  $V = 0$  which is indicated by the central black arrow in the SMIIS thermometer. For thermometry we measure the conductance at this peak ( $V = 0$ ) which is presented in Fig. 4.5(d). It manifests a nearly linear dependence in a wide temperature range with no saturation at low temperatures. The SMIIS proximity thermometer is noninvasive (measured at zero bias) and sensitive (no saturation) at low temperatures, in contrast to the NIS thermometer. At large bias voltages, some new features appear as the superconducting gap structure is affected by the proximity effect, different from the case

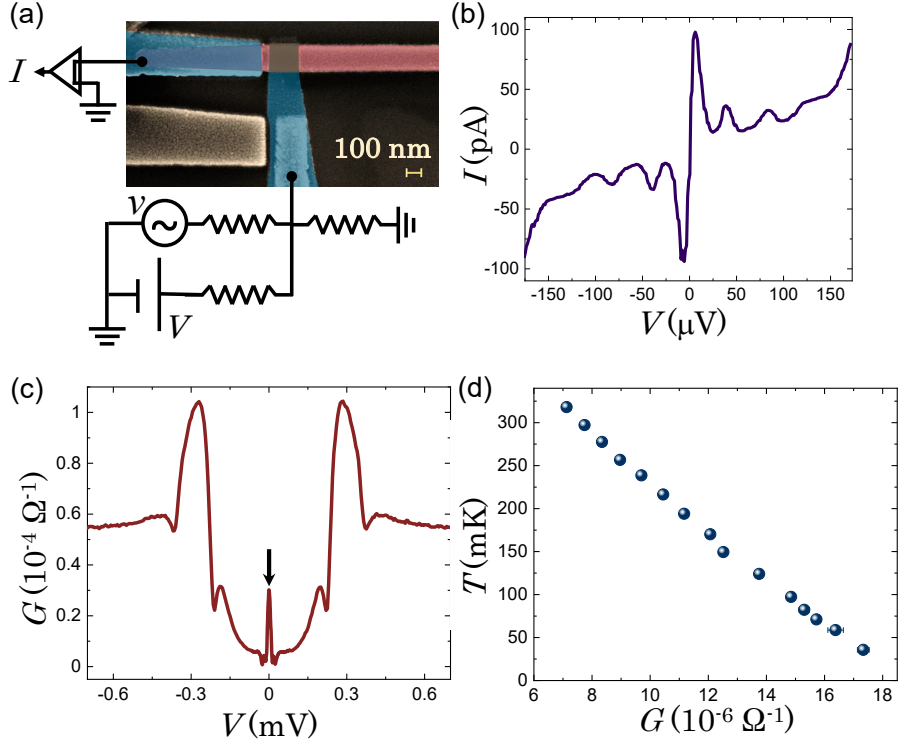


**Figure 4.5.** Main characteristics of the optimized SMIIS proximity thermometer. (a) The measurement setup including SEM image of the SMIIS structure with defined labels and the simplified schematic of the conductance measurement. (b) Measured  $I - V$  at  $T = 40$  mK. Several peaks appearing along with the supercurrent arise probably because of the multiple Andreev reflection due to the relatively high transparency of the junction or due to the electromagnetic environment [75]. (c) Bias dependence of the conductance of the proximity thermometer measured at  $T = 40$  mK. The black arrow indicates ZBA thermometry at  $V = 0$ . The possible explanation of other features is given in the text. (d) The thermometer calibration versus the bath temperature.

of pure BCS pattern for NIS thermometer which was shown in the upper inset of Fig. 4.1(b). In the proximitized normal metal, the standard BCS coherence peaks are now split due to the existence of the minigap around  $eV = \pm\Delta$  of an NIS junction.

## 4.2 RF thermometry

In order to detect microwave photons emitted by e.g., superconducting quantum circuits, one option is to develop a nanocalorimeter which is capable of measuring subkelvin energy quanta with microsecond time resolution. In calorimetry, we monitor the temperature of a small metallic absorber coupled to a phonon bath. Up to now, we only discussed DC measurements for both NIS and S<sup>M</sup>NIS thermometers. This DC-setup limits the bandwidth of the measurement to the kHz range due to the high impedance of the junctions (especially in the case of NIS) and specifically because of the stray capacitances of the measurement setup. Hence the DC-configuration is not suitable for fast temperature measurement. To overcome this obstacle, we need a RF-setup with a temperature sensitive element coupled to an absorber. For this we embedded the junctions (NIS and S<sup>M</sup>NIS) in a distributed *LC* resonator as schematically shown in the left side of Fig. 4.6. The prototype scheme of the readout was presented in Refs. [76, 77] and further discussed in Ref. [78]. This setup has been recently applied for Coulomb blockade thermometry which can be found in Publication XX. The right side of Fig. 4.6 demonstrates the actual setup (distributed *LC* resonator and SEM image of the S<sup>M</sup>NIS junction) corresponding to the left side. As shown in the figure, the *LC* resonator is connected to input and output RF lines via coupling capacitors  $C_1$  and  $C_2$ . Since we perform the readout in the transmission mode, one specific choice is that the input coupling is weak, which means that most of the input signal is reflected, and this way it decouples noise in the input line. The small coupling can be compensated by larger input signals. The ratio of output  $V_2$  and input  $V_1$  voltages,  $s \equiv 2V_2/V_1$ , see Fig. 4.6, is given by

$$s(\omega) = \frac{-i2\omega^3 R_L C_1 C_2 L}{\{1 - \omega^2 [LC_\Sigma + LC_2 R_L/R]\} + i\omega [L/R + R_L C_2 - \omega^2 L(C_1 + C)R_L C_2]}, \quad (4.16)$$

where  $C_\Sigma = C + C_1 + C_2$ , and  $R_L = 50\Omega$  denotes the impedance of the transmission-line.  $R$  is the inverse of the differential conductance  $G \equiv dI/dV$  of the junction. The resonance (angular) frequency can be obtained with the help of transmittance of power  $|s(\omega)|^2$ , meaning  $\partial|s(\omega)|^2/\partial\omega = 0$ . Using Eq. (4.16) and in the limit  $R_L/R \ll 1$ , we find the resonance (angular) frequency  $\omega_0 \simeq 1/[L(C + C_1 + C_2)]$ . Substituting  $\omega_0$  in Eq. (4.16) we have

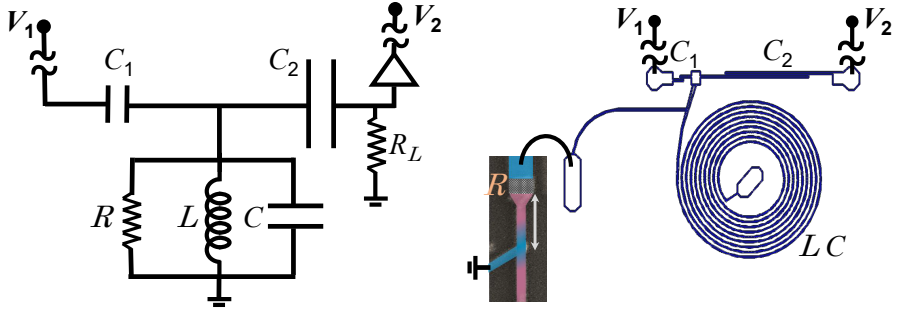


**Figure 4.6.** Basics of the RF transmission measurement. The measured element  $R$  is embedded in an  $LC$  tank circuit as shown schematically on the left and as real elements on the right. The image of the spiral is directly adapted from the photograph of it.

$s(\omega_0) = -2\omega_0^2 C_1 C_2 R_L R / [1 + \omega_0^2 C_2^2 R_L R]$  which can be simplified as

$$s(\omega_0) = -\frac{2C_1}{C_2} \frac{1}{1 + R_0 G}, \quad (4.17)$$

where  $R_0 = (\omega_0^2 R_L C_2^2)^{-1}$ . Thus, for  $G \rightarrow 0$ ,  $s(\omega_0) \rightarrow -2C_1/C_2$ , i.e., it obtains the value given by the ratio of the input and output couplings. The typical measured quantity is the logarithmic transmitted power in dBm,  $S_{21}(\omega_0) = 10 \lg(V_1^2 |s(\omega_0)|^2 / (4R_L P_0))$ , at resonance frequency, referenced to  $P_0 = 1 \text{ mW}$ . Using this definition and Eq. (4.17) we have

$$S_{21}(\omega_0) = S_0 - 20 \lg(1 + R_0 G), \quad (4.18)$$

where  $S_0 = 20 \lg(C_1 V_1 / (C_2 \sqrt{R_L P_0}))$  is a constant offset which in the actual setup includes also the attenuation and amplification in the lines. For low conductance of the junction  $G \ll R_0^{-1}$ , one can linearize the relation between  $S_{21}$  and  $G$  into the form

$$G = \frac{\ln(10)}{20R_0} (S_0 - S_{21}(\omega_0)), \quad (4.19)$$

Equation (4.18) or the linearized one (4.19) indicate that  $S_{21}$  is a measure of the negative of the differential conductance of the junction.

Figure 4.7(a) displays an SEM image of a typical SMIS structure embedded in the RF measurement setup. For a comparison between two types of thermometers, quasiparticle (QP) and zero-bias anomaly (ZBA), we take two samples where a copper normal-metal absorber in dark pink (Fig. 4.7(a)) has two different lengths  $\ell = 2 \mu\text{m}$  and  $\ell = 1 \mu\text{m}$ . This absorber is connected to three superconducting leads in blue. The upper one is a tunnel contact responsible for thermometry, the lower one is an auxiliary tunnel junction working as a hot electron injector. The third one is a direct clean metal-to-metal contact grounded at the sample stage which we introduced earlier, providing fixed chemical potential, and inducing proximity effect to the absorber. The distance between the clean contact

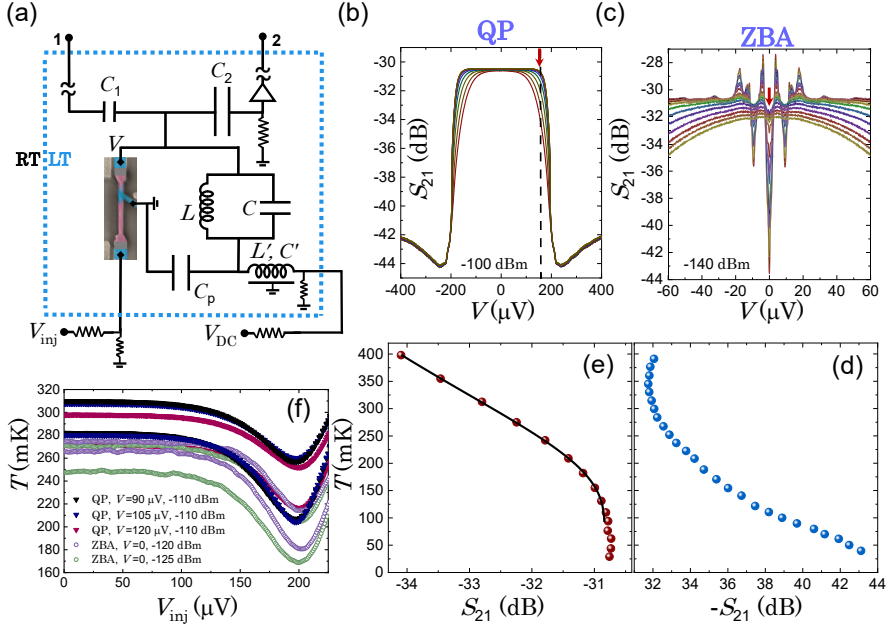


**Figure 4.7.** Radio-frequency measurement of a hybrid junction. (a) The actual resonance circuit showing the SQUID tunnel junction as the dissipative parallel element ( $R$ ) of the  $LC$ -resonator. The DC-biasing circuit via a bias-tee ( $L', C'$ ) is shown at the bottom. The area enclosed by the blue dashed line is that at low temperature on the sample stage. (b) Measurement of  $S_{21}$  as a function of bias voltage for a junction with vanishing proximity effect ( $L = 1 \mu\text{m}$ ). In this case  $S_{21}$  is close to the inverted conductance curve of a pure NIS tunnel junction. The various curves are taken at different temperatures in the range  $50 - 300$  mK, with increasing smearing towards higher  $T$ . The superconductor gap  $\Delta = 220 \mu\text{V}$  is determined independently by measuring the  $I - V$  curves of the sample. (c) A close-up of  $S_{21}$  versus  $V$  measurement in the low bias range for a junction with  $L = 0.5 \mu\text{m}$  again at various temperatures  $38 - 418$  mK. Here the characteristic zero-bias anomaly due to proximity supercurrent is the dominant feature showing strong temperature dependence especially at  $V = 0$ . (d) Dependence of temperature on  $-S_{21}$  at  $V = 0$  for the ZBA of (c). Nearly linear dependence is apparent down to  $\sim 30$  mK temperature. (e) Same as (d) for the quasiparticle thermometer (QP) of (b) at  $V = 156 \mu\text{V}$ , showing close to linear dependence above  $200$  mK and saturation (loss of temperature sensitivity) at  $T \lesssim 100$  mK. The solid line from Eq. (4.20) captures the temperature dependence with  $\tilde{r} = 3.66$  and  $S_0 = -30.83$  as the fitting parameters. (f) Comparison of the two-in-one thermometers, QP and ZBA, in their common operation range. The electron temperature measured by the two when the extra NIS tunnel contact is biased at  $V_{\text{inj}}$ , leading to cooling at  $V_{\text{inj}} \lesssim 200 \mu\text{V}$  and subsequent heating above this voltage. The data shows that the readings of the two thermometers agree reasonably well under these conditions.

and the upper junction is  $L = 1 \mu\text{m}$  for QP thermometer and  $L = 0.5 \mu\text{m}$  for ZBA. The superconductor lead of the junction is included in a parallel on-chip LC resonator which is connected to input and output rf lines via coupling capacitors  $C_1$  and  $C_2$  ( $C_1 \ll C_2$ ), and operating at the frequency  $f_0 \simeq 640 \text{ MHz}$ . The DC voltage  $V$  of the thermometer is connected via a bias tee ( $L'C'$  in Fig. 4.7(a)) and a voltage divider. This includes a resistor of about  $10 \Omega$  fixed at the printed circuit board of the sample box. For QP thermometer with  $L = 1 \mu\text{m}$ , we have a pure NIS configuration since the direct superconducting contact is far away from the thermometer junction and this leads to a vanishing proximity effect. The measurement of  $S_{21}$  for both QP and ZBA thermometers versus DC voltage bias  $V$  of the thermometer for a set of bath temperatures are presented in Figs. 4.7(b) and 4.7(c). In the panel 4.7(b) which is for the case of a junction with vanishing proximity effect ( $L = 1 \mu\text{V}$ ),  $S_{21}$  behaves like the inverted conductance of a pure NIS junction. By extracting the data points of  $S_{21}$  at different bath temperatures and a fixed voltage bias (shown by black dashed line and indicated by a red arrow), one obtains the calibration of QP thermometer which is shown in panel 4.7(e). The thermometer has a linear temperature dependence above  $200 \text{ mK}$  and it loses its sensitivity at temperatures  $T \lesssim 100 \text{ mK}$  demonstrated by the vanishing responsivity  $\mathcal{R} \equiv |dS_{21}/dT|$ . In this regime one can obtain an analytical expression for  $T$  versus  $S_{21}$ . As we discussed before, the  $I - V$  characteristics of a pure NIS junction at low temperatures and at voltages below the gap,  $eV \ll \Delta$ , and in the absence of leak current ( $\gamma = 0$ ) is given by  $I \simeq I_0 e^{-(\Delta - eV)/k_B T_e}$  (Eq. (4.4)). Then for  $R_0 G$  we have  $R_0 dI/dV = (eI_0 R_0 \exp(eV - \Delta))/k_B T_e$ . Substituting this expression in Eq. (4.18) we have

$$T = \frac{\Delta}{k_B} \left(1 - \frac{eV}{\Delta}\right) \frac{1}{\ln \tilde{r} - \ln(e^{\frac{\ln 10}{20}(S_0 - S_{21})} - 1)}, \quad (4.20)$$

where  $\tilde{r} = \sqrt{\pi\Delta/(2k_B T)} R_0 / R_T$ . Figure 4.7(e) displays the data points extracted from the transmission curves of panel 4.7(b) at fixed voltage bias  $V = 156 \mu\text{V}$  and  $-100 \text{ dBm}$  of the rf signal for different bath temperatures. In this panel the solid black line shows a fit to the corresponding experimental data based on Eq. (4.20). It is vivid that the theoretical expression captures nicely the experimental data. Here  $\tilde{r}$  and  $S_0$  are the fitting parameters and we ignored the logarithmic temperature dependence on  $\tilde{r}$ .

In the panel 4.7(c), the measurement of  $S_{21}$  versus  $V$  for the proximitized junction with  $L = 0.5 \mu\text{m}$  presents the zero-bias anomaly at zero-bias voltage which is strongly temperature dependent. The extracted  $-S_{21}$  at  $V = 0$  for different bath temperatures is presented in panel 4.7(d), which shows a nearly linear dependence down to  $\sim 30 \text{ mK}$ . The ZBA feature in the rf-measurement setup is similar to the one presented in the DC measurement (Fig. 4.5). Moreover, comparing 4.7(d) and 4.7(e) illustrates that the

**Table 4.1.** Comparison of different thermometry techniques employed in this work from the point of view of self-heating. All of these methods are applicable using the same proximitized NIS junction. In the traditional SINIS thermometry voltages near the gap due to quasiparticles current are measured. Due to voltage of about  $400 \mu\text{V}$ , the total power is large, about  $10^{-14} \text{ W}$  although mainly distributed to the external S electrode. Measuring the maximal proximity supercurrent at  $V = 10 \mu\text{V}$  (Fig. 4.5(b)) is also dissipative with about  $10^{-15} \text{ W}$  self-heating. The measurement of differential conductance of the proximity supercurrent around zero voltage yields a way lower dissipation: in the lock-in measurements of Fig. 4.5, excitation amplitude of  $1 \mu\text{V}$  was used, leading to  $10^{-17} \text{ W}$  power, whereas in the RF measurement at  $-140 \text{ dBm}$  excitation level, the dissipated power is as low as  $10^{-21} \text{ W}$ .

Method	$I [\text{pA}]$	$V [\mu\text{V}]$	$G [\mu\Omega^{-1}]$	Power [ $\text{fW}$ ]
SINIS	15	400	-	$\sim 10$
$I_{\max}$	$\sim 100$	$\sim 10$	-	$\sim 1$
ZBA (lock-in)	-	1	$\sim 10$	$\sim 0.01$
ZBA (RF)	-	0.02	$\sim 10$	$\sim 0.000001$

responsivity  $\mathcal{R}$  of ZBA thermometer at  $T < 200 \text{ mK}$  is  $\simeq 0.06 \text{ dB/mK}$ , which clearly exceeds  $\mathcal{R} \simeq 0.01 \text{ dB/mK}$  of the QP-thermometer in the temperature range of its applicability.

Now a question arises as to what extent the ZBA thermometer is reliable in electron thermometry? What temperature does it measure? Due to the lack of reference thermometer, we cannot make this comparison at the lowest temperatures. However, at higher temperatures one can prove that ZBA and QP are measuring essentially the same local temperature. In order to compare these two thermometers, we consider the sample with  $L = 0.5 \mu\text{m}$ . We manipulate the electronic temperature  $T_e$  of the normal-metal island by applying a bias voltage  $V_{\text{inj}}$  across the auxiliary junction, the lower junction of Fig. 4.7(a) with tunnel resistance  $R_{\text{inj}} \simeq 50 \text{ k}\Omega$ . The thermometer junction (the upper junction in 4.7(a)) monitors the electronic temperature of the normal metal. The influence of  $V_{\text{inj}}$  is the feature depicted in Fig. 4.7(f). In all curves the electronic temperature drops at  $V_{\text{inj}} \sim \Delta/e$  due to the quasiparticle cooling effect [59] discussed in Section 4.1.2 and shown in Fig. 4.3(a). In Fig. 4.7(f) we present  $T$  under different conditions; ZBA operating at two different powers and several bias values as a QP thermometer. Operating the thermometer in the two modes, ZBA or QP, indicates close to identical temperatures over the whole  $V_{\text{inj}}$  bias range. For clarity we show only a few curves under limited number of conditions. In Fig. 5 (b) of Publication VI we have demonstrated measurements under different conditions while measuring the minimum temperatures at  $V_{\text{inj}} \sim \Delta/e$  against bath temperature  $T$ . Based on the coincidence of the different sets of data in this figure, we conclude that all these thermometers measure, in a consistent way, the temperature of the electrons in the island.

### 4.3 Self-heating of the local thermometer

Thermometry is one of the cornerstones in developing a detector of radiation quanta. In this chapter we presented the development of on-chip thermometers, where they measure continuously the electronic temperature of the absorber for bolometry and calorimetry. The goal is to measure a microwave single photon of small energy in the range of  $100 \mu\text{eV}$  posing a great challenge [79]. In order to reach this milestone, we showed how to develop a noninvasive thermometer, operating at low enough temperature with reasonable noise level. In Table. 4.1, we compare from self-heating point of view different thermometry techniques employed in this chapter, all applicable using the same proximitized NIS junction! One can see that in the traditional SINIS thermometers by applying a fixed current of  $\sim 15 \text{ pA}$  and due to the voltage of  $\sim 400 \mu\text{V}$  near the gap, the thermometer itself dissipates  $10 \text{ fW}$  in the absorber, although mainly dissipated in the superconductor. This power is huge especially at low temperatures and specifically when it comes to detecting low energy quanta. Three other methods presented here are applicable when we use proximitized normal metal (S<sup>n</sup>NIS configuration). All offer better performance as compared to the SINIS thermometer from the self-heating point of view. In the second method by measuring the maximal proximity supercurrent (Fig. 4.4), the self-heating power can be reduced by one-order-of magnitude, i.e. it reaches  $1 \text{ fW}$  level. ZBA thermometry, where the differential conductance of the proximity supercurrent is measured, leads to less dissipation in the absorber. In the table we estimate the dissipated power in two different measurement configurations. In the lock-in measurements of Fig. 4.5, by applying  $f < 100 \text{ Hz}$  and excitation amplitude of  $1 \mu\text{V}$ , the dissipation power is about  $10^{-17} \text{ W}$  which shows clear improvement as compared to the previous methods. In the RF measurement for ZBA at  $-140 \text{ dBm}$  excitation level, the dissipated power is as low as  $10^{-21} \text{ W}$ , i.e. seven orders of magnitude smaller than in SINIS.

### 4.4 Sample fabrication

In this section we briefly describe the fabrication process for the samples used in Publication VI, Publication IX, and Publication XII. All these structures were fabricated by the standard methods of electron beam lithography (EBL) and multi-angle metal deposition by electron-beam evaporation and lift-off. We use commercial silicon wafer onto which a  $300 \text{ nm}$  silicon oxide layer by thermal oxidation has been grown. For making NIS and S<sup>n</sup>NIS junctions, we use the suspended germanium process [80, 81, 82] for achieving robust deposition mask. We build a tri-layer resist scheme onto the wafer as follows. The first layer is  $\sim 400 \text{ nm}$  of copolymer P(MMA-

MAA) which is spin-coated on the wafer at 5500 rpm for 1 min followed by baking on a hot plate at 180 °C for 30 – 40 min. The second layer is a thin layer of Ge with 22 nm thickness which is deposited by electron beam evaporation with slow rate of ~ 0.2 Å/s. The final layer is polymethyl-methacrylate (PMMA) which is spin coated on the wafer at 2500 rpm for 1 min and then baked on a hot plate at 160 °C for 1 min. The third layer at the top is mainly sensitive to the incident electrons, while the first layer at the bottom to the secondary electrons exposed to it at the EBL, which allows us to make undercut structures for multi-angle evaporation. Next step is mask preparation. For this, the layout of the sample is patterned on the top layer with EBL and the wafer is developed in a mixture of methyl isobutyl ketone (MIBK) and isopropanol (IPA) at a ratio of 1:3 at room temperature for 60 s followed by 30 s rinsing in pure IPA. The process is then followed with reactive ion etching (RIE) of Ge using carbon tetrafluoride CF<sub>4</sub> for ~ 140 s. After this step we recommend another wet development with MIBK:IPA 1:3 to assist in the undercut formation. In the second etching process with RIE, we use anisotropic and isotropic undercut etching with oxygen for about one hour to form the undercut. The chip with mask is then placed in an electron-beam evaporator equipped with a tilting stage. After reaching the desired pressure in the chamber we first deposit 20 nm of Al making the leads, followed by in-situ oxidation in pure O<sub>2</sub> (1 min at 1 mbar) resulting in a relatively transparent insulating layer of aluminum oxide. Next, another layer of Al with 20 nm thickness, provides the clean superconducting contact at the desired distance e.g. 50 nm from the thermometer junction. As the final layer, we deposit 35 nm Cu to form the absorber. Note that the effective thickness of Al layers may be somewhat smaller due to the partial oxidation of the film. The final stage of the fabrication is the lift-off of the germanium mask and the underlying resist stack. This process is carried out by a wet development in acetone for ~ 10 – 20 min followed by a rinse in pure IPA for 30 s.

We prepare the spiral resonator on a separate chip. Since we use only one-angle evaporation here, there is no need to prepare the tri-layer resist. One can use only one-layer resist but in order to have a reliable lift-off we use a standard two-layer process excluding Ge from the previous recipe with appropriate thicknesses and developers. After preparing the mask, we evaporate a 100 nm thick Al layer at zero angle, followed by the same lift-off process as above.

Fabrication of the rest of the structures described in this thesis, on which I provided theoretical input, have been described in Publication V, Publication VII, and Publication X and their either supplementary materials or method sections. These structures include the transmon qubits and coplanar waveguide resonators with resistive terminations.

## 4.5 Experimental considerations

To perform the experiments in this thesis, we need cryogenic temperatures, due to fundamental and practical reasons. As discussed in Publication XIV, to operate in the quantum regime, one needs low temperatures and physically small structures. This means that the temperature  $T$  has to be low enough such that  $k_B T < \hbar\Omega$ , where  $\hbar\Omega$  is the energy separation of the resonators and qubits. In our case  $\hbar\Omega/k_B \lesssim 1$  K. Moreover, based on the principle of our local thermometers, NIS and S $\ddot{\text{O}}$ IS, the working temperatures must be well below the critical temperature  $T_C$  of the superconductor in use, which is  $\sim 1$  K for Al. Finally, the calorimeter presented in this thesis works best at the lowest possible temperatures. The  $^3\text{He} - ^4\text{He}$  dilution refrigerator can provide the necessary sub-100 mK temperatures. A detailed description of the operating principle and design of a custom-made plastic dilution refrigerator, can be found in [83] and [84], respectively. We use both wet and dry dilution refrigerators which are able to reach base temperatures of  $\sim 50$  mK and  $\sim 10$  mK, respectively, to perform the experiments in this thesis. The results presented in Publication V, Publication VII, and Publication X were measured in both types of refrigerators. The measurements in Publication VI and Publication IX were done only in dry refrigerator while the measurements of Publication XII and Publication XIII only in a custom-made plastic dilution refrigerator. In most of the experiments, we used the calibrated  $\text{RuO}_x$  resistor thermometers to monitor the bath temperatures, while in more sensitive measurements like in Publication IX, the Coulomb blockade thermometer [85, 86] was used for calibration. The measurements were mostly performed in a carefully shielded and filtered setup. The details are described in Ref. [87]. Since all the superconducting qubit based measurements are sensitive to magnetic flux, the shielding setup was mandatory and it is described in Ref. [88]. For the RF measurements for calorimetry, we used the sample stage developed in Ref. [78] and the existing setup operating at around 600 MHz in the dry dilution refrigerator described in Refs. [76, 77].



# 5. Control of photonic heat in cQED structures

In this chapter, superconducting qubit [89, 90, 91] is introduced as a tunable element that mediates heat by microwave photons between two thermal baths. The fact that characteristic properties of superconducting qubits such as frequency, anharmonicity, and importantly the coupling between them can be designed easily and adjusted to the needs of the experiment in question, is one of the central advantages of such elements. In general controlling heat transport can be realized by magnetic [11, 92] or electric fields [93] acting on the qubits. This way one can realize heat valves, rectifiers, heat interferometers, quantum refrigerators, and heat engines in the future. There are several types of superconducting qubits, e.g., charge (also called a Cooper-pair box) [94], flux [95, 96], and transmon qubits [24] that are options to be used in such devices. In the experiment done in this thesis, we used a transmon-type qubit, which has levels whose positions can be controlled by magnetic flux through a dc-SQUID (superconducting quantum interference device) loop. For heat transport experiments, transmon behaves nearly as a harmonic oscillator. However, we will see its use as a rectifier. But the current ideas for active quantum refrigerators, a flux or a charge qubit would present a closer correspondence to the basic theory. However, at the typical experimental temperatures  $\lesssim 300 \text{ mK}$  even the transmon with its energy splitting of  $\gtrsim 0.5 \text{ K}$  behaves almost as a two-level system (since the thermal population of the third level is quite small at the low temperatures  $\sim e^{-5} < 0.01$ ) in static heat transport experiments. In all the experiments presented in this chapter, qubit is not driven. This means that the coherent properties of the qubit do not play central role. In the next chapter, the qubit in similar devices will be driven and the outcome will be discussed theoretically.

## 5.1 Quality factor

Up to now, we have discussed coupling between qubit and thermal bath (resistor) in a model-independent way. In reality typically we use a quarter

wavelength  $\lambda/4$  superconducting coplanar waveguide resonator to connect qubit with thermal bath. Now the question is what the quality factor of this resonator is while we embed a dissipative element ( $R$ ) at its end. Although characterizing such superconducting microwave resonators including dissipative elements is a technical challenge, it is necessary for us to implement and more importantly to understand the operation of it in hybrid quantum devices.

Consider a transmission line with finite length  $\ell$  at the position  $0 \leq x \leq \ell$  and terminated at  $x = \ell$  by a load impedance  $Z_L$ ; the impedance of this line (resonator) is then given by

$$Z = \frac{e^{i2k\ell} - \chi}{e^{i2k\ell} + \chi} Z_0, \quad (5.1)$$

where  $k$  is the wave number and  $Z_0 = \sqrt{\ell_0/c_0}$  the impedance of the transmission line at  $x = 0$  with  $\ell_0$ ,  $c_0$  the inductance and capacitance per unit length of the line, and  $\chi = (Z_0 - Z_L)/(Z_0 + Z_L)$  denotes the reflection coefficient [75]. In the limit where the transmission line is open at its end,  $Z_L \rightarrow \infty$ , we have  $\chi \rightarrow -1$ . Near the resonance, i.e., for  $k = k_0 + \delta k$  values for  $k_0\ell = \pi/2$  for  $\lambda/4$  resonator, we may expand  $Z$  and as a result we have  $Z = i\frac{\pi}{2}Z_0\delta(\frac{\omega_0}{\omega})$  with  $\omega_0$  the (angular) frequency of the resonator. For a small variation around resonance frequency we have  $\delta(\frac{\omega_0}{\omega}) = \frac{1}{2}(\frac{\omega}{\omega_0} - \frac{\omega_0}{\omega})$ . The impedance of a  $\lambda/4$  resonator can then be written as

$$Z \simeq i\frac{\pi}{4}Z_0\left(\frac{\omega}{\omega_0} - \frac{\omega_0}{\omega}\right). \quad (5.2)$$

In order to calculate the quality factor of the resonator terminated to a dissipative element  $R$  like the one presented in Fig. 5.1(a), we need first to obtain the energy loss in it. The panel (b) of this figure shows an equivalent lumped circuit for the resistor terminated resonator. Applying a sinusoidal drive voltage  $v = v_0 \sin(\omega t)$  into the circuit shown in Fig. 5.1(b) and with the help of Eq. (5.2), the power injected to the termination at the half-power points  $\omega = \omega_0 \pm \Delta\omega/2$ , where  $\Delta\omega$  is the width of the resonance peak, can be written as

$$P \simeq \frac{v_0^2}{R} \frac{1}{1 + (\frac{\pi Z_0}{4R})^2 (\frac{\omega}{\omega_0} - \frac{\omega_0}{\omega})^2} = \frac{v_0^2}{2R}. \quad (5.3)$$

The quality factor  $Q$  of the resistively terminated resonator is then by definition  $Q = \omega_0/\Delta\omega$  given by

$$Q = \frac{\pi Z_0}{4R}. \quad (5.4)$$

The  $\lambda/4$  resonator presented in Fig. 5.1(a) is made of Nb and at one end, it is terminated by a normal-metal resistor (Cu) via a superconductor (Al). Based on the technique presented in Publication VII for isolating the resonance of low-quality dissipative superconducting resonators, one needs to measure the transmittance spectra both below and above the transition

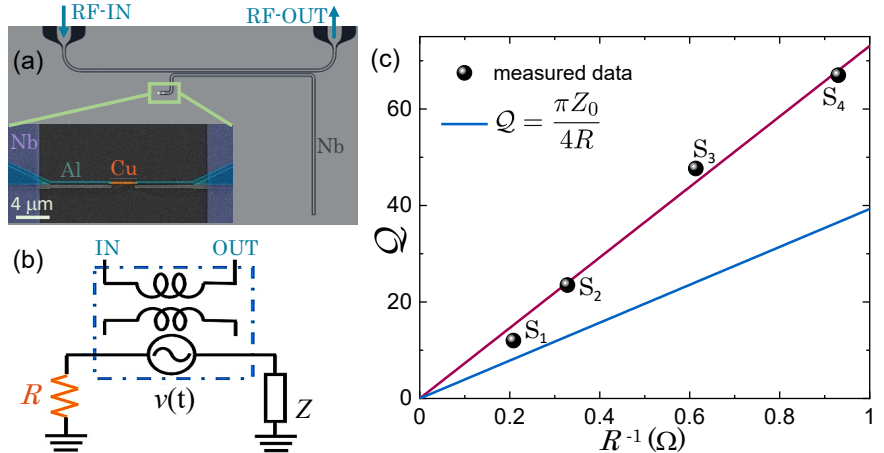


**Figure 5.1.** Quality factor of a resonator terminated by a dissipative element. (a) The image of the chip shows a  $\lambda/4$  resonator made of Nb inductively coupled to a transmission line used for applying the probe signal through input and output RF lines. The  $\lambda/4$  resonator is terminated at one end by a resistor (Cu) through a superconductor (Al) forming a Nb/Al/Cu/Al/Nb heterostructure, while the opposite end is open. Inset presents the SEM image of the dissipative constrictions, which is connected to the resonator at the right side and at the left side it is grounded. (b) An equivalent lumped circuit for a resonator terminated by resistance  $R$ . The coupling between the transmission line and  $\lambda/4$  resonator is presented by a mutual inductance symbol in a blue square, and  $R$  stands for the Cu termination. (c) Symbols illustrate the measured quality factor for four different samples,  $S_1 - S_4$ , which based on the thickness of the Cu and/or different contact resistance between the Nb/Al, have different quality factors. The red line presents the linear fit to the data while the blue one represents the theoretical prediction for this resonator. A possible origin of the difference between the two lines is explained in the text.

temperature of the intermediate superconductor with a lower energy gap (here Al) as compared to that of the superconducting resonator (here Nb). Figure. 5.1(c) shows the measured quality factor of a  $\lambda/4$  resonator as a function of inverse termination resistance  $1/R$  for four different samples  $S_1 - S_4$ . The blue line displays the theoretical expected  $Q$  given by Eq. (5.4) whereas the red line is a linear fit to the measured data.

The plausible source of this discrepancy is that admittance of the SNS (Al/Cu/Al) junction is composed of parallel dissipative (real) and reactive (imaginary) components,  $Y_{re}$  and  $Y_{im}$ , respectively. The actual quality factor  $Q$  is then enhanced with respect to the simple expression by a factor  $\varsigma \equiv (Y_{re}^2 + Y_{im}^2)/Y_{re}^2$  [97]. Let us first assume naively a tunnel Josephson junction with critical current  $I_c$  having inductance  $L_J = \hbar/(2eI_c)$ . In this case  $Y_{im} = (\omega_0 L_J)^{-1}$  and we assume  $Y_{re} = 1/R$ , which then leads to  $\varsigma \gtrsim 1$ . Here, we deal with an SNS junction instead of a tunnel junction. Since we are in the high frequency regime, based on the results in Ref. [97] we expect  $Y_{re} = 1/R$  and  $Y_{im} = (0.5...1)/R$ , depending on the phase across the junction, which in turn depends on the current through it [97]. We estimate that this can lead to an enhancement of the quality factor  $Q$  by approximately factor  $\varsigma \sim 2$ , which would explain the discrepancy.

## 5.2 Analysis of the photonic heat valve in the weak coupling regime

This section covers the contents presented in Publication V. Here, we calculate and measure the photonic heat transport between two baths through a superconducting qubit in so-called **local** and **global** regimes which are shown in Figs. 5.2, 5.3, and 5.4. In this device displayed in the lower panel of Fig. 5.3(a), a transmon-type qubit in the center, with level spacing  $\hbar\omega_Q$  which is tunable by magnetic flux  $\Phi$ , is capacitively coupled to two identical  $\lambda/4$  coplanar waveguide resonators made out of Nb with resonance frequency  $f_0 = \omega_0/2\pi \sim 5$  GHz. Each of these resonators is terminated by a normal-metal resistor made out of Cu acting as reservoir (thermal bath). This resonator-qubit-resonator assembly forms a heart of the quantum heat valve. The measurement of heat transport in such a circuit yields some fundamental questions of open quantum systems [98, 99, 100, 101, 102, 103, 104, 105, 106, 107]. In this device the coupling between reservoir-resonator  $\gamma$  and resonator-qubit  $g$ , both normalized by  $f_0$ , and the ratio  $r = \omega_Q/\omega_0$  are playing a crucial role in the heat transport in the device and determining in which regime the device is, meaning quantitatively the separation between a quantum system and its environment ("Heisenberg cut"). In the local regime (shown in the upper panel of Fig. 5.3(a)) where  $\gamma \gg g$ , the qubit acts as the quantum system and dissipative  $LC$  as its environment meaning that qubit decays to the bath via the resonator, on the other hand in the global regime (upper panel of Fig. 5.4(a)) where  $\gamma \ll g$  the resonator-qubit-resonator forms a hybrid system which is then weakly coupled to the heat baths. We perform experiment for both regimes and for modelling the whole setup in general we consider the weak coupling where one can apply standard perturbation theory to describe the power. In general, the power  $P_i$  to each reservoir  $i = 1, 2$ , reads in both pictures

$$P_i = \sum_{k,l} \rho_{kk} \varepsilon_{kl} \Gamma_{k \rightarrow l, i}, \quad (5.5)$$

where the sum runs over all the eigenstate indices  $k, l$ . Here  $\rho$  denotes the density matrix,  $\varepsilon_{kl}$  and  $\Gamma_{k \rightarrow l, i}$  are the energy difference and rate between these states for each reservoir. The relaxation to these engineered heat baths (reservoirs) is the predominant source of losses. In this case the quality factor of the resonator is  $\mathcal{Q} \equiv \gamma^{-1}$ . Based on the discussion in the previous section where we described the quality factor of a resonator terminated by a resistor is  $\mathcal{Q} = \pi Z_\infty / 4R$  (Eq. (5.4)). Here the resistance of the reservoir is  $R \sim 2\Omega$  which leads to  $\mathcal{Q} \sim 20$ , but depending on the transparency of the metallic interfaces, additional dissipation can significantly decrease the quality factor of the resonator.

### 5.2.1 Local regime

Figure 5.3(a) presents a schematic illustration and actual device of quantum heat valve in a so-called **local** regime. We first start with the calculation of the photonic heat transport between two heat baths through a superconducting qubit schematically shown in Fig. 5.2. We focus first on the left side of the circuit (shown in black line) where resistor  $R$  with temperature  $T$  is embedded in an  $LC$  circuit which is capacitively coupled to the qubit in the middle (shown in green line) through the capacitor  $C_g$ . Since we are in the weak coupling regime we assume that  $C_g$  is small. As we explained before the resistor produces the voltage noise  $v_n$  and in the loop using simple Kirchhoff's laws we have  $v_n - i(R + Z_{LC}) = 0$ . Here  $Z_{LC}$  denotes the impedance of the lumped  $LC$  circuit whose expression reads  $Z_{LC} = -iZ_0/(\frac{\omega}{\omega_0} - \frac{\omega_0}{\omega})$ , where  $Z_0 = \sqrt{L/C}$  and  $\omega_0 = 1/\sqrt{LC}$  is the resonance (angular) frequency of the  $LC$  circuit. The voltage drops across the  $LC$ ,  $v = iZ_{LC}$ , and qubit  $v_Q = C_g v / (C_Q + C_g) \simeq C_g v / C_Q$  are then given by

$$\begin{aligned} v &= \frac{1}{1 + i\mathcal{Q}(\frac{\omega}{\omega_0} - \frac{\omega_0}{\omega})} v_n, \\ v_Q &= \frac{C_g}{C_Q} \frac{1}{1 + i\mathcal{Q}(\frac{\omega}{\omega_0} - \frac{\omega_0}{\omega})} v_n \end{aligned} \quad (5.6)$$

where  $\mathcal{Q} = R/Z_0$  is the quality factor. The spectral density of noise for voltage across the qubit with the help of Eq. (5.6) then reads

$$S_{v_Q}(\omega) = \left( \frac{C_g}{C_Q} \right)^2 \frac{1}{1 + \mathcal{Q}^2(\frac{\omega}{\omega_0} - \frac{\omega_0}{\omega})^2} S_{v_n}(\omega). \quad (5.7)$$

Next, we need to obtain the transition rates in the qubit induced by the thermal noise of the resistor  $R$ . We know the total Hamiltonian for the circuit shown in Fig. 5.2(a) is  $\hat{\mathcal{H}} = \hat{\mathcal{H}}_0 + \hat{\mathbb{V}}$ , where  $\hat{\mathcal{H}}_0$  is the sum of the unperturbed Hamiltonians of the resistor, resonator and qubit. The coupling between the resonator and qubit which acts as a perturbation is the product of the noise and the charge operator of the qubit reads  $\hat{\mathbb{V}} = v_n \hat{q}$ , where  $\hat{q} = -i\sqrt{\frac{\hbar}{2Z_Q}}(\hat{a} - \hat{a}^\dagger)$  with  $Z_Q = \sqrt{L_Q/C_Q}$ . The golden rule transition rates between the two levels of the qubit (ground,  $|g\rangle$  and excited  $|e\rangle$  states) due to the resistor  $R$  are given by

$$\Gamma_{\uparrow,\downarrow} = \frac{1}{\hbar^2} |\langle g | \hat{q} | e \rangle|^2 S_{v_Q}(\pm\omega_Q). \quad (5.8)$$

Here, the  $+$  and  $-$  signs refer to the relaxation ( $\downarrow$ ) and excitation ( $\uparrow$ ) of the qubit, respectively. Substituting Eq. (5.7) and using  $S_{v_n}(\omega) = \frac{2R\hbar\omega}{1-e^{-\beta\hbar\omega}}$  as the voltage noise of a bare resistor with inverse temperature  $\beta = 1/k_B T$  at (angular) frequency  $\omega$ , the relaxation rate is given by

$$\Gamma_\downarrow = \frac{g}{1 + \mathcal{Q}^2(\frac{\omega_Q}{\omega_0} - \frac{\omega_0}{\omega_Q})^2} \frac{\omega_Q}{1 - e^{-\beta\hbar\omega_Q}}, \quad (5.9)$$

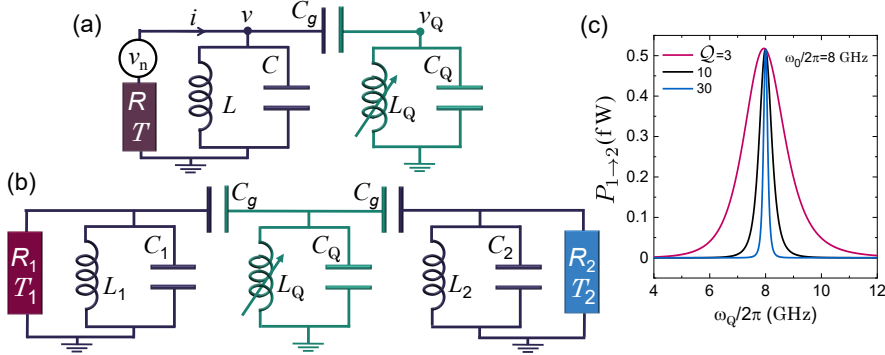


**Figure 5.2.** Quantum heat valve and rectifier in the weak coupling regime and at local picture. (a) Heat bath (resistor  $R$ ) coupled via a cavity ( $LC$  resonator) to the qubit with coupling capacitance  $C_g$ . This setup leads to transition rates that peak in Lorentzian manner when qubit energy matches that of the cavity. (b) Adding another heat bath via another cavity and coupling capacitor yields a two-bath system where the heat can be transported via the qubit. (c) Calculated heat transferred from the first bath (resistor  $R_1$ ) to the second one (resistor  $R_2$ ) as a function of qubit frequency with different values of common quality factor of identical resonators. In this panel the temperatures of the two baths are  $T_1 = 0.3$  K,  $T_2 = 0.1$  K, and the coupling is  $g = 0.03$ . This figure demonstrates the basic heat valve operation.

where  $g = \frac{R}{Z_Q} \left( \frac{C_g}{C_Q} \right)^2$  denotes the coupling term. Applying the detailed-balance conditions, the excitation rate also reads  $\Gamma_\uparrow = \Gamma_\downarrow e^{-\beta \hbar \omega_Q}$ . In order to transport heat (power) from one bath (resistor  $R_1$ ) to another (resistor  $R_2$ ) via the qubit, we now add a similar set to the right side of Fig. 5.2(a), as schematically shown in panel 5.2(b). Under steady state conditions we have from master equation  $\dot{\rho}_{gg} = \Gamma_\downarrow \rho_{ee} - \Gamma_\uparrow \rho_{gg} = 0$ , which yields the populations of the ground state and excited state of the qubit as

$$\rho_{gg} = \frac{\Gamma_\downarrow}{\Gamma_\Sigma} \text{ and } \rho_{ee} = \frac{\Gamma_\uparrow}{\Gamma_\Sigma}, \quad (5.10)$$

where  $\Gamma_{\downarrow(\uparrow)} = \Gamma_{\downarrow(\uparrow)}^{(1)} + \Gamma_{\downarrow(\uparrow)}^{(2)}$ ,  $\Gamma_\Sigma^{(i)} = \Gamma_\downarrow^{(i)} + \Gamma_\uparrow^{(i)}$  for  $i = 1, 2$ , and  $\Gamma_\Sigma = \Gamma_\Sigma^{(1)} + \Gamma_\Sigma^{(2)}$ . The power from the first bath to the second one is then given by

$$P_{1 \rightarrow 2} = \hbar \omega_Q (\Gamma_\downarrow^{(2)} \rho_{ee} - \Gamma_\uparrow^{(2)} \rho_{gg}). \quad (5.11)$$

Assuming identical resonators and resistors, meaning the same quality factor and resonance frequency,  $Q_1 = Q_2$  and  $\omega_0^{(1)} = \omega_0^{(2)} \equiv \omega_0$ , the power to the second bath is

$$P_{1 \rightarrow 2} = \frac{g \hbar \omega_0^2}{2} \frac{n(\beta_1 \hbar \omega_Q) - n(\beta_2 \hbar \omega_Q)}{[1 + Q^2(\frac{\omega_Q}{\omega_0} - \frac{\omega_0}{\omega_Q})^2][\coth(\frac{\beta_1 \hbar \omega_Q}{2}) + \coth(\frac{\beta_2 \hbar \omega_Q}{2})]}, \quad (5.12)$$

where  $n(\beta_i \hbar \omega) = (e^{\beta_i \hbar \omega} - 1)^{-1}$  for  $i = 1, 2$ .

We describe the actual system in Fig. 5.3(a), and assign it to be in the local regime by assuming that the resistor(s) and  $LC$ -resonator(s) are forming the structured environment for the qubit in the middle. The

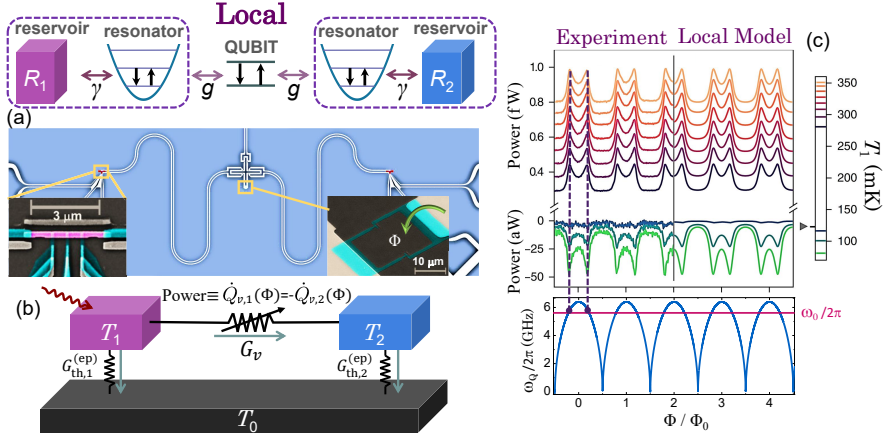


**Figure 5.3.** Local regime in quantum heat valve. (a) The top panel shows the schematic illustration of the local regime, where qubit acts as a system and resonator-reservoir as the environment with the coupling condition  $\gamma > g$ . The lower panel presents the quantum heat valve device where a transmon-type superconducting qubit, whose level spacing  $\hbar\omega_Q$  is tunable by magnetic flux  $\Phi$ , in the center is capacitively coupled to two identical  $\lambda/4$  coplanar waveguide superconducting resonators with length= 4.6 mm, each made out of Nb. Each resonator is terminated by a normal-metal resistor (Cu) acting as a reservoir. The left inset displays SEM image of one of the reservoirs (pink) in clean contact with Al (blue) leads. The temperature of the reservoir is monitored and controlled by three NIS probes (Cu/AlO<sub>x</sub>/Al). The SEM image of the SQUID in the transmon structure is shown in the right inset. This element can be controlled by  $\Phi$ . (b) Thermal model for the device shown in (a). Two finite-sized reservoirs are coupled to each other via a tunable element and each of them is connected to heat bath. (c) Modulation of photonic heat transport in the local regime. The lower panel displays the frequency of a transmon qubit  $\omega_Q/2\pi$  as a function of magnetic flux  $\Phi$  (Eq. (5.14)) normalized by magnetic flux quantum  $\Phi_0$ . The frequency of identical resonators  $\omega_0/2\pi \sim 5.61$  GHz meets the qubit  $\omega_Q/2\pi$  two times in a period. The parameters are  $E_C/h = 0.15$  GHz,  $E_{J0} = 35.7$  GHz, and  $d = 0.08$ . The upper panel illustrates the measured heat current power in this regime (Eq. (5.12)) versus  $\Phi/\Phi_0$ . In this set of measurement at  $T_0 = 55$  mK, temperature of the second reservoir is fixed at  $T_2 \sim 120$  mK, while each trace in (c) corresponds to a different temperature of the first reservoir  $T_1$  shown in the legend bar. The two Lorentzian peaks in each period, like the one shown in Fig. 5.2(c), illustrate the condition  $\omega_Q = \omega_0$  in each period indicated by violet dashed line. The three lowest temperature of  $T_1$  shown by green traces with peaks pointing downwards demonstrate cooling at the distance.

thermal model of the whole device is shown conceptually in panel 5.3(b), where the two reservoirs are connected via a tunable element and each reservoir is furthermore connected to the phonon bath. In this figure, heat over a distance of a few millimeters from bath to bath is transferred wirelessly (via capacitors) by microwave photons. In order to control and monitor the temperature of each reservoir we use a SINIS probe junction shown in the left inset of Fig. 5.3(a). Next question is how to measure the power. Experimentally, for small temperature differences  $T_2 - T_0$ , the power  $P_{1 \rightarrow 2} = -P_{2 \rightarrow 1}$ , by energy conservation is given by

$$P_{1 \rightarrow 2} = G_{\text{th},2}^{(\text{ep})}(T_2 - T_0), \quad (5.13)$$

where  $G_{\text{th},2}^{(\text{ep})} = 5\Sigma\mathcal{V}T_2^4$  is the thermal conductance to the phonon bath as we had before with  $\Sigma$  and  $\mathcal{V}$  as the electron-phonon coupling constant and volume of the normal-metal reservoir, respectively. For the transmon qubit, the (angular) frequency of the qubit as a function of applied magnetic field is given by

$$\omega_Q = \frac{\sqrt{8E_J(\Phi)E_C} - E_C}{\hbar}, \quad (5.14)$$

where  $E_C$  denotes the fixed charging energy of the junction and  $E_J(\Phi) = E_{J0}|\cos(\pi\Phi/\phi_0)\sqrt{1+d^2\tan^2(\pi\Phi/\phi_0)}|$  the Josephson energy of the transmon with  $E_{J0}$  the maximal Josephson coupling. Here,  $\phi_0 = h/2e$  is the magnetic flux quantum and  $d$  stands for the asymmetry of the SQUID in form of the relative difference of the Josephson energies of the two junctions in it. The lower panel of Fig. 5.3(c) shows the dependence of qubit frequency on magnetic field, based on the given parameters for local regime. The frequency of identical resonators  $\omega_0/2\pi \sim 5.61$  GHz shown with a red line, meets  $\omega_Q/2\pi$  two times in a period. The measurement of the power and the theoretical modeling for it (Eq. (5.12) without background contribution) are presented in the left and right side of the upper panel in 5.3(c). The dissipative  $LC$  resonator which acts as an environment for qubit in the local regime, has Lorentzian noise spectrum centered around its resonance frequency. Based on this figure, the qubit indeed acts as a valve which admits heat current (power) through only when  $\omega_Q = \omega_0$  indicated by the purple dashed lines which applies for both measured data and the theory prediction. The only fit parameter for Eq. (5.12) is the quality factor of the resonator  $Q = 3.15 \pm 0.14$ . Such a low quality factor clearly justifies the use of the local model since  $g/\gamma \equiv gQ \sim 0.05$ .

### 5.2.2 Global regime

In the opposite, so-called **global** regime, the system is composed of resonator-qubit-resonator entity which then interacts with dissipative environment formed of the two bare resistors (heat baths). This regime is schematically shown in Fig. 5.4(a). In order to obtain the amount of power transferred

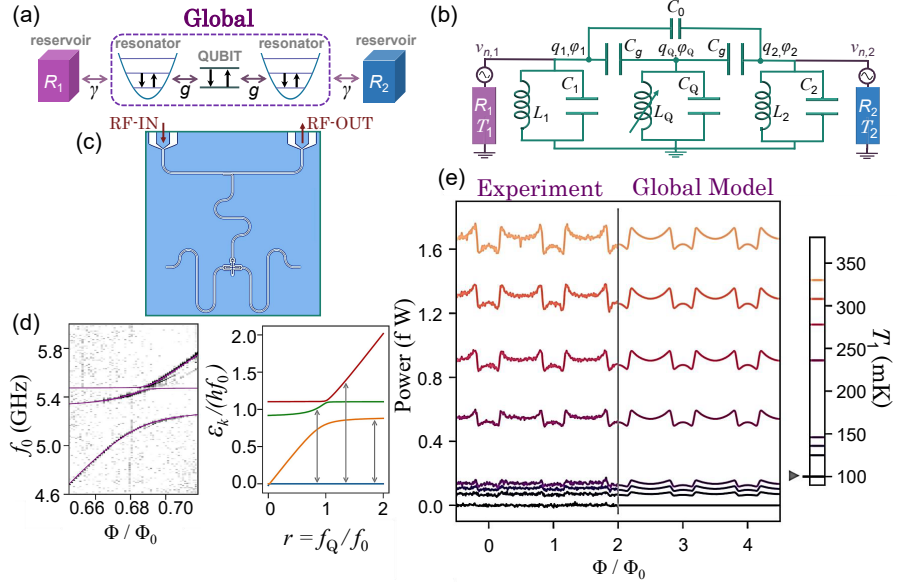


**Figure 5.4.** Global regime in quantum heat valve. (a) Schematic illustration of the global regime, where resonator-qubit-resonator assembly provides a hybrid system which is weakly coupled to the dissipative environment with the coupling condition  $\gamma < g$ . (b) The lumped-element approximation of the quantum heat valve, where the hybrid system is shown by green colour. (c) The optical image of the actual device used for spectroscopy measurement is shown. Here, the left and right  $\lambda/4$  resonators at their ends connected to the ground directly and the 7.4 GHz diagnostic resonator is inductively and capacitively ( $\sim 3.4$  fF) coupled to the RF feedline and to the top arm of the transmon island, respectively. (d, left) Two-tone transmission spectroscopy measurement centered in the  $\omega_Q \sim \omega_0$  region for the sample shown in the top panel. The parameters extracted from the data are:  $\omega_0 = 5.39$  GHz,  $g = 0.02$ ,  $\tilde{g} = -0.015$ , and the asymmetry parameter  $a = 0.008$ . (d, right) Calculated eigenenergies (Eq. (5.18)), with arrows indicating the allowed transitions between the states. For visual clarity, the parameters are:  $g = -\tilde{g} = 0.1$  and  $a = 0.05$ . (e) Modulation of photonic heat transport in the global regime. Measured heat current power in this regime is shown in the left side and the simulation of it (Eq. (5.24)) on the right as a function of  $\Phi/\Phi_0$ . In this measurement at  $T_0 = 45$  mK, temperature of the second reservoir is fixed at  $T_2 \sim 100$  mK, while each trace corresponds to a different temperature of the first reservoir  $T_1$  controlled in the regime 100 – 330 mK and shown in the legend bar.

from one bath to another, one needs first to analyze the hybrid system itself. The lumped-element circuit representing the quantum heat valve in the global regime is schematically illustrated in Fig. 5.4(b). In this circuit diagram, we introduce the shunting capacitor  $C_0$  which is responsible for direct resonator-resonator photon transfer mechanism. The Lagrangian of the circuit presented in 5.4(b)  $\mathcal{L}(\varphi_1, \dot{\varphi}_1, \varphi_Q, \dot{\varphi}_Q, \varphi_2, \dot{\varphi}_2)$  reads

$$\begin{aligned}\mathcal{L} = & \frac{1}{2}(C_1\dot{\varphi}_1^2 + C_g(\dot{\varphi}_Q - \dot{\varphi}_1)^2 + C_Q\dot{\varphi}_Q^2 + C_g(\dot{\varphi}_Q - \dot{\varphi}_2)^2 \\ & + C_0(\dot{\varphi}_1 - \dot{\varphi}_2)^2 + C_2\dot{\varphi}_2^2) - \frac{1}{2}\left(\frac{\varphi_1^2}{L_1} + \frac{\varphi_Q^2}{L_Q} + \frac{\varphi_2^2}{L_2}\right).\end{aligned}\quad (5.15)$$

We obtain the conjugate momenta  $q_i$  of node fluxes ( $\varphi_i$ ) using Legendre transformation  $q_n = \frac{\partial \mathcal{L}}{\partial \dot{\varphi}_n}$ . With the charge operators  $\hat{q}_i = -i\sqrt{\hbar/2Z_0}(\hat{a}_i - \hat{a}_i^\dagger)$  and  $\hat{q}_Q = -i\sqrt{\hbar/2Z_0}(\hat{b} - \hat{b}^\dagger)$ , the Hamiltonian is written as

$$\hat{\mathcal{H}} = (hf_0)[\hat{a}_1^\dagger\hat{a}_1 + \hat{a}_2^\dagger\hat{a}_2 + r\hat{b}^\dagger\hat{b} + g(\hat{b}\hat{a}_1^\dagger + \hat{b}^\dagger\hat{a}_1 + \hat{b}\hat{a}_2^\dagger + \hat{b}^\dagger\hat{a}_2) + \tilde{g}(\hat{a}_1\hat{a}_2^\dagger + \hat{a}_1^\dagger\hat{a}_2)], \quad (5.16)$$

where  $g = (4\pi Z_0 C_c f_r)^{-1}$  is the coupling energy between the qubit and each resonator,  $\tilde{g} = (4\pi Z_0 C_{12} f_r)^{-1}$  indicates the coupling between two resonators,  $r = f_Q/f_0$ , and  $Z_0 = \sqrt{L_r/C_r}$ . Here, we have set  $C_c^{-1} = C_g/(C_Q C_r)$  and  $C_{12}^{-1} = C_0/(2C_0 C_r + C_r^2) - 2C_0(C_0 + C_r)C_g/(C_r^2(2C_0 + C_r)^2)$ . We consider the qubit to be a simple  $LC$  circuit. Moreover, in order to write the Hamiltonian in the matrix form we assume the product basis  $\{|000\rangle, |100\rangle, |010\rangle, |001\rangle\}$  where the first entry refers to the left resonator, second one to the qubit, and the last one to the right resonator. Here, based on the low temperature regime,  $\beta_i \hbar \omega_0 \gg 1$ , we neglect the occupation of higher levels in the resonator harmonics, which in this limit is acceptable. In addition, we assume a minor difference  $a$  between the eigenfrequencies of the two resonators. In this basis, the matrix form of the Hamiltonian reads then

$$\mathcal{H} = hf_0 \begin{pmatrix} 0 & 0 & 0 & 0 \\ 0 & 1+a/2 & g & \tilde{g} \\ 0 & g & r & g \\ 0 & \tilde{g} & g & 1-a/2 \end{pmatrix}. \quad (5.17)$$

Diagonalizing this Hamiltonian, the dimensionless eigenenergies  $\lambda_k = \varepsilon_k/hf_0$  are given by

$$\lambda_1 = 0, \quad \lambda_2 = 1 - \tilde{g}, \quad \lambda_{3,4} = \frac{1}{2}[1 + \tilde{g} + r \mp \sqrt{\tilde{o}}], \quad (5.18)$$

where  $\tilde{o} = 1 + 2\tilde{g} + \tilde{g}^2 + 8g^2 - 2r - 2\tilde{g}r + r^2$ . These eigenenergies and the allowed transition rates between them are shown in the right side of Fig. 5.4(d). In order to directly measure the flux-dependent spectrum of the eigenstates

in this global regime, we use a design shown in 5.4(c), where the left and right resonators are directly grounded without resistors and a diagnostic resonator with higher frequency  $f_d \sim 7.4$  GHz is inductively coupled to the RF feedline and capacitively to the top arm of the transmon island. Two-tone spectroscopy is achieved by measuring the transmission of the diagnostic resonator. The result is shown in the left panel of Fig. 5.4(d), similar to the right panel. After establishing the non-dissipative hybrid system (resonator-qubit-resonator), we introduce the dissipation to this system by adding the two reservoirs. With the help of Eq. (5.2) and the circuit diagram presented in Fig. 5.4(b), the voltage seen by the resonator is given by

$$v(t) = \frac{R}{R + iZ_0(\omega/\omega_0 - \omega_0/\omega)} v_n(t), \quad (5.19)$$

where  $v_n(t)$  is the bare voltage noise of the resistor at inverse temperature  $\beta = 1/k_B T$  with its voltage-noise spectrum,  $S_{v_n}(\omega) = 2R\hbar\omega/(1 - e^{-\beta\hbar\omega})$ . Then we have

$$S_v(\omega) = \frac{1}{1 + Q^2(\omega/\omega_0 - \omega_0/\omega)^2} \frac{2R\hbar\omega}{1 - e^{-\beta\hbar\omega}}. \quad (5.20)$$

Using the golden rule expression to obtain the transition rates induced by heat bath B ( $R_1$  or  $R_2$ ) between eigenstates  $k$  and  $l$  reads  $\Gamma_{k \rightarrow l, B} = \frac{1}{\hbar^2} |\langle k | \hat{q}_B | l \rangle|^2 S_{v, B}(\omega_{kl})$ , Here  $S_{v, B}$  is the noise on the resonator coupled to bath B. Substituting Eq. (5.20) in the transition rates and setting  $\varepsilon_{kl} = \hbar\omega_0(\lambda_k - \lambda_l) \equiv \hbar\omega_{kl}$ , we have

$$\Gamma_{k \rightarrow l, B} = \frac{1}{Q_B} \frac{|\langle k | \hat{a}_B - \hat{a}_B^\dagger | l \rangle|^2}{1 + Q_B^2(\frac{\omega_{kl}}{\omega_0} - \frac{\omega_0}{\omega_{kl}})^2} \frac{\omega_{kl}}{1 - e^{-\beta_B \hbar\omega_{kl}}}, \quad (5.21)$$

where  $Q_B$  is the quality factor of the resonator attached to bath B at inverse temperature  $\beta_B$ . Based on the allowed transition rates shown in Fig. 5.4(d), the matrix elements in Eq. (5.21) are  $|\langle 1 | \hat{a}_B - \hat{a}_B^\dagger | 2 \rangle|^2 = 1/2$ ,  $|\langle 1 | \hat{a}_B - \hat{a}_B^\dagger | 3 \rangle|^2 = (1 + [(r - 1 - \tilde{g})/\sqrt{(r - 1 - \tilde{g})^2 + 8g^2}])/4$ , and  $|\langle 1 | \hat{a}_B - \hat{a}_B^\dagger | 4 \rangle|^2 = 1/2 - |\langle 1 | \hat{a}_B - \hat{a}_B^\dagger | 3 \rangle|^2$ . For obtaining the power between the baths, we need the diagonal elements of the density matrix. Under non-driven conditions they are given by

$$\dot{\rho}_{ii} = \sum_{j=1}^4 \{ \Gamma_{j \rightarrow i} \rho_{jj} - \Gamma_{i \rightarrow j} \rho_{ii} \}, \quad (5.22)$$

for  $i = 1..4$ . Here  $\Gamma_{i \rightarrow j} = \Gamma_{i \rightarrow j, 1} + \Gamma_{i \rightarrow j, 2}$ . By applying steady-state condition as  $\dot{\rho}_{ii} = 0$  and based on the allowed transition rates, we then have

$$\begin{aligned} \rho_{11} &= \Gamma_{2 \rightarrow 1} \Gamma_{3 \rightarrow 1} \Gamma_{4 \rightarrow 1} / \Upsilon \\ \rho_{22} &= \Gamma_{1 \rightarrow 2} \Gamma_{3 \rightarrow 1} \Gamma_{4 \rightarrow 1} / \Upsilon \\ \rho_{33} &= \Gamma_{1 \rightarrow 3} \Gamma_{2 \rightarrow 1} \Gamma_{4 \rightarrow 1} / \Upsilon \\ \rho_{44} &= \Gamma_{1 \rightarrow 4} \Gamma_{2 \rightarrow 1} \Gamma_{3 \rightarrow 1} / \Upsilon, \end{aligned} \quad (5.23)$$

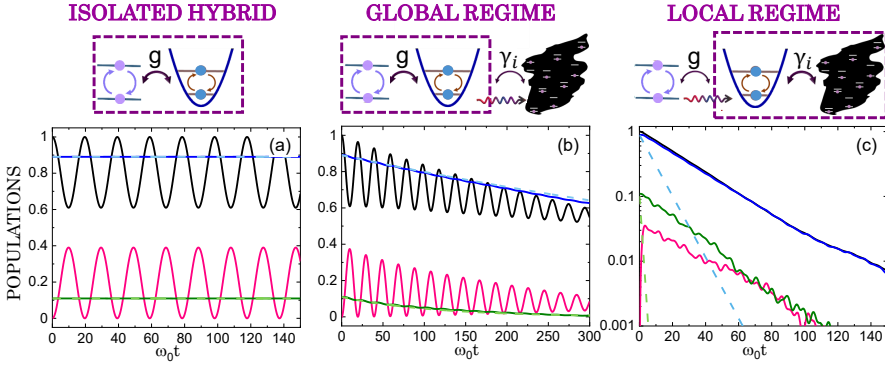


**Figure 5.5.** Relaxation of the qubit to heat bath in different operation regimes after the qubit (alone) has been prepared in its excited state. The upper panels in (a)-(c) present schematically the cross-over starting from isolated hybrid system (qubit-resonator) in (a) and the global and local regime in (b) and (c), respectively. The population of the qubit,  $|\mathcal{C}_Q(t)|^2$  (black solid line), cavity,  $|\mathcal{C}_C(t)|^2$  (red solid line), the first eigenstate of the hybrid system,  $\rho_{11}$  (blue solid line), and for the second eigenstate,  $\rho_{22}$  (green solid line), are shown in the lower panels of (a)-(c). In the same panels, the light blue and green dashed lines are the predictions of the global model for  $\bar{\rho}_{11}$  and  $\bar{\rho}_{22}$ , respectively. The common parameters are: the coupling between the qubit and cavity is  $\bar{g} = 0.1$ , the detuning  $D = -0.25$ , and the number of oscillators in the bath is  $N = 10^4$  with flat energy spectrum of width  $\Delta\omega = 2\Omega_0$ . In (a)  $\Gamma_0 = 0$ , i.e. it presents an isolated system with populations  $\rho_{11}$  ( $= \bar{\rho}_{11}$ ) and  $\rho_{22}$  ( $= \bar{\rho}_{22}$ ) from master equation (numerically from Eqs. (5.34)). In (b)  $\Gamma_0 = 0.01\Omega_0$  which presents exponential decay of the population in hybridized states as expected for global picture. In (c) coupling to the bath is strong,  $\Gamma_0 = \Omega_0$ , which leads to the breakdown of the global picture and entrance into the local regime with exponential decay of the qubit only (local picture).

where  $\Upsilon$  is the sum of all numerators of  $\rho_{ii}$  for  $i = 1..4$ . The power to the second bath  $R_2$  is then given by Eq. (5.5) as

$$P_{1 \rightarrow 2} = \frac{\hbar\omega_0^2}{\mathcal{Q}} \sum_{k,l} \rho_{kk} \frac{|\langle k | \hat{a}_2 - \hat{a}_2^\dagger | l \rangle|^2}{1 + \mathcal{Q}^2 (\frac{\omega_{kl}}{\omega_0} - \frac{\omega_0}{\omega_{kl}})^2} \frac{(\lambda_k - \lambda_l)^2}{1 - e^{-\beta_2 \hbar\omega_{kl}}}, \quad (5.24)$$

where we assumed  $\mathcal{Q} \equiv \mathcal{Q}_1 = \mathcal{Q}_2$ . The properties of this power are: (I) it is limited by the reciprocal quality factor  $\mathcal{Q}^{-1} \equiv \gamma$ , (II) affected, around  $\omega_Q = \omega_0$ , by fast variation of populations, energy splitting, and matrix elements, and finally (III) non-vanishing at all values of flux even far away from the resonance. The measured power for the sample in the global regime as a function of applied dimensionless flux  $\Phi/\Phi_0$  is shown in the left side of Fig. 5.4(e). The right side of this panel presents the theoretical curves provided by Eq. (5.24) with only one fitting parameter,  $\mathcal{Q} = 20$ , presenting the sample in the global regime.

### 5.3 Qubit-cavity-bath — cross-over from global to local regime

The previous discussion pointed towards two different operation regimes of the heat valve depending on the relative strength of the couplings within

the superconducting circuit and the dissipation due to the presence of the heat baths, respectively. In what follows we aim to address these regimes in a maximally reduced but still realistic setup, namely a qubit coupled via a cavity to a zero-temperature bath. The results of this section are presented in Publication XV. The system under study then allows us to witness and assess the cross-over between the two extreme regimes. Although  $T = 0$  is not giving the full picture, it nevertheless describes decay to a cold bath in satisfactory manner and shows the quantitative crossover between the two decay regimes when the  $\gamma/g$  ratio varies.

In what follows we assume that the heat bath is formed of  $N$  bosonic oscillators with a distribution of energies and coupling strength. The Hamiltonian of the qubit-cavity-bath setup like the one schematically presented in Fig. 5.5 is given by

$$\begin{aligned} \hat{\mathcal{H}}_{\text{QCB}} = & \hbar\omega_Q \hat{a}^\dagger \hat{a} + \hbar\omega_0 \hat{c}^\dagger \hat{c} + \sum_{i=1}^N \hbar\omega_i \hat{b}_i^\dagger \hat{b}_i \\ & + g(\hat{a}^\dagger \hat{c} + \hat{c}^\dagger \hat{a}) + \sum_{i=1}^N \gamma_i (\hat{c}^\dagger \hat{b}_i + \hat{c} \hat{b}_i^\dagger), \end{aligned} \quad (5.25)$$

where  $\hat{a} = |g\rangle\langle e|$  for the qubit with eigenstates  $|g\rangle$  (ground) and  $|e\rangle$  (excited) and  $\hat{c}^\dagger$  ( $\hat{c}$ ) and  $\hat{b}_i^\dagger$  ( $\hat{b}_i$ ) are the creation (annihilation) operators of the cavity (resonator) and oscillators in the bath, respectively. Further,  $\hbar\omega_j$  is the energy of  $j$ :th oscillator in the bath,  $g$  indicates the coupling between the qubit and cavity, and  $\gamma_i$  for those between cavity and bath oscillators. In addition, we take a flat distribution of oscillator energies around  $\omega_Q$ . The first three terms in Eq. (5.25), composed of the energy of the qubit, cavity and oscillator bath, respectively, form the non-interacting Hamiltonian  $\hat{\mathcal{H}}_{0,\text{QCB}} = \hbar\omega_Q \hat{a}^\dagger \hat{a} + \hbar\omega_0 \hat{c}^\dagger \hat{c} + \sum_{i=1}^N \hbar\omega_i \hat{b}_i^\dagger \hat{b}_i$ . The last two terms in (5.25),  $\hat{V}_{\text{QCB}} = g(\hat{a}^\dagger \hat{c} + \hat{c}^\dagger \hat{a}) + \sum_{i=1}^N \gamma_i (\hat{c}^\dagger \hat{b}_i + \hat{c} \hat{b}_i^\dagger)$ , are the qubit-cavity and cavity-bath coupling energies, respectively. We aim to solve the Schrödinger equation  $i\hbar\partial_t |\psi_I(t)\rangle = \hat{V}_I(t) |\psi_I(t)\rangle$ , where the indices  $I$  refer to the interaction picture with respect to the non-interacting Hamiltonian. The basis that we use is formed of the states  $\{|0\rangle = |1\ 0\ 0\ 0\dots\rangle, |1\rangle = |0\ 1\ 0\ 0\dots\rangle, |2\rangle = |0\ 0\ 1\ 0\dots\rangle, \dots, |j\rangle = |0\ 0\dots 1^{(j:\text{th})}\dots 0\rangle\}$ , where the left-most index refers to occupation of the qubit, next one to the cavity, and the rest to environmental oscillators. Therefore, we exclude multiple occupations. The initial state of the whole system (qubit, cavity and oscillator bath) is  $|\psi_I(0)\rangle \equiv |0\rangle$  meaning that only the qubit is in the excited state  $|e\rangle$  and cavity and bath are in the ground state. The time evolution of the state of the whole system,  $|\psi_I(t)\rangle = \sum_{i=0}^N \mathcal{C}_i(t) |i\rangle$ , then follows

$$i\hbar \dot{\mathcal{C}}_Q(t) = g e^{i(\omega_Q - \omega_0)t} \mathcal{C}_C(t)$$

$$\begin{aligned} i\hbar\dot{\mathcal{C}}_C(t) &= ge^{-i(\omega_Q-\omega_0)t}\mathcal{C}_Q(t) + \sum_k \gamma_k e^{i(\omega_0-\omega_k)t}\mathcal{C}_k(t) \\ i\hbar\dot{\mathcal{C}}_j(t) &= \gamma_j e^{-i(\omega_0-\omega_j)t}\mathcal{C}_C(t), \end{aligned} \quad (5.26)$$

where,  $\mathcal{C}_Q(t)$  is the amplitude and  $|\mathcal{C}_Q(t)|^2$  the population of the qubit,  $|\mathcal{C}_C(t)|^2$  for the cavity, and similarly  $|\mathcal{C}_j(t)|^2$  for the bath oscillators with  $j = 1, 2, \dots, N$ .

The global regime of our hybrid is shown in the upper panel of Fig. 5.5 (b). In this case the dimensionless Hamiltonian, normalized by  $\hbar\omega_0$ , for the bare system (in the absence of environment oscillators),  $\hat{\mathcal{H}}_{0,G}$ , and for the coupling energy (perturbation),  $\hat{V}_G$ , are given by

$$\hat{\mathcal{H}}_{0,G} = r\hat{a}^\dagger\hat{a} + \hat{c}^\dagger\hat{c} + \bar{g}(\hat{a}^\dagger\hat{c} + \hat{c}^\dagger\hat{a}) \quad (5.27)$$

$$\hat{V}_G = \sum_{i=1}^N \bar{\gamma}_i (\hat{c}^\dagger\hat{b}_i + \hat{c}\hat{b}_i^\dagger) \quad (5.28)$$

where  $r = \omega/\omega_0$ ,  $\bar{g} = g/\hbar\omega_0$  and  $\bar{\gamma}_i = \gamma_i/\hbar\omega_0$ . We employ the product basis for the hybrid as  $\{|00\rangle, |10\rangle, |01\rangle\}$  where the first entry refers to the qubit and the next one to the cavity. The eigenenergies  $\varepsilon_i$  of the Hamiltonian (5.27), also normalized by  $\hbar\omega_0$  are given by

$$\varepsilon_0 = 0, \quad \varepsilon_{1,2} = 1 + \frac{1}{2}[D \mp \sqrt{D^2 + 4\bar{g}^2}], \quad (5.29)$$

where the  $-$  and  $+$  signs refer to  $\varepsilon_1$  and  $\varepsilon_2$ , respectively, and  $D \equiv r - 1$  is the detuning of the qubit-cavity hybrid. The corresponding eigenstates are

$$|\tilde{0}\rangle = \begin{pmatrix} 1 \\ 0 \\ 0 \end{pmatrix}, \quad |\tilde{1}\rangle = \begin{pmatrix} 0 \\ \alpha_1 \\ \alpha_2 \end{pmatrix}, \quad |\tilde{2}\rangle = \begin{pmatrix} 0 \\ \alpha_3 \\ \alpha_4 \end{pmatrix}. \quad (5.30)$$

Here  $\alpha_1 = (D - \eta)/\sqrt{4\bar{g}^2 + (D - \eta)^2}$ ,  $\alpha_2 = 2\bar{g}/\sqrt{4\bar{g}^2 + (D - \eta)^2}$ ,  $\alpha_3 = (D + \eta)/\sqrt{4\bar{g}^2 + (D + \eta)^2}$ ,  $\alpha_4 = 2\bar{g}/\sqrt{4\bar{g}^2 + (D + \eta)^2}$ , and  $\eta = \sqrt{D^2 + 4\bar{g}^2}$ .

In order to find the transition rates  $\Gamma_{i \rightarrow j}$  between the eigenstates, we use the same method as before. First, we need to obtain the matrix elements  $\langle \tilde{i} | \hat{q}_c | \tilde{j} \rangle$  of the charge operator of the cavity  $\hat{q}_c = -i\sqrt{\frac{\hbar}{2Z_0}}(\hat{c} - \hat{c}^\dagger)$ , with cavity's impedance  $Z_0$ , and the voltage noise  $S_v(\omega_0)$  induced by the bath on the cavity at frequency  $\omega_0$ . Then we have

$$\Gamma_{i \rightarrow j} = \frac{1}{\hbar^2} |\langle \tilde{i} | \hat{q}_c | \tilde{j} \rangle|^2 S_v(\Omega_0). \quad (5.31)$$

We assume that the bath couples only to the cavity of the hybrid system (qubit and cavity) which is a realistic assumption, e.g., in superconducting circuit architectures where the physical separations are large. By applying

the voltage noise of a bare resistor, which we assume to be directly connected to the cavity, without coupling capacitor, the transition rates at zero bath temperature are given by

$$\Gamma_{1 \rightarrow 0} = \frac{\omega_0}{\mathcal{Q}} \alpha_2^2, \quad \Gamma_{2 \rightarrow 0} = \frac{\omega_0}{\mathcal{Q}} \alpha_4^2, \quad (5.32)$$

where  $\mathcal{Q} = Z_0/R$  is the quality factor of the cavity. Other rates vanish:  $\Gamma_{1 \rightarrow 2} = \Gamma_{2 \rightarrow 1} = 0$  due to a selection rule, and  $\Gamma_{0 \rightarrow 1} = \Gamma_{0 \rightarrow 2} = 0$  at  $T = 0$ . In the absence of coupling capacitor, we identify  $\Gamma_0 \equiv \omega_0/\mathcal{Q}$  in this setup. Based on this simple decay scheme we find the populations of the eigenstates  $\rho_{11}(t) = \rho_{11}(0) \exp(-\Gamma_{1 \rightarrow 0} t)$  and  $\rho_{22}(t) = \rho_{22}(0) \exp(-\Gamma_{2 \rightarrow 0} t)$ , where  $\rho_{11}(0) = \alpha_1^2$  and  $\rho_{22}(0) = \alpha_2^2$ . Similarly, since  $\dot{\rho}_{00} = \Gamma_{1 \rightarrow 0} \rho_{11} + \Gamma_{2 \rightarrow 0} \rho_{22}$  for the population  $\rho_{00}$  of the ground state, we find immediately the decay rate at  $t = 0$  to the ground state as  $\dot{\rho}_{00}(0) = 2\Gamma_0 \alpha_1^2 \alpha_2^2$ , i.e.

$$\dot{\rho}_{00}(0) = \frac{\Gamma_0/2}{1 + (\frac{1}{2g})^2 D^2}. \quad (5.33)$$

It thus obeys Lorentzian dependence on the detuning of the qubit-cavity with effective quality factor  $(2g)^{-1}$ .

In order to assess whether the global treatment works we write the values of the populations  $\tilde{\rho}_{11}(t)$  and  $\tilde{\rho}_{22}(t)$  from the numerical solution of the Schrödinger equation in the time-dependent eigenstates  $|\tilde{0}\rangle = |0\ 0\rangle$ ,  $|\tilde{1}\rangle = \alpha_1 e^{-i\omega_Q t} |1\ 0\rangle + \alpha_2 e^{-i\omega_0 t} |0\ 1\rangle$ , and  $|\tilde{2}\rangle = \alpha_3 e^{-i\omega_Q t} |1\ 0\rangle + \alpha_4 e^{-i\omega_0 t} |0\ 1\rangle$  as

$$\begin{aligned} \tilde{\rho}_{11}(t) &= |\langle \tilde{1} | \psi_I(t) \rangle|^2 = |\alpha_1 e^{-i\omega_Q t} \mathcal{C}_Q(t) + \alpha_2 e^{-i\omega_0 t} \mathcal{C}_C(t)|^2 \\ \tilde{\rho}_{22}(t) &= |\langle \tilde{2} | \psi_I(t) \rangle|^2 = |\alpha_3 e^{-i\omega_Q t} \mathcal{C}_Q(t) + \alpha_4 e^{-i\omega_0 t} \mathcal{C}_C(t)|^2. \end{aligned} \quad (5.34)$$

We now present quantitatively the cross-over starting from an isolated hybrid system via an open global one, and finally to the fully incoherent local qubit with increasing coupling  $\Gamma_0$  to the bath, as schematically shown in the upper panels of Fig. 5.5. We assume that at  $t < 0$  the system is in equilibrium at zero temperature in the state where all the oscillators (including the qubit and cavity) are in the ground state. The system is then initialized at  $t = 0$  in the state  $|1\ 0\ 0\dots\rangle$ , meaning that the qubit is driven to the excited state. In Fig. 5.5 we present the numerically solved  $|\mathcal{C}_Q(t)|^2$ , i.e. the population in the excited state of the qubit (black line),  $|\mathcal{C}_C(t)|^2$ , the excited state population of the cavity (red line), and  $\tilde{\rho}_{11}(t)$  and  $\tilde{\rho}_{22}(t)$  with blue and green solid lines, respectively. The corresponding populations  $\rho_{11}(t)$  and  $\rho_{22}(t)$  from the master equations of hybrid system are shown by light blue and green dashed lines.

In the isolated qubit-cavity system ( $\Gamma_0 \equiv 0$ ), schematically shown in the upper panel of Fig. 5.5(a) and the numerical solution in the bottom of this panel, the populations  $|\mathcal{C}_Q(t)|^2$  and  $|\mathcal{C}_C(t)|^2$  of the qubit and cavity oscillate

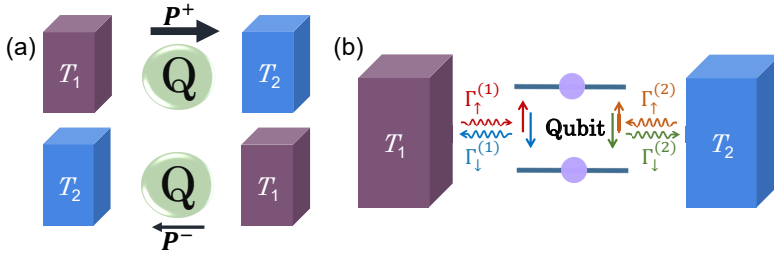


**Figure 5.6.** The principle of a thermal rectifier. (a) Two thermal baths at different temperatures  $T_1$  and  $T_2$  coupled to each other via a quantum system  $Q$ .  $P^+$  stands for power transmission in forward direction while by applying the identical but opposite temperature bias the backward power will be  $P^-$ . In the presence of nonlinearity and asymmetry in the system and couplings, there will be rectification when  $\mathfrak{R} = P^+/P^- \neq 1$ . (b) A qubit in the middle coupled to two thermal baths together with the associated transition rates.

out-of-phase in accordance with the solution of (5.26) for  $\gamma_i \equiv 0$  as

$$\begin{aligned} |\mathcal{C}_Q(t)|^2 &= 1 - |\mathcal{C}_C(t)|^2 = \frac{1}{2}[1 + \frac{D^2}{D^2 + 4\bar{g}^2} \\ &\quad + \frac{4\bar{g}^2}{D^2 + 4\bar{g}^2} \cos(\sqrt{D^2 + 4\bar{g}^2}t)]. \end{aligned} \quad (5.35)$$

Thus  $|\mathcal{C}_Q(t)|^2$  oscillates between  $D^2/(D^2 + 4\bar{g}^2)$  and 1. On the other hand, the populations in the eigenstates of the hybrid,  $\rho_{11}(t)$  ( $= \tilde{\rho}_{11}(t)$  in this case) and  $\rho_{22}(t)$  ( $= \tilde{\rho}_{22}(t)$ ), remain strictly constant, and their values are determined by the coupling  $\bar{g}$ . In panel (b) we introduce weak coupling of the cavity to the bath,  $\Gamma_0 = 0.01\Omega_0$ . In this situation the numerical solution of Eq. (5.26) shows that the global description given above applies: populations  $\tilde{\rho}_{11}(t)$  and  $\tilde{\rho}_{22}(t)$  decay exponentially fully overlapping with  $\rho_{11}(t)$  and  $\rho_{22}(t)$ , respectively, shown also in the figure. On the contrary, the populations of qubit  $|\mathcal{C}_Q(t)|^2$  and cavity  $|\mathcal{C}_C(t)|^2$  oscillate, but these oscillations are damped over time scale  $\sim \Gamma_0^{-1}$ .

Further increasing  $\Gamma_0$  well beyond the internal coupling  $\bar{g}$  leads to the failure of the global model. Figure 5.5(c) presents the case where  $\Gamma_0 = \Omega_0$ . In this regime, all the coherent behaviour of the qubit and the cavity has vanished, and the qubit alone,  $|\mathcal{C}_Q(t)|^2$ , follows closely  $\tilde{\rho}_{11}(t)$ , decaying exponentially from the excited state and the cavity remains mainly in the ground state,  $|\mathcal{C}_C(t)|^2 \simeq 0$ . Naturally the predictions of the global model for  $\rho_{11}(t)$  and  $\rho_{22}(t)$  fail in this regime as shown by the dashed lines.

Figures 5.5(c) indicates local regime where the Hamiltonian and perturbative terms are respectively given by  $\hat{\mathcal{H}}_{0,L} = \hbar\omega_Q \hat{a}^\dagger \hat{a} + \hbar\omega_0 \hat{c}^\dagger \hat{c} + \sum_{i=1}^N \hbar\omega_i \hat{b}_i^\dagger \hat{b}_i + \sum_{i=1}^N \gamma_i (\hat{c}^\dagger \hat{b}_i + \hat{c} \hat{b}_i^\dagger)$  and  $\hat{V}_L = g(\hat{a}^\dagger \hat{c} + \hat{a} \hat{c}^\dagger)$ .

Besides the cross-over between the two decay modalities, we have shown in this section that in all regimes the decay rate of the quantum system can be varied by detuning the qubit and the cavity.

## 5.4 Thermal rectifier

Naturally, there is no directional dependence of heat transport between two baths in a symmetric structure. Now a question arises what happens if we break the symmetry in such structures. The answer is, the heat current rectification becomes possible which is schematically shown in Fig. 5.6(a) where a quantum system is placed between two baths. In this case if the heat flow in one direction is different with respect to the one in the opposite direction, the quantum system acts as a rectifier. Optimally, a rectifier allows transport (charge, heat current) only in one direction. Here, we focus on the thermal rectifiers, where the magnitude of the forward and reverse heat currents are different under identical but opposite temperature biasing conditions. Heat rectification can be assessed theoretically in different ways and systems, as discussed e.g., in [108, 109, 110, 111, 112, 113, 114, 115, 116, 117, 118, 119, 120, 121]. Experimentally, thermal rectification was first observed by Starr in 1936 [122], but since then only a few experiments on heat current rectification exist, e.g., on phonons in carbon nanotubes [123], and electrons in semiconductor quantum dots [124], mesoscopic tunnel junctions [125] and suspended monolayer graphene [126].

### 5.4.1 Rectification in a two-level system

We start by looking at a simple system shown in Fig. 5.6(b), where a qubit (representative of a quantum system as in (a)) with energy level separation  $\hbar\omega_Q$  is coupled to two thermal baths at inverse temperature  $\beta_1 = 1/k_B T_1$  and  $\beta_2 = 1/k_B T_2$  with coupling terms  $g_1$  and  $g_2$ , respectively. The transition rates as they are shown in this figure, are given by

$$\begin{aligned}\Gamma_{\uparrow}^{(1)} &= g_1 \frac{\omega_Q}{e^{\beta_1 \hbar \omega_Q} - 1}, & \Gamma_{\uparrow}^{(2)} &= g_2 \frac{\omega_Q}{e^{\beta_2 \hbar \omega_Q} - 1} \\ \Gamma_{\downarrow}^{(1)} &= g_1 \frac{\omega_Q}{1 - e^{-\beta_1 \hbar \omega_Q}}, & \Gamma_{\downarrow}^{(2)} &= g_2 \frac{\omega_Q}{1 - e^{-\beta_2 \hbar \omega_Q}}.\end{aligned}\quad (5.36)$$

The population of the excited state of the qubit  $\rho_e$  under steady state conditions is given by

$$\rho_e = \frac{\Gamma_{\uparrow}}{\Gamma_{\uparrow} + \Gamma_{\downarrow}}, \quad (5.37)$$

where  $\Gamma_{\uparrow,(\downarrow)} = \Gamma_{\uparrow,(\downarrow)}^{(1)} + \Gamma_{\uparrow,(\downarrow)}^{(2)}$ , and as a result the population of the ground state of the qubit reads  $\rho_g = 1 - \rho_e$ . The expression for power to bath  $i$  is then

$$P_i = \hbar\omega_Q (\rho_e \Gamma_{\downarrow}^{(i)} - \rho_g \Gamma_{\uparrow}^{(i)}). \quad (5.38)$$

By definition, the thermal rectification is given by

$$\mathfrak{R} = \left| \frac{P_i^+}{P_i^-} \right|, \quad (5.39)$$

where  $\pm$  refers to the sign of the temperature bias meaning + for forward and - backward. With the help of Eqs. (5.36)-(5.39) we then have

$$\Re = \frac{g_1 + g_2 \coth\left(\frac{\beta_1 \hbar \omega_Q}{2}\right) \tanh\left(\frac{\beta_2 \hbar \omega_Q}{2}\right)}{g_1 \coth\left(\frac{\beta_1 \hbar \omega_Q}{2}\right) \tanh\left(\frac{\beta_2 \hbar \omega_Q}{2}\right) + g_2}, \quad (5.40)$$

which exhibits rectification. Any value  $\Re \neq 1$  corresponds to heat rectification while  $\Re = 1$  describes completely symmetric structure with no direction dependence in the heat current. Rectification (in a two-level system) depends on the statistics of transition rates. In the system above we used transition rates given by Bose-Einstein distribution ( $\Gamma_{\uparrow}^{(i)} = g_i n_i(E)$ ) which led to rectification in case of an asymmetric structure. Such rates are present when they are induced, e.g. by the thermal noise of a resistor, as in this thesis. But what if we consider different transition rates? For instance, we may take a single level quantum dot, where  $g'_i$  is determined by the barrier, and  $E$  is the energy level position of the dot with respect to the Fermi level, controlled by gate. In this case the transition rates are proportional to the Fermi distribution,  $\Gamma_{\uparrow}^{(i)} = g'_i f_i(E)$ . The detailed balance condition also applies here, and the population for the excited state (Eq. (5.37)) and the expression for the power (Eq. (5.38)) are as in the previous system. Let us assume for simplicity that the first bath has inverse temperature  $\beta$  and the second one is at zero temperature. Then we find the power to the second bath as

$$P_2 = \frac{g'_1 g'_2}{g'_1 + g'_2} E f(E). \quad (5.41)$$

Due to the symmetry with respect to indices 1 and 2, this system does not rectify heat, even if  $g'_1 \neq g'_2$ .

#### 5.4.2 Experiment on heat rectification using a resonator-qubit-resonator assembly

In order to have heat rectification, we require both non-linearity and asymmetry in the system under study [111, 117]. As it has been discussed in Publication X, in this section, we propose that resonator-qubit-resonator can serve as a thermal rectifier (diode), as schematically shown in Fig. 5.7(b). This setup is somewhat similar to the heat valve structure, but with unequal resonators which bring about the symmetry breaking. On the other hand, the anharmonicity of the transmon Josephson potential provides the necessary non-linearity for a thermal diode. In the optical micrograph of the sample presented in Fig. 5.7(c), there is a transmon-type qubit in the center, coupled to two coplanar waveguide resonators at  $\sim 3$  GHz and  $\sim 7$  GHz, respectively. Each of these resonators is terminated by a  $\sim 3 \mu\text{m}$  long normal-metal resistor (Cu) acting as a thermal bath. NIS probe junctions in each thermal bath are responsible for monitoring and

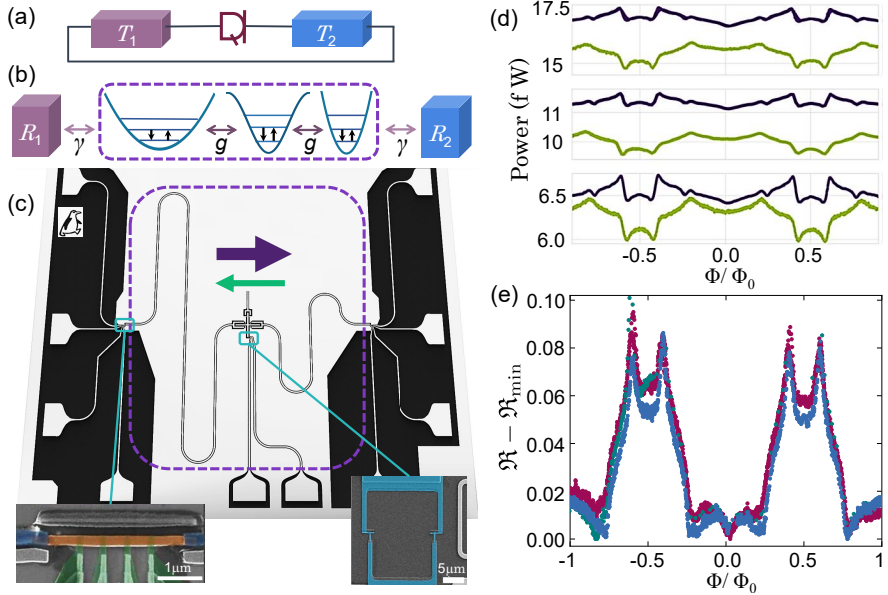


**Figure 5.7.** Thermal rectifier; principle, sample and result. A simple setup explaining the heat rectification principle where we assign the quantum heat rectifier in the middle by the purple symbol. A photon diode in purple rectangle composed of an anharmonic oscillator (qubit) in the middle coupled to two unequal  $LC$  resonators, placed between two resistors at different temperatures, is schematically shown in panel (b). (c) The actual sample realizing (b). A transmon-type qubit in the middle coupled to two superconducting coplanar waveguide resonators at  $\sim 3$  (left) and  $\sim 7$  GHz (right) resonance frequencies. Each of them is terminated with a normal-metal copper resistor, acting as a mesoscopic thermal bath. Right inset is the SEM image of the SQUID and the left one presents the SEM of a copper resistor in orange which is in clean contact to two superconducting aluminium contacts to the coplanar waveguide resonator. Four NIS ( $Cu/AlO_x/Al$ ) probe junctions are responsible for monitoring and controlling the temperature of the resistor. The purple and green stand for the forward and backward directions of power. (d) Dependence of heat current (power) between the two thermal baths as a function of dimensionless magnetic flux  $\Phi/\Phi_0$  in forward ( $P^+$ ,  $1 \rightarrow 2$ , purple line) and backward ( $P^-$ ,  $2 \rightarrow 1$ , green line) directions under identical but opposite temperature bias conditions. The bath is at a fixed temperature of 150 mK in each case. The temperature of the source resistor in the top subplots is 420 mK (corresponds to applying 1 pW), in the middle 400 mK (750 fW), and the lowest one 380 mK (600 fW). (e) Rectification ratio  $\mathfrak{R} = P^+/P^-$  versus dimensionless magnetic flux for the traces presented in (d) with their minimal value (non-tunable contribution) subtracted.

controlling the temperature of each bath. Therefore, one can measure the heat current through the structure (resonator-qubit-resonator) in forward to be the direction from the low to high frequency,  $P^+$ , and backward directions (from high to low frequency),  $P^-$ , under the same but opposite temperature biasing condition, respectively. This is schematically shown by the purple and green arrows. The measured transmitted heat current (power) as a function of (dimensionless) magnetic flux  $\Phi/\Phi_0$  is presented in Fig. 5.7(d) for three different temperatures from 380 to 420 mK. In all the measurements, the bath temperature was kept fixed at 150 mK. One can observe the qualitative difference of the heat transported based on the directionality, although the quantitative analysis of the flux dependence is quite challenging due to the somewhat complicated structure. The rectification ratio  $\Re$  versus  $\Phi/\Phi_0$  for the traces in Fig. 5.7(d) is presented in the panel 5.7(e). It is vivid that this ratio is strongly flux dependent. This means that the couplings  $g_1$  and  $g_2$  vary with  $\Phi$ . Most importantly, they depend on the detuning of the qubit with respect to each resonator. This leads to the observation of unequal flux dependences of the forward and backward heat currents. A way of explaining the rectification ratio is via Eq. (5.40) where  $g_1$ ,  $g_2$  and  $\omega_Q$  are flux dependent. The proposed thermal diode can reach about 10% rectification at best.

There are a few obvious changes in design by which one may optimize the system and increase the directionality. First, one may use a maximally anharmonic potential, i.e. a different type of a qubit. Transmon qubit is only weakly anharmonic. This means that at higher temperatures, one needs to consider the higher levels in this nearly harmonic potential not only the two lowest ones. Second, by removing the two unequal resonators and introducing other types of asymmetries to the system, one can easily simplify the setup and interpretation of the transmitted power will be easier as well. For example, one may make the coupling capacitances largely different from each other.

# 6. Dynamic properties of two-bath systems

Within the framework of quantum thermodynamics, realizing the dynamical control of open systems becomes crucial. Quantum heat engines [127, 128, 129, 130, 131, 132, 133, 134, 135, 136, 137, 138, 139, 140] and refrigerators [141, 142, 143, 144, 145, 146, 147, 148] are representatives in this respect. Recently, several devices have been proposed theoretically. Most of them may work in both classical and quantum regimes, and a few experimental realizations are given. Nonetheless, a better understanding of the quantum dynamics on the performance of quantum engines and refrigerators calls for more research. In this chapter we use a generic superconducting qubit e.g., a flux or transmon qubit as a working substance in a quantum refrigerator. In these qubits, the two level-system is formed of Josephson junctions for which  $E_J/E_C \gg 1$ , where  $E_J$  and  $E_C$  are the Josephson coupling energy and Cooper pair charging energy, respectively.

## 6.1 Quantum Otto refrigerator

In the basic Otto cycle which is widely used in present-day technology, the thermodynamic cycle consists of four strokes: two isochoric and two adiabatic ones, where in the isochoric processes, the system interacts with one of the two thermal reservoirs at different temperatures and during the two adiabatic ones, the baths are isolated from the system in between. In what follows we will quantitatively discuss the quantum Otto refrigerator which consists of two isentropic and two isochoric processes, based on the superconducting qubit in different frequency regimes. This system was described in Publication I.

### 6.1.1 Basic description

The schematic illustration of quantum Otto refrigerator is shown in Figs. 6.1(a) and 6.1(b). A flux qubit in the middle of Fig. 6.1(a) is a superconducting

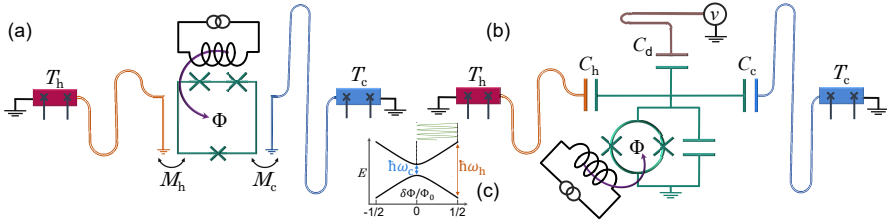


**Figure 6.1.** Schematic illustration of quantum refrigerators. A generic superconducting qubit (flux qubit in (a) and transmon in (b)) either inductively ( $M_i$  in (a)) or capacitively ( $C_i$  in (b)) coupled to two coplanar waveguide resonators with resonance (angular) frequencies  $\omega_c = 1/\sqrt{L_c C_c}$  and  $\omega_h = 1/\sqrt{L_h C_h}$ . These resonators are terminated by resistors  $R_c$  and  $R_h$  at temperatures  $T_c$  and  $T_h$ , respectively, the latter ones acting as the heat baths. The energy-level separation of the qubit can be tuned by applying either magnetic flux or electric field. (c) The qubit energy levels varied by the drive displayed on the top of the diagram.

loop interrupted by a number of Josephson junctions, in particular one of the junctions is smaller than others to form a two-level system. Then, the qubit is inductively coupled with mutual inductances  $M_h$  and  $M_c$  to two  $LC$  resonators with resonance frequencies  $\omega_h = 1/\sqrt{L_h C_h}$  and  $\omega_c = 1/\sqrt{L_c C_c}$  for the left and right resonators, respectively. Both resonators are terminated by normal-metal microstrip resistors  $R_h$  and  $R_c$  with temperatures  $T_h = 1/k_B\beta_h$  and  $T_c = 1/k_B\beta_c$  acting as hot and cold thermal baths for the left and right, respectively. In general, the two temperatures can take arbitrary values. The bias circuit on the top of the flux qubit controls the time-dependent magnetic flux  $\Phi(t)$  through the loop with  $q \equiv \delta\Phi(t)/\Phi_0$ , where  $\delta\Phi(t) = \Phi(t) - \Phi_0/2$  with  $\Phi_0$  the superconducting flux quantum, see Fig. 6.1(c). This adiabatic drive with frequency  $f$  tunes the qubit energy splitting at values between the resonator frequencies. Panel 6.1(b) shows an alternative design for the quantum Otto refrigerator with the same operation principles as in (a). In this structure, a transmon-type qubit is replaced with the flux qubit and the inductive couplings of the qubit to the resonators with capacitive couplings. In both panels, qubits are controlled by applying magnetic field, which is flux in the superconducting loop. It is also possible to control the level separation in the qubit by electric field, through the gate voltage via the capacitor  $C_d$  which is schematically shown in 6.1(b).

### The Otto-cycle and quasistatic performance

We start by describing the thermodynamic cycle of this quantum Otto refrigerator shown in Fig. 6.2. The cycle consists of four processes based on the driving protocol shown in Fig. 6.1(c). In this subsection, we consider a quasistatic cycle, where the population is given by the equilibrium one when connected to a bath, and it does not change when decoupled from the baths.

(1) *Isentropic compression*,  $q = 0 \rightarrow q = 1/2$ : In the first stroke, the qubit is

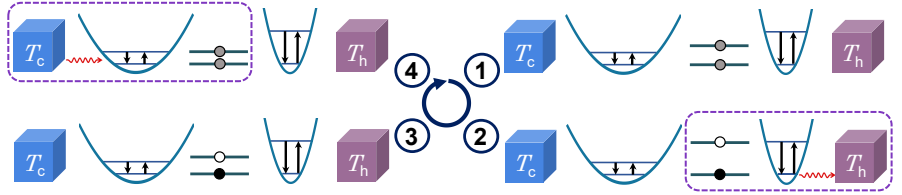


**Figure 6.2.** Thermodynamic cycle of the Otto refrigerator based on the superconducting qubit. The cycle is explained in the text.

not coupled with either of the two resonators and ideally is fully isolated from the two thermal baths. In this case the population of the excited level of the qubit  $\rho_{ee}^{(1)}$  is determined by the temperature of the cold bath  $T_c$  and we have  $\rho_{ee}^{(1)} = 1/(1 + e^{\beta_c \hbar \omega_c})$ .

(2) *Isochoric, thermalization with the hot bath,  $q = 1/2$ :* The qubit is coupled to hot bath with its level separation matching with that of the hot resonator. As a result, the heat current flows from the qubit to the hot resistor  $R_h$  and the population of the qubit is given by  $\rho_{ee}^{(2)} = 1/(1 + e^{\beta_h \hbar \omega_h})$ .

(3) *Isentropic expansion,  $q = 1/2 \rightarrow q = 0$ :* During the ramp, qubit is again isolated and decoupled from both thermal baths and its population is determined by the hot bath  $\rho_{ee}^{(3)} = 1/(1 + e^{\beta_h \hbar \omega_h})$ .

(4) *Isochoric, thermalization with the cold bath,  $q = 0$ :* In the final stroke, the qubit is brought back to its initial thermal state, i.e. to equilibrium with the cold bath, meaning its population reads  $\rho_{ee}^{(4)} = 1/(1 + e^{\beta_c \hbar \omega_c})$ . In this final step, the heat flows from the cold bath to the qubit.

The amount of energy injected to each bath is weighted by the change of the population of the qubit while in contact with the bath. Thus the amount of heat to the hot  $Q_h$  and cold baths  $Q_c$  are given by

$$\begin{aligned} Q_h &= \hbar \omega_h [\rho_{ee}^{(1)} - \rho_{ee}^{(2)}] \\ Q_c &= \hbar \omega_c [\rho_{ee}^{(3)} - \rho_{ee}^{(4)}]. \end{aligned} \quad (6.1)$$

In the case of refrigeration, meaning taking the energy from the cold bath, the heat to the  $R_c$  should be negative,  $Q_c < 0$ . With the help of Eq. (6.1), then we have  $\beta_c \hbar \omega_c < \beta_h \hbar \omega_h$ , meaning

$$\frac{\omega_c}{\omega_h} < \frac{T_c}{T_h}. \quad (6.2)$$

Bearing in mind that  $T_c < T_h$ , the condition for having a refrigerator is  $\omega_c < \omega_h$ . Then in this quasistatic cycle, the power of this refrigerator to the cold resistor  $R_c$ ,  $P_c$ , which is the amount of heat transferred  $Q_c$  to the cold bath times the frequency of driving  $f$ , is given in a quasistatic cycle by

$$P_c = \frac{\hbar \omega_c}{2} \left[ \tanh \left( \frac{\beta_h \hbar \omega_h}{2} \right) - \tanh \left( \frac{\beta_c \hbar \omega_c}{2} \right) \right] f, \quad (6.3)$$

which depends linearly on frequency. Similarly the energy transferred from the qubit to the hot bath  $R_h$  is then  $P_h = Q_h f$ . The efficiency of a

refrigerator  $\eta$ , usually called the coefficient of performance, is given by the ratio of the energy extracted from the cold bath in the steady state cycle to the total work done on the system,  $\eta = -Q_c/W$ . In the ideal case, where we ignore the parasitic losses in producing the flux drive of the qubit, we have  $W = Q_c + Q_h$ . Based on Eq. (6.1), the ideal efficiency of this Otto refrigerator is given by

$$\eta_{\text{ideal}} = \frac{1}{\frac{\omega_h}{\omega_c} - 1}, \quad (6.4)$$

which can be compared to the Carnot efficiency of a refrigerator  $\eta_{\text{Carnot}} = 1/(\frac{T_h}{T_c} - 1)$ .

### Beyond the quasistatic cycle

When the frequency of operation increases, it is not adequate to apply the quasistatic results. In this case we write the full master equation to follow the dynamics. The total Hamiltonian for the setup shown in Fig. 6.1 can be written as  $\hat{\mathcal{H}} = \hat{\mathcal{H}}_0 + \hat{\mathbb{V}}$ , where the non-perturbed Hamiltonian  $\hat{\mathcal{H}}_0$  is the sum of the Hamiltonians of the qubit and each of the  $RLC$  reservoirs and  $\hat{\mathbb{V}}$  is the coupling between the qubit and each reservoir. Up to now, we introduced the Hamiltonian of a qubit as  $\hat{\mathcal{H}}_Q = \hbar\omega_Q \hat{a}^\dagger \hat{a}$ , where  $\hat{a} = |g\rangle\langle e|$ . In this chapter, since we want to drive the qubit, we introduce the Hamiltonian of the qubit as  $\hat{\mathcal{H}}_Q = -E_0(\Delta\sigma_x + q\sigma_z)$ , where  $\sigma_x$  and  $\sigma_z$  are the Pauli matrices, and  $E_0$  denotes the overall energy scale of the qubit, such that the level spacing between the instantaneous eigenstates reads  $E = 2E_0\sqrt{q^2 + \Delta^2}$ . As shown in Fig. 6.1(c), the maximum and minimum level separations at  $q = 1/2$  and  $q = 0$  are  $E_1 = \hbar\omega_h$  and  $E_2 = \hbar\omega_c$ , respectively, and  $\Delta = E_2/(2E_0)$ . The main purpose is to calculate the cooling power for this refrigerator, and for this we should first obtain the transition rates and population of the qubit. The transition rates between the instantaneous eigenstates due to the presence of resistors  $j = h, c$  (thermal baths) can be obtained with the golden rule  $\Gamma_{\uparrow,\downarrow,j} = \frac{1}{\hbar^2} |\langle g | \frac{\partial \hat{\mathcal{H}}}{\partial \Phi} | e \rangle|^2 M_j^2 S_{I,j}(\pm E/\hbar)$ . Here the  $\pm$  signs correspond to relaxation and excitation, respectively, and  $S_{I,j}(\pm\omega) = \{R_j^2[1 + Q_j^2(\frac{\omega}{\omega_j} - \frac{\omega_i}{\omega})^2]\}^{-1} S_{V,j}(\omega)$  is the unsymmetrized noise of the qubit with  $S_{V,j}(\omega)$  the voltage noise of a bare resistor  $j$ . This final form is quite similar to the one in Eq. (5.9) that we obtained for the heat valve in the local regime. Next, using the standard master equation, one can obtain the time evolution of the qubit density matrix  $\rho(t)$  in the instantaneous eigenbasis [1, 149]. The standard quantum master equation in the instantaneous eigenbasis in the presence of the drive (given in Eq. (2.12)) and ignoring pure dephasing due to intentionally large relaxation rates close to the resonance frequency of the resonators, are given by

$$\dot{\rho}_{gg} = -\frac{\Delta}{q^2 + \Delta^2} \dot{q} \Re[\rho_{ge} e^{i\phi(t)}] - \Gamma_\Sigma \rho_{gg} + \Gamma_\downarrow$$

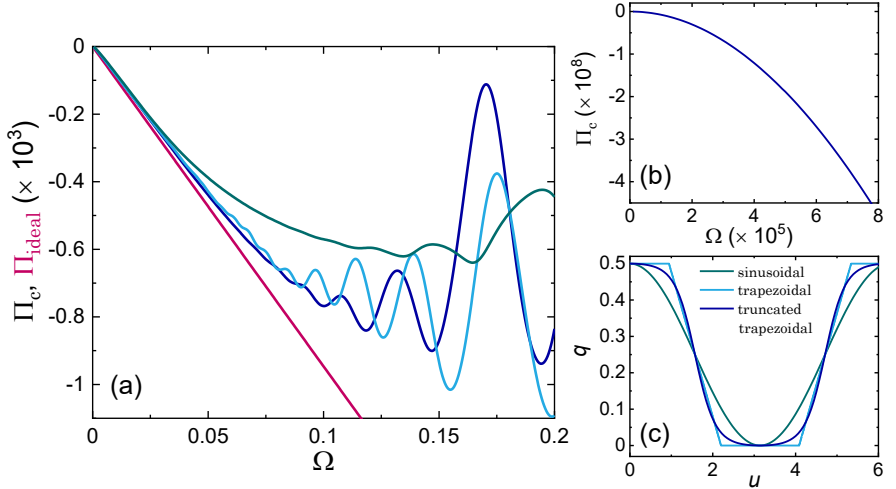


**Figure 6.3.** Cooling power of quantum Otto refrigerator and the three operation regimes. (a) Dimensionless power to the cold bath  $\Pi_c$  as a function of dimensionless frequency  $\Omega$  when both baths have the same temperature for three waveforms shown in (c) with the corresponding colour code. From the plot it is easy to distinguish two regimes: Otto cycle (approximately linear regime) at intermediate frequencies and nonadiabatic coherent regime (oscillatory part) at high frequencies. Both trapezoidal and truncated trapezoidal waveforms present better performance at lower frequencies while at high frequencies the sinusoidal one shows less oscillations. The red line presents the power to the cold bath for an ideal Otto cycle, Eq. (6.3). (b) Quadratic dependence of the power to the cold bath  $\Pi_c$  on  $\Omega$  in the very low frequency range. Panel (c) shows all driving waveforms used for demonstrating cooling power of the Otto refrigerator shown in (a). The (angular) frequencies of the resonators are  $\omega_c = 2E_0\Delta/\hbar$  and  $\omega_h = 2E_0\sqrt{1/4 + \Delta^2}/\hbar$ . The parameters used in the figure are:  $k_B T_c/E_0 = k_B T_h/E_0 = 0.3$ ,  $\Delta = 0.3$ ,  $g = g_c = g_h = 1$ , and  $\mathcal{Q} = \mathcal{Q}_c = \mathcal{Q}_h = 30$ .

$$\dot{\rho}_{ge} = \frac{\Delta}{q^2 + \Delta^2} \dot{q} (\rho_{gg} - 1/2) e^{-i\phi(t)} - \frac{1}{2} \Gamma_\Sigma \rho_{ge}, \quad (6.5)$$

where  $\dot{q}$  is the ramp rate,  $\phi(t) = \int_0^t E(t') dt' / \hbar$ ,  $\Gamma_\Sigma = \Gamma_{\Sigma,h} + \Gamma_{\Sigma,c}$ ,  $\Gamma_\downarrow = \Gamma_{\downarrow,h} + \Gamma_{\downarrow,c}$ , and  $\Gamma_{\Sigma,j} = \Gamma_{\uparrow,j} + \Gamma_{\downarrow,j}$ , for  $j = h, c$  for the hot and cold reservoir, respectively. Finally, the power to the resistor  $j$  from the qubit is given by

$$P_j = E(t) (\rho_{ee} \Gamma_{\downarrow,j} - \rho_{gg} \Gamma_{\uparrow,j}), \quad (6.6)$$

which we derived before. The result of the numerical calculation of this cooling power is shown in Fig. 6.3. At the same time we want to assess the influence of the different types of periodic driving waveforms  $q(u)$ , where  $u = 2\pi ft$  is dimensionless time, on the cooling power of the refrigerator. Along with the two well-known waveforms meaning, sinusoidal  $q(u) = \frac{1}{4}(1 + \cos u)$  and trapezoidal (specifically with symmetric form consisting of rising sections of 20% of the cycle time each, and plateaus of 30% duration each) waveforms we apply the truncated trapezoidal  $q(u) = \frac{1}{4}[1 + \tanh(a \cos u)/\tanh a]$ , specifically with  $a = 2$ . These rising times and the particular value of  $a$  yield nearly optimal performance under the conditions

of our numerical simulations for the two latter waveforms. Figure. 6.3 (c) demonstrates the illustration of these three waveforms.

### 6.1.2 Different operation regimes

Figure. 6.3(a) displays the dimensionless power  $\Pi_c \equiv P_c/(E_0^2/\hbar)$  as a function of dimensionless frequency of the drive  $\Omega = 2\pi\hbar f/E_0$  for the equal temperature case  $\beta_c = \beta_h$  and the three different waveforms. One can simply identify three operation regimes of the Otto refrigerator in different frequency ranges: nearly adiabatic regime at low frequencies, ideal Otto cycle in the intermediate frequency regime, and nonadiabatic coherent regime at high frequencies.

The most straightforward regime to explain is the ideal Otto cycle in the intermediate regime. The three curves in Fig. 6.3 show the dimensionless cooling power  $-\Pi_c$  for different waveforms where approximately in this frequency regime they are linear. As a reference, the red line illustrates the cooling power of an ideal Otto cycle with the slope given in Eq. (6.3). In the intermediate frequency range results with all the three waveforms follow this dependence almost quantitatively. Both the trapezoidal and truncated trapezoidal waveforms present better performance at higher frequencies.

The performance of the refrigerator in the nearly adiabatic regime at very low frequency range is presented in Fig. 6.3(b), where cooling power shows quadratic dependence on frequency. In Publication I, we obtained a semianalytic result in accordance with this quadratic dependence. In the analysis for heat valve in the local regime (Eq. (5.12)), the power had a Lorentzian shape which was dependent on the quality factor, i.e., the higher the quality factor, the sharper the peak and vice versa. Introducing a dissipative element in the resonator, decreases dramatically the quality factor. Therefore, due to the broad spectrum, qubit is not fully decoupled from the two baths during the ramp time which means that there will be a heat flow between the two baths decreasing the cooling power and quantitatively it gives the quadratic dependence on frequency.

### 6.1.3 Supremacy of incoherent cycles

In this subsection we want to have a look at what happens when the driving frequency is increased further beyond what was discussed above. One of the timely questions in quantum thermodynamics is whether quantum features like coherence can boost the performance of heat engines and refrigerators [137, 150, 151]. Answering to this question is not simple since in many models of such machines, quantum coherence is useful [131, 144, 152, 153, 154, 155, 156], although its adverse effect has also been reported [142, 157, 158, 159, 115]. The oscillations in power at

high frequency end in Fig. 6.3 (a), originating from coherent oscillations of the qubit in the isolated legs 1 and 3 increase dissipation in both baths, i.e. cooling power is decreasing and heating of the hot bath is increasing. In Publication I, the figure presenting the nonadiabatic coherent regime shows that this oscillatory regime starts from  $f_c \sim \omega_c/2\pi$  and extends up to  $f_h \sim \omega_h/2\pi$ . These effects are a precursor of what happens asymptotically at very high frequencies. In order to understand this high frequency regime better, we consider the same setup, a two-level system coupled alternately to two heat baths. Our suggested cooling cycle (Otto cycle) here is very similar to the one we had before but with small changes. In this cycle, qubit level is changed from  $\omega_c$  to  $\omega_h$  (and vice versa) infinitely fast and when the qubit interacts with each bath for a time interval  $\delta t$  which is finally reduced to minimum. In particular we are interested in high frequency regime when  $f = 1/(2\delta t) \rightarrow \infty$ . In order to analyze this cycle which consists of constant and abrupt legs in the cycle, instead of using usual master equation (which under these assumption will be possibly not justified under rapid change of the parameters), for the (de)compression legs we use the sudden approximation of quantum mechanics and for the thermalization legs, we adopt the standard Lindbladian evolution [1, 160]. The Hamiltonian of the qubit is as before,  $\hat{\mathcal{H}}_Q = -E_0(\Delta\sigma_x + q\sigma_z)$ , and its eigenstates in the basis  $|+\rangle = (1\ 0)^\dagger$  and  $|-\rangle = (0\ 1)^\dagger$  read

$$\begin{aligned} |g\rangle &= 2^{-1/2}(\sqrt{1-\eta(q)}|-\rangle + \sqrt{1+\eta(q)}|+\rangle), \\ |e\rangle &= 2^{-1/2}(\sqrt{1+\eta(q)}|-\rangle - \sqrt{1-\eta(q)}|+\rangle), \end{aligned} \quad (6.7)$$

where  $\eta(q) \equiv (q/\Delta)/\sqrt{1+(q/\Delta)^2}$ . We parametrized the density matrix  $\rho$  by  $\tilde{\mathcal{D}} \equiv \rho_{gg} - 1/2$ ,  $\tilde{\mathcal{R}} \equiv \Re(\rho_{ge}e^{i\phi})$  and  $\mathcal{I} \equiv \Im(\rho_{ge}e^{i\phi})$ . Here  $\phi = \int dt \Delta E/\hbar = \int dt (2E_0 \sqrt{q(t)^2 + \Delta^2})/\hbar$  denotes the phase that could be accumulated along the thermalization legs. After some derivations which are presented in Publication VIII, the power (heat current) to cold (hot) bath is given by

$$P_{c(h)} = \Delta E_{c(h)} \frac{\Gamma_\downarrow^{c(h)} \Gamma_\Sigma^{h(c)} (1 - e^{-\beta_{c(h)} \Delta E_{c(h)}})}{4(2\Gamma_\Sigma^{c(h)} + \Gamma_\Sigma^{h(c)})} > 0. \quad (6.8)$$

The positive sign indicates that in this limit both baths are heated, which demonstrates the disadvantageous effect of coherence on the performance of a quantum refrigerator. One can easily make some conclusions from the obtained results: (i) Both  $P_c$  and  $P_h$  reach a constant value which are independent on frequency  $f$  in this high frequency regime, (ii) both of them are positive meaning both baths are heated as we mentioned before, (iii) in the limit  $\eta(q_{\max}) \approx 1$  both powers,  $P_c$  and  $P_h$ , respectively. depend on  $\tilde{\mathcal{R}}$  and since  $\tilde{\mathcal{R}}$  is related to  $\rho_{ge}$ , these expressions explicitly show the relation between powers and coherence.

We next analyze the cooling power of a reference classical system where coherences  $\rho_{ge}$  are absent, i.e. the system obeys the corresponding diagonal

rate equation. In this case,  $\rho$  for infinitely fast expansion and compression will remain constant, but in the thermalization legs of infinitesimal dwelling time,  $\Gamma_{\Sigma}^B \delta t \ll 1$ , where the subscript B refers to the either cold or hot bath, the population changes according to

$$\rho_{gg}(\delta t) - \rho_{gg}(0) = [\Gamma_{\downarrow}^B - \Gamma_{\Sigma}^B \rho_{gg}(0)] \delta t. \quad (6.9)$$

Note that here we have set the initial time in each thermalization leg to zero. For the average power to the baths,  $P_{c(h)}$ , we obtain

$$P_{c(h)} = \frac{1}{2} \frac{\Gamma_{\downarrow}^c \Gamma_{\downarrow}^h}{\Gamma_{\Sigma}^c + \Gamma_{\Sigma}^h} (e^{-\beta_{h(c)} \Delta E_{h(c)}} - e^{-\beta_{c(h)} \Delta E_{c(h)}}) \Delta E_{c(h)}. \quad (6.10)$$

At equal temperatures  $\beta \equiv \beta_c = \beta_h$  and assuming  $\Delta E_h > \Delta E_c$ ,

$$P_c < 0 \text{ and } P_h > 0, \quad (6.11)$$

which means that the cold bath (with lower-level splitting) gets colder and the hot bath (with higher energy separation) heats up. Not only for equal temperatures, inequalities (6.11) apply for different temperatures when  $\beta_h \Delta E_h > \beta_c \Delta E_c$ . This proves that a classical cycle produces cooling even in the  $f \rightarrow \infty$  limit. In this sudden limit, the efficiency of the refrigerator is  $\epsilon = -P_c/(P_c + P_h)$ . With the help of Eq. (6.10) it is given by

$$\epsilon = \frac{\Delta E_c}{\Delta E_h - \Delta E_c} \quad (6.12)$$

which is precisely equivalent for an ideal low frequency Otto cycle given in Eq. (6.4). In Publication VIII we qualitatively argued that creating coherence costs energy; for the system interacting with the heat bath, this energy will be dissipated in the corresponding bath while thermalized. This phenomenon which in quantum thermodynamics is often called “quantum friction”, has been studied in different contexts [157, 158, 161, 162], and it can be considered as the reason of the failure of a quantum refrigerator in the high-frequency limit. Now the question arises whether there is a driving protocol which avoids creating coherence and thus restores cooling in our system. We found in Publication VIII such a protocol thus capable of cooling at higher frequencies. In [163], we analyzed another way of avoiding heating by applying a shortcut-to-adiabaticity protocol [164, 165, 166, 167] for our Otto refrigerator.

## 6.2 Multi-qubit Otto refrigerators

In recent years, quantum information processing and quantum computation based on superconducting qubits, have made remarkable progress in both theory and experiment. Some platforms, by coupling qubits together and integrating them to other circuit elements like resonators in

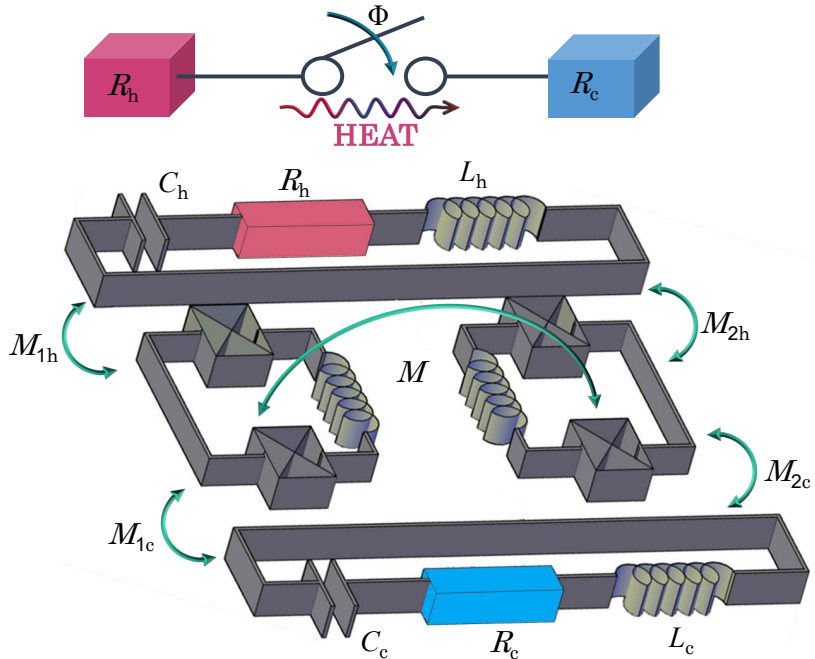


**Figure 6.4.** (top) Schematic illustration of the principle of a basic heat switch between two heat baths,  $R_c$  and  $R_h$ , at temperatures  $T_c$  and  $T_h$ , respectively. The switch can be controlled by magnetic flux  $\Phi$ ; when it is on, heat flows from  $R_h$  to  $R_c$ . (bottom) Proposed quantum heat switch, where the two resistors are embedded in two  $LC$  resonators and both coupled inductively to two coupled qubits.

order to build computationally effective quantum devices, have been realized [89, 168, 169, 170, 171, 172, 173, 174, 175, 176, 177, 178]. In the past decades, thanks to the improvement in materials and fabrication processes, the performance of superconducting nano circuits has likewise improved. However, heat transport properties and dissipation in such systems, from practical point of view in quantum thermodynamics field [151, 179], are poorly understood and only little investigated. In this section, we want to understand how the coupling between a pair of qubits affects the heat transport properties specifically in the setups that we discussed earlier for a single qubit. Up to now, the system under study was a generic qubit coupled either capacitively or inductively to two either equal or unequal dissipative  $LC$  resonators. We proved experimentally that in the case of equal resonators the setup acts as a valve/switch and in case of unequal resonators, we demonstrated theoretically that the setup works as a refrigerator. In this section, we deal with two coupled qubits instead of one in the same setup as before, as discussed in Publication II. The principle of heat switch between two heat baths (resistors  $R_c$  and  $R_h$  with temperatures  $T_c$  and  $T_h$ , respectively) is shown schematically in the top panel of Fig. 6.4. This switch can be controlled by magnetic flux  $\Phi$  in a way that when the switch is on (connected), the heat flows from the hot bath to the cold one.

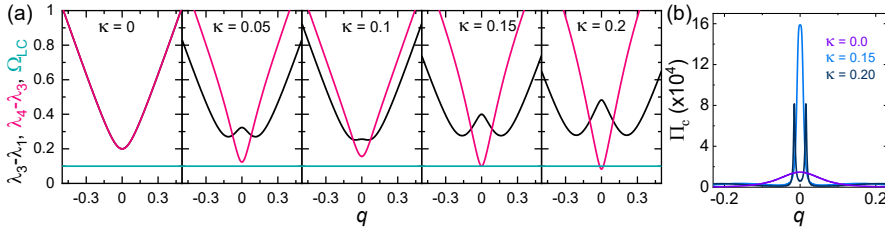


**Figure 6.5.** Performance of a heat switch with coupled qubits. (a) The energy level separation  $\lambda_3 - \lambda_1$  and  $\lambda_4 - \lambda_3$  shown by black and red lines, respectively, versus flux bias  $q$  for different values of coupling  $\kappa$ . The angular resonance frequency of the resonators  $\Omega_{LC} = 0.1$  is shown with light green line. (b) Transmitted dimensionless power  $\Pi_c = hP_c/E_0$  as a function of  $q$  for three values of coupling. The parameters for all panels are:  $E_0/k_B T_c = 20$ ,  $E_0/k_B T_h = 5$ ,  $\mathcal{Q} = \mathcal{Q}_c = Q_h = 10$ ,  $g = g_c = g_h = 1$ , and  $\Delta = 0.1$ .

This switch can be realized in a quantum circuit like the one shown in the lower panel of Fig. 6.4, where the two baths are connected together via an intermediate element with tunable parameters. Here we demonstrate that by adding another qubit to our known circuit (Fig. 5.3), one can boost the operation of the switch. In this figure, the two superconducting qubits in the center are coupled by mutual inductance  $M$ . Each of the qubits is connected to two dissipative resonators via mutual inductances  $M_{j,B}$ , where the subscripts  $j = 1, 2$  refer to the qubit number and  $B = c, h$  to the baths. As before, we apply flux to the qubit using the control parameter  $q = \delta\Phi(t)/\Phi_0$ . The total Hamiltonian for the setup shown in the lower panel of Fig. 6.4 is given by

$$\hat{\mathcal{H}} = \sum_{j=1,2} \hat{\mathcal{H}}_{Qj} + \sum_{B=c,h} \hat{\mathcal{H}}_B + \sum_{j,B} \hat{\mathcal{H}}_{cj,B} + \hat{\mathcal{H}}_{12} \quad (6.13)$$

where  $\hat{\mathcal{H}}_{Qj} = -E_j(\Delta_j \sigma_{x,j} + q \sigma_{z,j})$  indicates the Hamiltonian of each qubit, with  $E_j$  the overall energy scale of each qubit and  $2\Delta_j$  the dimensionless energy splitting at  $q = 0$ ,  $\hat{\mathcal{H}}_{12}$  is the coupling between qubits, and  $\hat{\mathcal{H}}_{cj,B} = g_B i_{n,B}(t) \sigma_{z,j}$  refers to the coupling energy of qubit  $j$  to bath  $B$ . Here,  $g_B = \frac{E_0 M_B}{\Phi_0}$  stands for the coupling of the heat bath  $B$  to each qubit, and  $i_{n,B}(t)$  presents the noise current of the cold/hot bath. As compared to the earlier discussion, the new element here,  $\hat{\mathcal{H}}_{12}$ , can be introduced as the energy corresponding to the standard inductive coupling of two current loops:  $\hat{\mathcal{H}}_{12} = MI_1 I_2$ , where  $I_j = \frac{\partial \hat{\mathcal{H}}_{Qj}}{\partial \Phi_j}$  is the current operator of qubit  $j$ . Using the expression given for  $\hat{\mathcal{H}}_{Qj}$ , we then have  $H_{12} = \gamma \sigma_{z,1} \sigma_{z,2}$ , where  $\gamma = ME_1 E_2 / \Phi_0^2$ . This setup works as a heat switch when we are in the local picture. For this reason, the Hamiltonian of the system  $\hat{\mathcal{H}}_S$  consists of these of the two qubits and their coupling as

$$\hat{\mathcal{H}}_S = - \sum_{j=1,2} E_j(\Delta_j \sigma_{x,j} + q \sigma_{z,j}) + \gamma \sigma_{z,1} \sigma_{z,2}. \quad (6.14)$$

For simplicity, we consider a fully symmetric structure  $E_0 \equiv E_1 = E_2$ ,  $\Delta \equiv \Delta_1 = \Delta_2$ , and  $g \equiv g_c = g_h$  and we choose the Bell basis where

we have  $\{|u_1\rangle = \frac{1}{\sqrt{2}}(|0_10_2\rangle + |1_11_2\rangle)$ ,  $|u_2\rangle = \frac{1}{\sqrt{2}}(|0_10_2\rangle - |1_11_2\rangle)$ ,  $|u_3\rangle = \frac{1}{\sqrt{2}}(|0_11_2\rangle + |1_10_2\rangle)$ ,  $|u_4\rangle = \frac{1}{\sqrt{2}}(|0_11_2\rangle - |1_10_2\rangle)\}$ , where the subscript  $j = 1, 2$  on the right-hand side refers to the qubit  $j$ . It is then straightforward to obtain the eigenenergies  $\lambda_i$  (normalized by  $E_0$ ) as

$$(\kappa + \lambda_i)[\lambda_i^3 - \kappa\lambda_i^2 - (\kappa^2 + 4q^2 + 4\Delta^2)\lambda_i + \kappa(\kappa^2 - 4q^2 + 4\Delta^2)] = 0, \quad (6.15)$$

where  $\kappa = \gamma/E_0$ , which determines the coupling between the two qubits. Among the eigenenergies only  $\lambda_2 = -\kappa$  does not depend on parameters except on the coupling term and we call  $|2\rangle$  a "protected state" as will become evident in what follows. The rest of the eigenenergies  $\lambda_1, \lambda_3, \lambda_4$  form a three-state system. Moreover, the normalized eigenstates are

$$|i\rangle = \frac{[(\kappa^2 - \lambda_i^2), 2q(\kappa + \lambda_i), -2\Delta(\kappa - \lambda_i), 0]^T}{\sqrt{(\kappa^2 - \lambda_i^2)^2 + 4q^2(\kappa + \lambda_i)^2 + 4\Delta^2(\kappa - \lambda_i)^2}}, \quad (6.16)$$

for  $i = 1, 3, 4$ , and  $|2\rangle = [0 \ 0 \ 0 \ 1]^T$ . Using Fermi's golden rule as before, one can calculate the transition rates between eigenstates  $i$  and  $j$  of the coupled qubits with energy spacing  $E_{ij} = E_0(\lambda_i - \lambda_j) = \omega_{ij}/\hbar$  which are dependent on the current noise produced by two baths at the frequency  $\omega_{ij}$ . These rates are given by

$$\Gamma_{i \rightarrow j, B} = \frac{g^2}{\hbar^2} |\langle i | \sigma_z^\Sigma | j \rangle|^2 S_{I,B}(\omega_{ij}), \quad (6.17)$$

where  $\sigma_z^\Sigma = \sigma_{z,1} + \sigma_{z,2}$ , and  $S_{I,B}(\omega_{ij})$  the unsymmetrized noise spectrum, is giveb by  $S_{I,B}(\omega_{ij}) = [1 + Q_B^2(\frac{\omega_{ij}}{\omega_{LC,B}} - \frac{\omega_{LC,B}}{\omega_{ij}})^2]^{-1} \frac{2\hbar\omega_{ij}}{R_B(1-e^{-\hbar\omega_{ij}/k_B T_B})}$  is with  $\omega_{LC,B} = 1/\sqrt{L_B C_B}$  denoting the bare resonance angular frequency of each  $LC$ -circuit with its quality factor  $Q_B = \sqrt{L_B/C_B}/R_B$ . Indeed  $|2\rangle$  is protected in this set-up since  $\sigma_z^\Sigma |2\rangle \equiv 0$ , and hence there is no transition to/from this state:  $\Gamma_{2 \rightarrow i, B} = \Gamma_{i \rightarrow 2, B} = 0$  for all  $i$  and  $B$ . The diagonal elements of the master equation for the coupled qubit system in the absence of time-dependent driving is given by

$$\dot{\rho}_{kk} = \sum_{j=1}^4 (\rho_{jj}\Gamma_{j \rightarrow k} - \rho_{kk}\Gamma_{k \rightarrow j}). \quad (6.18)$$

Under steady state conditions, the populations  $\rho_{ii}$  of the levels read

$$\rho_{ii} = \frac{\Gamma_{j \rightarrow k}\Gamma_{k \rightarrow i} + \Gamma_{j \rightarrow i}\Gamma_{k \rightarrow i} + \Gamma_{j \rightarrow i}\Gamma_{k \rightarrow j}}{\mathfrak{D}\mathfrak{en.}}, \quad (6.19)$$

where  $\mathfrak{D}\mathfrak{en.} = (\Gamma_{3 \rightarrow 1} + \Gamma_{3 \rightarrow 4})(\Gamma_{1 \rightarrow 4} + \Gamma_{4 \rightarrow 1}) + (\Gamma_{1 \rightarrow 4} + \Gamma_{3 \rightarrow 1})\Gamma_{4 \rightarrow 3} + \Gamma_{1 \rightarrow 3}(\Gamma_{3 \rightarrow 4} + \Gamma_{4 \rightarrow 1} + \Gamma_{4 \rightarrow 3})$ . Here,  $\Gamma_{i \rightarrow j}$  denotes the total transition rate ( $\Gamma_{i \rightarrow j} = \Gamma_{i \rightarrow j,C} + \Gamma_{i \rightarrow j,H}$ ) due to both the baths from eigenstate  $i$  to  $j$ . The indices assume values  $(i, j, k) = (1, 3, 4)$ , and their permutations.

In order to obtain the amount of power to the cold reservoir  $P_c$  in this setup, one needs to calculate  $P_c = \langle d\hat{\mathcal{H}}_{S,c}/dt \rangle$ , where  $d\hat{\mathcal{H}}_{S,c}/dt = \frac{i}{\hbar}[\hat{\mathcal{H}}_{c,c}, \hat{\mathcal{H}}_S]$

is the operator of power to the coupled qubits from the cold bath, and  $\hat{\mathcal{H}}_{c,c} = \hat{\mathcal{H}}_{c1,c} + \hat{\mathcal{H}}_{c2,c} = g(\sigma_{z,1} + \sigma_{z,2})i_{n,c}(t)$ . Then the expression for  $d\hat{\mathcal{H}}_{S,c}/dt$  is given by

$$d\hat{\mathcal{H}}_{S,c}/dt = \frac{2g}{\hbar}E_0\Delta(\sigma_{y,1} + \sigma_{y,2})i_{n,c}(t) = \frac{2g}{\hbar}E_0\Delta\sigma_y^\Sigma i_{n,c}(t). \quad (6.20)$$

The standard calculation of power transmitted between the hot and cold baths in linear response and in the interaction picture yields

$$P_c = -\frac{i}{\hbar}\int_{-\infty}^t dt' \langle [d\hat{\mathcal{H}}_{S,c,I}/dt(t), \hat{\mathcal{H}}_{c,c,I}(t')] \rangle. \quad (6.21)$$

The power in a two-qubit system is given by

$$P_c = \sum_{k,l} \rho_{kk} E_{kl} \Gamma_{k \rightarrow l, c}, \quad (6.22)$$

which is similar to the one that we obtained for a single-qubit system. The energy separation  $\lambda_3 - \lambda_1$  and  $\lambda_4 - \lambda_3$  are plotted in Fig. 6.5(a) with black and red lines, respectively, for different values of coupling between the two qubits  $\kappa$  as a function of flux bias  $q$ . The dimensionless angular resonance frequency of the identical resonators  $\Omega_{LC} = \hbar\omega_{LC}/E_0$  is also shown with the light green line. In the first panel, in the absence of coupling  $\kappa = 0$ , the two level separations are the same, meaning  $\lambda_3 - \lambda_1 = \lambda_4 - \lambda_3 = 2\sqrt{q^2 + \Delta^2}$ . Panel (b) displays the transmitted power as a function of flux for three selected values of coupling. One can explain the behavior of power based on energy separation presented in panel (a). The smallest Lorentzian peak belongs to  $\kappa = 0$  where the level separations are identical. The maximum transmitted power happens at  $\kappa = 0.15$  where the level separation  $\lambda_4 - \lambda_3$  at  $q = 0$  meets the resonance frequency of the resonators  $\Omega_{LC}$ . This optimum value of coupling  $\kappa_{opt}$  can be obtained easily using Eq. (6.15) at  $q = 0$  where  $\lambda_4 - \lambda_3 = \Omega_{LC}$  which leads to  $\kappa_{opt} = (4\Delta^2 - \Omega_{LC}^2)/2\Omega_{LC}$ . In Fig. 6.5(a), since  $\Delta = \Omega_{LC}$ , we have  $\kappa_{opt} = 3\Omega_{LC}/2 = 0.15$ . Naturally, by further increasing the coupling  $\lambda_4 - \lambda_3$  crosses  $\Omega_{LC}$  at two different values of  $q$ . This leads to appearance of two peaks in power but the total amount of power is less than at  $\kappa = 0.15$ , since in this case  $\lambda_3 - \lambda_1$  has larger value. This behavior of power is similar to one that was observed experimentally in the local regime of heat valve (Fig. 5.3). In Fig. 6.5(b) one can easily see that the transmitted power increases dramatically (in our example by one order of magnitude in the optimum coupling point) for coupled qubits as compared to the two individual ones. Moreover, the sharper peak for coupled qubits in comparison with the broader and weaker peak of single qubit indicates that coupled qubits provide a more selective heat switch.

### 6.2.1 Correlated versus uncorrelated baths

Up to now, we have assumed that the two qubits are affected by the same heat baths, as was depicted in Fig. 6.4. The dynamics of quantum

circuits composed of several qubits is known to depend on whether they are subject to the noise of one or several sources. An interesting question arises whether the noise sources affecting to the quantum elements are correlated or not [180, 181, 182, 183, 184, 185, 186, 159, 187, 188, 189]. In principle this distinction may arise depending on the physical distance of the source(s). Coupling of two qubits to either a single noise source or two uncoupled ones is shown schematically in Fig. 6.6(a). In Publication III we studied a minimal setup where such a distinction could be observed, namely a heat valve/switch or Otto refrigerator between either the same or different heat baths. We will see that in general the qubits form a four-level system. The two intermediate states are degenerate, and one of them is a dark state in the case of fully (anti)correlated noise sources, whereas in any other case, all the four states are accessible. We will see below how the degree of correlation of noise affects the properties of the heat valve/switch.

The total Hamiltonian describing the system and the environment shown in Fig. 6.6(a) is given by

$$\hat{\mathcal{H}} = \hat{\mathcal{H}}_{Q1} + \hat{\mathcal{H}}_{Q2} + \hat{\mathcal{H}}_N + \hat{V}_{N,1} + \hat{V}_{N,2}, \quad (6.23)$$

where along with the introduced Hamiltonian of the qubit  $\hat{\mathcal{H}}_{Qj}$ ,  $H_N$  denotes the Hamiltonian of the noise source(s), and  $\hat{V}_{N,1}, \hat{V}_{N,2}$  are the couplings of the qubits 1 and 2 to the noise source(s). Note that for our main argument, we assume that the two qubits are mutually decoupled ( $\kappa = 0$ ) although the selection rules to be presented hold also for coupled qubits. For quantitative analysis, we use the Bell states  $|u_i\rangle$  for  $i = 1 - 4$  as introduced before. Further, we assume a fully symmetric system, i.e.,  $E_0 \equiv E_1 = E_2$ , and  $\Delta \equiv \Delta_1 = \Delta_2$ . In this case, the eigenenergies of the Hamiltonian (in units of  $E_0$  and assuming  $\kappa = 0$ ) read

$$\lambda_1 = -2\sqrt{q^2 + \Delta^2}, \quad \lambda_2 = \lambda_3 = 0, \quad \lambda_4 = +2\sqrt{q^2 + \Delta^2} \quad (6.24)$$

and the corresponding eigenstates are given by

$$\begin{aligned} |1\rangle &= \frac{1}{\sqrt{2}}(|u_1\rangle + \frac{q}{\sqrt{q^2 + \Delta^2}}|u_2\rangle + \frac{\Delta}{\sqrt{q^2 + \Delta^2}}|u_3\rangle) \\ |2\rangle &= |u_4\rangle \\ |3\rangle &= \frac{\Delta}{\sqrt{q^2 + \Delta^2}}|u_2\rangle - \frac{q}{\sqrt{q^2 + \Delta^2}}|u_3\rangle \\ |4\rangle &= \frac{1}{\sqrt{2}}(|u_1\rangle - \frac{q}{\sqrt{q^2 + \Delta^2}}|u_2\rangle - \frac{\Delta}{\sqrt{q^2 + \Delta^2}}|u_3\rangle). \end{aligned} \quad (6.25)$$

For the noise sources, we use a generic form of linear coupling between each qubit and the noise source as

$$\hat{V}_N \equiv \sum_{m=1,2} \hat{V}_{N,m} = \sum_{m=1,2} \hat{A}_m \delta \hat{X}_m(t), \quad (6.26)$$

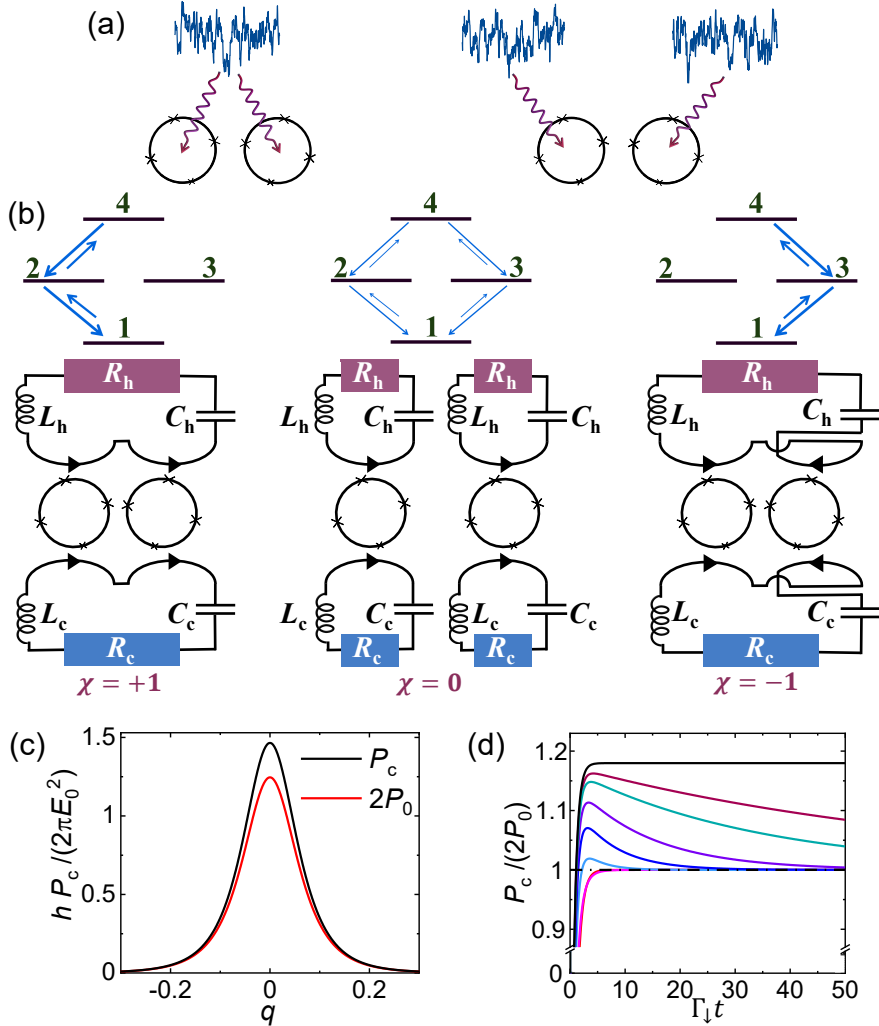


**Figure 6.6.** Comparing the impact of correlated, uncorrelated, and anticorrelated noise sources on a quantum device. (a) Two qubits are subjected to correlated (left) and uncorrelated (right) noise sources. (b) Schematic illustration of energies and transition rates of the four-level system of the decoupled qubits (top) and heat switch/Otto refrigerator configuration (bottom) for three different degrees of correlation of noise sources: correlated ( $\chi = 1$ ), uncorrelated ( $\chi = 0$ ), and anticorrelated  $\chi = -1$ . (c) Dimensionless power to the cold bath  $P_c$  under steady-state condition versus  $q$  for fully correlated/anticorrelated noise source (black line) and for other values of  $\chi$  (red line). (d)  $P_c / 2P_0$  as a function of dimensionless time  $\Gamma_{\downarrow} t$  when the system is initialized in  $|1\rangle$  at  $t = 0$  for different degrees of correlation:  $\chi = 0, 0.5, 0.8, 0.9, 0.95, 0.98, 0.99$ , and 1 from bottom to top. The parameters used in the panels (c) and (d) are:  $\hbar\omega_c/E_0 = \hbar\omega_h/E_0 = 0.1$ ,  $k_B T_h/E_0 = 0.2$ ,  $k_B T_c/E_0 = 0.05$ ,  $Q_c = Q_h = 10$ ,  $g_1 = g_2 = 1.0$ , and  $\Delta = 0.1$ .

where  $\hat{A}_m$  determines the coupling and  $\delta\hat{X}_m(t)$  is the time  $t$  dependent fluctuation of the quantity. Further we assume that all the noise sources and their couplings to the individual qubits are equal. As an important issue, here we investigate the cases of different degrees of correlation  $\chi_{mn}$  between two noise sources  $m$  and  $n$ , where for autocorrelation,  $\chi_{11} = \chi_{22} = +1$ , and for cross-correlation we set  $\chi_{12} = \chi_{21} = \chi$ , where  $-1 \leq \chi \leq +1$ . In this case the two-time noise correlators are then given by

$$\langle \delta\hat{X}_m(t') \delta\hat{X}_n(t) \rangle = \chi_{mn} \int_{-\infty}^{\infty} \frac{d\omega}{2\pi} e^{-i\omega(t'-t)} S(\omega), \quad (6.27)$$

with  $S(\omega)$  as the noise spectrum, and for simplicity we assume that the spectra of the two noise sources are equal. For what follows, we have  $\chi = 0$  for uncorrelated,  $\chi = +1$ , for fully correlated and  $\chi = -1$  for anticorrelated noise from independent sources. From practical point of view, one physical way of controlling  $\chi_{mn}$  is adjusting the distance of the noise sources from the quantum circuits (see, e.g., Ref. [190]). In our concrete circuit the degree of correlation can be controlled by the choice of the coupling scheme shown in the lower panels of Fig. 6.27 (b). Further, by introducing the mutual inductive coupling between each noise source to the other qubit as well, it would allow for arbitrary values of  $\chi$  in the interval  $-1 \leq \chi \leq +1$ . Using Fermi's golden rule, the transition rates from the  $k^{th}$  to the  $l^{th}$  instantaneous eigenstate due to the noise source(s) N are given by

$$\Gamma_{k \rightarrow l, N} = \frac{1}{\hbar^2} \sum_{m,n=1}^2 \langle k | \hat{A}_m | l \rangle \langle l | \hat{A}_n | k \rangle \chi_{mn} S_N(\omega_{kl}), \quad (6.28)$$

where  $\omega_{kl} = E_{kl}/\hbar = E_0(\lambda_k - \lambda_l)/\hbar$ , and  $S_N(\omega_{kl})$  is the noise induced by this source. These rates are the off-diagonal elements of

$$\Gamma^{(N)} = \begin{pmatrix} \dots & (1-\chi)\Gamma_{\uparrow}^{(N)} & (1+\chi)\Gamma_{\uparrow}^{(N)} & 0 \\ (1-\chi)\Gamma_{\downarrow}^{(N)} & \dots & 0 & (1-\chi)\Gamma_{\uparrow}^{(N)} \\ (1+\chi)\Gamma_{\downarrow}^{(N)} & 0 & \dots & (1+\chi)\Gamma_{\uparrow}^{(N)} \\ 0 & (1-\chi)\Gamma_{\downarrow}^{(N)} & (1+\chi)\Gamma_{\downarrow}^{(N)} & \dots \end{pmatrix} \quad (6.29)$$

where  $\Gamma_{\downarrow,\uparrow}^{(N)} = \frac{g^2}{\hbar^2} \frac{\Delta^2}{q^2 + \Delta^2} S_N(\pm\omega)$  is the corresponding rate for a single qubit,  $\hbar\omega = 2E_0\sqrt{q^2 + \Delta^2}$  is the level spacing, and  $g^2$  is the coupling constant between the noise source and the qubit, which is proportional to the mutual inductance squared in the case of flux coupling. For the decoupled qubits, the influence of degree of correlation on the transition rates between the energy levels is schematically shown in the upper panels of Fig. 6.27 (b) for three values of  $\chi$ . According to Eq. (6.29) and the illustration of 6.27 (b), for fully correlated  $\chi = +1$  and anticorrelated noise  $\chi = -1$ , the transitions to/from  $|2\rangle$  and  $|3\rangle$ , respectively, are forbidden and as a result they become protected states for these cases. In order to demonstrate the implication of

the correlation of noise in real circuits, we focus on the system shown in the lower panels of Fig. 6.6 (b) for different values of  $\chi$ . As before, the noise sources are the resistors  $R_B$  for  $B=c, h$  acting as thermal baths. In this case, the fluctuating quantity  $\delta \hat{X}_m(t)$  can be presented by electric current noise  $\delta i_m(t)$  and the coupling  $\hat{A}_m$  to be  $g_m \sigma_{z,m}$ , with  $g_m$  the coupling, e.g., by mutual inductance between each qubit and the fluctuating current. In the absence of qubit driven, the expression of master equations and power will be then similar to Eqs. (6.18) and (6.22). Naturally the question that will arise now, is how the degree of correlation influences the transmitted power. In order to obtain the steady state population, one needs to find the solution of  $\Gamma_{\text{tot}}^T \rho = 0$ , where  $\Gamma_{\text{tot}} = \Gamma^{(h)} + \Gamma^{(c)}$ , and  $\rho = (\rho_{11} \ \rho_{22} \ \rho_{33} \ \rho_{44})^T$ , which depends on the initial condition applied to the system. For simplicity we start with  $-1 < \chi < +1$ . In this case the steady state populations of the states are given by  $\rho_{11} = (1+r)^{2-1}$ ,  $\rho_{22} = \rho_{33} = r/(1+r)^2$ , and  $\rho_{44} = r^2/(1+r)^2$ , where  $r = \Gamma_{\uparrow}/\Gamma_{\downarrow}$  and  $\Gamma_{\uparrow,\downarrow} = \Gamma_{\uparrow,\downarrow}^{(h)} + \Gamma_{\uparrow,\downarrow}^{(c)}$ . In this case, the steady state populations are thus independent of the correlation  $\chi$ , i.e., in the long time limit with no time dependent drive, these populations are independent of the correlation  $\chi$ . The steady state power to the cold bath  $P_c$  then reads

$$P_c = 2(-\rho_{gg}\Gamma_{\uparrow,c} + \rho_{ee}\Gamma_{\downarrow,c})\hbar\omega_Q = 2P_0, \quad (6.30)$$

where  $P_0$  is the transmitted power by a single qubit in the instantaneous eigenbasis to the cold bath at  $q = 0$ . Thus, the steady state power for  $-1 < \chi < +1$  scales with the number of qubits and importantly is independent of the degree of correlation  $\chi$ . This power as a function of  $q$  is shown in Fig. 6.6(c) with the red line. Let us now discuss two extreme cases, the fully correlated and anticorrelated cases. For the fully correlated case,  $\chi = +1$ , if the system is initialized in the subspace  $\{|1\rangle, |3\rangle, |4\rangle\}$  we have  $\rho_{11} = 1/(1+r+r^2)$ ,  $\rho_{33} = r/(1+r+r^2)$ ,  $\rho_{44} = r^2/(1+r+r^2)$ , while  $\rho_{22} = 0$ . On the other hand, initializing in the state  $|2\rangle$  leads to  $\rho_{22} = 1$ , and the population of the other states will be zero, meaning  $\rho_{11} = \rho_{33} = \rho_{44} = 0$ , which demonstrates that  $|2\rangle$  is a protected state. For the fully anticorrelated case, the situation is analogous. The power for  $\chi = \pm 1$  with the best choice of the initial state, is plotted in Fig. 6.6(c) with a black line. Surprisingly, this power is larger than  $2P_0$ . In order to understand the origin of enhancement of power for  $\chi = \pm 1$  above that of the other values of  $\chi$ , one can look at the dynamic behavior of it. The power  $P_c$  normalized by the uncorrelated power  $2P_0$  as a function of dimensionless time  $\Gamma_{\downarrow}t$ , when the system is initialized in state  $|1\rangle$  at  $t = 0$ , is shown in Fig. 6.6(d) for different values of positive  $\chi$ . Based on this figure, It is clear that for  $\chi \rightarrow +1$ , the time to approach  $P_c = 2P_0$  becomes longer and longer, and for  $\chi = +1$  (black solid line) this relaxation time becomes infinite. If one initializes the system to state  $|2\rangle$  ( $|3\rangle$ ) instead, the power for  $\chi = 1$  ( $\chi = -1$ ) remains zero for the same reason.

## 7. Calorimetric quantum detector – ultimate resolution

Calorimeter is a detector that can measure small quantities of energy absorbed to a body whose temperature is monitored. At best it comes with the following features. First of all, a low temperature nanocalorimeter can be made extremely sensitive, thanks to ultra-small heat capacity of the absorber and the favorable properties of local thermometers. Secondly, calorimeter can be a non-invasive continuous detector that, unlike many other single-quantum detectors, does not demand reset with the associated dead time. A nanocalorimeter can be easily integrated, e.g., to a circuit QED implementation, making it attractive for applications to be discussed below. Thirdly, the calorimeter can typically absorb quanta of different magnitudes, thus having the bonus of detecting not only the events but also the energy of them. For all these reasons we focus here on discussing the principle, performance, and applications of a calorimeter towards single-microwave photon detection.

### 7.1 Temperature response of a calorimeter

Temperature response of a calorimeter has been discussed in Publication IX, Publication XI, Publication XIV, and Publication XV, and in Subsection 3.4.1. The basic principle is as follows. When a quantum with energy  $E$  is absorbed, the temperature of the calorimeter increases quickly by amount  $\Delta T(0) = E/\mathcal{C}$  (linear regime), where  $\mathcal{C}$  is the heat capacity of the absorber. After that the temperature relaxes exponentially back to equilibrium with time constant  $\tau = \mathcal{C}/G_{\text{th}}$ , where  $G_{\text{th}}$  is, as before, the thermal conductance to the heat bath. This is idealized and linearized behaviour of the temperature in the absence of noise and for a single event only. But already on this level we may assess the feasibility of such a measurement based on orders of magnitude of  $E$  and  $\mathcal{C} \simeq \gamma V T$  for a metallic calorimeter in the regime of our interest. Here  $\gamma \sim 100 \text{ JK}^{-2}\text{m}^{-3}$  for copper and  $V$  denotes the volume of the absorber. Taking a microwave photon of  $1 \text{ K} \times k_{\text{B}}$  energy and a metallic absorber of  $(0.1 \mu\text{m})^3$  volume at  $T = 10 \text{ mK}$ ,

we immediately find that the expected temperature rise of the absorber,  $\Delta T(0)$ , is of the same order as the temperature itself, making this detector highly attractive. In the following subsections we take a more quantitative look into this question including the intrinsic noise of the absorber.

### 7.1.1 Ideal calorimeter

Here we discuss an "ideal calorimeter" by which we mean the following. The temperature of the absorber, in the absence of absorption events, is affected only by thermal noise from an equilibrium bath. In our case the bath is usually the phonons affecting the temperature of  $\sim 10^8$  electrons forming the absorber itself. Furthermore, we assume that the thermometer is infinitely fast and it does not affect the absorber temperature (no self-heating) and there is no extra noise in measuring the temperature (noiseless amplifier). Under these assumptions we can find the ideal signal-to-noise ratio of the calorimeter detecting a photon.

In the time domain we may simulate the stochastic temperature history of the absorber as follows. The calorimeter coupled to the heat bath is schematically shown in Fig. 7.1(a). First, we write the Langevin equation for temperature of this absorber coupled to the bath at fixed temperature  $T_0$ , for small variations  $\delta T(t) = T(t) - T_0$  as

$$\mathcal{C}\delta\dot{T}(t) = -G_{\text{th}}\delta T(t) + \delta\dot{Q}(t), \quad (7.1)$$

which is essentially Eq. (3.45). In general  $\delta\dot{Q}(t)$  is the instantaneous heat current on the absorber, the fluctuating heat due to coupling to the bath. This stochastic exchange of heat between the absorber with the bath, here in equilibrium, is indicated schematically by the many vertical arrows between the two in Fig. 7.1(a). Discretizing time in steps  $\Delta t$  mainly for numerical purposes leads to a coarse grained version of Eq. (7.1) which reads

$$\mathcal{C}\frac{\delta T(t + \Delta t) - \delta T(t)}{\Delta t} = -G_{\text{th}}\delta T(t) + \delta\dot{Q}_{\text{av}}(t), \quad (7.2)$$

where  $\delta\dot{Q}_{\text{av}}(t) = (1/\Delta t) \int_t^{t+\Delta t} dt' \delta\dot{Q}(t')$  is the average heat current in this regime. Introducing the dimensionless time variable  $u = t/\tau$  and knowing that  $\tau = \mathcal{C}/G_{\text{th}}$  we have

$$\delta T(u + \Delta u) = [1 - \Delta u]\delta T(u) + \frac{\Delta u}{G_{\text{th}}} \delta\dot{Q}_{\text{av}}(t), \quad (7.3)$$

where  $\Delta u = \Delta t/\tau$ . Since we are dealing with fluctuations, we normalize the noise in a way that  $\delta\dot{Q}_{\text{av}}(t) = \langle \delta\dot{Q}_{\text{av}}^2(t) \rangle \xi(t)$ . Here the average noise of heat current  $\delta\dot{Q}_{\text{av}}(t)$  over time interval  $\Delta t$  leads to the root-mean-square (rms) of it as

$$\langle \delta\dot{Q}_{\text{av}}^2(t) \rangle = \frac{1}{\Delta t^2} \int_{t-\Delta t/2}^{t+\Delta t/2} dt' \int_{t-\Delta t/2}^{t+\Delta t/2} dt'' \langle \delta\dot{Q}(t') \delta\dot{Q}(t'') \rangle. \quad (7.4)$$

As we discussed before, according to the fluctuation-dissipation theorem, the low frequency spectral density in equilibrium is  $S_{\dot{Q}}(0) = \int dt' \langle \delta \dot{Q}(t') \delta \dot{Q}(t'') \rangle$ . We then obtain

$$\langle \delta \dot{Q}_{av}^2(t) \rangle = \frac{S_{\dot{Q}}(0)}{\Delta t} = \frac{2k_B T_0^2 G_{th}}{\Delta t}. \quad (7.5)$$

Substituting these expressions into Eq. (7.3), the coarse-grained equation is given by

$$\delta T(u + \Delta u) = [1 - \Delta u] \delta T(u) + \sqrt{\frac{2k_B T_0^2}{C} \xi(u) \sqrt{\Delta u}}. \quad (7.6)$$

Next question is how to determine the distribution of  $\xi$ . Based on probability theory, for a continuous probability distribution for real random variable, we assume a Gaussian distribution as

$$P(\delta \dot{Q}_{av}) = \frac{1}{\sqrt{2\pi \langle \delta \dot{Q}_{av}^2 \rangle}} e^{-\frac{\delta \dot{Q}_{av}^2}{2\langle \delta \dot{Q}_{av}^2 \rangle}}. \quad (7.7)$$

Based on the definition that we had for  $\xi(u)$ ,  $\delta \dot{Q}_{av}(u) \propto \xi(u)$ , in the same interval  $\Delta u$ , we should have  $P(\delta \dot{Q}_{av}) d\delta \dot{Q}_{av} = P(\xi) d\xi$ . Using Eq. (7.5) we have then

$$P(\xi) = \frac{1}{\sqrt{2\pi}} e^{-\xi^2/2}. \quad (7.8)$$

This means that  $\xi(u)$  is a Gaussian quantity that has unit width. Note that as long as  $\Delta t \ll \tau$ , the above results do not depend on the value of the time step. By a Monte Carlo simulation for Eq. (7.6) we then obtain the temperature history of the absorber with  $\xi(u)$  as the Gaussian distributed stochastic variable.

A key element in the calorimeter is a thermometer with sufficient bandwidth to provide temporal temperature traces. An example of such time traces is shown in Fig. 7.1(b). This time trace is from the experiment and it includes other sources of noise like amplifier noise superposed on the intrinsic noise. In our case the fundamental noise arises from electron-phonon coupling. For numerical simulation of Eq. (7.6), we assume a metallic resistor formed of a Fermi gas of about  $10^8$  electrons and fast electron-electron relaxation and weak coupling to the phonon bath. Here we use the values directly from the experiment. The metallic absorber is copper with heat capacity  $C/k_B = 100$ , at  $T_0 = 10$  mK and with the absorber volume  $V = (0.1 \mu\text{m})^3$  and the time step in the simulation is  $\Delta t = 0.001\tau$ . Solid black line in Fig. 7.1(c) displays a simulated time trace of the true absorber temperature based on the given parameters.

### 7.1.2 Influence of non-zero response time of a thermometer

In the previous subsection we assumed that the response time of the thermometer is zero, meaning changes in the thermometer follow temperature

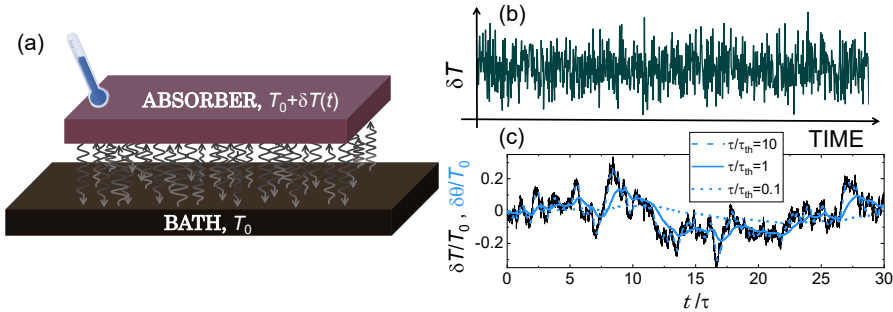


**Figure 7.1.** The calorimeter. The working principle of a calorimeter is schematically presented in (a). The normal-metal absorber (electron system) with instant temperature  $T_0 + \delta T(t)$  and heat capacity  $\mathcal{C}$  is subjected to the phonon heat bath at fixed temperature  $T_0$ . The heat exchange between the electrons and phonons is displayed by many vertical arrows. The fast thermometer records the absorber's temperature fluctuations  $\delta T(t)$ . An example of such a measured temporal temperature trace is shown in (b). The response of a calorimeter is presented in (c). Solid black line presents the exact time trace of absorber temperature in the absence of any photon absorption. Blue lines show the same trace but with three different thermometer readouts with different response times  $\tau_{th}$ . The parameters are  $\mathcal{V} = (0.1 \mu\text{m})^3$ ,  $\mathcal{C}/k_B = 100$ ,  $T_0 = 0.01 \text{ K}$ , and  $\Delta t = 0.001 \tau$ .

variations instantaneously. Here we model the actual temperature probe where we incorporate in the analysis the finite bandwidth of the thermometer. We consider that the response time of the thermometer is  $\tau_{th}$  and the measured temperature  $\theta(t)$  follows the actual simulated temperature  $T(t)$  by  $\dot{\theta}(t) = -\tau_{th}^{-1}[\theta(t) - \delta T(t)]$ . Using the same dimensionless time step  $\Delta u = \Delta t/\tau$  we easily obtain

$$\theta(u + \Delta u) = \theta(u) - \frac{\tau}{\tau_{th}}[\theta(u) - \delta T(u)]\Delta u. \quad (7.9)$$

Thus, for  $\tau/\tau_{th} \ll 1$ ,  $\theta(u) = \text{const.}$ , i.e., the thermometer does not follow the changing temperature in the absorber. In the other limit when  $\tau/\tau_{th} \gg 1$ , the read-out temperature is  $\theta(u) \simeq T(t)$  meaning that the thermometer follows accurately the actual temperature. In Fig. 7.1 (c) blue lines present the numerical results of  $\theta(t)$  for three different values of  $\tau/\tau_{th}$ . It is vivid that by decreasing the ratio of  $\tau/\tau_{th}$ , the measured temperature trace  $\theta(t)$  is getting more smeared deviating from the true temperature  $\delta T(t)$ . Moreover, we use this figure as a reference (background noise) for actual event when an incident quanta with energy  $E$  are being absorbed by the absorber.

### 7.1.3 SNR ratio of a calorimeter in response to absorption of quanta

In this subsection, we study the calorimeter operation in action while single quanta are being absorbed by it. Along with the evolution dictated by the electron-phonon coupling, we add in Eq. (7.6), the energy absorption

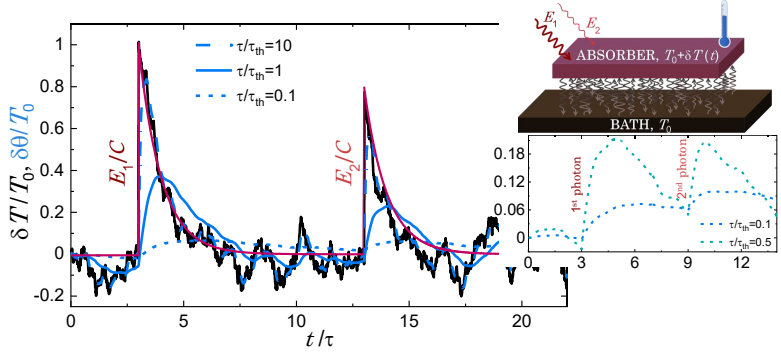


**Figure 7.2.** Temperature response of a calorimeter. (upper inset) The same calorimeter as in Fig. 7.1(a), is exposed to two incoming photons with energies  $E_1 = 1.0 \text{ K} \times k_B$  and  $E_2 = 0.8 \text{ K} \times k_B$  at different times  $t_1/\tau = 3$  and  $t_2/\tau = 13$ , respectively. (main panel) The exact normalized absorber temperature  $\delta T(t)/T_0$  shown with black line, presents two jumps in temperature with magnitudes  $\Delta T_1 = E_1/C$  and  $\Delta T_2 = E_2/C$  within presented time interval with both jumps clearly exceeding the noise level of equilibrium fluctuations. (lower panel) Two temporal temperature traces of the absorber for the case  $\tau/\tau_{\text{th}} < 1$  illustrate the overlapping pulses with the same energies,  $E_1$  and  $E_2$ , at times  $t_1/\tau = 3$  and  $t_2/\tau = 9$ , respectively. The parameters are  $\mathcal{V} = (0.1 \mu\text{m})^3$ ,  $C/k_B = 100$ ,  $T_0 = 0.01 \text{ K}$ , and  $\Delta t = 0.01 \tau$ .

events  $\delta\dot{Q}(t) = \sum_i E_i \delta(t - t_i)$ . Here,  $E_i$  is the magnitude of the absorbed energy in form of heat released in the absorber instantaneously times  $t_i$ . After absorption of each quantum at time  $t_i$ , a sudden temperature rise with magnitude  $\Delta T_i = E_i/C$  occurs in the absorber. We present in Fig. 7.2 a stochastic simulation of the temperature history of a metallic absorber under the previously introduced experimental conditions as in Fig 7.1(c) but with  $\Delta t = 0.01\tau$ . The time scale  $\tau$  is here again determined by the coupling of electrons to phonons. In the simulation, two quanta of energy  $E_1 = 1.0 \text{ K} \times k_B$  and  $E_2 = 0.8 \text{ K} \times k_B$  are absorbed at  $t_1/\tau = 3$  and  $t_2/\tau = 13$ , respectively, which is schematically also shown in the upper inset of Fig. 7.2. This figure demonstrates the three key features of the calorimetric single-microwave photon detector: (i) The resolution of this method is sufficient to observe such photons taken the experimental conditions. (ii) The detector operates continuously without a need to be reset after the absorption event. In principle it can observe photons even if the time interval of the events is smaller than  $\tau$  although in such a case the pulses overlap partly. The lower inset of Fig. 7.2 shows clearly such overlapping pulses with  $\tau/\tau_{\text{th}} = 0.1$ . (iii) The detector can accept photons of any energy  $E$ , the signal height is essentially linear in  $E$ , and the only limitation of detecting a photon is the SNR determined by the temperature noise. The black line presents the true temperature of the absorber. The "filtered" temperature traces are shown by blue lines in the figure. A slow response of the thermometer leads to loss of the sharp rise of temperature at the absorption instant and makes the detector more prone to overlapping signals due to the decay time  $\tau_{\text{th}}$  instead of  $\tau$  after

the pulse. On the other hand the effective noise level is also suppressed. The ratio  $\tau/\tau_{\text{th}} = 10$  is quite achievable with the techniques we use in the experiments Publication VI and Publication IX and the smearing of the temperature trace is very moderate in this case.

## 7.2 Experimental assessment of a calorimetric quantum detector

In this section we present how we reached the bound of fundamental thermal fluctuations in a nanoscale detector at very low temperatures and thus take an important step in ultrasensitive calorimetry and bolometry, demonstrating that it is possible to detect thermally, e.g., quantum trajectories with superconducting circuits [79, 191, 192] or single microwave photons in circuit QED. Moreover, a combination of fast, accurate and effectively non-invasive thermometry has allowed us to investigate the temperature fluctuations, and it also opens up for a broad range of fundamentally important experiments in quantum thermodynamics and quantum technology requiring fast and accurate heat flow characterization. Further, we will discuss how effective temperature fluctuations obey equilibrium fluctuation-dissipation theorem (FDT), and we also characterize them in out-of-equilibrium, in the presence of an electrical bias.

### 7.2.1 Principles in the experiment

Fluctuations are naturally present in all physical systems, but are very prominent at nanoscale. Fluctuations of electrical current (Johnson-Nyqvist noise) were investigated already 90 years ago [35, 36]. Temperature fluctuations are equally fundamental, but much more challenging to measure. As we discussed before, for the system presented in Fig. 7.1(a), there are two origins for temperature fluctuations in the absorber: random time and energy exchange of heat current between the electron and phonon systems. We derived in Section 3.4.1 that under steady state conditions and at low frequencies, the noise spectrum of the absorber temperature reads  $S_T(0) = 2k_B T_0^2/G_{\text{th}}$ . In order to measure this quantity under equilibrium and nonequilibrium conditions we use the system and setup presented in Fig. 4.7(a) but with optimised sample. The normal metallic absorber (N) is a  $\ell = 1 \mu\text{m}$  long copper wire and its full volume is about  $\mathcal{V} = (0.1 \mu\text{m})^3$ . As shown in Fig. 4.7(a), this absorber is coupled to two aluminum superconducting leads (S) on the top and bottom via tunnel barriers (I). The contact at the distance of  $L = 50 \text{ nm}$  (optimized structure) and at an inclined angle downwards is also of aluminum, but with a direct metal to metal contact and grounded on the sample stage, allowing for superconducting proximity in the copper absorber. This proximity effect makes the thermometer tunnel junction on the right to exhibit a zero-bias anomaly due to Cooper pair

current via this S<sub>M</sub>IS structure. We illustrated that the favorable property of this junction is its temperature dependent zero-bias conductance that can be used as a thermometer down to lowest temperatures with very low dissipation. The auxiliary tunnel junction at the bottom is used for injecting nonequilibrium electrons into the absorber when biased. The S<sub>M</sub>IS thermometer is embedded in an on-chip *LC* resonator allowing for fast readout on micro-second timescales. The resonator coupled to input  $V_1$  and output  $V_2$  RF lines operates at resonance frequency  $f_0 = \omega_0/2\pi = 620$  MHz. Moreover, the resonator is coupled to a bias-tee which admits DC biasing at voltage  $V$ . The measured signal  $S_{21}$  obtained by the RF transmission measurement is performed at a finite sampling rate in order to acquire statistics of the time dependence of the absorber temperature  $\delta T(t)$ . Measuring this signal at resonance frequency yields the conductance of the S<sub>M</sub>IS junction as  $S_{21}(\omega_0) = S_0 - R_0 G$  (Eq. (4.19)) with  $R_0$  and  $S_0$  as constants depending on the setup and also the attenuation and amplification in the lines. First we need to calibrate the thermometer. For this, we measure  $S_{21}$  averaged for about one second. A typical measurement of  $S_{21}$  versus  $V$  was shown earlier in Fig. 4.7 (c). The ZBA at  $V = 0$  is the feature that we use for thermometry. The inset of Fig. 2(b) in Publication IX displays a nearly linear temperature dependence of the average transmission  $\langle S_{21} \rangle$  at zero bias at temperatures below 150 mK.

### *Background noise*

We perform our measurement at 10 kHz sampling rate. Monitoring  $S_{21}(t)$  yields the instantaneous absorber temperature over a chosen time interval. From that we obtain the total fluctuations (variance)  $\langle \delta S_{21,\text{tot}}^2 \rangle$  in a bandwidth of  $\Delta f \approx 10$  kHz. Since the fluctuations of the total readout  $\langle \delta S_{21,\text{tot}}^2 \rangle$  are composed of the noise of interest  $\langle \delta S_{21}^2 \rangle$  and background noise  $\langle \delta S_{21,\text{bg}}^2 \rangle$ , we need to find a way to remove the unfavourable noise, mainly amplifier noise and further instrumental noise. We assume that the noise sources are uncorrelated. Therefore, the actual noise from the sample is given by  $\langle \delta S_{21}^2 \rangle = \langle \delta S_{21,\text{tot}}^2 \rangle - \langle \delta S_{21,\text{bg}}^2 \rangle$ . We directly measure  $\langle \delta S_{21,\text{bg}}^2 \rangle$  by carefully off-tuning the interesting fluctuations from the sample itself. This is achievable by performing two things simultaneously. First, we apply bias  $V \simeq 85$   $\mu$ V to the thermometer, where at this position and at low temperatures  $S_{21,\text{bg}}(t)$  does not depend on the temperature unlike ZBA at  $V = 0$ . Second, we measure  $S_{21,\text{bg}}(t)$  at either above or below the resonance frequency  $f_0$ , as shown in Fig. 7.3. The measured transmission can be written as  $S_{21} = 20 \lg(v/\tilde{v})$  with  $v$  the output of the last stage amplifier and  $\tilde{v} = \sqrt{50 \Omega \times 1 \text{ mW}} \simeq 224$  mV. In order to obtain the noise of this expression in the linear regime we have  $\delta S_{21} = \frac{20}{\ln 10} \frac{\delta v}{v}$ . Since we have  $v = \tilde{v} 10^{\langle S_{21} \rangle / 20}$ , the rms values of the measured  $S_{21}$  under background measurement are

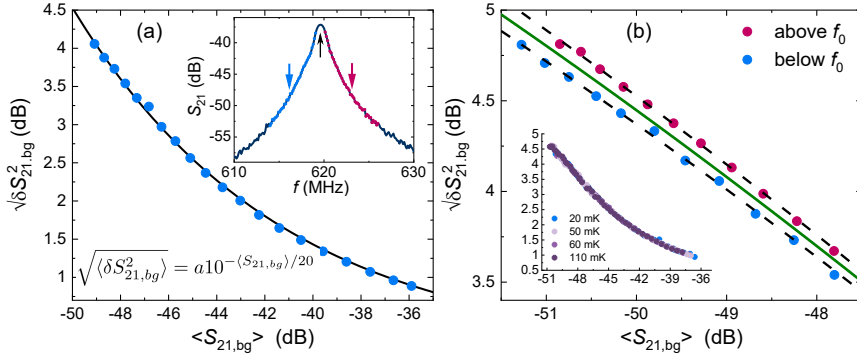


**Figure 7.3.** Measurements of the background noise. All the data presented here are taken at  $V = 85 \mu\text{V}$  (far away from the thermometer regime, ZBA, at  $V = 0$ ) where at low temperatures there is no  $T$  dependence, and at nonresonant frequencies, either below or above the resonance frequency  $f_0$  (presented in blue and red dots, respectively), to exclude the actual noise from the sample. Inset in (a) displays a typical measurement of  $S_{21}$  versus frequency  $f$ , where the position of  $f_0$  is pinpointed by upward-black arrow. The regions where the background measurement has been done are also shown by symbols and downward arrows.

(a) A parametric plot of the background noise measurements,  $\sqrt{\langle \delta S_{21,bg}^2 \rangle}$  versus  $\langle S_{21,bg} \rangle$  shown by blue dots, at frequencies below  $f_0$  down to 614 MHz. The black solid line demonstrates the predicted dependence of Eq. (7.10) with  $a = \frac{20}{\ln 10} \frac{\sqrt{\langle \delta v^2 \rangle}}{\bar{v}} = 0.0143$  as a fitting parameter. As explained in the text, the value then yields the noise temperature of the amplifier to be  $T_n = 4.9 \text{ K}$ . (b) The same background measurement as in (a) but now with data from both below and above  $f_0$  in the range of polynomial fitting which have been shown by black dashed lines. The average between the two dashed lines (green solid line) indicates the basis of subtraction for the measured data to exclude the true noise of the sample. The inset in (b) is the same measurement as in (a) but at different bath temperatures to prove that the background measurements do not depend on the temperature in this range.

given by

$$\sqrt{\langle \delta S_{21,\text{bg}}^2 \rangle} = \frac{20}{\ln 10} \frac{\sqrt{\langle \delta v^2 \rangle}}{\tilde{v}} 10^{\langle S_{21,\text{bg}} \rangle / 20}. \quad (7.10)$$

Figure 7.3 (a) presents the measurement of background noise  $\sqrt{\langle \delta S_{21,\text{bg}}^2 \rangle}$  as a function of  $\langle S_{21} \rangle$  at frequencies below  $f_0$ . The black solid line is from Eq. (7.10) that fits the experimental data with only one fitting parameter,  $\sqrt{\langle \delta v^2 \rangle}$ . One can use this fitting parameter for a sanity check of the performed measurement. Using 60 dB as a total gain of the amplifier chain, we obtain that the noise temperature of the amplifier is  $\sim 4.9$  K, which is in line with the given value by the manufacturer (Caltech CITLF2 cryogenic SiGe low-noise amplifier). Another check is presented in the inset of Fig. 7.3 (b) where the same measurements as in (a) are performed at different bath temperatures. All the measured data collapse and prove that there is no temperature dependence in the background measurements. The background measurements at frequencies both above and below the resonance (see Fig. 7.3 (b)) differ slightly from each other. This is because there is a weak dependence of the amplifier noise on frequency. Since at large attenuations,  $\delta S_{21}$  versus  $\delta v/v$  is not linear, the exponential dependence of Eq. (7.10) is not obeyed strictly. Therefore we resort to polynomial fits in two regimes, to capture the dependence over the full range. These polynomial fits to the data are shown by black dashed line in Fig. 7.3 (b). Therefore for the background noise we take the mean value between the two measurements as the reference which is shown by the green solid line. We thus assume that the frequency dependence of the noise is more or less smooth in the narrow range of  $\sim 10$  MHz around  $f_0$ , and interpolate the data accordingly.

### 7.2.2 Results on equilibrium fluctuations

In the previous subsection we explained how to determine the noise of interest from the actual sample  $\langle S_{21} \rangle$ . Since the responsivity here is given by  $\mathcal{R} \equiv d\langle S_{21} \rangle/dT$  and we have a linear calibration at low  $T$ , the temperature noise of the absorber is given by  $\langle \delta T^2(t) \rangle = \mathcal{R}^{-2} \langle S_{21}^2 \rangle$ . The quantity of interest while dealing with thermal detectors is the noise-equivalent temperature  $\text{NET}$ , i.e. the low-frequency temperature fluctuations  $\text{NET} \equiv \sqrt{S_T} = \sqrt{\langle \delta T^2(t) \rangle / (2\Delta f)}$ . This quantity for our normal-metal absorber in equilibrium after subtraction of the background noise is presented in Fig. 7.4 as a function of bath temperature. Next, the question is how to connect the result from the experimental data to the fundamental concepts of noise. We calculated above the low-frequency effective temperature fluctuations as  $S_T(0) = 2k_B T_0^2 / G_{\text{th}}$ . In a short glance one may guess that the contribution of  $G_{\text{th}}$  comes here only from the electron-phonon coupling,  $G_{\text{th}}^{(\text{ep})} = 5\sum V T_0^4$  (Section 3.2). Yet, the tendency of  $\text{NET}$  in Fig. 7.4(a) does not prove this claim at the lowest temperatures. This simply means

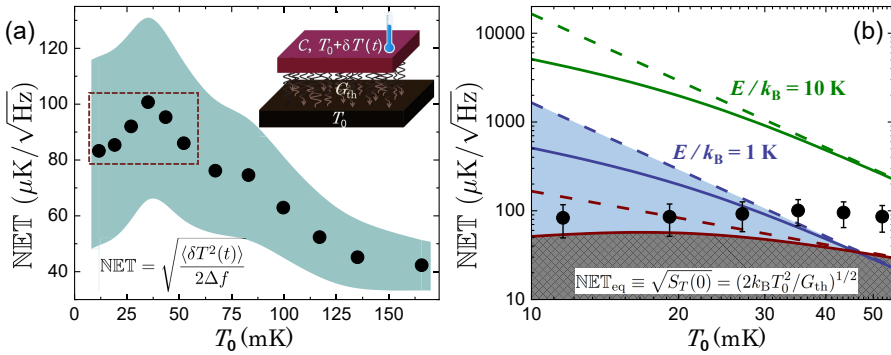


**Figure 7.4.** Equilibrium fluctuations. Measured low-frequency fluctuations in form of noise equivalent temperature  $\text{NET} \equiv \sqrt{S_T}$ , shown by black symbols in both panels (a) and (b) and obtained via the measurement of  $\langle \delta T^2(t) \rangle$  with  $\Delta f = 10 \text{ kHz}$ , as a function of bath temperature in (a). The data symbols correspond to the equilibrium noise of the sample where the mean background noise (green solid line in Fig. 7.3(b)) is subtracted. The shaded area demonstrates the uncertainty in the subtraction (the area between the two black dashed lines in Fig. 7.3(b)). (b) This panel shows the predicted noise-equivalent temperature  $\text{NET}$  in equilibrium for a normal-metal absorber under different conditions: with photon contribution from the environment ( $\alpha = 10^{-4}$ , solid lines) or without it ( $\alpha = 0$ , dashed lines). The symbols are the experimental ones in the dashed square in (a). The fundamental noise-equivalent temperature in equilibrium  $\text{NET}_{\text{eq}}$  under the experimental conditions is presented by red lines. The grey shaded area exhibits the prohibited area due to the fundamental temperature noise in equilibrium. The required  $\text{NET}$  of the detector to observe a photon with energy  $E$ , given by  $\text{NET} = E/\sqrt{C G_{\text{th}}}$ , is shown in this panel for two different energies. The parameters are  $\Sigma = 2 \times 10^9 \text{ WK}^{-5} \text{ m}^{-3}$  [10] and  $V = 10^{-21} \text{ m}^3$ .

that here we have other sources for the thermal conductance at lowest temperatures. The thermal conductance is then given by

$$G_{\text{th}} = 5\Sigma\mathcal{V}T_0^4 + \alpha g T_0. \quad (7.11)$$

The first term which has dominant contribution at higher temperatures arises from electron-phonon coupling and the second term is due to the radiative heat transfer by thermal photons [37], at the lowest temperatures. For the photonic contribution in the second term,  $\alpha$  denotes the coupling constant and according to previous experiments is  $\ll 1$  [12] for a circuit without engineered coupling to the external bath. Here,  $G_Q = gT_0$  is the quantum of the thermal conductance with  $g = \pi k_B^2/6\hbar$ . The NET based on Eq. (7.11) is then given by

$$\begin{aligned} \text{NET} &= \sqrt{\frac{2k_B}{5\Sigma\mathcal{V}}} T^{-1} \quad \text{for } T_0 \gg T_{\text{co}} \\ \text{NET} &= \sqrt{\frac{2k_B}{\alpha g}} T^{1/2} \quad \text{for } T_0 \ll T_{\text{co}}, \end{aligned} \quad (7.12)$$

where  $T_{\text{co}} = (\frac{\alpha g}{10\Sigma\mathcal{V}})^{1/3}$  is the cross-over temperature between the two regimes with maximum NET. The noise-equivalent temperature versus  $T_0$  for two cases, with (solid lines) and without (dashed lines) photonic contribution, for fundamental temperature fluctuations in equilibrium,  $\text{NET}_{\text{eq}} = \sqrt{2k_B T_0^2/G_{\text{th}}}$ , and the required  $\text{NET} = E/\sqrt{C G_{\text{th}}}$  for a photon with two different energies are presented in Fig. 7.4(b). We insert the experimental data below 50 mK from the panel (a) in this plot. The data are a little above the prohibited region determined by  $\text{NET}_{\text{eq}}$ . This demonstrates that with this setup we approached the bound of fundamental equilibrium fluctuations of temperature at  $T \lesssim 30$  mK. Since the fluctuations in the absorber temperature have a direct impact on the performance of thermal detectors like calorimeters and bolometers, and it determines the energy resolution of it, reaching this limit is important.

### 7.2.3 Discussion

In this section we want to summarize some central properties of the thermal detector that we investigated up to now.

**N versus N:** In the estimations and analysis that we have done, we assumed that the absorber is made of a normal metal. Strictly speaking this is not correct for our system. Since we are using SNS junction as a thermometer, the clean metal-to-metal contact induces proximity effect to the whole absorber at the lowest temperatures, which has direct influence on both the heat capacity and the thermal conductance. In Section 3.5 we pointed out that the heat capacity of a superconductor is smaller than that in a normal metal. For the proximitized normal metal the heat

capacity is reduced with respect to the pure normal one which enhances the sensitivity of our calorimeter. Moreover, on the scale of Thouless energy  $E_{\text{Th}} = \hbar D^2/\ell^2 \sim 10 \mu\text{eV}$ , the proximity effect suppresses the DOS around the Fermi level which then leads to decrease of the electron-phonon coupling [193, 194] and as a result increases  $\text{NET}$  at low frequencies. Here,  $D = 0.01 \text{ m}^2/\text{s}$  is the diffusion constant of the copper film. The energy resolution of a detector, as we discussed before, reads  $\delta\varepsilon = \sqrt{\mathcal{C}G_{\text{th}}S_T}$ . For a practical detector where  $S_T$  is coming from both the thermometer, its readout and the intrinsic temperature fluctuations, decreasing both the heat capacity and thermal conductance would improve the performance in terms of the energy resolution.

**Relaxation times:** Temperature is determined by a spatially uniform energy distribution of electrons in the absorber. We may assign a temperature for the absorber since there is a large number of carriers,  $\sim 10^8$ , in the  $\ell = 1 \mu\text{m}$  long copper strip. Second, electron-electron relaxation time ( $\sim 1 \text{ ns}$  [195]) is much faster than any other relaxation time including the electron-phonon time ( $\sim 1 \mu\text{s}$  [196]). These reasons lead to forming a local Fermi-Dirac distribution by carriers to which the temperature of the absorber is coded in. In addition, since the heat diffusion time in the absorber,  $\sim 0.1 \text{ ns}$ , is much faster than the electron-phonon time, the temperature of the absorber is well-defined and spatially uniform.

**Energy sensitivity:** An essential parameter is the energy resolution of the detector. THz detectors do exist, e.g. in [197, 198, 199, 49]. Our aim is to detect microwave photons which are in GHz regime. This range is common in most cQED and in general superconducting quantum circuit experiments. The blue and green lines in Fig. 7.4 (b) present the required  $\text{NET}$  for detecting microwave photons with energies  $E_1 = 1.0 \text{ K} \times k_{\text{B}}$  and  $E_1 = 10 \text{ K} \times k_{\text{B}}$ . These lines at sub 30 mK are well above the fundamental temperature fluctuations  $\text{NET}_{\text{eq}}$ . The experimental data, as explained above, is closely following the latter line of  $\text{NET}_{\text{eq}}$ . All this indicates the possibility of detecting such photons with our detector in this temperature range. In this panel the ratio  $\text{NET}/\text{NET}_{\text{eq}}$  gives the expected SNR of the experiment. For the microwave photon with energy  $E_1 = 1.0 \text{ K} \times k_{\text{B}}$ , we have  $\text{SNR} \sim 10$ , which gives a promising starting point. As a proof of concept we once more return to the main panel of Fig. 7.2 where we have a double photon absorption event with energies  $1.0 \text{ K} \times k_{\text{B}}$  and  $0.8 \text{ K} \times k_{\text{B}}$ . These energies can be emitted by e.g., a standard superconducting qubit or a multilevel system like maser [200, 201, 202, 203]. In the Fig. 7.2 the noise floor of temperature fluctuations due to the coupling of normal-metal absorber to the phonon bath, mimicking our detector, is about one order of magnitude smaller than the temperature jumps caused by the absorption of the mentioned photons.

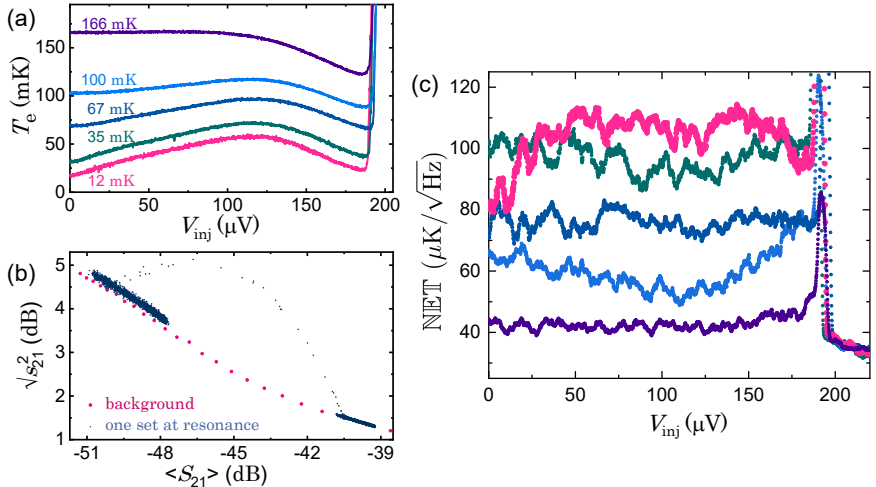


**Figure 7.5.** Nonequilibrium temperature fluctuations. (a) Average electronic temperature of the absorber as a function of applied voltage bias  $V_{\text{inj}}$  on the auxiliary junction. The written temperature above each curve refers to the fixed bath temperature  $T_0$ . (b) Parametric plot of  $\sqrt{\langle \delta S_{21}^2 \rangle}$  versus  $\langle S_{21} \rangle$  for one set of measurements at base temperature and at resonance frequency. Each black dot corresponds to one  $V_{\text{inj}}$  which is in the range of  $0 \leq V_{\text{inj}} \leq 3\Delta/e$ . Pink dots present the same data given in the main panel of Fig. 7.3 (b) of a background measurement. (c) Nonequilibrium temperature noise as a function of  $V_{\text{inj}}$  with the same colour code as in (a). The observed features are explained in the text.

#### 7.2.4 Results on nonequilibrium fluctuations

In this subsection we present nonequilibrium fluctuations of the effective temperature of the absorber. Up to now the measurements were performed in equilibrium meaning that the auxiliary NIS junction with tunnel resistance  $20 \text{ k}\Omega$  about  $950 \text{ nm}$  away from the clean contact (the lower junction in Fig. 4.7 (a)) was unbiased. Applying bias  $V_{\text{inj}}$  to this junction can drive the system to nonequilibrium. We have discussed earlier that biasing a NIS junction in both DC (simulation, Fig. 4.3(a)) and RF (Fig. 4.7(f)) setups, that can locally cool the normal metal acting as a refrigerator. The bias dependence of the average temperature of the absorber  $T$ , which is obtained from  $\langle S_{21} \rangle$  and converted to temperature with the help of calibration  $T$  versus  $\langle S_{21} \rangle$ , for a few different bath temperatures is presented in Fig. 7.5(a). Figure 7.5(b) demonstrates a parametric plot of  $\sqrt{\langle \delta S_{21}^2 \rangle}$  versus  $\langle S_{21} \rangle$  for one set at resonance frequency and base temperature, but with different injected voltage bias shown by black symbols. As a reference, the background measurement is shown by red circles, below the actual measurements at resonance. In a nonequilibrium process in this configuration, there are mainly two uncorrelated sources for heat current noise: (i) injecting hot electrons into the absorber  $S_Q^{(\text{inj})}$ , (ii) coupling to the phonon bath  $S_Q^{(\text{ep})} \equiv S_Q^{(\text{eq})} = 2k_B T_0^2 G_{\text{th}}$ . For the first contribution, injected

electrons change the average temperature of the absorber and due to the stochastic nature of tunneling they cause noise in heat current. In Subsection 4.1.1, we have discussed the heat current noise of a NIS junction at low frequency for tunneling (Eq. (4.14)) and presented it in Fig. 4.3 (b). In general, for  $n$  uncorrelated noise sources, the expression for temperature fluctuations is given by  $S_T = \sum_n S_Q^{(n)}/G_{\text{th}}$  which in this case can be written as  $S_T = (S_Q^{(\text{eq})} + S_Q^{(\text{inj})})/G_{\text{th}}$ .

The measurement of nonequilibrium effective temperature fluctuations as a function of applied injected voltage bias  $V_{\text{inj}}$  is displayed in Fig. 7.5(c). There are three different regimes that we can identify. First: in the subgap regime,  $V_{\text{inj}} \lesssim \Delta/e$  and at low temperatures, the equilibrium heat current noise due to the coupling to phonons is roughly constant whereas the one in tunneling is exponentially suppressed [204]. Since in this regime, the average temperature of the absorber does not change, the temperature fluctuations stay almost constant. There is an intriguing detail in the base temperature data at low values of  $V_{\text{inj}}$ . Unlike the data at bath temperatures  $T_0 \geq 35 \text{ mK}$ , the  $T_0 = 12 \text{ mK}$  data shows an initial increase from  $\text{NET} \simeq 80 \mu\text{K}/\sqrt{\text{Hz}}$  at  $V_{\text{inj}} = 0$  reaching  $\text{NET} \simeq 110 \mu\text{K}/\sqrt{\text{Hz}}$  at  $V_{\text{inj}} \simeq 50 \mu\text{V}$ . This feature, which clearly exceeds the noise level in the measurement is fully consistent with what is shown in Fig. 7.4(a) and Fig. 7.5(a). Namely due to the increase of equilibrium NET at  $T \lesssim 30 \text{ mK}$  (Fig. 7.4(a)) and the increase of  $T$  with increase of  $V_{\text{inj}}$  (Fig. 7.5(a)), this particular data set at  $T_0 = 12 \text{ mK}$  shows the increase that is accounted merely by the equilibrium noise. The rest of the data at higher temperatures in this regime do not show this feature simply because  $T_0$  exceeds the point of maximum NET at  $\sim 30 \text{ mK}$  for these sets. Second: existence of sharp peaks around the gap voltage,  $V \simeq \Delta/e$ . The real source of such feature is not quite clear for us. One can find a similarity between these measured peaks with the theoretical prediction e.g., in Ref. [205] for the bias dependence of thermal current fluctuations at the gap in a SINIS structure. Since the cooling takes place in this regime (Fig. 7.5(a)), an alternative explanation for this feature is the existence of voltage noise which directly transforms to temperature noise due to the strong voltage dependence of temperature. Third: above the gap,  $V > \Delta/e$ , there is a sudden decrease of temperature fluctuations NET (see Fig. 7.5(c)), where all the measured traces collapse on each other. As seen in Fig. 7.5(a), injecting a lot of hot electrons in the normal-metal absorber at voltages above the gap, leads to a sudden increase in temperature. This in turn translates into increased  $G_{\text{th}}$ , and as a result the temperature noise decreases.

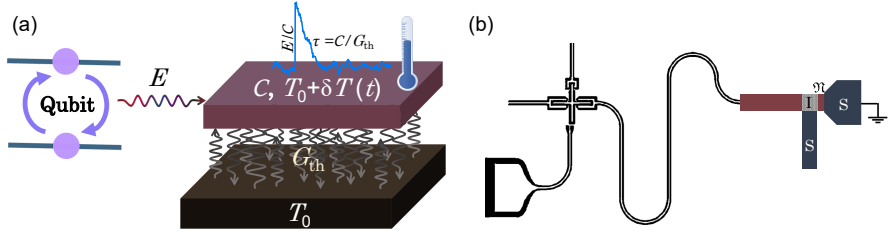


**Figure 7.6.** Two-level system (qubit) coupled to an absorber which is connected to a heat bath at fixed temperature  $T_0$ . Qubit relaxes to its ground state and as a result it emits a photon with energy  $E$  to the absorber. The temperature change in the absorber in form of instantaneous temperature rise and subsequent decay (shown by blue line) can be monitored with a fast thermometer. (b) A physical realization of the experiment for the setup shown in (a). A transmon type superconducting qubit, the cross shaped structure on the left, is capacitively coupled to the meander-shaped coplanar wave resonator in the middle. The resonator at its other end is terminated by a normal-metal resistor acting as the absorber. The fast thermometer (SQUID structure) monitors the instantaneous temperature change in the absorber.

### 7.3 Proposal of microwave photon detection

Up to now we demonstrated experimentally that temperature fluctuations in our calorimeter are close to the fundamental fluctuation limit at low frequencies, and under these conditions, with ideal detection, it is expected to be capable of detecting an absorption event with energy  $\sim 1 \text{ K} \times k_B$ , which is in the range of a photon emitted by e.g. a standard superconducting qubit. In this section we propose coupling such a qubit to the calorimeter as schematically shown in Fig. 7.6(a). The level separation of qubit is  $\hbar\omega_Q$  and in our model the absorber is formed of  $N$  oscillators with energy of the  $j$ :th oscillator equal to  $\hbar\omega_j$ . For simplicity we assume here that the qubit is coupled directly to the oscillator  $j$  with coupling strength  $\gamma_j$ . The total Hamiltonian then reads  $\hat{\mathcal{H}} = \hbar\omega_Q \hat{a}^\dagger \hat{a} + \sum_{i=1}^N \hbar\omega_i \hat{b}_i^\dagger \hat{b}_i + \sum_{i=1}^N \gamma_i (\hat{a}^\dagger \hat{b}_i + \hat{a} \hat{b}_i^\dagger)$ , where  $\hat{a} = |g\rangle \langle e|$  for the qubit with eigenstates  $|g\rangle$  (ground) and  $|e\rangle$  (excited) and  $\hat{b}_i^\dagger$  ( $\hat{b}_i$ ) is the creation (annihilation) operators of the oscillators in the bath. The way we solve the decay of the qubit to the oscillator bath is similar to the one explained in Section 5.3 for qubit-resonator-oscillator bath system. In this case, the set of equations representing Schrödinger equation, are

$$\begin{aligned} i\hbar \dot{\mathcal{C}}_0(t) &= \sum_{j=1}^N \gamma_j e^{i(\Omega-\omega_j)t} \mathcal{C}_j(t) \\ i\hbar \dot{\mathcal{C}}_i(t) &= \gamma_i e^{-i(\Omega-\omega_i)t} \mathcal{C}_0(t). \end{aligned} \quad (7.13)$$

where  $|\mathcal{C}_0(t)|^2$  denotes the population of the qubit, and  $|\mathcal{C}_j(t)|^2$  for the bath oscillator  $j$ . Although based on the simulations and analysis, detecting a single microwave photon event with said energies in a continuous manner is possible, we aim to present a way to boost the SNR for detecting

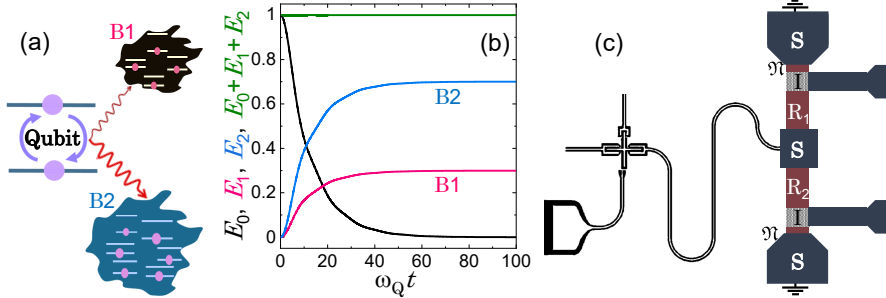


**Figure 7.7.** Splitting the qubit-emitted energy  $\hbar\omega_Q$  into two heat baths (absorbers). (a) The principle of the process. The two absorbers on the right are assumed to be at zero temperature. (b) Results of solutions of the Schrödinger equation of the decay process in (a) with chosen parameters as a function of normalized time  $\omega_Q t$ . Here the number of oscillators in B1 is  $N_1 = 3 \times 10^5$  and in B2,  $N_2 = 7 \times 10^5$ . The decay rate of the qubit to two baths is  $0.084\omega_Q$ . (c) A physical realization of the experiment in a superconducting qubit setup. The x-shaped transmon qubit on the left which can be excited by a flux or gate pulse is coupled capacitively to a coplanar wave resonator. At the other end this  $\lambda/4$  resonator is terminated by the parallel connection of two resistors that serve as thermally uncoupled absorbers. The temperatures of the two resistors are measured by fast thermometers simultaneously. Cross-correlation measurement of the two boosts the SNR of detection.

low energy photons. The practical way to realize the detector described here is to employ circuit quantum electrodynamics techniques combined with calorimeters based on on-chip resistors monitored by tunnel junction thermometers as detailed above. A possible design is shown in Fig. 7.6(b). A transmon-type qubit is formed of a split Josephson junction forming a flux-controllable SQUID. Alternatively, a transmon can be controlled by gate voltage. The purpose of this control is to initialize the qubit to the desired state. The qubit itself is coupled to a harmonic oscillator which is formed of a superconducting coplanar wave resonator, whose resonance frequency is determined by its length. If the coupling between the two is capacitive, it is favorable to employ a quarter wavelength resonator which has current maximum at one end terminated by the resistive bath. In what follows we propose splitting a quantum to uncoupled baths. As schematically shown in Fig. 7.7(a), in theory we split the  $N$  bath oscillators to two baths such that  $N_1$  of them are in bath B1 and the  $N_2 = N - N_1$  in B2. In this case the time evolution of the oscillators in two uncoupled baths is again governed by Eqs. (7.13) and the energies of the baths at time  $t$  are  $E_1 = \sum_{k=1}^{N_1} \hbar\omega_k |\mathcal{C}_k(t)|^2$  and  $E_2 = \sum_{k=N_1+1}^N \hbar\omega_k |\mathcal{C}_k(t)|^2$ . Figure 7.7(b) presents numerical simulations of decaying qubit (black line) to two baths and as a result rising energies in both of them. These energies are associated with the initial temperature of each bath and they can be measured simultaneously with proper thermometers [46]. Here, as earlier, we assume that the response time of the thermometers is slower than the energy release of the qubit to each bath and faster than the energy release rate to the phonon bath. Such a time-window exists based on our measurement

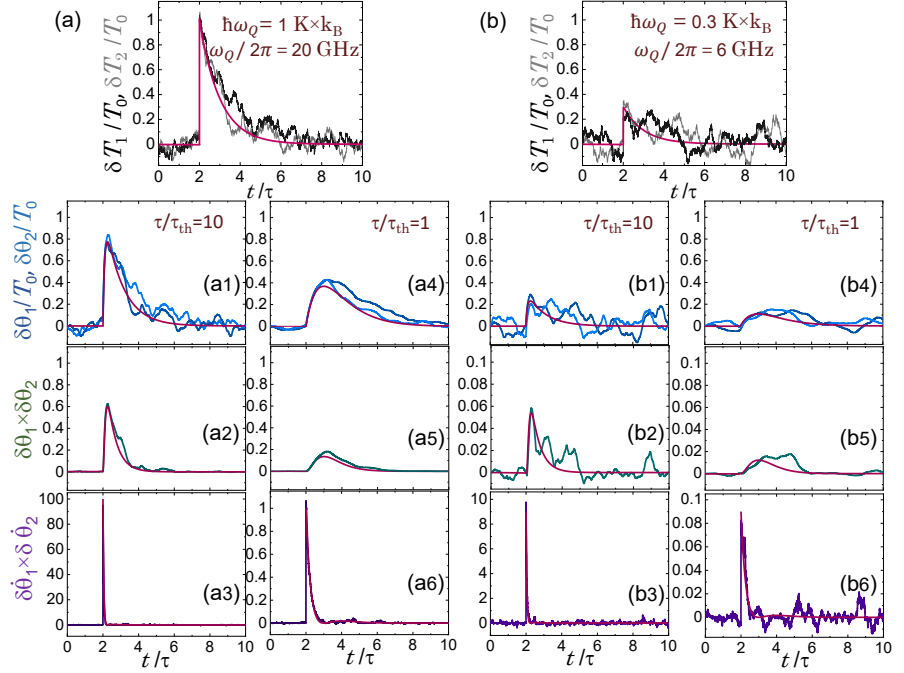


**Figure 7.8.** Predicted results of a cross-correlation measurement. Temperature histories of the two nominally identical resistors while the energy  $\hbar\omega_Q$  with  $\omega_Q/2\pi = 20$  GHz is absorbed at  $t = 2\tau$ . The black and grey lines are the results of stochastic simulations for the actual temperatures whereas the red line is the temperature trace of each absorber when ignoring the thermal noise. (a1)-(a3) show the simulated traces when the thermometer bandwidth is given by  $\tau/\tau_{\text{th}} = 10$ . (a1) displays the two temperatures traces  $\theta_i$ . (a2) and (a3) demonstrate two types of cross-correlation measurements  $\theta_1(t)\theta_2(t)$  and  $\dot{\theta}_1(t)\dot{\theta}_2(t)$ , respectively. The red lines again show the analytical prediction of the temperature trace while omitting the thermal noise. (a4)-(a6) are as (a1)-(a3) but now with a slower thermometer:  $\tau/\tau_{\text{th}} = 1$ . (b) and (b1)-(b6) are as (a) and (a1)-(a6) but with  $\omega_Q/2\pi = 6$  GHz.

technique. The decay rate of the qubit state, i.e., the relaxation rate, is determined by the coupling strength of the transmon to the resonator, their mutual detuning, and the quality factor of the resonator determined by the resistive load  $R$ . The qubit decays over a time given by  $\mathcal{Q}/\omega_Q$ , which is typically of the order of tens or hundreds of nano-seconds. Here,  $\mathcal{Q}$  is the quality factor of the resonator. This relaxation rate is much faster than that from the absorber to the phonon bath which is typically  $10 - 100 \mu\text{s}$  at low temperatures. There are two obvious ways to embed the two resistors (absorbers) at the end of the resonator, either in series or parallel. Only the parallel case is depicted in Fig. 7.7(c). Since the two baths are thermally isolated from each other (provided by the existence of superconductor in between and being at low temperatures) their temperature noises are likely to be uncorrelated which gives the possibility to boost the **SNR** by such a cross-correlation measurement. We use again the Langevin equation (Eq. (7.1)) for the symmetric case  $R_1 = R_2$  to produce numerically and analytically the two temperature traces with uncorrelated noises. As an example we monitor the relative temperature response of each bath  $\theta_i$  for the absorption of a photon with energy  $1 \text{ K} \times k_B$  for Fig. 7.8(a) and  $0.3 \text{ K} \times k_B$  in panel 7.8(b). The measured temperature of the bath  $\theta_i(t)$ , apart from noise, is then given by

$$\theta_i(t) = \Delta T_i \frac{\tau}{\tau - \tau_{\text{th}}} (e^{-t/\tau} - e^{-t/\tau_{\text{th}}}), \quad (7.14)$$

where  $\Delta T_i = \hbar\omega_Q/\mathcal{C}_i$ . Usually with fast thermometers with short response time  $\tau_{\text{th}} = 0.01\tau$ , with  $\tau = \mathcal{C}/G_{\text{th}}$  denoting the electron-phonon time constant, it is sufficient to detect  $1 \text{ K} \times k_B$  photon directly with reasonable **SNR** in the absence of instrumental noise. But most of the time, this is not the case. By applying the cross-correlation technique [46, 206] either taking the product  $\theta_1(t)\theta_2(t)$  or the product of the derivatives  $\dot{\theta}_1(t)\dot{\theta}_2(t)$  are given by

$$\langle \theta_1(t)\theta_2(t) \rangle = \Delta T_0^2 \left( \frac{\tau}{\tau - \tau_{\text{th}}} \right)^2 (e^{-2t/\tau} + e^{-2t/\tau_{\text{th}}} - 2e^{-(1/\tau+1/\tau_{\text{th}})t}) \quad (7.15)$$

$$\langle \dot{\theta}_1(t)\dot{\theta}_2(t) \rangle = \Delta T_0^2 \left( \frac{\tau}{\tau - \tau_{\text{th}}} \right)^2 \left( \frac{\tau^2}{\tau_{\text{th}}^2} e^{-2t/\tau_{\text{th}}} + e^{-2t/\tau} - 2\frac{\tau}{\tau_{\text{th}}} e^{-(1/\tau+1/\tau_{\text{th}})t} \right),$$

in the absence of noise. In the special case of  $\tau/\tau_{\text{th}} = 1$  the solutions for  $\theta_i(t)$  and  $\dot{\theta}_i(t)$  are given by

$$\theta_i = \Delta T_i \frac{t}{\tau} e^{-t/\tau} \text{ and } \dot{\theta}_i(t) = \Delta T_i \left( 1 - \frac{t}{\tau} \right) e^{-t/\tau}. \quad (7.16)$$

As a result we then have  $\langle \theta_1(t)\theta_2(t) \rangle = \Delta T_0^2 \frac{t^2}{\tau^2} e^{-2t/\tau}$  and  $\langle \dot{\theta}_1(t)\dot{\theta}_2(t) \rangle = \Delta T_0^2 \left( 1 - \frac{t}{\tau} \right)^2 e^{-2t/\tau}$ . With this method, the **SNR** will improve significantly as seen in Fig. 7.8 and one can try to meet more challenging conditions. In panels 7.8(ai) and 7.8(bi), for  $i = 1 - 6$ , we show the results for  $\tau/\tau_{\text{th}} = 10$  and  $\tau/\tau_{\text{th}} = 1$ , respectively, along with the analytical results shown by

the red lines. Based on panel 7.8(b6) one can easily see that with slower response time ( $\tau = \tau_{\text{th}}$ ) and lower energy of a photon it is quite impossible to detect  $0.3 \text{ K} \times k_{\text{B}}$  with a single thermometer. Yet the cross-correlation technique, in particular the  $\dot{\theta}_1(t)\dot{\theta}_2(t)$  method, would allow one to detect the photon with good SNR under these conditions as well.



## 8. Summary and outlook

This thesis presented experimental and theoretical results on a largely uncharted area of research, quantum thermodynamics on a chip, which we coined as circuit quantum thermodynamics (cQTD). It describes phenomena and devices which map the open quantum systems physics into concrete macroscopic quantum circuits, in our case made of superconductors, typically qubits and cavities, coupled to heat baths formed of nearly free electron mesoscopic conductors and phonons on the chip.

The main achievements in the thesis are both theoretical and experimental, in some places combining the two interests. The opening work for me was the introduction and theoretical description of a quantum Otto refrigerator formed of a superconducting qubit coupled via different cavities (resonators) to the cold and hot heat baths. It demonstrated the feasibility of such a device on a chip with significant cooling power and efficiency, but it also brought up the concepts of classical and quantum components of heat in different operation regimes. In particular, at higher operation frequencies the qubit dynamics becomes coherent with non-classical contributions in the measurable quantities.

The work on a quantum Otto refrigerator opened a wealth of activities in our research group as well as elsewhere. Soon after it, experiments on a structure like the Otto refrigerator were initiated. Experimental facilities to measure quasi-static properties of quantum heat transport via a qubit were readily available. A quantum heat valve was demonstrated experimentally on which some of the theoretical results of the work on Otto refrigerator were directly applicable. We modelled the heat valve based on these results explaining the Lorentzian filtering of the heat current under the resonance conditions when the qubit and the two nominally identical qubits have equal level spacing. It came as a surprise that this result applied only for some of the experiments, namely those with a low quality factor of the cavities. This led us to think of the setup from another angle. Namely, with a higher quality factor of the resonator the quantum system is not the qubit alone, but the cavities together with the qubit form a joint multi-level system interacting with the bare heat baths. This is the

conventional situation in superconducting quantum information circuits (circuit quantum electrodynamic circuits, cQED), where the quality factors are still ways higher than in cQTD due to the absence of engineered heat baths. Our theoretical achievement in this work was the successful analysis of the system in the two different regimes, which we associate to the discussion of local and global regimes in quantum thermodynamics.

Moving forward, we realized in the group a circuit with a transmon qubit and two resonators with mutually different frequencies, both terminated by a heat bath. It is already a candidate for the realization of the Otto refrigerator. Thanks to the asymmetry in this structure, it provides, under steady biasing conditions, a way to realize a heat diode, a rectifier, where the reciprocity of heat transport is not valid. In conjunction with an experiment in our group we developed models of heat rectification in these circuits and analyzed how to maximize the rectification effect.

My main achievements in the second half of the thesis were within the investigation of the noise of heat current and in an experimental realization of a quantum calorimeter. In this experiment the fundamental level of effective temperature noise could be observed and analyzed from the point of view of the ultimate energy resolution of a quantum calorimeter. Developing and applying an optimized thermometer based on proximity supercurrent in a tunnel junction (“ZBA thermometer”) as the readout device for the temperature of the calorimeter, we managed to measure low electron temperatures with minimal self-heating and back-action on the calorimeter itself. At temperatures in the range 30 mK and below, the thermal noise was shown to be low enough for resolving an energy impact from a single microwave photon emitted by a superconducting qubit. After this experimental milestone, I focused in my thesis on having theoretically a closer look on the decay process of a qubit to a heat bath and how with this understanding we can further improve the energy resolution of a calorimeter. We combined the quantum trajectory analysis with a heat bath where energy is exchanged randomly at a finite temperature with a phonon superbath and constructed stochastic temperature histories simulating an absorption process: this work confirmed our earlier conclusions on the energy resolution of such a calorimeter in the low temperature regime. Further, we analyzed the qubit and the heat bath system by forming the bath of bosonic oscillators and solving the Schrödinger equation numerically in time for the whole system under realistic experimental conditions. This work led us to propose a “photon splitting” scheme, where via a cross-correlation measurement one expects to enhance the signal-to-noise ratio significantly in detecting small quanta of energy, even with a slow detector. The final part of this thesis was devoted to quantum noise of heat, where, again forming the resistors out of oscillator baths, we could address in a straightforward way not only the average heat current but also its noise at arbitrary frequencies. An important ingredient in these

last theoretical works was making the one-to-one connection between the abstract model and the actual circuit parameters and elements.

The two directions conceived and worked out in my thesis pave ways for next steps in quantum thermodynamics on superconducting circuits. Concerning the quantum refrigerator, realizing an Otto cycle experimentally using either a charge qubit or a flux qubit looks more than feasible in the nearest future [207, 208]. The advantage of the first option here is that control of the qubits can be achieved by gate voltages instead of local magnetic fields, which reduces the risk of producing parasitic dissipation on the chip, when large control currents can be avoided. The advantage of flux qubits would be to go beyond the weak coupling regime that has been investigated up to now. Once realized in one form or the other, a cyclic (Otto) refrigerator would be a test bed of many interesting phenomena. These include the questions of whether the quantum coherences are always harmful in operating the devices, i.e. is it that quantum friction should be avoided, and what is the power of the refrigerator at high frequencies beyond the classical operation regime. A very important question is whether one can in practice improve the operation in terms of cooling power and efficiency by special driving protocols, avoiding the said coherences. Also concepts of heat engines instead of refrigerators are largely missing even in theoretical literature. How could one realize that in the superconducting qubit plus cavity setup? One more interesting question is whether one could harness thermal fluctuations as the source of work in these devices, which would then make them into quantum absorption refrigerators: this question relates to both parts of my thesis.

The future interest of quantum heat transport, heat noise and in particular ultrasensitive calorimeters is both in basic science but also in applications. Not going into detail of the latter, we just emphasize that a single quantum is the elementary content of information in a quantum circuit. Thus, being able to detect it in a continuous manner would make a difference. The intriguing questions of quantum heat transport and noise, with many theoretical results presented in this thesis, are largely unexplored experimentally till now. There is a hierarchy of experiments on quantum heat current, where we are just moving from the first to the second level. The first level is measuring the mean heat current, composed of averaging an impact of millions of microwave photons on the absorber, as done in many of the experiments presented. The next step is the measurement of the noise of heat current: in the present thesis it was done for equilibrium phonons impacting the electrons in a calorimeter, but experiments on the noise produced by a quantum system mediating the heat current are still missing. The final level of these experiments is the detection of individual quanta as largely discussed in this thesis. It would lead to the understanding of quantum heat transport on the finest level, quantum by quantum. In particular it would lead to a new

research area, even a research field in circuits, namely stochastic quantum thermodynamics.

# References

- [1] H.-P. Breuer and F. Petruccione. *The theory of open quantum systems*. Oxford University Press, 2002.
- [2] Jukka P. Pekola. Towards quantum thermodynamics in electronic circuits. *Nature Phys.*, 11:118–123, 2015.
- [3] F. Binder, L.A. Correa, C. Gogolin, J. Anders, and G. Adesso, editors. *Thermodynamics in the quantum regime, fundamental aspects and new directions*. 1999195195. Springer International Publishing, 2018.
- [4] Jukka P. Pekola. Quantum thermodynamics at low temperatures. *Europhysics News*, 52(3):15–17, 2021.
- [5] Sebastian Deffner and Steve Campbell. *Quantum Thermodynamics*. 2053–2571. Morgan and Claypool Publishers, 2019.
- [6] M. L. Roukes, M. R. Freeman, R. S. Germain, R. C. Richardson, and M. B. Ketchen. Hot electrons and energy transport in metals at millikelvin temperatures. *Phys. Rev. Lett.*, 55:422–425, Jul 1985.
- [7] F. C. Wellstood, C. Urbina, and John Clarke. Hot-electron effects in metals. *Phys. Rev. B*, 49:5942–5955, Mar 1994.
- [8] V. F. Gantmakher. The experimental study of electron-phonon scattering in metals. *Rep. Prog. Phys.*, 37(3):317, 1974.
- [9] K. Schwab, E. A. Henriksen, J. M. Worlock, and M. L. Roukes. Measurement of the quantum of thermal conductance. *Nature*, 404:974–977, April 2000.
- [10] L. B. Wang, O.-P. Saira, D. S. Golubev, and J. P. Pekola. Crossover between electron-phonon and boundary-resistance limits to thermal relaxation in copper films. *Phys. Rev. Applied*, 12:024051, Aug 2019.
- [11] Matthias Meschke, Wiebke Guichard, and Jukka P. Pekola. Single-mode heat conduction by photons. *Nature*, 444:187–190, 2006.
- [12] Andrey V. Timofeev, Meri Helle, Matthias Meschke, Mikko Möttönen, and Jukka P. Pekola. Electronic refrigeration at the quantum limit. *Phys. Rev. Lett.*, 102:200801, May 2009.
- [13] M. Partanen, K. Y. Tan, J. Govenius, R. E. Lake, M. K. Mäkelä, T. Tanttu, and M. Möttönen. Quantum-limited heat conduction over macroscopic distances. *Nat. Phys.*, 12:460, 2016.
- [14] Kuan Yen Tan, Matti Partanen, Russell E. Lake, Joonas Govenius, Shumpei Masuda, and Mikko Möttönen. Quantum-circuit refrigerator. *Nat. Commun.*, 8:15189, 2017.

- [15] R. N. Simons. *Coplanar Waveguide Circuits, Components and Systems, Wiley Series in Microwave and Optical Engineering*. Wiley InterScience, New York, 2001.
- [16] M. G  ppla, A. Fragner, M. Baur, R. Bianchetti, S. Filipp, J. M. Fink, P. J. Leek, G. Puebla, L. Steffen, and A. Wallraff. Coplanar waveguide resonators for circuit quantum electrodynamics. *J. Appl. Phys.*, 104:113904, 2008.
- [17] D. M. Pozar. *Microwave Engineering*. John Wiley and Sons, New York, 2011.
- [18] Ani Nersisyan, Stefano Poletto, Nasser Alidoust, Riccardo Manenti, Russ Renzas, Cat-Vu Bui, Kim Vu, Tyler Whyland, Yuvraj Mohan, Eyob A. Sete, Sam Stanwyck, Andrew Bestwick, and Matthew Reagor. Manufacturing low dissipation superconducting quantum processors. In *2019 IEEE International Electron Devices Meeting (IEDM)*, pages 31.1.1–31.1.4, 2019.
- [19] C. R. H. McRae, H. Wang, J. Gao, M. R. Vissers, T. Brecht, A. Dunsworth, D. P. Pappas, and J. Mutus. Materials loss measurements using superconducting microwave resonators. *Rev. Sci. Instrum.*, 91:091101, 2020.
- [20] B. D. Josephson. Possible new effects in superconductive tunnelling. *Physics Letters*, 1(7):251–253, 1962.
- [21] B. D. Josephson. The discovery of tunnelling supercurrents. *Rev. Mod. Phys.*, 46:251–254, Apr 1974.
- [22] Michael Tinkham. *Introduction to Superconductivity*. Dover Publications, 2nd edition edition, 2004.
- [23] R. C. Jaklevic, John Lambe, A. H. Silver, and J. E. Mercereau. Quantum interference effects in josephson tunneling. *Phys. Rev. Lett.*, 12:159–160, Feb 1964.
- [24] Jens Koch, Terri M. Yu, Jay Gambetta, A. A. Houck, D. I. Schuster, J. Majer, Alexandre Blais, M. H. Devoret, S. M. Girvin, and R. J. Schoelkopf. Charge-insensitive qubit design derived from the cooper pair box. *Phys. Rev. A*, 76:042319, Oct 2007.
- [25] E. Paladino, Y. M. Galperin, G. Falci, and B. L. Altshuler.  $1/f$  noise: Implications for solid-state quantum information. *Rev. Mod. Phys.*, 86:361–418, Apr 2014.
- [26] Ryogo Kubo. Statistical-mechanical theory of irreversible processes. i. general theory and simple applications to magnetic and conduction problems. *J. Phys. Soc. Jpn.*, 12:570–586, 1957.
- [27] Herbert B. Callen and Theodore A. Welton. Irreversibility and generalized noise. *Phys. Rev.*, 83:34–40, Jul 1951.
- [28] N. W. Ashcroft and N. David Mermin. *Solid State Physics*. Holt, Rinehart and Winston, New York, 1976.
- [29] Dmitri V. Averin and Jukka P. Pekola. Violation of the fluctuation-dissipation theorem in time-dependent mesoscopic heat transport. *Phys. Rev. Lett.*, 104:220601, Jun 2010.
- [30] Fei Zhan, Sergey Denisov, and Peter H  nggi. Electronic heat transport across a molecular wire: Power spectrum of heat fluctuations. *Phys. Rev. B*, 84:195117, Nov 2011.
- [31] Danilo Sergi. Energy transport and fluctuations in small conductors. *Phys. Rev. B*, 83:033401, Jan 2011.

- [32] A. N. Cleland. *Foundations of Nanomechanics: From Solid-State Theory to Device Applications*. Springer, New York, 2003.
- [33] A. L. Fetter and J. D. Walecka. *Quantum Theory of Many-Particles Systems*. McGraw-Hill, San Francisco, 1971.
- [34] D. Golubev and L. Kuzmin. Nonequilibrium theory of a hot-electron bolometer with normal metal-insulator-superconductor tunnel junction. *J. Appl. Phys.*, 89:6464, 2001.
- [35] J. B. Johnson. Thermal agitation of electricity in conductors. *Phys. Rev.*, 32:97–109, Jul 1928.
- [36] H. Nyquist. Thermal agitation of electric charge in conductors. *Phys. Rev.*, 32:110–113, Jul 1928.
- [37] D. R. Schmidt, R. J. Schoelkopf, and A. N. Cleland. Photon-mediated thermal relaxation of electrons in nanostructures. *Phys. Rev. Lett.*, 93:045901, Jul 2004.
- [38] J. Pendry. Quantum limits to the flow of information and entropy. *Journal of Physics A*, 16:2161–2171, 1983.
- [39] L. M. A. Pascal, H. Courtois, and F. W. J. Hekking. Circuit approach to photonic heat transport. *Phys. Rev. B*, 83:125113, Mar 2011.
- [40] George Thomas, Jukka P. Pekola, and Dmitry S. Golubev. Photonic heat transport across a josephson junction. *Phys. Rev. B*, 100:094508, Sep 2019.
- [41] A.O Caldeira and A.J Leggett. Quantum tunnelling in a dissipative system. *Annals of Physics*, 149(2):374–456, 1983.
- [42] Ulrich Weiss. *Quantum dissipative systems, Series in Modern Condensed Matter Physics, Vol. 10*. World Scientific, 2001.
- [43] Rosario Fazio, F. W. J. Hekking, and D. E. Khmelnitskii. Anomalous thermal transport in quantum wires. *Phys. Rev. Lett.*, 80:5611–5614, Jun 1998.
- [44] S. P. Langley. The bolometer. *Nature*, 57:620, 1898.
- [45] P. L. Richards. Bolometers for infrared and millimeter waves. *Journal of Applied Physics*, 76(1):1–24, 1994.
- [46] M.L. Roukes. Yoctocalorimetry: phonon counting in nanostructures. *Physica B: Condensed Matter*, 263–264:1–15, 1999.
- [47] J. Govenius, R. E. Lake, K. Y. Tan, and M. Möttönen. Detection of zepto-joule microwave pulses using electrothermal feedback in proximity-induced josephson junctions. *Phys. Rev. Lett.*, 117:030802, Jul 2016.
- [48] S. Kempf, A. Fleischmann, L. Gastaldo, and C. Enss. Physics and applications of metallic magnetic calorimeters. *J. Low Temp. Phys.*, 193:365–379, 2018.
- [49] S. Lara-Avila, A. Danilov, D. Golubev, H. He, K. H. Kim, R. Yakimova, F. Lombardi, T. Bauch, S. Cherednichenko, and S. Kubatkin. Towards quantum-limited coherent detection of terahertz waves in charge-neutral graphene. *Nat. Astron.*, 3:983–988, 2019.
- [50] Gil-Ho Lee, Dmitri K. Efetov, Woochan Jung, Leonardo Ranzani, Evan D. Walsh, Thomas A. Ohki, Takashi Taniguchi, Kenji Watanabe, Philip Kim, Dirk Englund, and Kin Chung Fong. Graphene-based josephson junction microwave bolometer. *Nature*, 586:42–46, 2020.

- [51] Roope Kokkoniemi, Joonas Govenius, Visa Vesterinen, Russell E. Lake, András M. Gunyhó, Kuan Y. Tan, Slawomir Simbierowicz, Leif Grönberg, Janne Lehtinen, Mika Prunnila, Juha Hassel, Antti Lamminen, Olli-Pentti Saira, and Mikko Möttönen. Nanobolometer with ultralow noise equivalent power. *Commun. Phys.*, 2:124, 2019.
- [52] L. S. Kuzmin, A. L. Pankratov, A. V. Gordeeva, V. O. Zbrozhek, V. A. Shamporov, L. S. Revin, A. V. Blagodatkin, S. Masi, and P. de Bernardis. Photon-noise-limited cold-electron bolometer based on strong electron self-cooling for high-performance cosmology missions. *Commun. Phys.*, 2:104, 2019.
- [53] R. Kokkoniemi, J.-P. Girard, D. Hazra, A. Laitinen, J. Govenius, R. E. Lake, I. Sallinen, V. Vesterinen, M. Partanen, J. Y. Tan, K. W. Chan, K. Y. Tan, P. Hakonen, and M. Möttönen. Bolometer operating at the threshold for circuit quantum electrodynamics. *Nature*, 586:47, 2020.
- [54] E. M. Lifshitz and L. P. Pitaevskii. *Statistical physics, Part I*. Pergamon Press, third edition, 1980.
- [55] J. Bardeen, L. N. Cooper, and J. R. Schrieffer. Theory of superconductivity. *Phys. Rev.*, 108:1175–1204, Dec 1957.
- [56] O. V. Lounasmaa. *Experimental Principles and Methods below 1 K*. Academic Press, London, 1974.
- [57] M. Nahum and John M. Martinis. Ultrasensitive-hot-electron microbolometer. *Applied Physics Letters*, 63(22):3075–3077, 1993.
- [58] M. Nahum, T. M. Eiles, and John M. Martinis. Electronic microrefrigerator based on a normal-insulator-superconductor tunnel junction. *Applied Physics Letters*, 65(24):3123–3125, 1994.
- [59] Francesco Giazotto, Tero T. Heikkilä, Artu Luukanen, Alexander M. Savin, and Jukka P. Pekola. Opportunities for mesoscopics in thermometry and refrigeration: Physics and applications. *Rev. Mod. Phys.*, 78:217–274, Mar 2006.
- [60] A. V. Feshchenko, L. Casparis, I. M. Khaymovich, D. Maradan, O.-P. Saira, M. Palma, M. Meschke, J. P. Pekola, and D. M. Zumbühl. Tunnel-junction thermometry down to millikelvin temperatures. *Phys. Rev. Applied*, 4:034001, Sep 2015.
- [61] R. C. Dynes, V. Narayanamurti, and J. P. Garno. Direct measurement of quasiparticle-lifetime broadening in a strong-coupled superconductor. *Phys. Rev. Lett.*, 41:1509–1512, Nov 1978.
- [62] R. C. Dynes, J. P. Garno, G. B. Hertel, and T. P. Orlando. Tunneling study of superconductivity near the metal-insulator transition. *Phys. Rev. Lett.*, 53:2437–2440, Dec 1984.
- [63] K Gloos, P J Koppinen, and J P Pekola. Properties of native ultrathin aluminium oxide tunnel barriers. *Journal of Physics: Condensed Matter*, 15(10):1733–1746, mar 2003.
- [64] Dmitri V. Averin and Jukka P. Pekola. Nonadiabatic charge pumping in a hybrid single-electron transistor. *Phys. Rev. Lett.*, 101:066801, Aug 2008.
- [65] T. Aref, V. F. Maisi, M. V. Gustafsson, P. Delsing, and J. P. Pekola. Andreev tunneling in charge pumping with SINIS turnstiles. *EPL (Europhysics Letters)*, 96(3):37008, oct 2011.

- [66] Tine Greibe, Markku P. V. Stenberg, C. M. Wilson, Thilo Bauch, Vitaly S. Shumeiko, and Per Delsing. Are “pinholes” the cause of excess current in superconducting tunnel junctions? a study of andreev current in highly resistive junctions. *Phys. Rev. Lett.*, 106:097001, Feb 2011.
- [67] V. F. Maisi, O.-P. Saira, Yu. A. Pashkin, J. S. Tsai, D. V. Averin, and J. P. Pekola. Real-time observation of discrete andreev tunneling events. *Phys. Rev. Lett.*, 106:217003, May 2011.
- [68] Marco Marín-Suárez, Joonas T. Peltonen, and Jukka P. Pekola. Active quasiparticle suppression in a non-equilibrium superconductor. *Nano Lett.*, 20(7):5065, 2020.
- [69] J. P. Pekola, V. F. Maisi, S. Kafanov, N. Chekurov, A. Kemppinen, Yu. A. Pashkin, O.-P. Saira, M. Möttönen, and J. S. Tsai. Environment-assisted tunneling as an origin of the dynes density of states. *Phys. Rev. Lett.*, 105:026803, Jul 2010.
- [70] D. V. Anghel, A. Luukanen, and J. P. Pekola. Performance of cryogenic microbolometers and calorimeters with on-chip coolers. *Applied Physics Letters*, 78(4):556–558, 2001.
- [71] Leon N. Cooper. Superconductivity in the neighborhood of metallic contacts. *Phys. Rev. Lett.*, 6:689–690, Jun 1961.
- [72] G. E. Blonder, M. Tinkham, and T. M. Klapwijk. Transition from metallic to tunneling regimes in superconducting microconstrictions: Excess current, charge imbalance, and supercurrent conversion. *Phys. Rev. B*, 25:4515–4532, Apr 1982.
- [73] A. F. Andreev. The thermal conductivity of the intermediate state in superconductors. *Sov. Phys. JETP*, 19:1228, 1964.
- [74] T. M. Klapwijk. Proximity effect from an andreev perspective. *Journal of Superconductivity*, 17:593, 2004.
- [75] Gert-Ludwig Ingold and Yu. V. Nazarov. Charge tunneling rates in ultra-small junctions. *arXiv:cond-mat/0508728*, 2005.
- [76] S. Gasparinetti, K. L. Viisanen, O.-P. Saira, T. Faivre, M. Arzeo, M. Meschke, and J. P. Pekola. Fast electron thermometry for ultrasensitive calorimetric detection. *Phys. Rev. Applied*, 3:014007, Jan 2015.
- [77] Klaara L Viisanen, Samu Suomela, Simone Gasparinetti, Olli-Pentti Saira, Joachim Ankerhold, and Jukka P Pekola. Incomplete measurement of work in a dissipative two level system. *New Journal of Physics*, 17(5):055014, may 2015.
- [78] Klaara Viisanen. *Fast thermometry and energy relaxation measurements on metallic calorimeters*. phdthesis, Aalto Univ., 2020.
- [79] J P Pekola, P Solinas, A Shnirman, and D V Averin. Calorimetric measurement of work in a quantum system. *New Journal of Physics*, 15(11):115006, nov 2013.
- [80] Yu. A. Pashkin, Y. Nakamura, and J. S. Tsai. Room-temperature al single-electron transistor made by electron-beam lithography. *Appl. Phys. Lett.*, 76:2256, 2000.
- [81] Jukka P. Pekola, Olli-Pentti Saira, Ville F. Maisi, Antti Kemppinen, Mikko Möttönen, Yuri A. Pashkin, and Dmitri V. Averin. Single-electron current sources: Toward a refined definition of the ampere. *Rev. Mod. Phys.*, 85:1421–1472, Oct 2013.

- [82] M. Meschke, A. Kemppinen, and J. P. Pekola. Accurate coulomb block-adethermometry up to 60 kelvin. *Phil. Trans. R. Soc. A*, 374:20150052, 2015.
- [83] F. Pobell. *Matter and methods at low temperaturess*, 3rd ed. Springer, 2007.
- [84] J. P. Pekola and J. P. Kauppinen. Insertable dilution refrigerator for characterization of mesoscopic samples. *Cryogenics*, 34(10):843, 1994.
- [85] J. P. Pekola, K. P. Hirvi, J. P. Kauppinen, and M. A. Paalanen. Thermometry by arrays of tunnel junctions. *Phys. Rev. Lett.*, 73:2903–2906, Nov 1994.
- [86] O. M. Hahtela, A. Kemppinen, J. Lehtinen, A. J. Manninen, E. Mykkänen, M. Prunnila, N. Yurttagul, F. Blanchet, M. Gramich, B. Karimi, E. T. Mannila, J. Muhojoki, J. T. Peltonen, and J. P. Pekola. Coulomb blockade thermometry on a wide temperature range. *Conference on Precision Electromagnetic Measurements (CPEM)*, pages 1–2, 2020.
- [87] Olli-Pentti Saira. *Electrostatic control of quasiparticle transport in superconducting hybrid nanostructures*. phdthesis, 2013.
- [88] Jorden Senior. *Heat transport in superconducting quantum circuits*. phdthesis, Aalto Univ., 2019.
- [89] John Clarke and Frank K. Wilhelm. Superconducting quantum bits. *Nature*, 453:1031–1042, 2008.
- [90] Morten Kjaergaard, Mollie E. Schwartz, Jochen Braumüller, Philip Krantz, Joel I.-J. Wang, Simon Gustavsson, and William D. Oliver. Superconducting qubits: Current state of play. *Annual Review of Condensed Matter Physics*, 11(1):369–395, 2020.
- [91] A. Wallraff, D. I. Schuster, A. Blais, L. Frunzio, R.-S. Huang, J. Majer, S. Kumar, S. M. Girvin, and R. J. Schoelkopf. Strong coupling of a single photon to a superconducting qubit using circuit quantum electrodynamics. *Nature*, 431:162, 2004.
- [92] Matti Partanen, Jan Goetz, Kuan Yen Tan, Kassius Kohvakka, Vasilii Sevriuk, Russell E. Lake, Roope Kokkoniemi, Joni Ikonen, Dibyendu Hazra, Akseli Mäkinen, Eric Hyyppä, Leif Grönberg, Visa Vesterinen, Matti Silveri, and Mikko Möttönen. Exceptional points in tunable superconducting resonators. *Phys. Rev. B*, 100:134505, Oct 2019.
- [93] Olivier Maillet, Diego Subero, Joonas T. Peltonen, Dmitry S. Golubev, and Jukka P. Pekola. Electric field control of radiative heat transfer in a superconducting circuit. *Nat. Commun.*, 11:4326, 2020.
- [94] Y. Nakamura, Yu. A. Pashkin, and J. S. Tsai. Coherent control of macroscopic quantum states in a single-cooper-pair box. *Nature*, 398:786–788, 1999.
- [95] J. E. Mooij, T. P. Orlando, L. Levitov, Lin Tian, Caspar H. van der Wal, and Seth Lloyd. Josephson persistent-current qubit. *Science*, 258(5430):1036–1039, 1999.
- [96] T. P. Orlando, J. E. Mooij, Lin Tian, Caspar H. van der Wal, L. S. Levitov, Seth Lloyd, and J. J. Mazo. Superconducting persistent-current qubit. *Phys. Rev. B*, 60:15398–15413, Dec 1999.
- [97] Pauli Virtanen, F. Sebastián Bergeret, Juan Carlos Cuevas, and Tero T. Heikkilä. Linear ac response of diffusive sns junctions. *Phys. Rev. B*, 83:144514, Apr 2011.

- [98] Patrick P Hofer, Martí Perarnau-Llobet, L David M Miranda, Géraldine Haack, Ralph Silva, Jonatan Bohr Brask, and Nicolas Brunner. Markovian master equations for quantum thermal machines: local versus global approach. *New Journal of Physics*, 19(12):123037, dec 2017.
- [99] Ángel Rivas, A. Douglas K. Plato, Susana F. Huelga, and Martin B. Plenio. Markovian master equations: a critical study. *New Journal of Physics*, 12(11):113032, nov 2010.
- [100] Erik Aurell and Federica Montana. Thermal power of heat flow through a qubit. *Phys. Rev. E*, 99:042130, Apr 2019.
- [101] L Magazzù and M Grifoni. Transmission spectra of an ultrastrongly coupled qubit-dissipative resonator system. *Journal of Statistical Mechanics: Theory and Experiment*, 2019(10):104002, oct 2019.
- [102] Gabriele De Chiara, Gabriel Landi, Adam Hewgill, Brendan Reid, Alessandro Ferraro, Augusto J Roncaglia, and Mauro Antezza. Reconciliation of quantum local master equations with thermodynamics. *New Journal of Physics*, 20(11):113024, nov 2018.
- [103] Adam Hewgill, Gabriele De Chiara, and Alberto Imparato. Quantum thermodynamically consistent local master equations. *Phys. Rev. Research*, 3:013165, Feb 2021.
- [104] Amikam Levy and Ronnie Kosloff. The local approach to quantum transport may violate the second law of thermodynamics. *EPL (Europhysics Letters)*, 107(2):20004, jul 2014.
- [105] Jake Iles-Smith, Neill Lambert, and Ahsan Nazir. Environmental dynamics, correlations, and the emergence of noncanonical equilibrium states in open quantum systems. *Phys. Rev. A*, 90:032114, Sep 2014.
- [106] T Motz, M Wiedmann, J T Stockburger, and J Ankerhold. Rectification of heat currents across nonlinear quantum chains: a versatile approach beyond weak thermal contact. *New Journal of Physics*, 20(11):113020, nov 2018.
- [107] Marco Cattaneo, Gian Luca Giorgi, Sabrina Maniscalco, and Roberta Zambrini. Local versus global master equation with common and separate baths: superiority of the global approach in partial secular approximation. *New Journal of Physics*, 21(11):113045, nov 2019.
- [108] M. Terraneo, M. Peyrard, and G. Casati. Controlling the energy flow in nonlinear lattices: A model for a thermal rectifier. *Phys. Rev. Lett.*, 88:094302, Feb 2002.
- [109] Baowen Li, Lei Wang, and Giulio Casati. Thermal diode: Rectification of heat flux. *Phys. Rev. Lett.*, 93:184301, Oct 2004.
- [110] Teemu Ojanen. Selection-rule blockade and rectification in quantum heat transport. *Phys. Rev. B*, 80:180301, Nov 2009.
- [111] Dvira Segal and Abraham Nitzan. Spin-boson thermal rectifier. *Phys. Rev. Lett.*, 94:034301, Jan 2005.
- [112] Björn Sothmann, Rafael Sánchez, Andrew N. Jordan, and Markus Büttiker. Rectification of thermal fluctuations in a chaotic cavity heat engine. *Phys. Rev. B*, 85:205301, May 2012.
- [113] Rafael Sánchez, Björn Sothmann, and Andrew N Jordan. Heat diode and engine based on quantum hall edge states. *New Journal of Physics*, 17(7):075006, jul 2015.

- [114] Tomi Ruokola, Teemu Ojanen, and Antti-Pekka Jauho. Thermal rectification in nonlinear quantum circuits. *Phys. Rev. B*, 79:144306, Apr 2009.
- [115] Rafael Sánchez, Björn Sothmann, and Andrew N. Jordan. Effect of incoherent scattering on three-terminal quantum hall thermoelectrics. *Physica E: Low-dimensional Systems and Nanostructures*, 75:86–92, 2016.
- [116] Andreu Riera-Campeny, Mohammad Mehboudi, Marisa Pons, and Anna Sanpera. Dynamically induced heat rectification in quantum systems. *Phys. Rev. E*, 99:032126, Mar 2019.
- [117] T Motz, M Wiedmann, J T Stockburger, and J Ankerhold. Rectification of heat currents across nonlinear quantum chains: a versatile approach beyond weak thermal contact. *New Journal of Physics*, 20(11):113020, nov 2018.
- [118] Cahit Kargı, M. Tahir Naseem, Tomáš Opatrný, Özgür E. Müstecaplıoğlu, and Gershon Kurizki. Quantum optical two-atom thermal diode. *Phys. Rev. E*, 99:042121, Apr 2019.
- [119] Lennart Bours, Björn Sothmann, Matteo Carrega, Elia Strambini, Alessandro Braggio, Ewelina M. Hankiewicz, Laurens W. Molenkamp, and Francesco Giazotto. Phase-tunable thermal rectification in the topological squirt. *Phys. Rev. Applied*, 11:044073, Apr 2019.
- [120] Donald Goury and Rafael Sánchez. Reversible thermal diode and energy harvester with a superconducting quantum interference single-electron transistor. *Appl. Phys. Lett.*, 115:092601, 2019.
- [121] Bibek Bhandari, Paolo Andrea Erdman, Rosario Fazio, Elisabetta Paladino, and Fabio Taddei. Thermal rectification through a nonlinear quantum resonator. *Phys. Rev. B*, 103:155434, Apr 2021.
- [122] C. Starr. The copper oxide rectifier. *Physics*, 7:15, 1936.
- [123] C. W. Chang, D. Okawa, A. Majumdar, and A. Zettl. Solid-state thermal rectifier. *Science*, 314:1121–1124, 2006.
- [124] R Scheibner, M König, D Reuter, A D Wieck, C Gould, H Buhmann, and L W Molenkamp. Quantum dot as thermal rectifier. *New Journal of Physics*, 10(8):083016, aug 2008.
- [125] Maria José Martínez-Pérez, Antonio Fornieri, and Francesco Giazotto. Rectification of electronic heat current by a hybrid thermal diode. *Nature Nanotech.*, 10:303–307, 2015.
- [126] Haidong Wang, Shiqian Hu, Koji Takahashi, Xing Zhang Hiroshi Takematsu, and Jie Chen. Experimental study of thermal rectification in suspended monolayer graphene. *Nat. Commun.*, 8:15843, 2017.
- [127] R. Alicki and R. Kosloff. *Thermodynamics in the Quantum Regime*. Number pp. 1-33. Springer, Cham, 2018.
- [128] Michele Campisi and Rosario Fazio. The power of a critical heat engine. *Nat. Commun.*, 7:11895, 2016.
- [129] Patrick P. Hofer, J.-R. Souquet, and A. A. Clerk. Quantum heat engine based on photon-assisted cooper pair tunneling. *Phys. Rev. B*, 93:041418, Jan 2016.
- [130] Ronnie Kosloff and Amikam Levy. Quantum heat engines and refrigerators: Continuous devices. *Annu. Rev. Phys. Chem.*, 65(1):365–393, 2014. PMID: 24689798.

- [131] M. O. Scully, M. S. Zubairy, G. S. Agarwal, and H. Walther. Extracting work from a single heat bath via vanishing quantum coherence. *Science*, 299:862, 2003.
- [132] H. T. Quan, Yu-xi Liu, C. P. Sun, and Franco Nori. Quantum thermodynamic cycles and quantum heat engines. *Phys. Rev. E*, 76:031105, Sep 2007.
- [133] Patrick P. Hofer and Björn Sothmann. Quantum heat engines based on electronic mach-zehnder interferometers. *Phys. Rev. B*, 91:195406, May 2015.
- [134] G. Marchegiani, P. Virtanen, F. Giazotto, and M. Campisi. Self-oscillating josephson quantum heat engine. *Phys. Rev. Applied*, 6:054014, Nov 2016.
- [135] Johannes Roßnagel, Samuel T. Dawkins, Karl N. Tolazzi, Obinna Abah, Eric Lutz, Ferdinand Schmidt-Kaler, and Kilian Singer. A single-atom heat engine. *Science*, 352:325, 2016.
- [136] Venu Mehta and Ramandeep S. Johal. Quantum otto engine with exchange coupling in the presence of level degeneracy. *Phys. Rev. E*, 96:032110, Sep 2017.
- [137] Raam Uzdin, Amikam Levy, and Ronnie Kosloff. Equivalence of quantum heat machines, and quantum-thermodynamic signatures. *Phys. Rev. X*, 5:031044, Sep 2015.
- [138] Nicole Yunger Halpern, Christopher David White, Sarang Gopalakrishnan, and Gil Refael. Quantum engine based on many-body localization. *Phys. Rev. B*, 99:024203, Jan 2019.
- [139] A V Dodonov, D Valente, and T Werlang. Quantum power boost in a nonstationary cavity-QED quantum heat engine. *Journal of Physics A: Mathematical and Theoretical*, 51(36):365302, jul 2018.
- [140] Yuji Shirai, Kazunari Hashimoto, Ryuta Tezuka, Chikako Uchiyama, and Naomichi Hatano. Non-markovian effect on quantum otto engine: Role of system-reservoir interaction. *Phys. Rev. Research*, 3:023078, Apr 2021.
- [141] Obinna Abah and Eric Lutz. Optimal performance of a quantum otto refrigerator. *Europhys. Lett.*, 113(6):60002, mar 2016.
- [142] Kay Brandner and Udo Seifert. Periodic thermodynamics of open quantum systems. *Phys. Rev. E*, 93:062134, Jun 2016.
- [143] A. O. Niskanen, Y. Nakamura, and J. P. Pekola. Information entropic superconducting microcooler. *Phys. Rev. B*, 76:174523, Nov 2007.
- [144] Patrick P. Hofer, Martí Perarnau-Llobet, Jonatan Bohr Brask, Ralph Silva, Marcus Huber, and Nicolas Brunner. Autonomous quantum refrigerator in a circuit qed architecture based on a josephson junction. *Phys. Rev. B*, 94:235420, Dec 2016.
- [145] David Sánchez, Rafael Sánchez, Rosa López, and Björn Sothmann. Nonlinear chiral refrigerators. *Phys. Rev. B*, 99:245304, Jun 2019.
- [146] M Tahir Naseem, Avijit Misra, and Özgür E Müstecaplıoğlu. Two-body quantum absorption refrigerators with optomechanical-like interactions. *Quantum Science and Technology*, 5(3):035006, jun 2020.
- [147] Obinna Abah, Mauro Paternostro, and Eric Lutz. Shortcut-to-adiabaticity quantum otto refrigerator. *Phys. Rev. Research*, 2:023120, May 2020.
- [148] Andrea Solfanelli, Marco Falsetti, and Michele Campisi. Nonadiabatic single-qubit quantum otto engine. *Phys. Rev. B*, 101:054513, Feb 2020.

- [149] J. P. Pekola, D. S. Golubev, and D. V. Averin. Maxwell's demon based on a single qubit. *Phys. Rev. B*, 93:024501, Jan 2016.
- [150] R Alicki. The quantum open system as a model of the heat engine. *J. Phys. A: Math. Gen.*, 12(5):L103, may 1979.
- [151] Sai Vinjanampathy and Janet Anders. Quantum thermodynamics. *Contemporary Physics*, 57(4):545–579, 2016.
- [152] Saar Rahav, Upendra Harbola, and Shaul Mukamel. Heat fluctuations and coherences in a quantum heat engine. *Phys. Rev. A*, 86:043843, Oct 2012.
- [153] Alexander Streltsov, Gerardo Adesso, and Martin B. Plenio. Colloquium: Quantum coherence as a resource. *Rev. Mod. Phys.*, 89:041003, Oct 2017.
- [154] J Jaramillo, M Beau, and A del Campo. Quantum supremacy of many-particle thermal machines. *New J. Phys.*, 18(7):075019, jul 2016.
- [155] V. Holubec and Tomáš Novotný. Effects of noise-induced coherence on the performance of quantum absorption refrigerators. *J. Low Temp. Phys.*, 192:147, 2018.
- [156] Patrice A. Camati, Jonas F. G. Santos, and Roberto M. Serra. Coherence effects in the performance of the quantum otto heat engine. *Phys. Rev. A*, 99:062103, Jun 2019.
- [157] Ronnie Kosloff and Tova Feldmann. Discrete four-stroke quantum heat engine exploring the origin of friction. *Phys. Rev. E*, 65:055102, May 2002.
- [158] George Thomas and Ramandeep S. Johal. Friction due to inhomogeneous driving of coupled spins in a quantum heat engine. *Eur. Phys. J. B*, 87:166, 2014.
- [159] Michael Kilgour and Dvira Segal. Coherence and decoherence in quantum absorption refrigerators. *Phys. Rev. E*, 98:012117, Jul 2018.
- [160] J. P. Pekola, V. Brosco, M. Möttönen, P. Solinas, and A. Shnirman. Decoherence in adiabatic quantum evolution: Application to cooper pair pumping. *Phys. Rev. Lett.*, 105:030401, Jul 2010.
- [161] A Alecce, F Galve, N Lo Gullo, L Dell'Anna, F Plastina, and R Zambrini. Quantum otto cycle with inner friction: finite-time and disorder effects. *New J. Phys.*, 17(7):075007, jul 2015.
- [162] S. Deng, A. Chenu, P. Diao, F. Li, S. Yu, I. Coulamy, A. del Campo, and H. Wu. Superadiabatic quantum friction suppression infinite-time thermodynamics. *Sci. Adv.*, 4:5909, 2018.
- [163] Ken Funo, Neill Lambert, Bayan Karimi, Jukka P. Pekola, Yuta Masuyama, and Franco Nori. Speeding up a quantum refrigerator via counterdiabatic driving. *Phys. Rev. B*, 100:035407, Jul 2019.
- [164] Erik Torrontegui, Sara Ibáñez, Sofía Martínez-Garaot, Michele Modugno, Adolfo del Campo, David Guéry-Odelin, Andreas Ruschhaupt, Xi Chen, and Juan Gonzalo Muga. Chapter 2 - shortcuts to adiabaticity. In Ennio Arimondo, Paul R. Berman, and Chun C. Lin, editors, *Advances in Atomic, Molecular, and Optical Physics*, volume 62 of *Advances In Atomic, Molecular, and Optical Physics*, pages 117–169. Academic Press, 2013.
- [165] Xi Chen, A. Ruschhaupt, S. Schmidt, A. del Campo, D. Guéry-Odelin, and J. G. Muga. Fast optimal frictionless atom cooling in harmonic traps: Shortcut to adiabaticity. *Phys. Rev. Lett.*, 104:063002, Feb 2010.

- [166] E. Torrontegui, S. Martínez-Garaot, A. Ruschhaupt, and J. G. Muga. Shortcuts to adiabaticity: Fast-forward approach. *Phys. Rev. A*, 86:013601, Jul 2012.
- [167] Sebastian Deffner, Christopher Jarzynski, and Adolfo del Campo. Classical and quantum shortcuts to adiabaticity for scale-invariant driving. *Phys. Rev. X*, 4:021013, Apr 2014.
- [168] M. H. Devoret and R. J. Schoelkopf. Superconducting circuits for quantum information: an outlook. *Science*, 339:1169, 2013.
- [169] Alexandre Blais, Ren-Shou Huang, Andreas Wallraff, S. M. Girvin, and R. J. Schoelkopf. Cavity quantum electrodynamics for superconducting electrical circuits: An architecture for quantum computation. *Phys. Rev. A*, 69:062320, Jun 2004.
- [170] T. Hime, P. A. Reichardt, B. L. T. Plourde, T. L. Robertson, C.-E. Wu, A. V. Ustinov, and J. Clarke. Solid-state qubits with current-controlled coupling. *Science*, 314:1427, 2006.
- [171] J. Majer, J. M. Chow, J. M. Gambetta, Jens Koch, B. R. Johnson, J. A. Schreier, L. Frunzio, D. I. Schuster, A. A. Houck, A. Wallraff, A. Blais, M. H. Devoret, S. M. Girvin, and R. J. Schoelkopf. Coupling superconducting qubits via a cavity bus. *Nature*, 449:443, 2007.
- [172] J. M. Gambetta, A. A. Houck, and Alexandre Blais. Superconducting qubit with purcell protection and tunable coupling. *Phys. Rev. Lett.*, 106:030502, Jan 2011.
- [173] Gengyan Zhang, Yanbing Liu, James J. Raftery, and Andrew A. Houck. Suppression of photon shot noise dephasing in a tunable coupling superconducting qubit. *npj Quantum Information*, 3:1, 2017.
- [174] Dvir Kafri, Chris Quintana, Yu Chen, Alireza Shabani, John M. Martinis, and Hartmut Neven. Tunable inductive coupling of superconducting qubits in the strongly nonlinear regime. *Phys. Rev. A*, 95:052333, May 2017.
- [175] Bao-qing Guo, Tong Liu, and Chang-shui Yu. Quantum thermal transistor based on qubit-qutrit coupling. *Phys. Rev. E*, 98:022118, Aug 2018.
- [176] Dario Ferraro, Michele Campisi, Gian Marcello Andolina, Vittorio Pellegrini, and Marco Polini. High-power collective charging of a solid-state quantum battery. *Phys. Rev. Lett.*, 120:117702, Mar 2018.
- [177] Pranav Mundada, Gengyan Zhang, Thomas Hazard, and Andrew Houck. Suppression of qubit crosstalk in a tunable coupling superconducting circuit. *Phys. Rev. Applied*, 12:054023, Nov 2019.
- [178] P. Scarlino, D. J. van Woerkom, U. C. Mendes, J. V. Koski, A. J. Landig, C. K. Andersen, S. Gasparinetti, C. Reichl, K. Ensslin W. Wegscheider, T. Ihn, A. Blais, and A. Wallraff. Coherent microwave-photon-mediated coupling between a semiconductor and a superconducting qubit. *Nat. Commun.*, 10:3011, 2019.
- [179] John Goold, Marcus Huber, Arnau Riera, Lídia del Rio, and Paul Skrzypczyk. The role of quantum information in thermodynamics—a topical review. *J. Phys. A: Math. Theor.*, 49:143001, 2016.
- [180] D. V. Averin and R. Fazio. Active suppression of dephasing in josephson-junction qubits. *JETP Lett.*, 78:664, 2003.
- [181] James P. Clemens, Shabnam Siddiqui, and Julio Gea-Banacloche. Quantum error correction against correlated noise. *Phys. Rev. A*, 69:062313, Jun 2004.

- [182] E. Novais and Harold U. Baranger. Decoherence by correlated noise and quantum error correction. *Phys. Rev. Lett.*, 97:040501, Jul 2006.
- [183] Yong Hu, Zheng-Wei Zhou, Jian-Ming Cai, and Guang-Can Guo. Decoherence of coupled josephson charge qubits due to partially correlated low-frequency noise. *Phys. Rev. A*, 75:052327, May 2007.
- [184] Rochus Klesse and Sandra Frank. Quantum error correction in spatially correlated quantum noise. *Phys. Rev. Lett.*, 95:230503, Nov 2005.
- [185] F. Yoshihara, Y. Nakamura, and J. S. Tsai. Correlated flux noise and decoherence in two inductively coupled flux qubits. *Phys. Rev. B*, 81:132502, Apr 2010.
- [186] Jan Jeske and Jared H. Cole. Derivation of markovian master equations for spatially correlated decoherence. *Phys. Rev. A*, 87:052138, May 2013.
- [187] Gonzalo Manzano, Gian-Luca Giorgi, Rosario Fazio, and Roberta Zambrini. Boosting the performance of small autonomous refrigerators via common environmental effects. *New Journal of Physics*, 21(12):123026, dec 2019.
- [188] Gabriele De Chiara and Mauro Antezza. Quantum machines powered by correlated baths. *Phys. Rev. Research*, 2:033315, Aug 2020.
- [189] Zachary G. Nicolaou, Michael Sebek, István Z. Kiss, and Adilson E. Motter. Coherent dynamics enhanced by uncorrelated noise. *Phys. Rev. Lett.*, 125:094101, Aug 2020.
- [190] Håkon Brox, Joakim Bergli, and Yuri M Galperin. Bloch-sphere approach to correlated noise in coupled qubits. *Journal of Physics A: Mathematical and Theoretical*, 45(45):455302, oct 2012.
- [191] Z. K. Minev, S. O. Mundhada, S. Shankar, P. Reinhold, R. Gutiérrez-Jáuregui, R. J. Schoelkopf, M. Mirrahimi, H. J. Carmichael, and M. H. Devoret. To catch and reverse a quantum jump mid-flight. *Nature*, 570:200, 2019.
- [192] R. Vijay, D. H. Slichter, and I. Siddiqi. Observation of quantum jumps in a superconducting artificial atom. *Phys. Rev. Lett.*, 106:110502, Mar 2011.
- [193] T. T. Heikkilä and Francesco Giazotto. Phase sensitive electron-phonon coupling in a superconducting proximity structure. *Phys. Rev. B*, 79:094514, Mar 2009.
- [194] Danilo Nikolic, Denis M. Basko, and Wolfgang Belzig. Electron cooling by phonons in superconducting proximity structures. *Phys. Rev. B*, 102:214514, Dec 2020.
- [195] H. Pothier, S. Guéron, Norman O. Birge, D. Esteve, and M. H. Devoret. Energy distribution function of quasiparticles in mesoscopic wires. *Phys. Rev. Lett.*, 79:3490–3493, Nov 1997.
- [196] K. L. Viisanen and J. P. Pekola. Anomalous electronic heat capacity of copper nanowires at sub-kelvin temperatures. *Phys. Rev. B*, 97:115422, Mar 2018.
- [197] R A Lewis. A review of terahertz detectors. *Journal of Physics D: Applied Physics*, 52(43):433001, aug 2019.
- [198] Jian Wei, David Olaya, Boris S. Karasik, Sergey V. Pereverzev, Andrei V. Sergeev, and Michael E. Gershenson. Ultrasensitive hot-electron nanobolometers for terahertz astrophysics. *Nature Nanotech.*, 3:496–500, 2008.

- [199] M. Nahum and John M. Martinis. Ultrasensitive-hot-electron microbolometer. *Appl. Phys. Lett.*, 63:3075, 1993.
- [200] N. Didier, Ya. M. Blanter, and F. W. J. Hekking. Quantum dynamics of a driven three-level josephson-atom maser. *Phys. Rev. B*, 82:214507, Dec 2010.
- [201] J. Q. You, Yu-xi Liu, C. P. Sun, and Franco Nori. Persistent single-photon production by tunable on-chip micromaser with a superconducting quantum circuit. *Phys. Rev. B*, 75:104516, Mar 2007.
- [202] Bijay Kumar Agarwalla, Manas Kulkarni, and Dvira Segal. Photon statistics of a double quantum dot micromaser: Quantum treatment. *Phys. Rev. B*, 100:035412, Jul 2019.
- [203] George Thomas, Azat Gubaydullin, Dmitry S. Golubev, and Jukka P. Pekola. Thermally pumped on-chip maser. *Phys. Rev. B*, 102:104503, Sep 2020.
- [204] F. Brange, P. Samuelsson, B. Karimi, and J. P. Pekola. Nanoscale quantum calorimetry with electronic temperature fluctuations. *Phys. Rev. B*, 98:205414, Nov 2018.
- [205] M. A. Laakso, T. T. Heikkilä, and Yuli V. Nazarov. Theory of temperature fluctuation statistics in superconductor-normal metal tunnel structures. *Phys. Rev. B*, 85:184521, May 2012.
- [206] T. M. Buehler, D. J. Reilly, R. P. Starrett, Andrew D. Greentree, A. R. Hamilton, A. S. Dzurak, and R. G. Clark. Single-shot readout with the radio-frequency single-electron transistor in the presence of charge noise. *Applied Physics Letters*, 86(14):143117, 2005.
- [207] Andrew Guthrie, Christoforus Dimas Satrya, Yu-Cheng Chang, Paul Menczel, Franco Nori, and Jukka P. Pekola. A cooper-pair box architecture for cyclic quantum heat engines. *arXiv:2109.03023*, September 2021.
- [208] Rishabh Upadhyay, George Thomas, Yu-Cheng Chang, Dmitry S. Golubev, Andrew Guthrie, Azat Gubaydullin, Joonas T. Peltonen, and Jukka P. Pekola. Robust strong coupling architecture in circuit quantum electrodynamics. *arXiv:2107.11135*, July 2021.





ISBN 978-952-64-0737-1 (printed)  
ISBN 978-952-64-0738-8 (pdf)  
ISSN 1799-4934 (printed)  
ISSN 1799-4942 (pdf)

**Aalto University**  
**School of Science**  
**Department of Applied Physics**  
[www.aalto.fi](http://www.aalto.fi)

BUSINESS +  
ECONOMY

ART +  
DESIGN +  
ARCHITECTURE

SCIENCE +  
TECHNOLOGY

CROSSOVER

DOCTORAL  
THESES